

**Incorporating Green Chemistry Principles in  
Heterogeneous Catalysis Operations**

by

Deborah Boroughs Bacik

A dissertation submitted to the Graduate Faculty of  
Auburn University  
in partial fulfillment of the  
requirements for the Degree of  
Doctor of Philosophy

Auburn, Alabama  
August 6, 2011

Keywords: green chemistry, nanoscale synthesis, catalytic hydrodechlorination,  
supercritical fluids, hydrogen peroxide, Fischer-Tropsch synthesis

Copyright 2011 by Deborah Boroughs Bacik

Approved by

Christopher B. Roberts, Chair, Professor of Chemical Engineering  
Virginia A. Davis, Associate Professor of Chemical Engineering  
Mario R. Eden, Associate Professor of Chemical Engineering  
Steven Taylor, Professor of Biosystems Engineering

## Abstract

Many commercial processes for the production of chemicals involve harsh organic solvents as well as numerous by-products that are detrimental to the environment. For many years it was common practice to implement a process in manufacturing, without consideration of the environmental impact, simply because the process worked. The twelve principles of green chemistry, which are widely accepted by the scientific community, present an ideology for addressing these environmental concerns. The twelve principles include several important topics such as the incorporation of benign solvents, solvent-free processes, highly selective catalysts, waste reduction and prevention, and the design of less energy-intensive chemical processes. The focus of this dissertation involved the substitution of harsh organic solvents with more environmentally benign solvents, the development and use of more selective catalysts for an environmental application, the development of a more atom-efficient synthetic approach for the production of commodity chemicals, and the synthesis of petrochemicals from a renewable feedstock.

This work presents the development of more selective catalysts from a green approach, and examines the activity of these catalysts in the remediation of soil and groundwater contaminated with chlorinated compounds. Trichloroethylene (TCE) is one of the most common organic pollutants detected in both soil and groundwater. TCE is a potent carcinogen and is resistant to the natural attenuation process. Therefore, the

presence of TCE in the environment is a significant health and safety concern. Catalytic hydrodechlorination is an innovative technology developed specifically for the remediation of soil and groundwater contaminated with chlorinated hydrocarbons. The aqueous phase synthesis of sodium carboxymethyl cellulose (CMC) stabilized palladium (Pd) nanoparticles and their application as molecular catalysts in the hydrodechlorination of TCE has been examined. Liu et al. (2008) previously studied the batch hydrodechlorination of TCE using unsupported CMC-Pd nanoparticle catalysts dispersed within the aqueous phase. Despite the high activity of these unsupported catalysts for TCE degradation, a homogeneously dispersed Pd catalyst is not practical for any environmental application. Thus, the ability to support and retain the very expensive Pd nanoparticles is essential. In this study, all of the supported Pd nanoparticle catalysts had a lower catalytic activity than the unsupported particles that were homogeneously dispersed within the aqueous solutions. Even so, the supported Pd nanoparticles showed considerable activity towards TCE degradation and provided an opportunity to efficiently retain and recover the active Pd catalyst material.

Also presented in this dissertation, is the successful utilization of a benign oxidant in a more atom-efficient synthetic approach for the production of commodity chemicals. Hydrogen peroxide ( $\text{H}_2\text{O}_2$ ) is generally considered a benign oxidant that is a promising alternative to conventional oxidants. The current method for producing  $\text{H}_2\text{O}_2$  involves a complicated anthraquinone (AQ) process. Unfortunately, this route requires multiple unit operations, is highly energy intensive, and results in the generation of several significant waste streams. The AQ route, although successful, certainly is not green and is far too costly to allow for use of  $\text{H}_2\text{O}_2$  as a benign oxidant in chemical

processing. The most efficient method for H<sub>2</sub>O<sub>2</sub> production, in terms of the principles of green chemistry, is the direct reaction of hydrogen and oxygen. Three probe reactions were examined in order to explore the in-situ generation of H<sub>2</sub>O<sub>2</sub>. In addition, experimental information on the in-situ generation of hydrogen peroxide for the production of pyridine oxide was integrated with process systems engineering analysis to enable systematic comparison between the different processing options. Analysis of the optimized models shows that in-situ generation of H<sub>2</sub>O<sub>2</sub> results in a more energy efficient and less environmentally harmful alternative to the conventional approach.

The synthesis of petrochemicals using a renewable feedstock, as proposed in the twelve principles, is also presented in this work. C<sub>1</sub> chemistry is an area of development that utilizes molecules containing a single carbon atom not only for the synthesis of many valuable organic chemicals and intermediates, but also as an alternative feedstock in the production of fuels. These C<sub>1</sub> molecules can be obtained from resources such as biomass, coal, and natural gas. Fischer-Tropsch synthesis is an alternative process that was developed in Germany during the 1920s for the catalytic conversion of synthesis gas, or syngas (a mixture of CO and H<sub>2</sub>), to transportation fuels and other value-added chemicals. Syngas can be derived from biomass, which is an excellent option since it is both a renewable and sustainable source of energy. Thus, employing Fischer-Tropsch Synthesis (FTS) with biomass-derived syngas is an excellent and green alternative for the petrochemical industry.

Conducting FTS under supercritical fluid solvent conditions affords unique opportunities to manipulate the Fischer-Tropsch reaction environment in order to enhance production of liquid fuels and value-added chemicals (such as  $\alpha$ -olefins) from syngas. In

addition, supercritical fluid solvents combine the desirable properties of gas-like diffusion along with liquid-like heat transfer and solubility to overcome several of the current industrial limitations of FTS. The phase behavior of a Fischer-Tropsch reaction feed mixture at both subcritical and supercritical conditions was investigated in order to understand the critical properties of the FTS mixtures. Knowledge of the critical properties for a particular system will allow for the appropriate design of chemical reactors, choice of separation and extraction equipment, and determination of the proper operating conditions. In this study, the critical properties for three specific mole ratios ( $\text{H}_2$ : CO: n-Hexane) were determined, and correlations between the phase behavior of the supercritical Fischer-Tropsch mixtures and the catalytic performance studies under subcritical and supercritical conditions were examined.

Together these investigations show that by incorporating the twelve principles of green chemistry in heterogeneous catalysis operations, it is possible to attain similar results as those obtained from the conventional processing options while reducing the ecological footprint.

## Acknowledgements

First and foremost, I would like to thank my wonderful husband, Matthew Bacik, for his unconditional love and support throughout this endeavor. Thank you for your gracious tolerance of all of the inconveniences, both big and small, which accompanied my educational pursuit. Also, thank you for the countless sacrifices and numerous adjustments made to your plans so that we could remain in the same geographical location. Most of all, I thank you for continually believing in me and my ability to achieve this accomplishment. I couldn't have gotten here without you!

I would also like to express my sincere gratitude to my advisor, Dr. Christopher B. Roberts, for the continued support that he offered throughout my graduate studies at Auburn University. He took note of my abilities, and provided me with the opportunity to reach my potential. I most certainly could not have accomplished my goals without him in my corner, for that I will always be grateful. I would also like to thank each member of my committee for the invaluable pieces of advice offered along the way. They always challenged me to reach for the best of my capabilities. A special thanks to Dr. Mario Eden for our fruitful collaboration and the countless hours he dedicated to the hydrogen peroxide simulation work.

Additionally, I would like to thank both past and current members of the Roberts research group for their insightful discussions and friendship over the years. Specifically,

I would like to thank Dr. Nimir Elbashir and Dr. Juncheng Liu for their particular contributions to portions of this dissertation work. Thanks also to Dr. Chandler McLeod and Dr. Joseph Durham for sharing their laboratory expertise and often times assistance when things were broken. I would also like to express my sincerest gratitude to both Man Zhang and her advisor, Dr. Dongye Zhao, in Civil Engineering for our successful collaboration on the hydrodechlorination work and the contributions that each made to portions of this dissertation work. I would especially like to thank Man Zhang for her friendship and support during the completion of my degree.

Special thanks are due to Brian Schweiker for his willingness to fix anything and fix it quickly. I would also like to thank other members of the Chemical Engineering staff for their kindness, encouragement, and support over the years. These special people include Sue Ellen Abner, Jennifer Harris, Karen Cochran, and Georgetta Dennis. I will never forget your kind hospitality. In addition, I would like to thank Dr. Michael Miller for his assistance with the transmission electron microscopy work.

Last, but certainly not least, I thank my family for their continued support over my lifetime. In particular, I would like to thank my father, Roy Boroughs, for teaching me the importance of a strong work ethic. I also thank my mother, Nancy Boroughs, for constantly cheering me to the finish line. Thanks are due to my brother, Michael Boroughs, for his strong, fighting spirit. You have had one of the most difficult journeys through this life, but always manage to keep your head held high. I also would like to thank my brother, David Boroughs, for his uncanny sense of comedic timing and for teaching me the value of laughter. This dissertation would not have been possible

without each one of you. I dedicate this work to my beautiful daughters, Sophia and Madeleine Bacik. May you always reach for the stars.



## Table of Contents

Abstract.....	ii
Acknowledgements.....	vi
List of Tables .....	xi
List of Figures and Schemes.....	xii
List of Abbreviations .....	xix
Chapter 1: Introduction .....	1
1.1 Introduction to Green Chemistry .....	1
1.2 Green Nanotechnology .....	3
1.3 Green Catalysis .....	5
1.4 Summary of Chapters in Dissertation.....	5
Chapter 2: Synthesis and Application of Pd Nanoparticle Catalysts in the Hydrodechlorination of TCE Using a Green Polysugar Approach.....	8
2.1 Introduction.....	8
2.1.1 Ex-Situ Pump-and-Treat.....	10
2.1.2 In-Situ Treatment .....	11
2.1.3 Monitored Natural Attenuation .....	15
2.1.4 Catalytic Hydrodechlorination .....	16
2.2 Experimental Methods.....	18
2.2.1 Materials.....	18

2.2.2 Experimental Procedures.....	19
2.3 Results and Discussion .....	29
2.3.1 Effect of Capping Ligand .....	29
2.3.2 Effect of Capping Ligand Concentration .....	30
2.3.3 Effect of Synthesis Temperature .....	39
2.3.4 Effect of Ligand Exchange.....	50
2.3.5 Effect of Nanoparticle Processing.....	54
2.4 Hydrodechlorination of TCE .....	62
2.4.1 Unsupported Pd Nanoparticle Catalysts.....	62
2.4.2 Alumina-Supported Pd Nanoparticle Catalysts.....	63
2.5 Hydrodechlorination Kinetics.....	65
2.5.1 Effect of CMC Concentration .....	65
2.5.2 Chloride Evolution .....	75
2.5.3 Catalyst Induction Period .....	75
2.6 XRD Characterization of the Pd Nanoparticle Catalysts on Al <sub>2</sub> O <sub>3</sub> .....	80
2.7 Effect of Catalyst Calcination on TCE Degradation Kinetics .....	87
2.8 Catalyst Stability.....	92
2.9 Effect of Catalyst Reduction Gas Composition.....	95
2.10 Effect of Support Material .....	98
2.11 BET Surface Area Measurements.....	99
2.12 FT-IR Spectroscopic Analysis of Catalysts .....	102
2.13 High Resolution TEM Characterization .....	103
2.14 Conclusions.....	118

Chapter 3: Applications of In-Situ Generated Hydrogen Peroxide in Supercritical Carbon Dioxide Solvent Media.....	119
3.1 Introduction.....	119
3.2 Propylene Epoxidation.....	123
3.2.1 Chlorohydrin Process.....	124
3.2.2 Hydroperoxidation Process.....	125
3.2.1 Direct Oxidation Routes .....	127
3.3 Adipic Acid.....	132
3.4 Pyridine Oxidation .....	136
3.5 Experimental Methods .....	137
3.5.1 Materials .....	137
3.5.2 Apparatus .....	139
3.5.3 Experimental Procedure.....	139
3.5.4 Gas Chromatograph Calibration .....	146
3.6 Results and Discussion .....	147
3.6.1 Propylene Epoxidation.....	147
3.6.2 Oxidation of Cyclohexanone .....	150
3.6.3 Oxidation of Pyridine.....	158
3.6.4 Simulation and Optimization of Pyridine Oxide Production.....	164
3.7 Conclusions.....	171
Chapter 4: Understanding the Phase Behavior and Critical Point Measurements for Fischer-Tropsch Synthesis in Supercritical Hexane Media.....	174
4.1 Introduction.....	174
4.2 Experimental Methods .....	178

4.2.1 Materials .....	178
4.2.2 Apparatus .....	178
4.2.3 Experimental Procedure.....	180
4.3 Results and Discussion .....	183
4.4 Conclusions.....	201
Chapter 5: Conclusions .....	203
References.....	209

## List of Tables

1-1	The Twelve Principles of Green Chemistry .....	7
2-1	Mean particle size and standard deviation for Pd nanoparticles synthesized with (a) CMC capping ligand and (b) PVP capping ligand at various temperatures .....	49
2-2	Average particle size and reaction rate constants for the aqueous phase hydrodechlorination of TCE in the presence of supported and unsupported Pd nanoparticle catalysts synthesized using various amounts of CMC capping agent ...	69
2-3	Initial TOF and catalyst dispersions ( $D_{Pd}$ ) for the aqueous phase hydrodechlorination of TCE in the presence of supported and unsupported Pd nanoparticle catalysts synthesized using various amounts of CMC capping agent .....	70
2-4	Specific surface areas for $Al_2O_3$ and $Al_2O_3$ -supported Pd nanoparticles prepared using various concentrations of CMC capping ligand .....	79
3-1	Control studies for the batch production of adipic acid via the oxidation of cyclohexanone by molecular oxygen .....	151
3-2	Oxidation of cyclohexanone over a Pd/TS-1 catalyst using in-situ generated $H_2O_2$ as the oxidant .....	154
3-3	Energy Analysis for Pyridine Oxidation Processes .....	169
4-1	Experimentally determined critical point data obtained from phase behavior studies .....	187
4-2	The product distributions of SCH-FTS reaction mixture at $240^\circ C$ and 65 bar. Syngas ( $H_2/CO$ ) feed ration is 2:1, the volumetric space velocity is $93.75 hr^{-1}$ and the hexanes to syngas molar ratio is 3 to 1 .....	200

## List of Figures and Schemes

2-1	TEM images of dodecanethiol capped Pd nanoparticles extracted from the aqueous phase where stabilized with (a) 0.15 wt% CMC (b) 0.15 wt% PVP at 20°C.....	31
2-2	Particle size distribution histograms for dodecanethiol capped Pd nanoparticles extracted from the aqueous phase stabilized with both 0.15 wt% CMC and 0.15 wt% PVP at 20°C.....	32
2-3	TEM images of dodecanethiol capped Pd nanoparticles extracted from the aqueous phase where stabilized with (a) 0.075 wt% CMC (b) 0.075 wt% PVP at 20°C.....	34
2-4	Particle size distribution histograms for dodecanethiol capped Pd nanoparticles extracted from the aqueous phase stabilized with both 0.075 wt% CMC and 0.075 wt% PVP at 20°C .....	35
2-5	TEM images of dodecanethiol capped Pd nanoparticles extracted from the aqueous phase where stabilized with (a) 0.05 wt% CMC (b) 0.005 wt% CMC at 20°C .....	36
2-6	Particle size distribution histograms for dodecanethiol capped Pd nanoparticles extracted from the aqueous phase stabilized with both 0.005 wt% CMC and 0.005 wt% PVP at 20°C .....	37
2-7	The effect of CMC concentration on the (a) mean particle diameter and (b) standard deviation of Pd nanoparticles at room temperature.....	38
2-8	TEM images of dodecanethiol capped Pd nanoparticles extracted from the aqueous phase where stabilized with (a) 0.15 wt% CMC (b) 0.15 wt% PVP at 35°C.....	41
2-9	Particle size distribution histograms for dodecanethiol capped Pd nanoparticles extracted from the aqueous phase stabilized with both 0.15 wt% CMC and 0.15 wt% PVP at 35°C.....	42
2-10	TEM images of dodecanethiol capped Pd nanoparticles extracted from the aqueous phase where stabilized with (a) 0.15 wt% CMC (b) 0.15 wt% PVP at 50°C .....	43
2-11	Particle size distribution histograms for dodecanethiol capped Pd nanoparticles extracted from the aqueous phase stabilized with both 0.15 wt% CMC and 0.15 wt% PVP at 50°C .....	44

2-12	TEM images of dodecanethiol capped Pd nanoparticles extracted from the aqueous phase where stabilized with (a) 0.075 wt% CMC (b) 0.075 wt% PVP at 50°C .....	46
2-13	Particle size distribution histograms for dodecanethiol capped Pd nanoparticles extracted from the aqueous phase stabilized with both 0.075 wt% CMC and 0.075 wt% PVP at 50°C .....	47
2-14	Effect of synthesis temperature on the mean particle diameter for Pd nanoparticles synthesized using (a) 0.15 wt% CMC (b) 0.15 wt% PVP in the aqueous phase .....	48
2-15	TEM images of Pd nanoparticles (a) stabilized with 0.15 wt% PVP at 35°C in the aqueous phase, and subsequently (b) extracted from the aqueous phase to the organic phase using dodecanethiol capping agent .....	52
2-16	Particle size distribution histograms for Pd nanoparticles (a) stabilized with 0.15 wt% PVP in the aqueous phase at 35°C, and subsequently (b) extracted from the aqueous phase to the organic phase using dodecanethiol capping agent.....	53
2-17	TEM images of Pd nanoparticles (a) stabilized with 0.15 wt% PVP in the aqueous phase at 50°C, and subsequently (b) extracted from the aqueous phase to the organic phase using dodecanethiol capping agent .....	55
2-18	Particle size distribution histograms for Pd nanoparticles (a) stabilized with 0.15 wt% PVP in the aqueous phase at 50°C, and subsequently (b) extracted from the aqueous phase to the organic phase using dodecanethiol capping agent.....	56
2-19	TEM images of Pd nanoparticles (a) stabilized with 0.075 wt% PVP in the aqueous phase at 50°C, and subsequently (b) extracted from the aqueous phase to the organic phase using dodecanethiol capping agent .....	57
2-20	Particle size distribution histograms for Pd nanoparticles (a) stabilized with 0.075 wt% PVP in the aqueous phase at 50°C, and subsequently (b) extracted from the aqueous phase to the organic phase using dodecanethiol capping agent.....	58
2-21	TEM images of Pd nanoparticles stabilized with 0.005 wt% CMC in the aqueous phase at 20°C (a) before rotary evaporation (b) after rotary evaporation .....	60
2-22	Particle size distribution histograms for Pd nanoparticles stabilized with 0.005 wt% CMC in the aqueous phase at 20°C (a) before rotary evaporation (b) after rotary evaporation.....	61
2-23	Aqueous phase hydrodechlorination of TCE catalyzed by unsupported CMC-stabilized Pd nanoparticles synthesized using a 0.15 wt% CMC solution. Data from the control experiment (only CMC in the system) is presented for comparison with degradation data .....	71

2-24	Plot of $\ln ([TCE]_t/[TCE]_0)$ against time of the aqueous phase hydrodechlorination of TCE catalyzed by unsupported CMC-stabilized Pd nanoparticles synthesized using a 0.15 wt% CMC solution .....	72
2-25	Aqueous phase hydrodechlorination of TCE catalyzed by alumina-supported Pd nanoparticles synthesized using various CMC concentrations. Data from the control experiment (only alumina in the system) is presented for comparison with degradation data .....	73
2-26	Plot of $\ln ([TCE]_t/[TCE]_0)$ against time of the aqueous phase hydrodechlorination of TCE catalyzed by alumina-supported Pd nanoparticles synthesized using various CMC concentrations .....	74
2-27	Plot of $\ln ([TCE]_t/[TCE]_0)$ against time of the aqueous phase hydrodechlorination of TCE catalyzed by alumina-supported Pd nanoparticles synthesized using a 0.05 wt% CMC solution .....	78
2-28	XRD patterns of $Al_2O_3$ and $Al_2O_3$ -supported Pd nanoparticles. Pd loading was 0.33 wt% on the $Al_2O_3$ support material .....	81
2-29	XRD pattern of $Al_2O_3$ support material collected from a broad scan of the material from $10^\circ$ to $85^\circ$ using a Rigaku Miniflex powder X-ray diffractometer .....	82
2-30	XRD pattern of alumina-supported Pd nanoparticles collected from a narrow scan of the catalyst from $80^\circ$ to $85^\circ$ using a Rigaku Miniflex powder X-ray diffractometer. Pd loading was 0.33 wt% on the $Al_2O_3$ support material .....	83
2-31	XRD patterns of $Al_2O_3$ and alumina-supported Pd nanoparticles along with the expected line positions for both $Al_2O_3$ and Pd material. Bragg angles ( $2\theta$ ) from $5^\circ$ to $100^\circ$ were scanned at $0.06^\circ$ with a counting time of 5 seconds at each step .....	85
2-32	XRD patterns of $Al_2O_3$ and alumina-supported Pd nanoparticles along with the expected line position for Pd near $82^\circ$ . Bragg angles ( $2\theta$ ) from $75^\circ$ to $90^\circ$ were scanned at $0.01^\circ$ with a counting time of 10 seconds at each step .....	86
2-33	Effect of calcination conditions on the catalyst activity for the hydrodechlorination of TCE catalyzed by alumina-supported Pd nanoparticles synthesized using a 0.005 wt% CMC solution .....	90
2-34	Plot of $\ln ([TCE]_t/[TCE]_0)$ against time of the aqueous phase hydrodechlorination of TCE catalyzed by alumina-supported Pd nanoparticles synthesized using a 0.005 wt% CMC solution .....	91
2-35	Plot of $\ln ([TCE]_t/[TCE]_0)$ against time of the aqueous phase hydrodechlorination of TCE catalyzed by alumina-supported Pd nanoparticles synthesized using a 0.15	



wt% CMC solution. This study included a total of six degradation reactions, recycling the same catalyst in each run.....	94
2-36 Plot of $\ln ([TCE]_t/[TCE]_0)$ against time of the aqueous phase hydrodechlorination of TCE catalyzed by alumina-supported Pd nanoparticles synthesized using a 0.15 wt% CMC solution. Effect of catalyst reduction gas composition.....	96
2-37 Plot of $\ln ([TCE]_t/[TCE]_0)$ against time of the aqueous phase hydrodechlorination of TCE catalyzed by a conventional alumina-supported Pd catalyst. Initial total TCE concentration was 50 mg/L. Effect of catalyst reduction gas composition.....	97
2-38 Aqueous phase hydrodechlorination of TCE catalyzed by Pd on both $Al_2O_3$ and TS-1 support materials.....	100
2-39 Plot of $\ln ([TCE]_t/[TCE]_0)$ against time of the aqueous phase hydrodechlorination of TCE catalyzed by Pd on both $Al_2O_3$ and TS-1 support materials .....	101
2-40 FT-IR spectrum for CMC-Pd nanoparticles prepared using a 0.15 wt% CMC aqueous solution and calcined at 80°C.....	104
2-41 FT-IR spectrum for CMC-Pd nanoparticles prepared using a 0.15 wt% CMC aqueous solution and calcined at 120°C.....	105
2-42 FT-IR spectrum for CMC-Pd nanoparticles prepared using a 0.15 wt% CMC aqueous solution and calcined at 320°C.....	106
2-43 FT-IR spectrum for CMC-Pd nanoparticles prepared using a 0.15 wt% CMC aqueous solution and calcined at 500°C.....	107
2-44 HRTEM image of CMC-stabilized Pd nanoparticles prepared in the aqueous phase using a 0.15 wt% CMC solution at a magnification of 800,000.....	110
2-45 HRTEM image of CMC-stabilized Pd nanoparticles prepared in the aqueous phase using a 0.15 wt% CMC solution at a magnification of 800,000 after applying a mask in Fourier space to reduce the noise from the carbon substrate .....	111
2-46 HRTEM image of 0.15 wt% CMC-stabilized Pd nanoparticles dispersed in the aqueous phase at a magnification of 800,000 .....	112
2-47 HRTEM image of CMC-stabilized Pd nanoparticles synthesized in the aqueous phase using a 0.005 wt% CMC solution at a magnification of 200,000.....	113
2-48 HRTEM image of Pd nanoparticles (0.33 wt% Pd) supported on $Al_2O_3$ at a magnification of 60,000 .....	114

2-49 HRTEM image of Pd nanoparticles (0.33 wt% Pd) supported on Al <sub>2</sub> O <sub>3</sub> before the aqueous phase dechlorination of TCE at a magnification of 300,000 .....	115
2-50 HRTEM image of 0.34 wt% Pd supported on Al <sub>2</sub> O <sub>3</sub> after the aqueous phase dechlorination of TCE at a magnification of 250,000 .....	116
2-51 EDS spectrum for the overall area shown in Figure 2-48 for the 0.34 wt% Pd on Al <sub>2</sub> O <sub>3</sub> catalyst .....	117
Scheme 3-1 Anthraquinone Autoxidation Manufacturing Route for Hydrogen Peroxide .....	120
Scheme 3-2 Chlorohydrin Manufacturing Route for Propylene Oxide .....	124
Scheme 3-3 Tert-butyl-hydroperoxide Manufacturing Route for Propylene Oxide.....	126
Scheme 3-4 Ethylbenzene Process for Producing Propylene Oxide .....	127
Scheme 3-5 Industrial Manufacturing Process for Producing Adipic Acid .....	133
Scheme 3-6 Biocatalytic Process for Manufacturing Adipic Acid .....	134
3-1 Experimental apparatus for the in-situ generation of H <sub>2</sub> O <sub>2</sub> over a Pd/TS-1 catalyst in CO <sub>2</sub> reaction media. This apparatus was used in the oxidation of propylene to propylene oxide, cyclohexanone to adipic acid, and pyridine to pyridine oxide .....	140
3-2 Effect of O <sub>2</sub> :H <sub>2</sub> ratio on the direct oxidation of cyclohexanone by H <sub>2</sub> O <sub>2</sub> to produce adipic acid .....	155
3-3 Effect of H <sub>2</sub> :cyclohexanone ratio on the direct oxidation of cyclohexanone by H <sub>2</sub> O <sub>2</sub> to produce adipic acid.....	156
3-4 Effect of reaction pressure on the direct oxidation of cyclohexanone by H <sub>2</sub> O <sub>2</sub> to produce adipic acid.....	157
3-5 Effect of O <sub>2</sub> /H <sub>2</sub> molar ratio on the in-situ generation of H <sub>2</sub> O <sub>2</sub> directly from H <sub>2</sub> and O <sub>2</sub> . Reactants included H <sub>2</sub> (6.2mmol), pyridine (6.2mmol), and H <sub>2</sub> O (27.8mmol)	160
3-6 Effect of H <sub>2</sub> concentration on the in-situ generation of H <sub>2</sub> O <sub>2</sub> directly from H <sub>2</sub> and O <sub>2</sub> . Reactants included pyridine (6.2mmol), H <sub>2</sub> O (27.8mmol), and an O <sub>2</sub> :H <sub>2</sub> ratio = 1	161
3-7 Effect of catalyst mass on the in-situ generation of H <sub>2</sub> O <sub>2</sub> directly from H <sub>2</sub> and O <sub>2</sub> . Reactants included H <sub>2</sub> (12.4mmol), pyridine (6.2mmol), H <sub>2</sub> O (27.8mmol), and an O <sub>2</sub> :H <sub>2</sub> ratio = 1 .....	162

3-8	Effect of metal loading on the in-situ generation of H <sub>2</sub> O <sub>2</sub> directly from H <sub>2</sub> and O <sub>2</sub> . Reactants included H <sub>2</sub> (12.4mmol), pyridine (6.2mmol), H <sub>2</sub> O (27.8mmol), and an O <sub>2</sub> :H <sub>2</sub> ratio = 1 .....	163
3-9	Oxidation of pyridine using hydrogen peroxide from the anthraquinone process ...	167
3-10	Oxidation of pyridine using in-situ generated hydrogen peroxide .....	168
3-11	Performance comparison for pyridine oxide production .....	170
4-1	Phase behavior experimental apparatus.....	179
Scheme 4-1	Flow chart demonstrating the method used to determine the critical properties of H <sub>2</sub> , CO, and hexane mixtures at specified compositions.....	181
4-2	Experimentally determined vapor-liquid equilibrium data for pure n-pentane demonstrating a critical point at a temperature of 196.2 °C and a pressure of 35.0 bar .....	184
4-3	Experimentally determined vapor-liquid equilibrium data for pure n-hexane demonstrating a critical point at a temperature of 234.0 °C and a pressure of 30.0 bar .....	185
4-4	Plot of experimentally determined critical temperature versus mole fraction of syngas .....	188
4-5	Plot of the experimentally determined critical pressure versus mole fraction of syngas .....	189
4-6	Critical temperature versus mole fraction of methane for the methane/n-pentane system .....	190
4-7	Critical pressure versus mole fraction of ethane for ethane/n-heptane system .....	191
4-8	Critical points represent the terminus of the two phase boundary for a given syngas/hexane mixture.....	193
4-9	Experimentally determined two phase region for mixture 2 .....	194
4-10	Experimentally determined critical temperature and pressure for the reaction mixture represented by the solvent, reactant gases (CO, H <sub>2</sub> ), and products demonstrating a critical point at a temperature of 238.2°C and a pressure of 37.2 bar .....	197

4-11 Effect of reaction temperature on CO conversion and chain-growth probability ( $\alpha$ -value) at 65 bar.....	198
4-12 Effect of reaction pressure on CO conversion and chain-growth probability ( $\alpha$ -value) at 250°C.....	199

## List of Abbreviations

Al <sub>2</sub> O <sub>3</sub>	Aluminum Oxide
AO	Anthraquinone Autoxidation Process
AQ	Anthraquinone
a <sub>s</sub>	Specific Surface Area
CHAO	Cyclohexanone
CO	Carbon Monoxide
CO <sub>2</sub>	Carbon Dioxide
CMC	Sodium Carboxymethyl Cellulose
D <sub>Pd</sub>	Palladium Dispersion
DCE	Dichloroethylene
ECD	Electron Capture Detector
FID	Flame Ionization Detector
FTIR	Fourier Transform Infrared Spectroscopy
FTS	Fischer Tropsch Synthesis
H <sub>2</sub>	Hydrogen
H <sub>2</sub> O <sub>2</sub>	Hydrogen Peroxide
HRTEM	High-resolution Transmission Electron Microscope
ICP	Inductively Coupled Plasma Spectroscopy

$k_{app}$	Apparent Reaction Rate Constant
$k_{obs}$	Observed Reaction Rate Constant
$k_{SA}$	Surface-Area-Based Reaction Rate Constant
$N_2O$	Nitrous Oxide
$O_2$	Oxygen
PCE	Perchloroethylene
PO	Propylene Oxide
PVP	Poly (vinylpyrrolidone)
SCF	Supercritical Fluid
SCH	Supercritical Hexane
SD	Standard Deviation
TCD	Thermal Conductivity Detector
TCE	Trichloroethylene
TEM	Transmission Electron Microscope
TOF	Turn Over Frequency
TFA	Trifluoroacetic Acid
TS-1	Titanium Silicalite
VC	Vinyl Chloride
VLE	Vapor-liquid Equilibrium
VOCs	Volatile Organic Compounds
WAR	Waste Reduction Algorithm
XRD	X-ray Diffraction

# Chapter 1

## INTRODUCTION

### 1.1 Introduction to Green Chemistry

In years past, economic development was often carried out without consideration of the long-term associated risks to the environment. The use of non-renewable resources was standard practice in process design, and it was all too common to implement an environmentally harmful process in manufacturing simply because the process worked. However, the National Environmental Policy Act (NEPA) of 1969 made environmental responsibility a national policy. In this Act, Congress acknowledged that environmental deterioration was a direct result of both economic and social expansion. Thus, it is our civil duty to restore and preserve the quality of our environment. According to NEPA, it is essential that we “create and maintain conditions under which man and nature can exist in productive harmony, and fulfill the social, economic, and other requirements of present and future generations of Americans” (Congress, 1969).

In 1983, the World Commission on Environment and Development, the Brundtland Commission, focused on the concept of sustainable development. It was recognized by the UN General Assembly that environmental awareness should be a global effort, and that sustainability must be the basis for the responsible development of all nations. According to the Brundtland Commission, sustainability

means “meeting the needs of the present without compromising the ability of the future generations to meet their own needs” (UN, 1987).

Many commercial processes for production of chemicals involve harsh organic solvents as well as numerous by-products that are detrimental to the environment. A rising environmental awareness and increasingly stringent environmental laws demand alternative synthetic routes in the production of various commercially useful products. The twelve principles of green chemistry, which are widely accepted by the scientific community, present an ideology for addressing these environmental concerns (see table 1-1) (Anastas and Warner, 1998). Green chemistry is “the utilization of a set of principles that reduces or eliminates the use or generation of hazardous substances in the design, manufacture, and application of chemical products” (Anastas and Warner, 1998). The twelve principles include several important topics such as the incorporation of benign solvents, possibly the elimination of solvents altogether, the use of more selective catalysts, the minimization of unnecessary chemical intermediates, and the design of less energy intensive chemical processes. The twelve principles encourage both scientists and engineers to improve current industrial processes through application of these guidelines.

Current areas of research include the use of green solvents (DeSimone, 2002; Sheldon, 2005; Yan *et al.*, 2010), supercritical carbon dioxide reaction media (Leitner, 2002; Subramaniam *et al.*, 2002; Beckman, 2003), solvent-free routes (Thomas *et al.*, 2001; Jeon *et al.*, 2005), the design of high performance catalysts (Centi and Perathoner, 2003; Thomas and Raja, 2005), and the use of renewable resources (Behr *et al.*, 2008; Van de Vyver *et al.*, 2009; Vennestrom *et al.*, 2010). The principal focus of this work has been the substitution of harsh organic solvents with more environmentally benign



1. It is better to prevent waste than to treat or clean up waste after it is formed.
2. Synthetic methods should be designed to maximize the incorporation of all materials used in the process into the final product.
3. Wherever practicable, synthetic methodologies should be designed to use and generate substances that possess little or no toxicity to human health and the environment.
4. Chemical products should be designed to preserve efficacy of function while reducing toxicity.
5. The use of auxiliary substances (e.g. solvents, separation agents, etc.) should be made unnecessary wherever possible, and innocuous when used.
6. Energy requirements should be recognized for their environmental and economic impacts and should be minimized. Synthetic methods should be conducted at ambient temperature and pressure.
7. A raw material or feedstock should be renewable rather than depleting wherever technically and economically practicable.
8. Unnecessary derivatization (blocking group, protection/deprotection, temporary modification of physical/chemical processes) should be avoided whenever possible.
9. Catalytic reagents (as selective as possible) are superior to stoichiometric reagents.
10. Chemical Products should be designed so that at the end of their function they do not persist in the environment and break down into innocuous degradation products.
11. Analytical methodologies need to be further developed to allow for real-time, in-process monitoring and control prior to the formation of hazardous substances.
12. Substances and the form of a substance used in a chemical process should be chosen so as to minimize the potential for chemical accidents, including releases, explosions, and fires.

**Table 1-1.** The Twelve Principles of Green Chemistry (Anastas and Warner 1998).

solvents, and the development of a more atom-efficient synthetic approach for the production of commodity chemicals. Specifically, this research focused on the green synthesis of palladium nanoparticles for an environmental application, the production of commodity chemicals utilizing a benign oxidant in green solvent media, and the production of petrochemicals using starting materials derived from biomass.

## **1.2 Green Nanotechnology**

Nanoscience is the study of engineered materials having a length-scale of 100 nm or less on at least one dimension with size-dependent physical properties. In recent years, synthesis techniques have been developed in order to fabricate nanoscale structures such as nanoparticles, nanolayers, and nanotubes (Brust *et al.*, 1994; Elam *et al.*, 2002; Koch, 2002). The field of nanotechnology has expanded rapidly over the past decade contributing significantly to our understanding of the unique properties and potential of these newly synthesized nanomaterials, as well as to the associated health and environmental aspects (NNI 2011).

The optical, chemical, and physical properties of nanomaterials are highly size-dependent, and can vary immensely from that of the bulk materials (Adair *et al.*, 1998; Poole and Owens, 2003). Thus, it is plausible that the toxicity of nanoparticles are widely different than that of the corresponding bulk materials (Science Policy Council, 2005; Albrecht *et al.*, 2006). The size of the particles and the surface chemistry can influence the toxicity imparted by a material (Colvin, 2003; Magrez *et al.*, 2006; Nel *et al.*, 2006; Chithrani *et al.*, 2006 ). Decreasing the particle size increases the surface-to-

volume ratio of the particle; thus, more atoms are on the surface rather than the interior of the particle. Often, the MSDS sheets for nanomaterials list the same properties and restrictions as the bulk counterparts (Colvin, 2003). However, in some cases studies have shown that ultrafine particles are actually more toxic to human health than larger particles of the same composition (Ferin *et al.*, 1991; Donaldson *et al.*, 2000).

Human health can be affected through occupational exposure, consumer exposure, and exposure through both soil and groundwater in the ecosystem. As such, it is important to design nanomaterials with these aspects in mind. For example, one study demonstrated that fullerenes, which are typically hydrophobic nanomaterials, can form stable colloidal dispersions in water (McHedlov-Petrosyan *et al.*, 1997; Alargova *et al.*, 2001; Deguchi *et al.*, 2001; Andrievsky *et al.*, 2002). Therefore, even at very low concentrations (<10 ppm), these compounds could have a potential environmental impact. Defining the hazards associated with exposure to nanomaterials and establishing proper safety guidelines are essential to meeting the demands of the rapidly expanding nanotechnology industry.

In addition to the need for a thorough understanding of the health and environmental aspects of the nanomaterials themselves, it is also important to implement the principles of green chemistry and engineering to the processes used for producing these materials. Specifically, green nanoscience takes the concept of green chemistry and applies it to the design, production, and application of nanomaterials (McKenzie and Hutchison, 2004). A green approach to producing nanoscale materials could result in the reduction or elimination of the hazards typical in nanomaterials fabrication. Current areas of research include waste prevention and reduction, the development of more

efficient materials (Warner and Hutchison, 2003), improvements to process safety, greener techniques for materials synthesis and processing (Breslow 1998, Li 2000), and improvements in energy efficiency.

### **1.3 Green Catalysis**

Catalysis is certainly considered one of the most important tools for the development of greener processes and products; thus, it is often referred to as a “pillar” of green chemistry (Anastas *et al.*, 2001). There are several advantages associated with catalysis which include waste reduction, increased selectivity, lower energy consumption, catalytic amounts of materials rather than stoichiometric quantities, and the use of less toxic materials. The ‘command and control’ approach to waste management was a widely accepted practice for a number of years. However, during the 1990s there was a shift from regulatory control to pollution prevention. Catalysis offers not only green benefits, but also several economic advantages. For example, the design of highly selective catalysts can improve the selectivity of a reaction; thereby, minimizing the formation of undesired by-products. If a process does not generate waste products then the need for separation, removal, and disposal of those hazardous waste materials is eliminated. A more efficient process requires less energy, while less energy consumed lowers the overall cost of the technology. These economic advantages motivate industry to incorporate greener methodologies.

### **1.4 Summary of Chapters in this Dissertation**

This dissertation work is targeted towards the application of several of these green chemistry principles in the synthesis and application of heterogeneous catalysts.

Specifically, Chapter 2 involves the application of green chemistry principles in the synthesis of the catalysts themselves. Many synthetic methods use harsh organics to create catalysts with limited control. This chapter presents the use of green nanoparticle catalyst synthesis methods that employ simple polysugar stabilizing ligands in aqueous phase reaction environment. In addition to green nanosynthesis methods, this chapter examines the application of polysugar-stabilized nanoparticles as catalysts in the environmental remediation of trichloroethylene to produce biodegradable ethane. Chapter 3 deals with an improved method for the production of commodity chemicals, namely the use of supercritical CO<sub>2</sub> as a benign reaction environment for the direct synthesis of hydrogen peroxide and its application. Experimental data were collected on the performance (i.e. yield, conversion, and selectivity) of the pyridine oxidation reaction along with analysis of the product distribution. These data serve as the basis for the development of rigorous process simulation models used to analyze the potential of the green supercritical phase (SCF) process and compare it to the traditional AQ process for the manufacture of hydrogen peroxide. Chapter 4 involves another commercially viable heterogeneous catalyst system to make alternative fuels. Specifically, this chapter involves an improved understanding of the reaction environment phase behavior in supercritical phase Fischer-Tropsch synthesis of fuels from synthesis gas.

## Chapter 2

### SYNTHESIS AND APPLICATION OF Pd NANOPARTICLE CATALYSTS IN THE HYDRODECHLORINATION OF TRICHLOROETHYLENE USING A GREEN POLYSUGAR APPROACH

This chapter focuses on the collaborative efforts between Deborah Bacik in the Department of Chemical Engineering and Man Zhang in the Department of Civil Engineering to examine the hydrodechlorination of trichloroethylene using palladium (Pd) nanoparticles as catalysts. The author expresses her sincere gratitude to both Man Zhang and her advisor, Dr. Dongye Zhao, for their fruitful collaboration in providing the kinetic experiments and insightful discussions. Specifically, the collection of kinetic data related to the degradation of TCE within the aqueous phase was performed by Man Zhang in Dr. Zhao's laboratories in Civil Engineering at Auburn University.

#### **2.1 Introduction**

Trichloroethylene (TCE) is one of the most common organic pollutants detected in both soil and groundwater (Zogorski *et al.*, 2006; Moran *et al.*, 2007). It has primarily been used as a solvent for cleaning and degreasing in the dry cleaning and automotive industries. TCE is a potent carcinogen and is resistant to the natural attenuation process.

Therefore, the presence of TCE in the environment is a significant health and safety concern. According to the United States Environmental Protection Agency (EPA), nearly 65% of sites requiring cleanup have been contaminated with chlorinated compounds (NRC, 1994; U.S. EPA, 2004; Quinn *et al.*, 2005). Unfortunately, these contaminants persist in the environment since they are often present as dense nonaqueous phase liquids (DNAPLs) having very low aqueous solubilities (Russell *et al.*, 1992; U.S. EPA, 2004). Chlorinated compounds target the immune, endocrine, and central nervous systems (U.S. EPA, 2001; ATSDR, 2003). Both acute and chronic exposure to TCE can result in liver and kidney damage, dizziness, confusion, headaches, facial numbness, and heart effects. Several types of cancer are associated with TCE exposure including liver, kidney, lymphatic, and lung. Considering the persistence of TCE in the environment and the long-term health effects associated with chlorinated contaminants, site cleanup is essential.

The remediation of contaminated sites requires a site-specific approach, which is often very expensive and time-consuming. Fortunately, the implementation of more stringent regulatory controls for use of chlorinated solvents in manufacturing has resulted in the replacement of chlorinated solvents with more environmentally-friendly alternatives (Sherman *et al.*, 1998). There has been an overall reduction in the use of chlorinated solvents in commercial processes; however, years of heavy usage and poor disposal of chlorinated compounds has resulted in a significant environmental problem (U.S. EPA, 1994). Various technologies have been developed for the successful remediation of soil and groundwater contaminated with these harmful pollutants (U.S. EPA, 2010). However, site cleanup is often a cost-intensive process spanning several

years. The estimated cost of remediation of contaminated waste sites across the United States is approximately \$750 billion over the next 30 years (NRC, 1994; Chiras, 2010).

The Capitol City Plume is a National Priorities List (NPL) Superfund site located in Montgomery, AL (U.S. EPA, 2000). This site is a specific example of an uncontrolled hazardous waste site which demonstrates the expense typically involved and time-commitment required for waste removal or treatment. In 1993 a hazardous waste site was discovered in Montgomery, AL containing both perchloroethylene (PCE) and TCE. It was proposed as a site to the NPL in 2000, and remedial investigations to establish a plan of action are still underway in 2011. Depending on the technology required for remediation, it may take several years to complete the process. In addition, it is estimated that \$18.6 million will be necessary to complete the cleanup of this Superfund site. This particular example illustrates that the treatment of soil and groundwater contamination can be a very costly and time-consuming endeavor. The remediation technologies currently available for waste treatment are described below.

### **2.1.1 Ex-Situ Pump-and-Treat**

Pump-and-treat is a typical method used for treating both soil and groundwater contaminated with volatile organic compounds (VOCs) (Mercer *et al.*, 1990). This technology was used to treat nearly 67% of contaminated sites within the U.S. during 2004 (U.S. EPA, 2004). Additionally, the pump-and-treat method was used in combination with other remediation technologies to clean up 84% of contaminated sites in 2004. In the pump-and-treat method, organic pollutants are eliminated by pumping the VOCs to the surface through trenches followed by an aboveground treatment. Current



technologies for the aboveground remediation of contaminated groundwater include adsorption by activated carbon, air-stripping, biodegradation, and chemical treatment (Russell *et al.*, 1992; Suthersan, 1997; Wong *et al.*, 1997). In adsorption by activated carbon, spent carbon is replaced rather than regenerated since activated carbon is very inexpensive. The saturated carbon is then disposed of in a landfill. Air-stripping is alternative aboveground treatment; whereby, the volatilized organics are either vented to the atmosphere or contacted with activated carbon and subsequently released to the atmosphere. The challenge with using these remediation technologies is that TCE is being removed from both the soil and groundwater only to contaminate another part of the environment rather than being eliminated. Unfortunately, this method also leaves residual VOCs which can migrate and sorb to the organic matter in the soil during pumping. Thus, the sorbed VOCs can be a long-term source of contamination as they gradually dissolve back into the clean groundwater once water levels return to normal (NRC, 1994). Remediation using pump-and-treat technology is a very slow process that can take several years to complete, and may not be entirely effective at eliminating the contamination from the environment.

### **2.1.2 In-Situ Treatment**

In-situ groundwater remediation involves the cleanup of hazardous waste materials at the contamination site using technologies such as air sparging, bioremediation, flushing, thermally enhanced recovery, and permeable reactive barriers (PRBs) without extraction of VOCs from the aquifer (Suthersan, 1997; Wong *et al.*, 1997). The use of in-situ groundwater treatment technologies has increased over the past thirty years, since these

technologies are often more cost effective than ex-situ treatment methods. Another advantage of the in-situ approach is that the extraction of VOCs is not required; thus, exposure to hazardous substances is limited. The in-situ treatment of ground water was used for the cleanup of 13% of contaminated sites within the U.S. during 2004 (U.S. EPA, 2004).

### **Air Sparging**

Air sparging is an in-situ remediation technology in which air is injected and bubbled through contaminated groundwater (Suthersan, 1997; Wong *et al.*, 1997; U.S. EPA, 2004; U.S. EPA, 2010). Upon contact with the air, the contaminants are volatilized and moved from the groundwater to the unsaturated zone soil. A soil vapor extraction system (SVE) is used in conjunction with the sparging technology in order to strip the vapor phase VOCs from the soil and also to control the movement of the vapor plume. One advantage associated with this technology is that the air supplied to the contaminated groundwater for sparging also provides oxygen to naturally occurring microorganisms and aids in the bioremediation of hazardous pollutants both above and below the water table. However, air flow through the saturated zone can be non-uniform making it difficult to control the movement of harmful vapors released from the groundwater.

### **Bioremediation**

Bioremediation is a specific treatment in which microorganisms are used to change contaminated soil and groundwater into something less toxic (Suthersan 1997; Wong *et al.*, 1997; U.S. EPA, 2004; U.S. EPA, 2010). Microorganisms can degrade the

contaminants either by using VOCs as a food source or cometabolizing them along with another food source. In order to be successful, the in-situ bioremediation method must provide an environment to grow and sustain the microorganisms. Therefore, this technology requires the control of variables in the habitat such as oxygen content, moisture, nutrients, temperature, and pH. The operation and maintenance costs associated with bioremediation are fairly low as compared to other remediation technologies, but it is a long-term process spanning several years. One challenge associated with this method is that chlorinated intermediates, such as vinyl chloride, are often formed during the degradation process. Unfortunately, vinyl chloride is more harmful to the environment than the starting VOCs. Thus, further remediation is required in order to mitigate the long-term hazards of these chlorinated intermediates.

### **Flushing**

Flushing is an in-situ remediation technology that includes the application of water along with aqueous surfactants or co-solvents in order to solubilize contaminants trapped within the soil and groundwater (Suthersan 1997; Wong *et al.*, 1997; U.S. EPA, 2004; U.S. EPA, 2010). The surfactants or co-solvents serve to lower the interfacial tension and facilitate the solubilization of pollutants. Both ethanol and isopropyl alcohol are solvents typically utilized in the flushing of VOCs from soil and groundwater. The water/solvent mixture is injected into both the soil and subsurface, then extracted and removed along with the dissolved VOCs for subsequent aboveground treatment. This process is fairly short-term lasting anywhere from a few weeks to a few months. However, a major

concern with this technology is that the water/solvent/contaminant mixture could migrate off-site or leave residual surfactant or solvent in the subsurface.

### **Thermally Enhanced Recovery**

Thermally enhanced recovery is an in-situ remediation technology during which heat is applied to the waste site in order to volatilize or even destroy the pollutants through pyrolysis (Suthersan 1997; Wong *et al.*, 1997; U.S. EPA, 2004; U.S. EPA, 2010). SVE technology is used in conjunction with the thermal treatment to remove volatilized chemicals from the unsaturated zone. Hot air injection, conductive heating, electrical resistive heating, and radio frequency heating are specific types of thermal treatment used for remediation. This technology is a more efficient and cost effective approach to site cleanup as compared to other remediation technologies. However, this process is limited to non-chlorinated contaminants since it is not effective at removing chlorinated compounds that are dissolved in groundwater. In addition, this technology may result in the destruction of microorganisms within the unsaturated zone that are beneficial to their habitat.

### **Permeable Reactive Barriers (PRBs)**

Permeable reactive barriers (PRBs) are used in the in-situ remediation of groundwater containing harmful pollutants (Suthersan 1997; Wong *et al.*, 1997; U.S. EPA, 2010). As the groundwater plume passes over the PRB wall, water is allowed to pass through while the contaminants are retained within the barrier material. Zero-valent metals, sorbents, and microbes are some of the materials that have been used as treatment agents within the

PRB wall. The contaminants are either retained or degraded during this process. Zero-valent iron (ZVI) has been used along with the PRB technology for the treatment of more than 120 contaminated sites within the past decade (ITRC, 2005). This remediation technology works best when utilized at low pollutant concentrations and shallow depths (Gavaskar *et al.*, 1998). Even though the system is rather simple, the reactivity of the ZVI particles is relatively low. Therefore, the efficient removal of VOCs from the waste site is limited with this remediation technology. Additionally, toxic intermediates more persistent than the starting materials are often formed during this process (Orth and Gillham, 1996; Arnold and Roberts, 2000). Improvements are necessary to implement soil and groundwater remediation using PRBs on a larger scale.

### **2.1.3 Monitored Natural Attenuation**

Monitored natural attenuation is a remediation technology that relies on the natural attenuation process in order to degrade contaminants present in both soil and groundwater under a controlled environment (Suthersan 1997; Wong *et al.*, 1997; U.S. EPA, 2010). The natural attenuation process includes biological, chemical, and physical methods to reduce pollutants without the aid of human involvement. Some of the processes include biodegradation, dispersion, sorbents, dilution, and radioactive decay. This technology was used to treat 11% of contaminated sites within the U.S. during 2004 (U.S. EPA, 2004). The main advantages associated with this process are the overall reduction in remediation costs, less human contact with harmful chemicals, and this process can be paired with other remediation technologies for enhanced site cleanup. However, the time span necessary for site remediation may far exceed that of other available technologies.

Furthermore, the intermediates generated during the natural attenuation process can be more toxic than the starting compounds. In addition, there is a risk for migration of pollutants off-site to uncontaminated areas.

#### **2.1.4 Catalytic Hydrodechlorination**

Catalytic hydrodechlorination is an innovative technology developed specifically for the remediation of soil and groundwater contaminated with chlorinated hydrocarbons (Lowry and Reinhard, 1999; Alonso *et al.*, 2002 ; He and Zhao, 2008; Liu *et al.*, 2008). During this process, TCE is hydrogenated in the presence of a catalyst (i.e. Pd, Au) to yield biodegradable ethane. Michael Wong (2008) and colleagues have proposed a Langmuir-Hinshelwood type mechanism for the hydrodechlorination of TCE. According to this mechanism, the chlorine atoms are removed in series and replaced by hydrogen atoms. Wong *et al.* (2008) has also shown that less chlorinated compounds react faster than TCE or PCE, which explains why no chlorinated intermediates build-up in the system. Since the catalytic hydrodechlorination of TCE is a surface-mediated process, increasing the surface area of the catalyst can improve the degradation rate (Nutt *et al.*, 2005; Nutt *et al.*, 2006; He and Zhao, 2007; Liu *et al.*, 2008). Thus, reducing the size of the catalyst to nanometer-sized particles provides an opportunity to have a more effective catalyst.

The study of metal nanoparticles has been of particular interest for several decades now due to their tunable chemical, physical, and optical properties (Daniel and Astruc 2004; Astruc *et al.*, 2005; Wantanabe *et al.*, 2006), as well as unique catalytic properties (Ohde *et al.*, 2002; Gopidas *et al.*, 2003; Astruc *et al.*, 2005; Astruc, 2007; Lien and Zhang, 2007). Metal nanoparticles can be produced in solution by reducing a metal salt in the presence of a capping agent. The functional groups of capping ligands

can be used to interact with the surface of the particle to suppress its' growth and to sterically stabilize the particle (Templeton *et al.*, 2000; Shenhar and Rotello, 2003; Love *et al.*, 2005). Brust *et al.* (1994) developed a one-step method for preparing alkyl stabilized metal nanoparticles by incorporating a phase-transfer catalyst that allows the transfer of metal ions into an organic phase. As such, it is within the organic phase that ions are reduced while nucleation and growth of the particles subsequently occurs. Unfortunately, this technique involves expensive phase-transfer catalysts, is solvent-intensive, and produces a broad particle size distribution (Sigman *et al.*, 2004; McLeod *et al.*, 2005).

The aqueous phase synthesis of metal nanoparticles using “green” capping agents such as glucose (Raveendran *et al.*, 2003; Liu *et al.*, 2005; Liu *et al.*, 2006), starch (Raveendran *et al.*, 2003; Raveendran *et al.*, 2006; Vigneshwaran *et al.*, 2006), and carboxymethylcellulose (Magdassi *et al.*, 2003; He and Zhao, 2007; He *et al.*, 2007) has been examined to determine the ability of each ligand to effectively cap and stabilize the particles within solution. The advantages associated with using these materials as capping agents is that they are all very inexpensive, nontoxic, and biodegradable.

In this chapter, we will explore the aqueous phase synthesis of sodium carboxymethyl cellulose (CMC) stabilized Pd nanoparticles and subsequent extraction of the formed particles into an organic phase. The third principle in the twelve principles of green chemistry states that, “Wherever practicable, synthetic methodologies should be designed to use and generate substances that possess little or no toxicity to human health and the environment” (Anastas and Warner 1998). Utilizing sugar and polysugar capping agents in aqueous media offer “green” alternatives to the conventional techniques that are

employed in synthesizing nanoparticles (Liu *et al.*, 2006; He and Zhao, 2007; Liu *et al.*, 2007; Liu *et al.*, 2008). CMC is a water-soluble polysaccharide with both carboxylate and hydroxyl functional groups available for interaction with the surface of nanoparticles. Polyvinylpyrrolidone (PVP) is another water-soluble polymeric capping agent used in the aqueous phase synthesis of nanoparticles (Zhang *et al.*, 1996; Sun *et al.*, 2002; Wang *et al.*, 2010; Mohapatra *et al.*, 2011). In addition, we will investigate the effectiveness of supported CMC-Pd nanoparticles as catalysts in the hydrodechlorination of TCE.

## **2.2 Experimental Methods**

### **2.2.1 Materials**

$\text{Na}_2\text{PdCl}_4 \cdot 3\text{H}_2\text{O}$  precursor (99%, Strem Chemicals), sodium carboxymethyl cellulose ( $M_w$ : 90,000, Sigma-Aldrich), polyvinylpyrrolidone ( $M_w$ : 55,000, Sigma-Aldrich), sodium borohydride (99.99%, Sigma-Aldrich), hydrochloric acid (Fisher Scientific), dodecanethiol, (98+%, Sigma-Aldrich), n-hexane (97.0%, Sigma-Aldrich), and deionized water (Fisher Scientific) were all used as received without further purification for nanoparticle synthesis and extraction. Hydrogen gas (UHP grade, Airgas South) and a 5% hydrogen/nitrogen specialty gas mixture (certified standard, Airgas South) were both used as received for catalyst reductions. Aluminum oxide (Alfa Aesar), titanium silicalite (Sud-Chemie), Ambersorb 572 (Supelco), and Ambersorb 563 (Supelco) supporting materials were all used as received. Trichloroethylene (99.5+%, Sigma-Aldrich), methanol (ACS grade, Fisher Chemical), hexanes (pesticide residue analysis grade, Fisher Scientific), hydrogen gas (UHP grade, Airgas South), and deionized water (Fisher



Scientific) were all used as received without further purification for the hydrodechlorination of TCE.

## **2.2.2 Experimental Procedures**

### **CMC-Stabilized Palladium Nanoparticle Synthesis**

The experimental apparatus used for the aqueous phase synthesis of CMC stabilized Pd nanoparticles included a Radleys Carousel 6 Reaction Station, which allowed for simultaneous mixing of up to six separate nanoparticle synthesis reactions. The Reaction Station included 250 mL (6) round-bottomed flasks with individual glass reflux necks, a magnetic stirrer/hotplate, and 6 stir bars, radial gas distribution system, and 6 PTFE caps. For the typical aqueous phase synthesis of CMC-stabilized Pd nanoparticles, a 0.15 wt% CMC solution was prepared by diluting 0.150 g of the capping ligand in 100 mL of deionized water at room temperature. The solution was stirred until the capping agent was completely dissolved. A 1000  $\mu\text{L}$  aliquot of a 0.05 M  $\text{Na}_2\text{PdCl}_4 \cdot 3\text{H}_2\text{O}$  solution was added to the 0.15 wt% CMC solution, while continuously stirring. A 0.05 M  $\text{NaBH}_4$  solution was allowed to age for approximately 20 minutes, and then a 3600  $\mu\text{L}$  aliquot of this reducing agent solution was added to the CMC-salt solution at a stir rate of 500 rpm to initiate nanoparticle synthesis, growth, and stabilization. It is noted that this represents a four times molar excess of reducing agent to ensure the complete reduction in all cases (Liu *et al.*, 2009). The system was aged for 24 hours under constant stirring. An analogous procedure was followed for the aqueous phase synthesis of PVP-stabilized Pd nanoparticles.

### **Nanoparticle Deposition onto Support Materials**

The incipient wetness impregnation technique was followed for preparation of all supported catalysts. After 24 hours of aging, the CMC-stabilized nanoparticle dispersions were concentrated to a volume of 5 mL by using a rotary evaporator. The concentrated nanoparticle solution, containing the appropriate amount of palladium to achieve a desired metal loading, was added dropwise until the total pore volume for the support material was reached. The material was then dried in an oven at 353 K overnight. The steps were repeated until all of the nanoparticle solution (5 mL) was added to the support material. After drying, calcination of the catalyst was carried out at 773 K for 5 hours in air. Subsequent reduction of the supported palladium catalyst was performed at 673 K for 4 hours in the presence of hydrogen.

### **Transmission Electron Microscopy Analysis**

Transmission electron microscopy (TEM) analysis was used to obtain the average particle size and particle size distribution for the CMC-stabilized Pd nanoparticles. After aging for 24 hours, the particles were extracted from the aqueous phase in which they were synthesized into an organic phase from which TEM samples were prepared for characterization. Specifically, Pd nanoparticles were extracted from the aqueous phase into a hexane phase by adding 10 mL of hexane to 20 mL of the aqueous phase CMC-capped Pd nanoparticle dispersion. This was followed by the addition of 100  $\mu\text{L}$  of dodecanethiol and 5 drops of hydrochloric acid (HCl), respectively. HCl was added in order to weaken the strong interactions existing between the CMC capping ligand and the surface of the Pd nanoparticles by protonating the  $-\text{COO}^-$  functional groups (Liu *et al.*,

2007). Once the interaction between the CMC capping ligand and the Pd nanoparticle surface was sufficiently weakened, dodecanethiol was able to form a chemical bond with the surface of the Pd nanoparticle and solvate the nanoparticles within the hexane phase. The two phase system was vigorously shaken in order to provide good contact between dodecanethiol and the surface of the Pd nanoparticle. After phase separation, the Pd nanoparticle dispersion in hexane was removed from the aqueous phase and washed with deionized water. The organic phase was washed two more times with deionized water in order to remove excess acid from the system and to provide a good sample for evaluation by TEM. All extractions were performed at room temperature.

To prepare TEM samples, the Pd nanoparticle dispersion in hexane was concentrated by evaporating two-thirds of the hexane solvent by flowing air over the system at room temperature and atmospheric pressure. Two droplets of the concentrated dodecanethiol-capped Pd nanoparticle dispersion in hexane were placed on a 300 mesh nickel-Formvar/carbon TEM grid. The solvent was allowed to evaporate from the grid at ambient conditions. The particles were analyzed using a Zeiss EM 10 TEM at an operating voltage of 60 kV. Both Image J and Microsoft Excel software were used to determine the average particle size, and to create a particle size distribution histogram. In each case, images of more than 5,000 particles were analyzed. Standard deviation (SD) and relative standard deviation (RSD) were calculated for each sample using Equations (2-1) and (2-2), where  $D_{\text{mean}}$  is defined as the mean diameter of the sample.

$$SD = \sqrt{\frac{\sum (x - \bar{x})^2}{n}} \quad (2-1)$$

$$RSD = \frac{SD}{D_{mean}} \quad (2-2)$$

### **High-Resolution Transmission Electron Microscopy Analysis**

High-resolution transmission electron microscopy (HRTEM) analysis was performed at the University of Kentucky's Department of Chemical and Materials Engineering by Dr. Naresh Shah in order to determine the morphology and approximate particle size for both the unsupported and alumina-supported CMC-stabilized Pd nanoparticles. A JEOL 2010F microscope with a field emission electron source operating at 200 keV accelerating voltage was used for HRTEM analysis of the samples. To prepare HRTEM samples for the unsupported CMC-Pd nanoparticles, one droplet of the CMC-stabilized palladium nanoparticle aqueous dispersion was placed on a Quantifoil<sup>®</sup> TEM grid. The aqueous solvent was allowed to evaporate from the grid at ambient conditions. The alumina-supported catalyst powder (212 -355  $\mu\text{m}$ ) was crushed to a smaller size using a miniature mortar and pestle, and approximately 1 mg of this powder was placed in 3-5 ml of acetone. The suspension was ultrasonicated for about 5 minutes using an Omni rupture (250W) ultrasonic probe. A few drops of this suspension were placed on a Quantifoil<sup>®</sup> TEM grid for HRTEM analysis. Bright field images were captured using a Gatan 1024x1024 pixel CCD camera with a typical acquisition time of 1 second. Image collection and post processing was done using Gatan Digital Micrograph software. Comparison was made to images obtained from traditional TEM analysis at Auburn University using a Zeiss EM 10 TEM at an operating voltage of 60 kV.

EDS spectra were collected using an Oxford EDS detector and Gatan Digital Micrograph software. EDS spectra were collected for approximately 1 minute live time using a smaller condenser aperture and after condensing the electron beam down to the region of interest.

### **Fourier Transform Infrared Spectroscopic Analysis**

ATR-FTIR spectroscopy was used in order to obtain the absorption spectra for both unsupported and supported CMC-stabilized Pd nanoparticle catalysts. These catalysts were calcined in air at temperatures ranging from 80°C to 500°C prior to analysis. The spectra were acquired using a PerkinElmer Spectrum 2000 spectrometer equipped with a liquid nitrogen cooled MCT detector. The samples were analyzed using a horizontal attenuated total reflection (HATR) accessory, which consisted of a steel plate that rested on top of an optical alignment box with an attenuated total reflection (ATR) element attached to its surface. The optical alignment box contained two planar and focal mirrors, which can be adjusted to focus the infrared beam on the incident face of the ATR crystal. All spectra were recorded at 80°C at 4.0 cm<sup>-1</sup> resolution with 500 co-added scans. A ZnSe ATR crystal (50 x 20 x 2 mm<sup>3</sup>, 45° face angle) was used in order to obtain spectral data in the range of 4000 cm<sup>-1</sup> to 550 cm<sup>-1</sup>.

To prepare the unsupported Pd nanoparticles for FTIR analysis, 1-2 mL of a 0.15 wt% CMC-stabilized Pd nanoparticle dispersion was added to an aluminum pan and calcined in air at a specified temperature for one hour. After calcination, the nanoparticle dispersion was re-dispersed with sonication in deionized water for 5 minutes. 1-2 drops of the Pd nanoparticle water dispersion were drop cast onto the ZnSe ATR element. The

sample was dried onto the surface of the ZnSe crystal by heating to 80°C under flowing nitrogen.

To prepare the supported Pd nanoparticles for FTIR analysis, 1-2 mg of a 0.33 wt% Pd/Al<sub>2</sub>O<sub>3</sub> catalyst was weighed out and added to an aluminum pan and calcined in air at a specified temperature for one hour. After calcination, the catalyst was finely ground using a mortar and pestle and re-dispersed in deionized water with sonication for 5 minutes. 1-2 drops of the Pd nanoparticle water dispersion were drop cast onto the ZnSe ATR crystal. The sample was dried onto the surface of the ZnSe crystal by heating to 80°C under flowing nitrogen.

### **Powder X-ray Diffraction**

Characterization by X-ray diffraction (XRD) was performed at Auburn University by the author and at West Virginia University's Department of Physics by Dr. Mohindar Sheera and Dr. Vivek Singh in order to determine the average crystallite size and crystalline structure for the alumina-supported Pd nanoparticle catalysts. For studies conducted at Auburn University, the X-ray diffraction patterns were measured using a Rigaku Miniflex powder X-ray diffractometer with a Cu K $\alpha$ 1 radiation source at 30 Kv, 15 mA and a miniflex goniometer. Bragg angles ( $2\theta$ ) between the range of 10° and 85° were scanned at a speed of 1°/minute with a step size of 0.05°.

For studies conducted at West Virginia University, the X-ray diffraction patterns were measured using a Rigaku D/Max B system with a Cu K $\alpha$ 1 ( $\lambda = 1.54185 \text{ \AA}$ ) radiation source. Each catalyst sample (about 1 cm<sup>2</sup> area) was loaded onto a special silicon plate using ethanol/acetone for adhesion, and then mounted vertically into the X-ray

diffractometer. All samples were run twice using two different sensitivities. First, samples were run with a  $2\theta$  scan from  $5^\circ$  to  $100^\circ$  using a step size of  $0.06^\circ$  and a counting time of 5 seconds. In the second higher sensitivity scan of  $2\theta$  from  $75^\circ$  to  $90^\circ$ , the step size was reduced from  $0.06^\circ$  to  $0.01^\circ$  and the counting time at each step was increased from 5 seconds to 10 seconds.

### **Chemisorption**

Chemisorption was used to determine the active metal surface area, percent metal dispersion, and average crystallite size for the CMC-stabilized Pd nanoparticle catalysts supported on  $\text{Al}_2\text{O}_3$ . A Quantachrome AS1 surface analysis module was used to perform carbon monoxide chemisorption on each of the Pd catalysts studied in the hydrodechlorination of TCE. The Quantachrome AS1 software package (Version 1.55) was used for data analysis. The cell was loaded with approximately 0.5 grams of calcined catalyst, and the system was evacuated for 35 minutes in order to clean the surface of the material and remove any moisture.  $\text{H}_2$  reduction was carried out at  $400^\circ\text{C}$  for 1.5 hours followed by evacuation of the system for 30 minutes. All surface Pd atoms were assumed to be in the reduced metallic state prior to uptake measurements. The formation of a CO monolayer has been reported at  $25^\circ\text{C}$  with a stoichiometry of one or two CO molecules to one Pd atom (Canton 2002, Monteiro 2001, Yates 1967). A stoichiometry of one CO molecule to one Pd atom was assumed for all chemisorption measurements obtained during this study. All isotherms were acquired at  $25^\circ\text{C}$ . An equilibration time of 3 minutes was chosen in order to guarantee the formation of a CO monolayer, but minimize the bulk diffusion and spillover of CO onto the alumina

support. The combined CO uptake, including both physisorbed and chemisorbed CO, was used to calculate the catalyst dispersion. Dispersion ( $D_{Pd}$ ) was estimated using Equation 2-3.

$$D_{Pd} = \frac{N_m S A_m}{100L} \quad (2-3)$$

$N_m$  is the CO uptake ( $\mu\text{mol/g}$ ),  $S$  is the adsorption stoichiometry,  $M$  is the molecular weight of Pd, and  $L$  is the percentage metal loading. The active metal surface area,  $s$ , was estimated using Equation 2-4.

$$s = \frac{N_m S A_m}{166} \quad (2-4)$$

$A_m$  is the cross-sectional area occupied by each active surface Pd atom ( $7.8740 \text{ \AA}^2/\text{Pd}$  atom). The average crystallite size was estimated using Equation 2-5.

$$d = \frac{100Lf}{sZ} \quad (2-5)$$

$Z$  is the density of Pd ( $12.020 \text{ g/ml}$ ),  $s$  is the active metal surface area, and  $f$  is the shape factor. A spherical shape was assumed, which has a shape factor of 6.

### **Physisorption BET Analysis**



Physisorption measurements were performed and BET theory was applied in order to determine the specific surface area for the alumina-supported Pd nanoparticle catalysts prepared using various CMC concentrations. The surface area measurements were collected at West Virginia University's Department of Physics by Mohita Yalamanchi using a Micromeritics AutoChem II 2920 automated catalyst characterization system. Each sample was outgassed in a helium gas flow at 50 mL/min while the temperature was ramped to 350°C at 50°C/min. After holding the temperature constant at 350°C for 30 minutes, the sample surroundings were then brought to ambient conditions and a mixture of 30% N<sub>2</sub>/balance helium was passed through the sample. The sample was immersed in a liquid nitrogen (LN<sub>2</sub>) bath to measure the uptake of nitrogen. The N<sub>2</sub> dewar was then immediately replaced by a dewar of water at ambient temperature, and the amount of desorbed N<sub>2</sub> was measured. The BET equation was used to calculate the specific surface area. All samples were duplicated, and the variations in the surface area between different samples were at most ca. 20%.

### **Characterization by Inductively Coupled Plasma Spectroscopy**

The aqueous phase from the hydrodechlorination experiments was analyzed using an inductively coupled plasma (ICP) spectrometer in order to determine if any Pd was leached from the alumina support material into the aqueous phase during the TCE degradation reaction. After each experiment, the alumina-supported Pd nanoparticle catalyst was separated from the aqueous phase via centrifugation at 1500 RPM for 5 minutes. The aqueous phase was then removed from the reactor and analyzed by a

Varian Vista MPX Axial ICP at a Pd wavelength of 340.458. The result reported is an average of two exposures.

### **Homogeneous and Heterogeneous Pd Nanoparticle Catalyzed TCE Degradation**

It is noted that the collection of kinetic data related to the degradation of TCE within the aqueous phase was performed by Man Zhang in Dr. Zhao's laboratories in Civil Engineering at Auburn University.

For the batch hydrodechlorination experiments using unsupported palladium nanoparticle catalysts, 93.6 mL of deionized water along with 6.44 mL of the Pd nanoparticle aqueous dispersion (0.146 mM Pd) was added to a 127 mL serum bottle. A stir bar was included for proper agitation. The system was purged with hydrogen gas for twenty minutes to displace any dissolved oxygen and to saturate both the aqueous phase and headspace with H<sub>2</sub>. The system was then sealed with a Teflon Mininert valve and spiked with 25 µL (179 g/L in methanol) of a TCE stock solution to yield an initial TCE concentration of 50 mg/L. The TCE solution was added under constant stirring and the system was sampled at regular time intervals. The degradation of TCE was monitored for ten minutes by removing 100 µL of the aqueous phase at constant intervals using a gastight syringe. The sample was transferred to a 2 mL GC vial and extracted into 1 mL of hexane. A HP 6890 GC fitted with a micro-electron capture detector (ECD) and a RTX-624 capillary column (32m x 0.32mm) was used for analysis of all samples. The data was collected using a HP GC Chemstation. A chlorine mass balance was performed in order to confirm the complete conversion of TCE to biodegradable products. For this set of experiments, after the system was sampled at a specific time interval the reaction

was stopped by purging with air to remove any unreacted TCE. A Dionex ion chromatography system was used to measure the chloride concentration in a 1 mL aliquot. All experiments were at least duplicated.

For the batch hydrodechlorination studies using supported palladium nanoparticle catalysts, 0.1 grams of catalyst (0.031 mM Pd) was added to a 127 mL serum bottle along with 100 mL of deionized water. A stir bar was included for proper agitation. The system was purged with hydrogen gas for twenty minutes to displace any dissolved oxygen and to saturate both the aqueous phase and headspace with H<sub>2</sub>. The system was then sealed with a Teflon Mininert valve and spiked with 25 µL (179 g/L in methanol) of a TCE stock solution to yield an initial TCE concentration of 50 mg/L. The TCE solution was added under constant stirring and the system was sampled at regular time intervals. The degradation of TCE was monitored for thirty minutes by removing 100 µL of the aqueous phase at constant intervals using a gastight syringe. The sample was transferred to a 2 mL GC vial and extracted into 1 mL of hexane. A HP 6890 GC fitted with a micro-electron capture detector (ECD) and a RTX-624 capillary column (32m x 0.32mm) was used for analysis of all samples. The data was collected using a HP GC Chemstation. A chlorine mass balance was performed in order to confirm the complete conversion of TCE to biodegradable products. For this set of experiments, after the system was sampled at a specific time interval the reaction was stopped by purging with air to remove any unreacted TCE. A Dionex ion chromatography system was used to measure the chloride concentration in a 1 mL aliquot. All experiments were at least duplicated.

## 2.3 Results and Discussion

The effect of capping ligand, capping ligand concentration, and synthesis temperature on both the particle size and size distribution of the CMC and PVP-stabilized Pd nanoparticles has been examined.

### 2.3.1 Effect of Capping Ligand

Both CMC and PVP were used as capping agents in the one-step aqueous phase synthesis of Pd nanoparticles. TEM images for Pd nanoparticles synthesized and stabilized with 0.15 wt% CMC and 0.15 wt% PVP at ambient conditions are shown in Figure 2-1. The Pd nanoparticles were synthesized within the aqueous phase at very dilute concentrations. For TEM imaging, it was desired to obtain more concentrated nanoparticle dispersions. Thus, the water-soluble ligands were exchanged with dodecanethiol in order to extract and concentrate the Pd nanoparticles into an organic phase. It is noted that the transfer of the Pd nanoparticles from the aqueous phase into the organic phase did not significantly affect the particle size or size distribution (Liu *et al.*, 2007). The dispersed Pd nanoparticles were of small size and spherical shape for both capping agents. Figure 2-2 shows the typical size distribution obtained for the room temperature aqueous phase synthesis of Pd nanoparticles with both 0.15 wt% CMC and 0.15 wt% PVP capping ligand concentrations. The particles synthesized with a 0.15 wt% CMC aqueous solution were observed to have a mean diameter of 2.70 nm with a fairly narrow size distribution (SD = 0.80 nm, RSD = 0.310). For particles synthesized with a 0.15 wt% PVP aqueous solution, slightly smaller nanoparticles having a mean diameter of 2.51 nm and a much broader size distribution were obtained (SD = 1.48 nm, RSD = 0.591). Although both

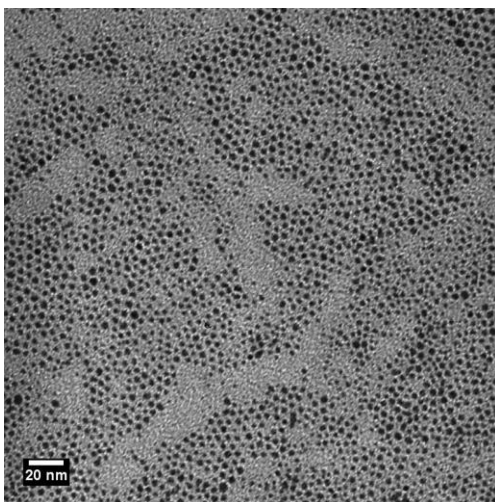
capping agents generated Pd nanoparticles of roughly the same size, CMC appears to be more effective at suppressing the growth of the particles given its narrower size distribution ( $SD = 0.80$  nm,  $RSD = 0.310$ ). The interactions for both CMC and PVP capping ligands with the particle surface will be discussed in more detail later.

### **2.3.2 Effect of Capping Ligand Concentration**

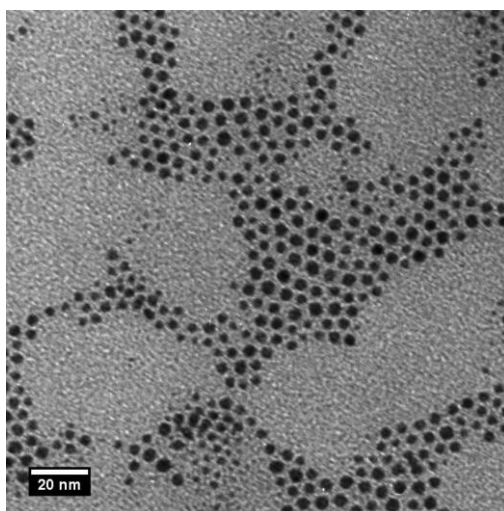
The concentrations of both CMC and PVP capping agents were varied in order to determine their effect on the particle size and distribution.

#### **0.075 wt% Stabilizing Agent**

TEM images for Pd nanoparticles stabilized with 0.075 wt% CMC and 0.075 wt% PVP at ambient conditions are shown in Figure 2-3. Decreasing the capping ligand concentration from 0.15 wt% (shown in Figure 2-1) to 0.075 wt% (shown in Figure 2-3), results in slightly larger particles that retain their spherical shape. Capping agents act to suppress the growth of nanoparticles by interacting with the surface of the particles to prevent agglomeration. It is, therefore, expected that decreasing the concentration of the capping ligand should result in the synthesis of particles of increased size. Figure 2-4 illustrates the typical size distributions of the nanoparticles obtained from the room temperature aqueous phase synthesis of Pd nanoparticles using 0.075 wt% CMC and 0.075 wt% PVP solutions. The Pd nanoparticles synthesized and stabilized with 0.075 wt% CMC were observed to have a mean diameter of 2.77 nm with a fairly narrow size distribution ( $SD = 0.66$  nm,  $RSD = 0.293$ ); whereas, particles synthesized with 0.15 wt% CMC had a mean diameter of 2.70 nm ( $SD = 0.80$  nm,  $RSD = 0.310$ ).

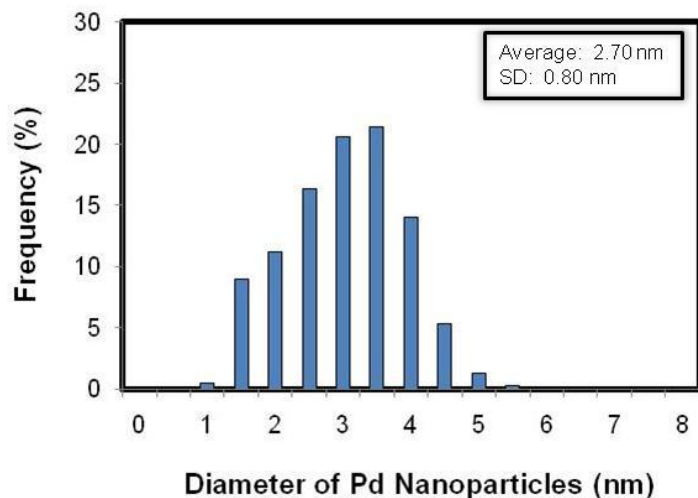


(a)

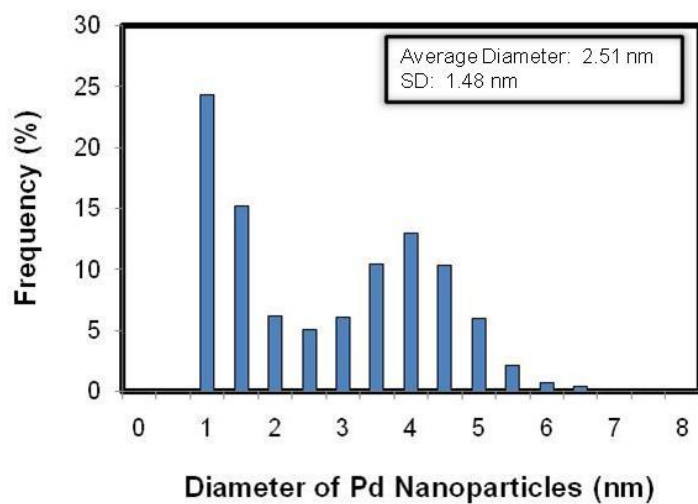


(b)

**Figure 2-1.** TEM images of dodecanethiol capped Pd nanoparticles extracted from the aqueous phase where stabilized with (a) 0.15 wt% CMC (b) 0.15 wt% PVP at 20°C. The Pd nanoparticles were extracted from the aqueous phase, after 24 hours of aging, into the hexane phase and subsequently deposited onto a TEM grid.



(a)



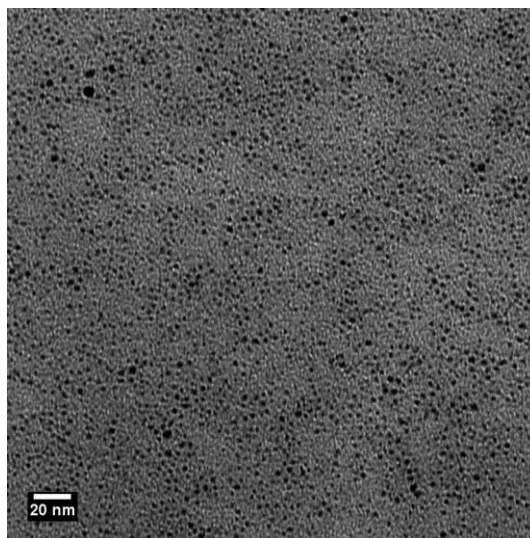
(b)

**Figure 2-2.** Particle size distribution histograms for dodecanethiol capped Pd nanoparticles extracted from the aqueous phase where stabilized with (a) 0.15 wt% CMC (b) 0.15 wt% PVP at 20°C. The Pd nanoparticles were extracted from the aqueous phase, after 24 hours of aging, into the hexane phase and subsequently deposited onto a TEM grid. More than 5,000 particles were analyzed for each sample.

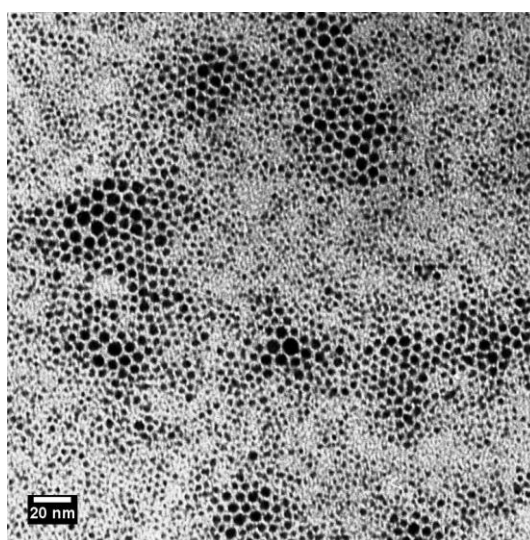
The particles synthesized and stabilized with 0.075 wt% PVP had a mean diameter of 2.86 nm (SD = 1.29, RSD = 0.450); whereas, particles synthesized with 0.15 wt% PVP had a mean diameter of 2.51 nm (SD = 1.48 nm, RSD = 0.591). Reducing the concentration of the stabilizing ligand resulted in larger Pd nanoparticles with a broader size distribution for both the CMC and PVP capping agents.

Concentrations ranging from 0.05 wt% to 0.005 wt% CMC were also examined for the room temperature aqueous phase synthesis of Pd nanoparticles. TEM images for Pd nanoparticles stabilized with 0.05 wt% CMC and 0.005 wt% CMC at ambient conditions are shown in Figure 2-5. The Pd nanoparticles are of small size (< 10 nm) and spherical morphology. Figure 2-6 presents a typical size distribution obtained for the room temperature aqueous phase synthesis of Pd nanoparticles using a 0.05 wt% CMC solution. The Pd nanoparticles stabilized with 0.05 wt% CMC had a mean diameter of 2.80 nm (SD = 0.88, RSD = 0.313); whereas, particles synthesized with 0.15 wt% CMC had a mean diameter of 2.70 nm (SD = 0.80 nm, RSD = 0.310). The particle size is effectively the same and a broader distribution is observed when the capping ligand concentration is reduced by a factor of three from 0.15 wt% to 0.05 wt% CMC. Even though there is less capping agent available in solution at the concentration of 0.05 wt%, CMC is still highly effective at capping the Pd nanoparticles. A typical size distribution for the Pd nanoparticles synthesized using a 0.005 wt% CMC aqueous solution at room temperature is shown in Figure 2-6. The Pd nanoparticles synthesized and stabilized with 0.005 wt% CMC had a mean diameter of 4.31 nm (SD = 1.63, RSD = 0.376); while the particles synthesized with 0.15 wt% CMC had a mean diameter of 2.70 nm (SD = 0.80 nm, RSD = 0.310). A larger particle size is observed and a much broader particle size



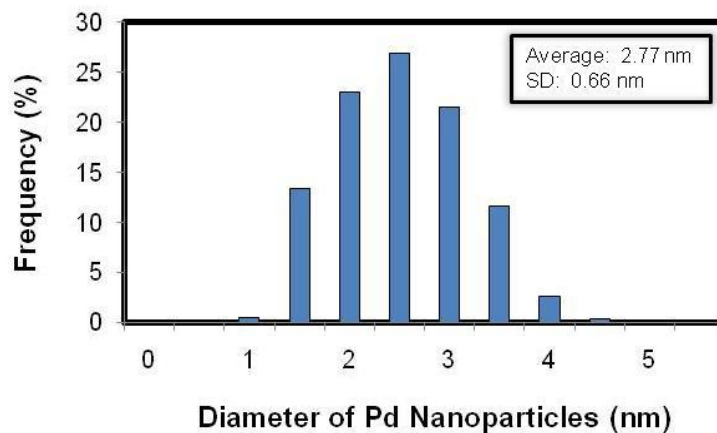


(a)

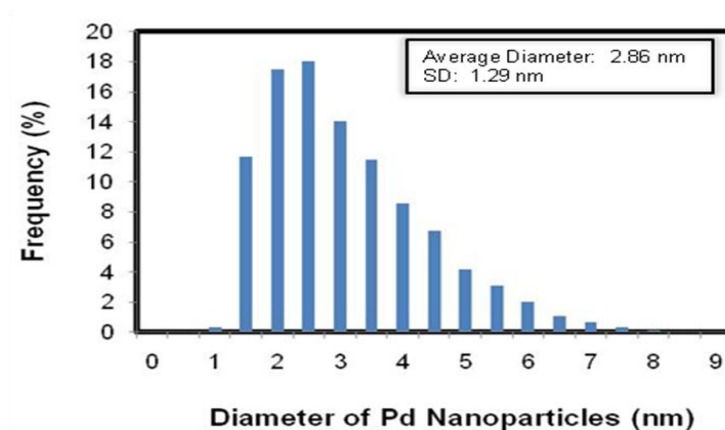


(b)

**Figure 2-3.** TEM images of dodecanethiol capped Pd nanoparticles extracted from the aqueous phase where stabilized with (a) 0.075 wt% CMC (b) 0.075 wt% PVP at 20°C. The Pd nanoparticles were extracted from the aqueous phase, after 24 hours of aging, into the hexane phase and subsequently deposited onto a TEM grid.

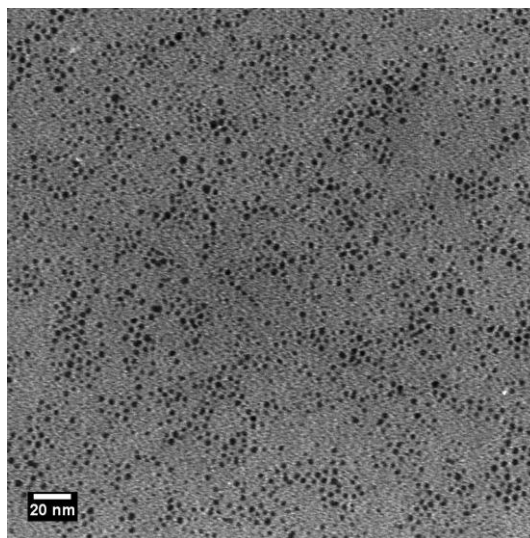


(a)

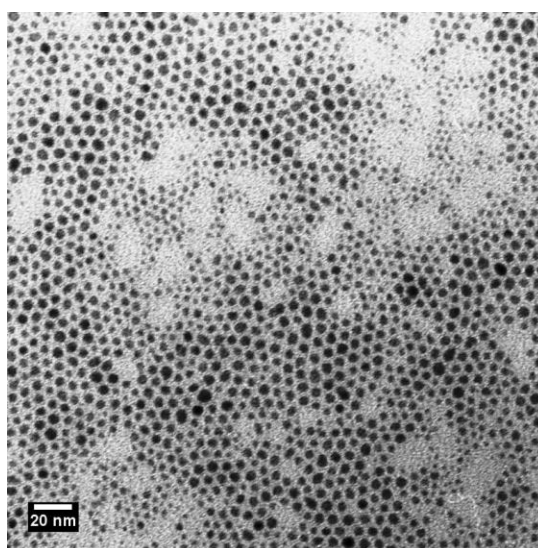


(b)

**Figure 2-4.** Particle size distribution histograms for dodecanethiol capped Pd nanoparticles extracted from the aqueous phase where stabilized with (a) 0.075 wt% CMC (b) 0.075 wt% PVP at 20°C. The Pd nanoparticles were extracted from the aqueous phase, after 24 hours of aging, into the hexane phase and subsequently deposited onto a TEM grid. More than 5,000 particles were analyzed for each sample.

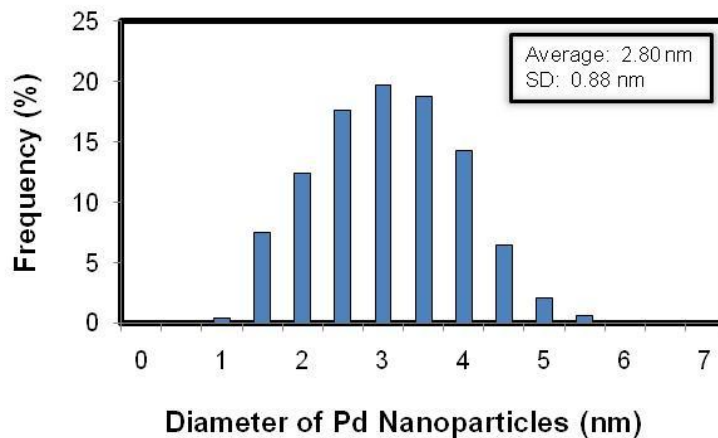


(a)

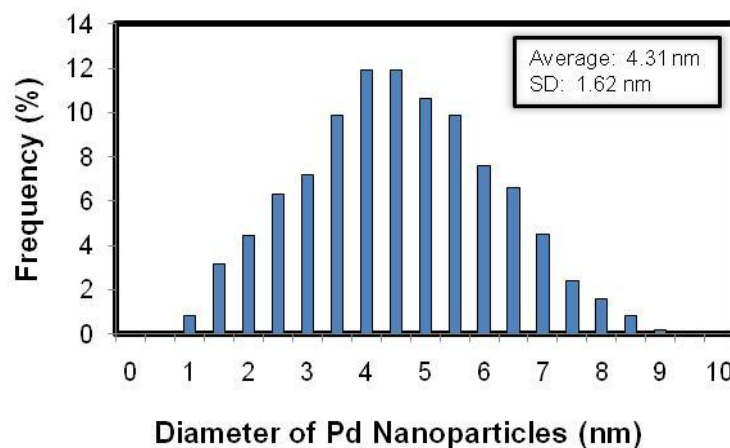


(b)

**Figure 2-5.** TEM images of dodecanethiol capped Pd nanoparticles extracted from the aqueous phase where stabilized with (a) 0.05 wt% CMC (b) 0.005 wt% CMC at 20°C. The Pd nanoparticles were extracted from the aqueous phase, after 24 hours of aging, into the hexane phase and subsequently deposited onto a TEM grid.

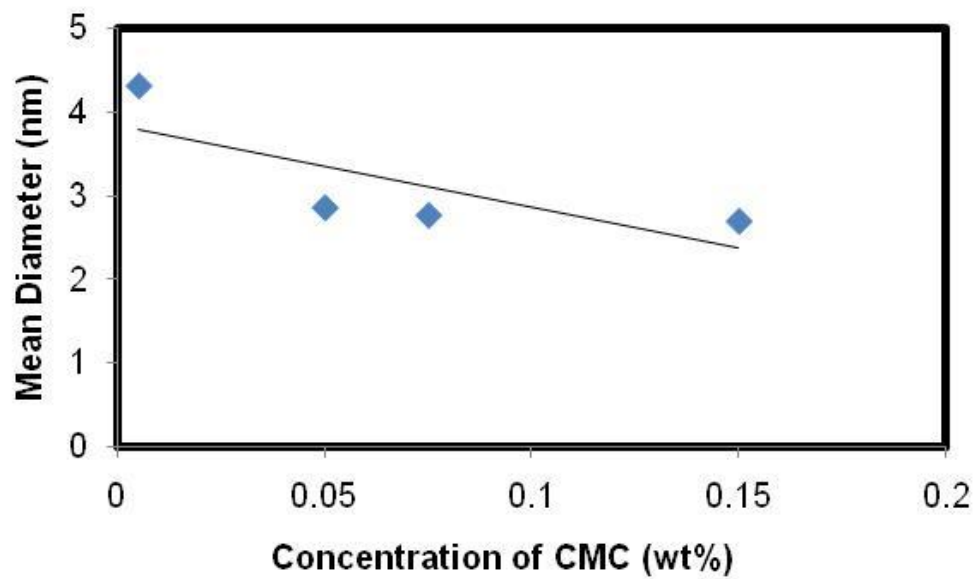


(a)

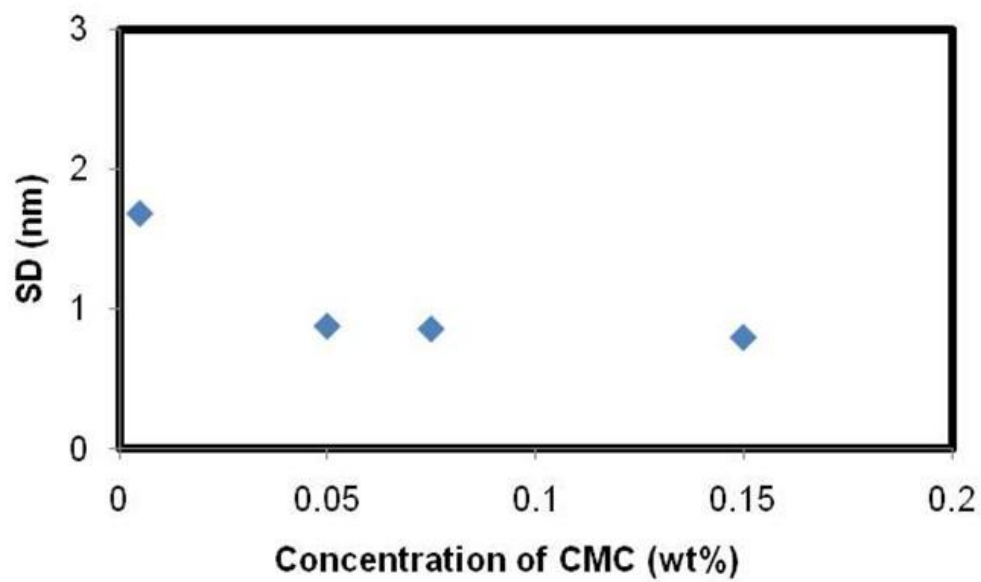


(b)

**Figure 2-6.** Particle size distribution histograms for dodecanethiol capped Pd nanoparticles extracted from the aqueous phase where stabilized with (a) 0.05 wt% CMC (b) 0.005 wt% CMC at 20°C. The Pd nanoparticles were extracted from the aqueous phase, after 24 hours of aging, into the hexane phase and subsequently deposited onto a TEM grid. More than 5,000 particles were analyzed for each sample.



(a)



(b)

**Figure 2-7.** The effect of CMC concentration on the (a) mean particle diameter and (b) standard deviation of Pd nanoparticles at room temperature.

particle size distribution is obtained when the capping ligand concentration is reduced by a factor of thirty from 0.15 wt% to 0.005 wt% CMC. Even so, the particles are still very small in size (< 10 nm). Figure 2-7 shows the effect of CMC concentration on the mean particle diameter and standard deviation. Thus, CMC is highly effective at capping and stabilizing Pd nanoparticles in aqueous solution over a broad range of concentrations employed.

### **2.3.3 Effect of Synthesis Temperature**

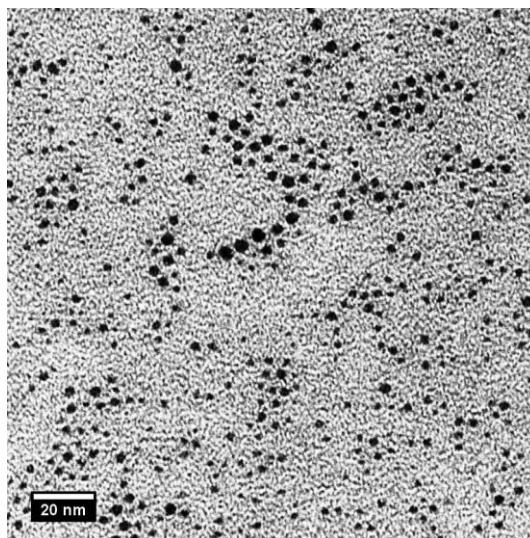
The effect of synthesis temperature on the particle size and size distribution was also examined.

#### **0.15 wt% Stabilizing Agent**

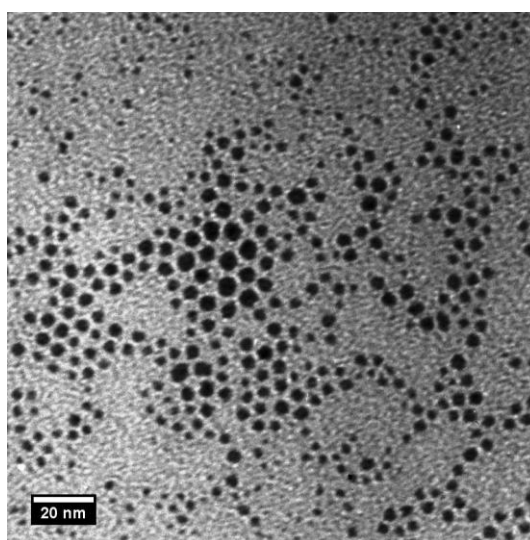
TEM images for Pd nanoparticles synthesized and stabilized with both 0.15 wt% CMC and 0.15 wt% PVP solutions at 35°C are shown in Figure 2-8. The particles were of small size (< 10 nm) and spherical shape. The particle size distributions obtained for the aqueous phase synthesis of Pd nanoparticles with both 0.15 wt% CMC and 0.15 wt% PVP at the elevated temperature of 35°C are shown in Figure 2-9. Pd nanoparticles synthesized and stabilized with 0.15 wt% CMC at 35°C had a mean diameter of 1.77 nm (SD = 0.49, RSD = 0.352); whereas, particles synthesized with 0.15 wt% CMC at 20°C had a mean diameter of 2.70 nm (SD = 0.80 nm, RSD = 0.310). Therefore, smaller particles were observed at 35°C for the aqueous phase synthesis of Pd nanoparticles using CMC as the stabilizer. The effect of temperature was also examined using PVP as the stabilizing agent. Pd nanoparticles synthesized and stabilized with 0.15 wt% PVP at 35°C had a mean diameter of 1.86 nm (SD = 1.28 nm, RSD = 0.688); while, particles

synthesized with 0.15 wt% PVP at 20°C had a mean diameter of 2.51 nm (SD = 1.48 nm, RSD = 0.591). Again, smaller particles were observed at the elevated temperature of 35°C for the aqueous phase synthesis of Pd nanoparticles using PVP as the stabilizer.

TEM images for Pd nanoparticles synthesized and stabilized with both 0.15 wt% CMC and 0.15 wt% PVP solutions at a further elevated temperature of 50°C are shown in Figure 2-10. The particle size distributions obtained for the aqueous phase synthesis of Pd nanoparticles with 0.15 wt% CMC and 0.15 wt% PVP at an elevated temperature of 50°C are shown in Figure 2-11. The nanoparticles synthesized and stabilized with 0.15 wt% CMC at 50°C had a mean diameter of 1.73 nm (SD = 0.76, RSD = 0.438); while particles synthesized with 0.15 wt% CMC at 20°C had a mean diameter of 2.70 nm (SD = 0.80 nm, RSD = 0.310). Pd nanoparticles synthesized and stabilized with 0.15 wt% PVP at 50°C had a mean diameter of 1.72 nm (SD = 0.73, RSD = 0.423); whereas, particles synthesized with 0.15 wt% PVP at 20°C had a mean diameter of 2.51 nm (SD = 1.48 nm, RSD = 0.591). Figure 2-14 shows the effect of synthesis temperature on the mean particle diameter and standard deviation for Pd nanoparticles synthesized and stabilized using a 0.15 wt% capping ligand concentration. It was determined that a smaller average particle size was obtained as the synthesis temperature was increased from 20°C to 50°C, for Pd nanoparticles synthesized and stabilized in the aqueous phase using a 0.15 wt% capping ligand concentration. In order to further investigate the effect of synthesis temperature on Pd nanoparticle size and size distribution, experiments were also conducted using a 0.075 wt% capping ligand concentration at various synthesis temperatures.



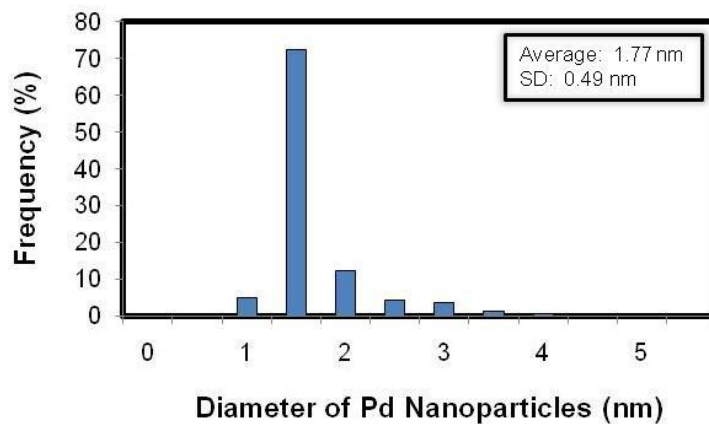
(a)



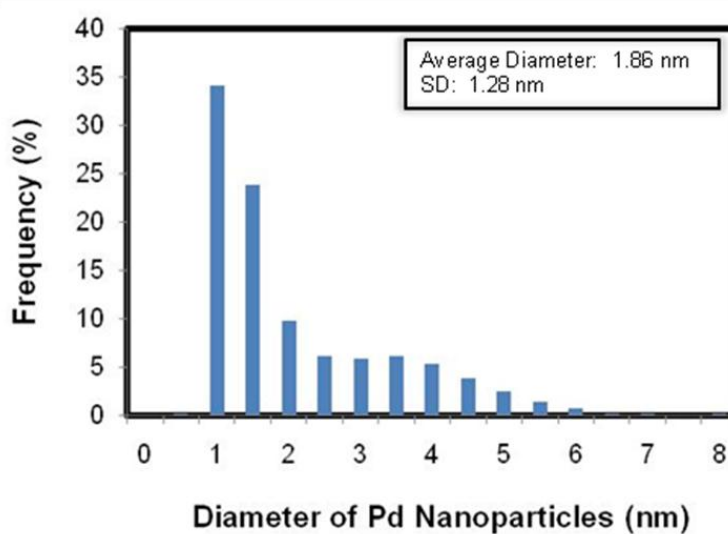
(b)

**Figure 2-8.** TEM images of dodecanethiol capped Pd nanoparticles extracted from the aqueous phase where stabilized with (a) 0.15 wt% CMC (b) 0.15 wt% PVP at 35°C. The Pd nanoparticles were extracted from the aqueous phase, after 24 hours of aging, into the hexane phase and subsequently deposited onto a TEM grid.



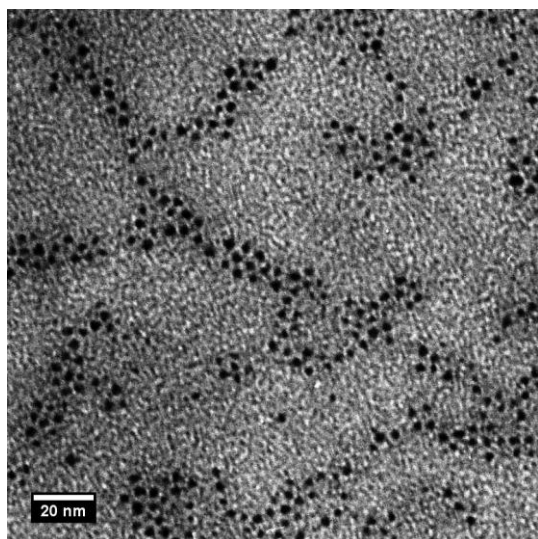


(a)

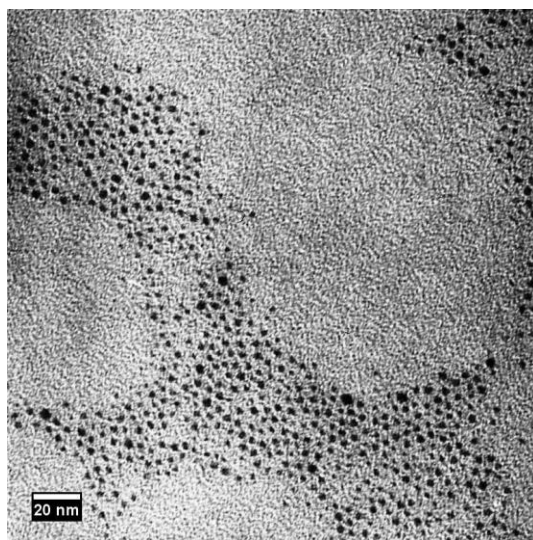


(b)

**Figure 2-9.** Particle size distribution histograms for dodecanethiol capped Pd nanoparticles extracted from the aqueous phase where stabilized with (a) 0.15 wt% CMC (b) 0.15 wt% PVP at 35°C. The Pd nanoparticles were extracted from the aqueous phase, after 24 hours of aging, into the hexane phase and subsequently deposited onto a TEM grid. More than 5,000 particles were analyzed for each sample.

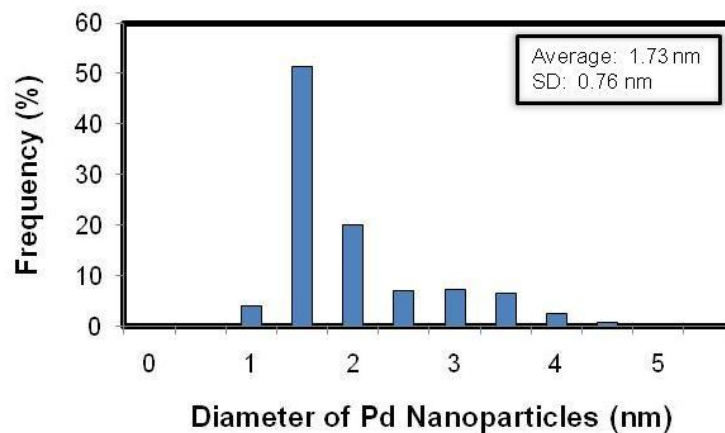


(a)

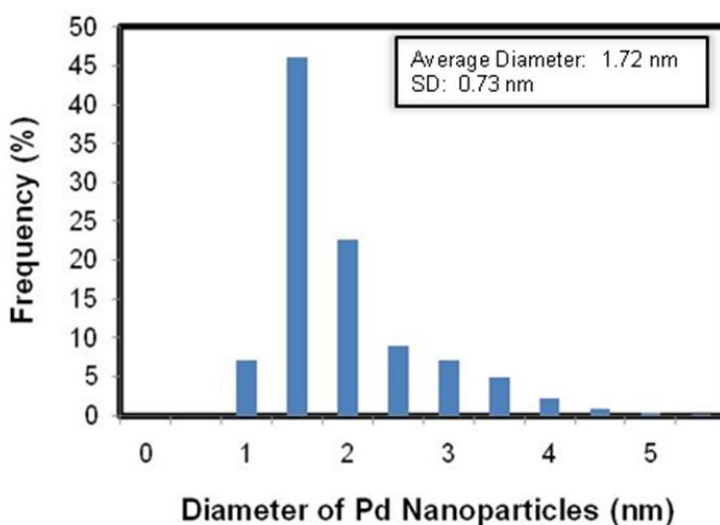


(b)

**Figure 2-10.** TEM images of dodecanethiol capped Pd nanoparticles extracted from the aqueous phase where stabilized with (a) 0.15 wt% CMC (b) 0.15 wt% PVP at 50°C. The Pd nanoparticles were extracted from the aqueous phase, after 24 hours of aging, into the hexane phase and subsequently deposited onto a TEM grid.



(a)

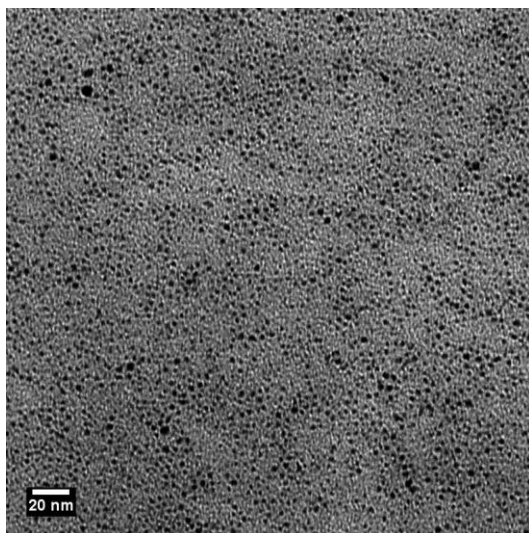


(b)

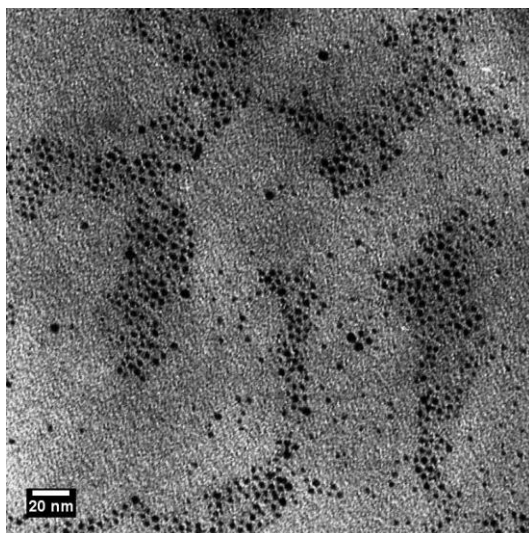
**Figure 2-11.** Particle size distribution histograms for dodecanethiol capped Pd nanoparticles extracted from the aqueous phase where stabilized with (a) 0.15 wt% CMC (b) 0.15 wt% PVP at 50°C. The Pd nanoparticles were extracted from the aqueous phase, after 24 hours of aging, into the hexane phase and subsequently deposited onto a TEM grid. More than 5,000 particles were analyzed for each sample.

### **0.075 wt% Stabilizing Agent**

TEM images for Pd nanoparticles stabilized with both 0.075 wt% CMC and 0.075 wt% PVP solutions at 50°C are shown in Figure 2-12. The particle size distributions obtained from the aqueous phase synthesis of Pd nanoparticles using both 0.075 wt% CMC and 0.075 wt% PVP solutions at an elevated temperature of 50°C are shown in Figure 2-13. The Pd nanoparticles synthesized and stabilized with 0.075 wt% CMC at 50°C had a mean diameter of 2.11 nm (SD = 0.88 nm, RSD = 0.416); whereas, particles synthesized using 0.075 wt% CMC at 20°C had a mean diameter of 2.77 nm (SD = 0.88 nm, RSD = 0.293). Pd nanoparticles synthesized and stabilized with 0.075 wt% PVP at 50°C had a mean diameter of 2.02 nm (SD = 0.89 nm, RSD = 0.441), while particles synthesized with 0.075 wt% PVP at 20°C had a mean diameter of 2.51 nm (SD = 1.48 nm, RSD = 0.591). It is noted that the mean particle size decreased and a narrower particle size distribution was obtained with this further increase in synthesis temperature for Pd nanoparticles synthesized and stabilized with a 0.075 wt% capping ligand concentration. This behavior was also observed for particles synthesized using a 0.15 wt% capping ligand concentration. Increasing the synthesis temperature from 20°C to 50°C increased the hydration of the capping ligand in solution by disrupting the intermolecular forces between ligand molecules and improving the solute-solvent interaction. Enhancing the hydration of the capping ligand in solution allowed for more effective interactions between the available functional groups and the surface of the Pd nanoparticle. At elevated synthesis temperatures, both CMC and PVP were more efficient at capping and suppressing the particle growth resulting in smaller average particle sizes. The mean

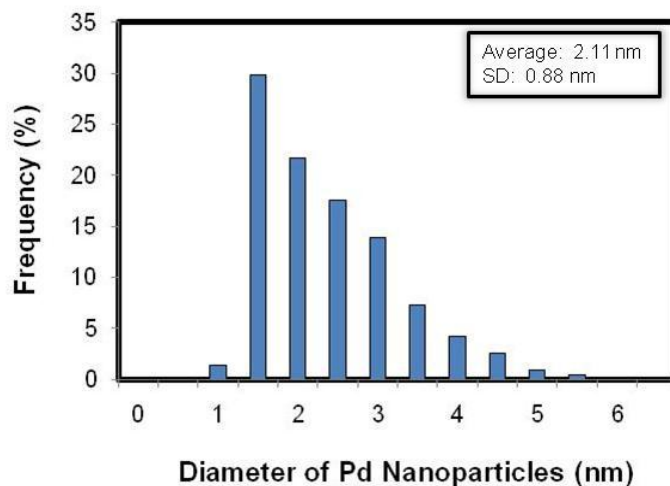


(a)

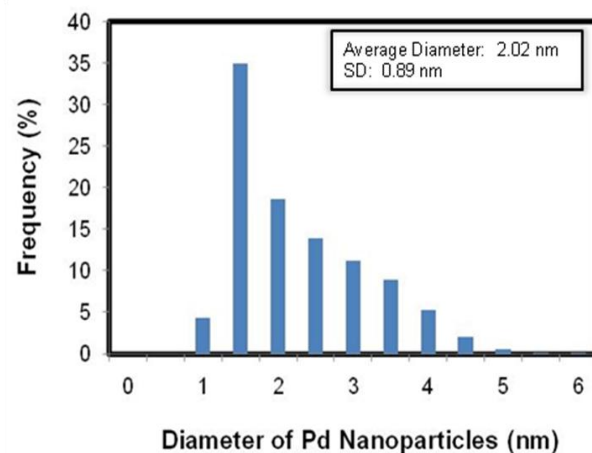


(b)

**Figure 2-12.** TEM images of dodecanethiol capped Pd nanoparticles extracted from the aqueous phase where stabilized with (a) 0.075 wt% CMC (b) 0.075 wt% PVP at 50°C. The Pd nanoparticles were extracted from the aqueous phase, after 24 hours of aging, into the hexane phase and subsequently deposited onto a TEM grid.

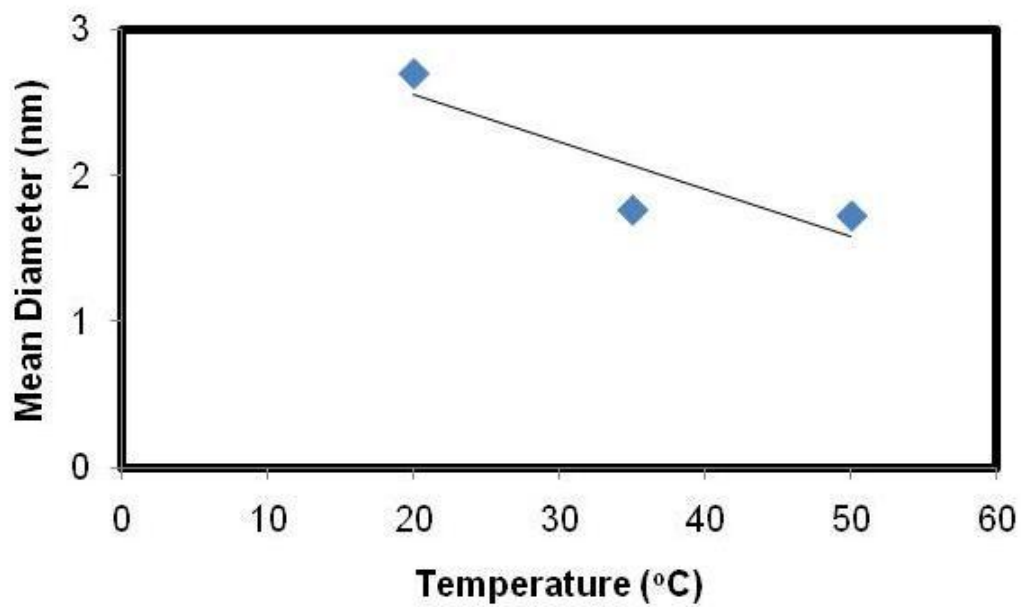


(a)



(b)

**Figure 2-13.** Particle size distribution histograms for dodecanethiol capped Pd nanoparticles extracted from the aqueous phase where stabilized with (a) 0.075 wt% CMC (b) 0.075 wt% PVP at 50°C. The Pd nanoparticles were extracted from the aqueous phase, after 24 hours of aging, into the hexane phase and subsequently deposited onto a TEM grid. More than 5,000 particles were analyzed for each sample.



(a)

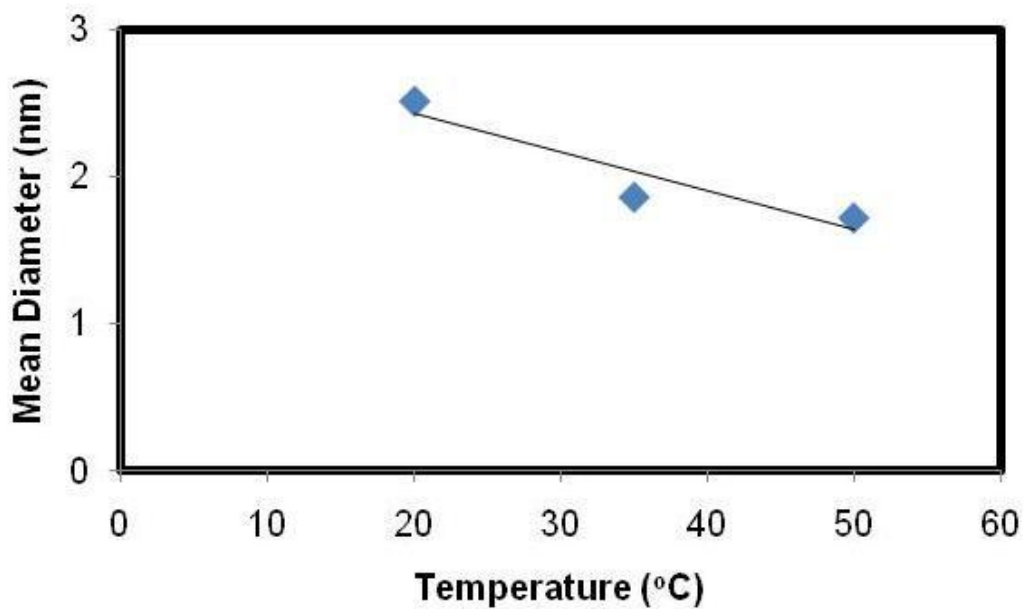


**Figure 2-14.** Effect of synthesis temperature on the mean particle diameter for Pd nanoparticles synthesized using (a) 0.15 wt% CMC (b) 0.15 wt% PVP in the aqueous phase.

CMC (wt%)	20°C Synthesis Diameter (nm)	SD (nm)	35°C Synthesis Diameter (nm)	SD (nm)	50°C Synthesis Diameter (nm)	SD (nm)
0.15	2.70	0.80	1.77	0.72	1.73	0.76
0.075	2.77	0.66	---	---	2.11	0.88
0.05	2.80	0.88	---	---	---	---
0.005	4.31	1.62	---	---	---	---

(a)

PVP (wt%)	20°C Synthesis Diameter (nm)	SD (nm)	35°C Synthesis Diameter (nm)	SD (nm)	50°C Synthesis Diameter (nm)	SD (nm)
0.15	2.51	1.48	1.86	1.28	1.73	0.73
0.075	2.86	1.29	---	---	2.02	0.89

(b)

**Table 2-1.** The mean particle size and standard deviation for Pd nanoparticles synthesized with (a) CMC capping ligand and (b) PVP capping ligand at various temperatures.



particle sizes and standard deviations obtained at the different synthesis temperatures are listed in Table 2-1.

### **2.3.4 Effect of Ligand Exchange**

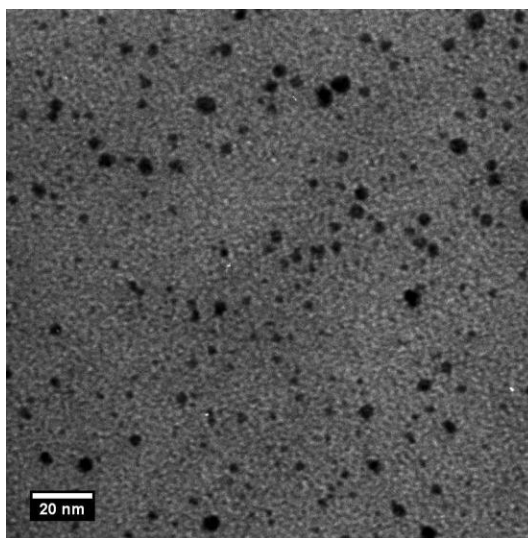
Due to the very dilute concentration of the Pd nanoparticle aqueous dispersions, the water-soluble ligands were exchanged with dodecanethiol in order to extract and concentrate the Pd nanoparticles into an organic phase for TEM analysis. Liu et al. (2007) demonstrated that the transfer of the Pd nanoparticles from the aqueous phase into the organic phase did not significantly affect the particle size or size distribution. In order to ensure that the exchange process did not affect the size and size distribution of the measured particles the effect of the ligand exchange was investigated.

#### **0.15 wt% PVP Stabilizing Agent**

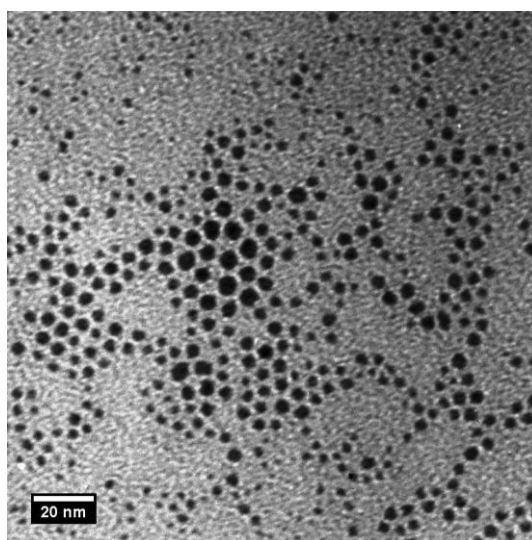
For example, a TEM image for Pd nanoparticles synthesized at 35°C and stabilized with 0.15 wt% PVP in the aqueous phase is shown in Figure 2-15. Also shown in Figure 2-15 is an image of the same Pd nanoparticles after their extraction from the aqueous phase to the hexane phase by introducing dodecanethiol as a ligand in the organic phase. The dodecanethiol effectively displaces the PVP from the surface of the nanoparticles, thereby enabling efficient phase transfer. The TEM images show that the Pd nanoparticles retain their small size (< 10 nm) and spherical shape after PVP is exchanged with dodecanethiol and the particles are extracted into the hexane phase. The dodecanethiol capped Pd nanoparticles had a mean diameter of 1.86 nm (SD = 1.28 nm, RSD = 0.688), while particles stabilized with 0.15 wt% PVP at 35°C had a mean

diameter of 1.22 nm (SD = 0.55 nm, RSD = 0.446). The particle size distributions obtained for the 35°C synthesis of Pd nanoparticles capped with both 0.15 wt% PVP in water and the same particles capped with dodecanethiol in the hexane phase are shown in Figure 2-16.

TEM images for Pd nanoparticles synthesized at 50°C and stabilized with 0.15 wt% PVP in the aqueous phase and the corresponding dodecanethiol capped particles in hexane are shown in Figure 2-17. The TEM images show that the Pd nanoparticles retain their small size (< 10 nm) and spherical shape after PVP is exchanged with dodecanethiol and extracted into the hexane phase. The dodecanethiol capped Pd nanoparticles had a mean diameter of 1.72 nm (SD = 0.73 nm, RSD = 0.423), while particles stabilized with 0.15 wt% PVP at 50°C had a mean diameter of 2.04 nm (SD = 0.91 nm, RSD = 0.446). The particle size distributions obtained for the 50°C synthesis of Pd nanoparticles capped with 0.15 wt% PVP in water and the subsequently extracted dodecanethiol capped nanoparticles in hexane are shown in Figure 2-18. It was determined that the dodecanethiol capped Pd nanoparticles had particle sizes and size distributions comparable to those obtained for Pd nanoparticles synthesized and stabilized in the aqueous phase using a 0.15 wt% PVP solution. In order to further investigate the effect of the ligand exchange on Pd nanoparticle size and size distribution, experiments were also conducted using a 0.075 wt% PVP aqueous solution.

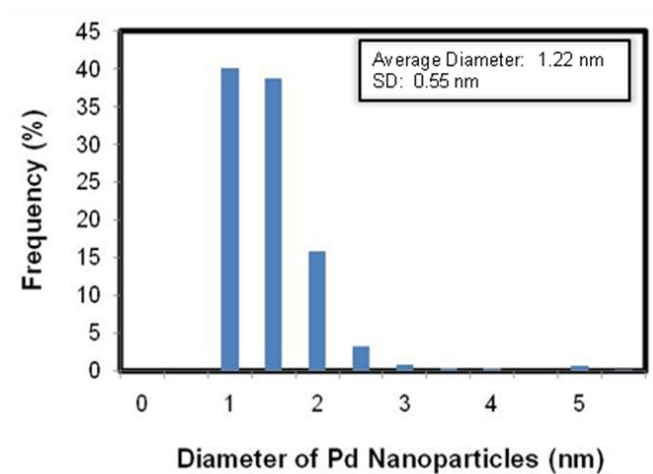


(a)

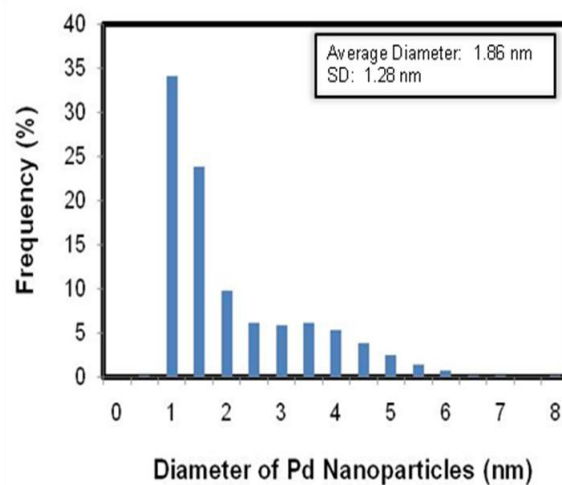


(b)

**Figure 2-15.** TEM images of Pd nanoparticles (a) stabilized with 0.15 wt% PVP at 35°C in the aqueous phase, and subsequently (b) extracted from the aqueous phase to the organic phase using dodecanethiol capping agent. The Pd nanoparticles were extracted from the aqueous phase, after 24 hours of aging, into the hexane phase and subsequently deposited onto a TEM grid.



(a)



(b)

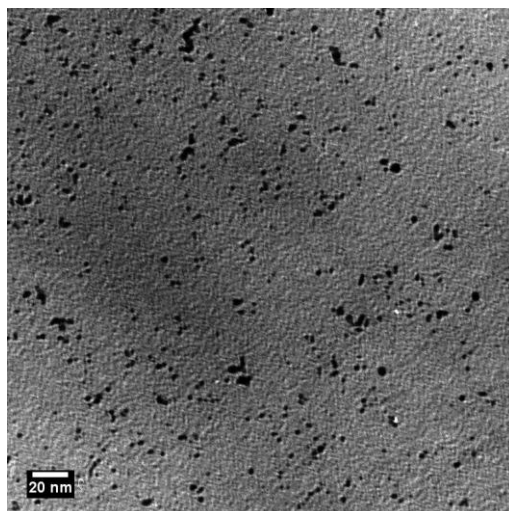
**Figure 2-16.** Particle size distribution histograms for Pd nanoparticles (a) stabilized with 0.15 wt% PVP in the aqueous phase at 35°C, and subsequently (b) extracted from the aqueous phase to the organic phase using dodecanethiol capping agent. The Pd nanoparticles were extracted from the aqueous phase, after 24 hours of aging, into the hexane phase and subsequently deposited onto a TEM grid.

### **0.075 wt% PVP Stabilizing Agent**

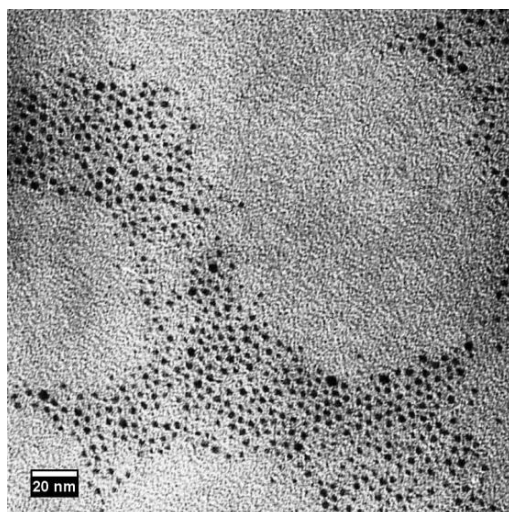
TEM images for Pd nanoparticles synthesized at 50°C and stabilized with 0.075 wt% PVP in the aqueous phase and the corresponding dodecanethiol capped particles in hexane are shown in Figure 2-19. The TEM images again show that the Pd nanoparticles retain their small size and spherical shape after PVP is exchanged with dodecanethiol and extracted into the hexane phase. The dodecanethiol capped Pd nanoparticles had a mean diameter of 2.02 nm (SD = 0.89 nm, RSD = 0.441), while particles stabilized with 0.075 wt% PVP at 50°C had a mean diameter of 1.67 nm (SD = 0.62 nm, RSD = 0.371). The particle size distributions obtained for the 50°C synthesis of Pd nanoparticles capped with 0.075 wt% PVP in water and the subsequently extracted dodecanethiol capped nanoparticles in hexane are shown in Figure 2-20. This series of experiments successfully demonstrated that transferring the Pd nanoparticles from the aqueous phase into the hexane phase by exchanging the polysugar ligand with dodecanthiol capping agent did not significantly affect the particle size or size distribution, which is important since it is necessary to perform a ligand exchange for improved imaging during TEM analysis.

### **2.3.5 Effect of Nanoparticle Processing**

The CMC-stabilized Pd nanoparticle aqueous dispersions were synthesized at very dilute concentrations in order to obtain particles of small size with narrow particle size distributions. The incipient wetness impregnation technique was used to prepare all supported catalysts. In order to facilitate an efficient deposition of the aqueous nanoparticle dispersions onto the various supporting materials, the Pd nanoparticle

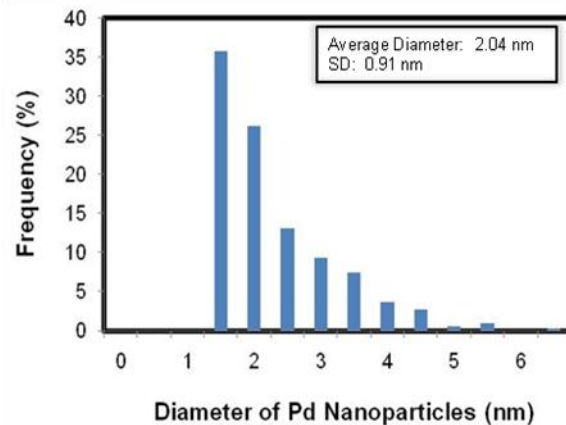


(a)

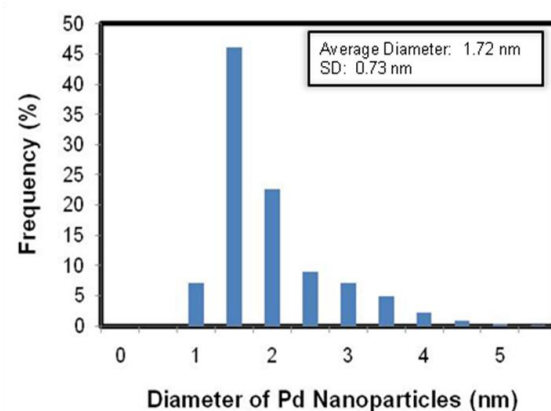


(b)

**Figure 2-17.** TEM images of Pd nanoparticles (a) stabilized with 0.15 wt% PVP in the aqueous phase at 50°C, and subsequently (b) extracted from the aqueous phase to the organic phase using dodecanethiol capping agent. The Pd nanoparticles were extracted from the aqueous phase, after 24 hours of aging, into the hexane phase and subsequently deposited onto a TEM grid.

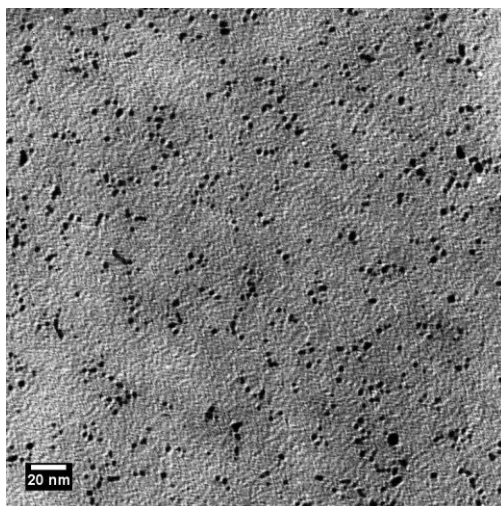


(a)

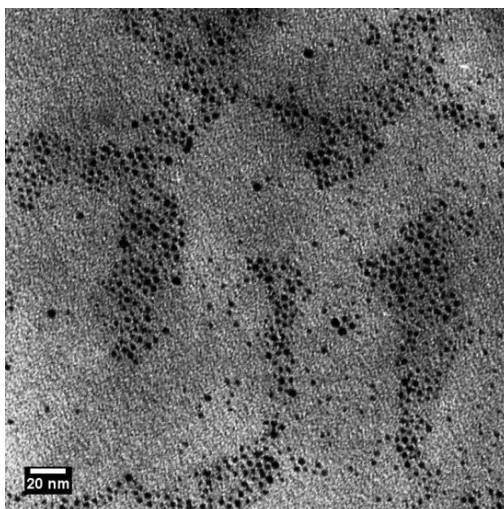


(b)

**Figure 2-18.** Particle size distribution histograms for Pd nanoparticles (a) stabilized with 0.15 wt% PVP in the aqueous phase at 50°C, and subsequently (b) extracted from the aqueous phase to the organic phase using dodecanethiol capping agent. The Pd nanoparticles were extracted from the aqueous phase, after 24 hours of aging, into the hexane phase and subsequently deposited onto a TEM grid. More than 5,000 particles were analyzed for each sample.



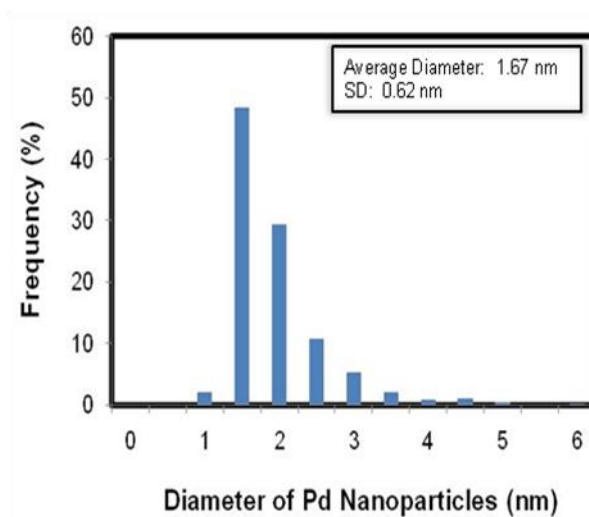
(a)



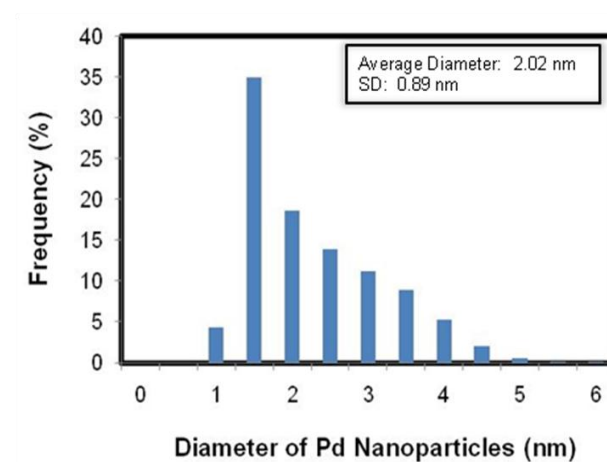
(b)

**Figure 2-19.** TEM images of Pd nanoparticles (a) stabilized with 0.075 wt% PVP in the aqueous phase at 50°C, and subsequently (b) extracted from the aqueous phase to the organic phase using dodecanethiol capping agent. The Pd nanoparticles were extracted from the aqueous phase, after 24 hours of aging, into the hexane phase and subsequently deposited onto a TEM grid.





(a)

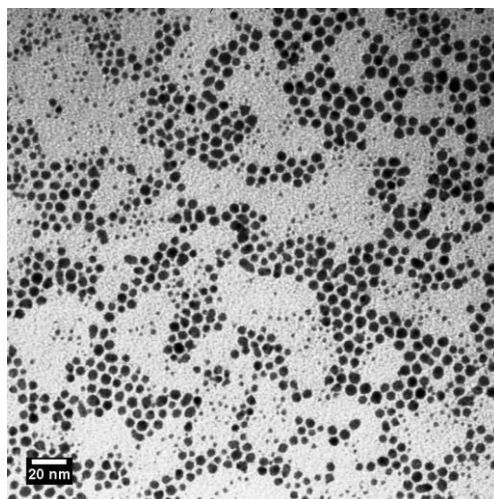


(b)

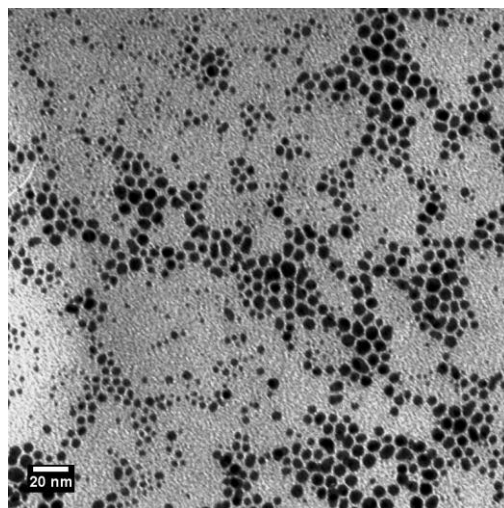
**Figure 2-20.** Particle size distribution histograms for Pd nanoparticles (a) stabilized with 0.075 wt% PVP in the aqueous phase at 50°C, and subsequently (b) extracted from the aqueous phase to the organic phase using dodecanethiol capping agent. The Pd nanoparticles were extracted from the aqueous phase, after 24 hours of aging, into the hexane phase and subsequently deposited onto a TEM grid. More than 5,000 particles were analyzed for each sample.

dispersions were concentrated prior to deposition. A rotary evaporator was used to efficiently remove most of the water and concentrate the CMC-stabilized Pd nanoparticles in aqueous solution. Experiments were conducted in order to evaluate the effect of process conditions on the average particle size and size distribution.

TEM images for Pd nanoparticles stabilized at ambient conditions with 0.005 wt% CMC before and after concentration in the aqueous phase are shown in Figure 2-21. For both the unconcentrated and concentrated aqueous solutions, the water-soluble ligands were exchanged with dodecanethiol in order to extract the Pd nanoparticles into an organic phase for purposes of TEM imaging. Before processing with the rotary evaporator, the Pd nanoparticles were of small size ( $< 10$  nm) and spherical morphology as illustrated in Figure 2-21. It is noted that the CMC-stabilized Pd nanoparticles retained their small size ( $< 10$  nm) and spherical shape after processing at 0.080 bar and  $50^{\circ}\text{C}$  (see Figure 2-22). The particle size distributions obtained for Pd nanoparticles stabilized at ambient conditions with 0.005 wt% CMC before and after rotary evaporation are shown in Figure 2-22. Before evaporation, the Pd nanoparticles had a mean diameter of 3.67 nm (SD = 1.95 nm, RSD = 0.531). After evaporation, the Pd nanoparticles had a mean diameter of 3.84 nm (SD = 1.74 nm, RSD = 0.454). This set of experiments demonstrated that concentrating the 0.005 wt% CMC-capped Pd nanoparticles in aqueous solution using a rotary evaporator at reduced pressure and elevated temperature did not have a significant effect on the average particle size, morphology, or particle size distribution.

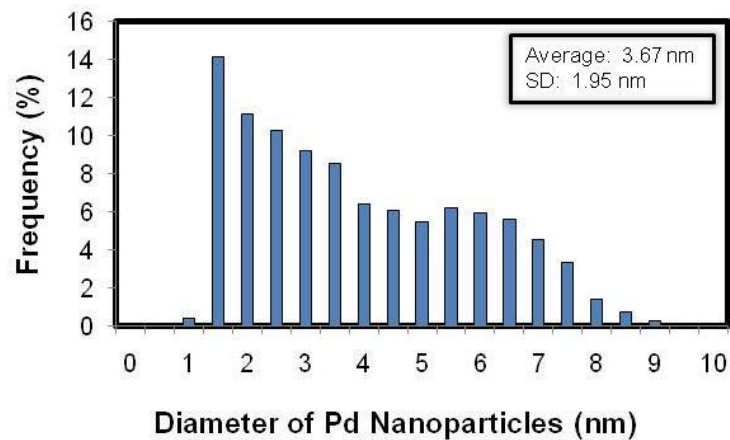


(a)

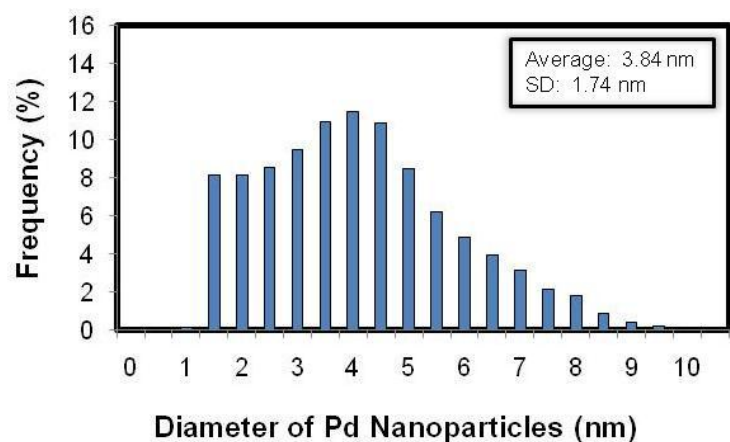


(b)

**Figure 2-21.** TEM images of Pd nanoparticles stabilized with 0.005 wt% CMC in the aqueous phase at 20°C (a) before rotary evaporation (b) after rotary evaporation.



(a)



(b)

**Figure 2-22.** Particle size distribution histograms for Pd nanoparticles stabilized with 0.005 wt% CMC in the aqueous phase at 20°C (a) before rotary evaporation (b) after rotary evaporation. More than 5,000 particles were analyzed for each sample.

## 2.4 Hydrodechlorination of TCE

### 2.4.1 Unsupported Pd Nanoparticle Catalysts

Liu et al. (2008) studied the batch hydrodechlorination of TCE using unsupported CMC-Pd nanoparticle catalysts dispersed in the aqueous phase. Experiments using unsupported CMC-capped Pd nanoparticles dispersed in the aqueous phase were repeated in the current study in order to confirm and reproduce these results, and in order to make direct comparisons between these unsupported nanoparticles and the supported catalysts described above. Control tests were previously performed with CMC and hydrogen (in the absence of Pd) to verify that CMC was not able to catalyze the degradation of TCE without Pd. The 0.15 wt% CMC-stabilized Pd nanoparticle catalysts (0.01 mM Pd) as synthesized by Liu et al. (2008) degraded nearly 81% of the TCE within the first four minutes of initiating the hydrodechlorination reaction as shown in Figure 2-23. The 0.15 wt% CMC-capped Pd nanoparticle catalysts (0.01 mM Pd) synthesized in this study demonstrated a very similar effectiveness for TCE dechlorination with almost 84% of the TCE degraded within the first four minutes as shown in Figure 2-23. Comparing the average particle size and size distribution for the 0.15 wt% CMC-stabilized Pd nanoparticles synthesized by Liu et al. (average diameter = 2.5 nm, SD = 0.8 nm) with those synthesized in the current study (average diameter = 2.7 nm, SD = 0.8 nm), we see that the particles are approximately the same size and have nearly the same size distribution. These experiments show that the CMC-stabilized Pd nanoparticle synthesis process was successfully and effectively replicated.

## 2.4.2 Alumina-Supported Pd Nanoparticle Catalysts

Since the focus of this study is on supported Pd nanoparticle catalyst systems, control tests for the batch hydrodechlorination of TCE over supported catalysts were conducted in the presence of the blank alumina support material and hydrogen (in the absence of Pd). These experiments confirm that  $\text{Al}_2\text{O}_3$  does not have the ability to catalyze the hydrodechlorination of TCE in the absence of Pd as shown in Figure 2-25. Once it was established that the support material was unable to catalyze the dechlorination of TCE, a series of experiments were performed using the  $\text{Al}_2\text{O}_3$  supported Pd nanoparticles. The nanoparticles were prepared using the CMC-based aqueous phase synthesis method followed by their deposition onto the alumina support material using incipient wetness impregnation.

In the presence of the various supported Pd nanoparticle catalysts, we observed the complete dechlorination of TCE in very short time spans (< 30 minutes). It is noted that in each of the following systems, the concentration of Pd in the reactor was (3.27 mg/L). The Pd concentration was held constant in order to make direct comparison of the activities of each of the following supported nanoparticle catalyst systems. Of the different catalyst samples studied, the system prepared using the 0.15 wt% CMC-Pd nanoparticles (average diameter = 2.7 nm, SD = 0.8 nm) supported on alumina were the most effective at catalyzing the degradation of TCE as illustrated in Figure 2-25. Almost 80% of the TCE had been removed and degraded from the aqueous phase within 15 minutes of initiating the reaction using this catalyst. In the case of the catalyst prepared using the 0.05 wt% CMC-Pd nanoparticles (average diameter = 2.8 nm, SD = 0.9 nm) supported by alumina, nearly 70% of the TCE had been degraded within the same 15

minute time span. The 0.05 wt% CMC-Pd nanoparticles supported on alumina were still very effective at degrading TCE. When using the catalyst prepared using the 0.005 wt% CMC-Pd nanoparticles (average diameter = 4.3 nm, SD = 1.6 nm), only ca. 55% of TCE was degraded after 15 minutes. The larger nanoparticle sizes obtained in this particular system resulted in a lower surface area to volume ratio for the active Pd catalyst material. Considering the same mass of Pd was loaded into the reactor for each experiment, a lower overall activity was therefore observed for the larger nanoparticle sizes. Since the hydrodechlorination of TCE is a surface-mediated process (Nutt *et al.*, 2005; Nutt *et al.*, 2006; He and Zhao, 2007; Liu *et al.*, 2008), reducing the available surface area for catalysis slows the rate of reaction.

Interestingly, the Pd catalysts in the heterogeneous system that were prepared using the 0.15 wt% CMC and 0.05 wt% CMC aqueous solutions had very similar particle sizes and size distributions, but exhibited distinctly different kinetics (see Figure 2-26). This discrepancy in the kinetics observed for the supported Pd nanoparticles indicates that the improvements in catalytic activity attained were a result of not only the increased surface area, but also the nature of the deposition as affected by the CMC stabilization. The nature of the deposition process can influence the manner in which the nanoparticles are dispersed onto the support material; thereby, influencing the associated available catalytic Pd surface area.

It is noted that all of the supported Pd nanoparticle catalysts had a lower catalytic activity than the unsupported particles that were homogeneously dispersed in the aqueous solutions (Liu *et al.*, 2008). There is naturally less surface area available upon which the catalysis can occur when particles are adhered to a surface rather than homogeneously

dispersed within the aqueous phase; therefore, a lower activity was achieved for each of the supported Pd catalysts. Additionally, the TCE must diffuse through the aqueous phase and the pores of the supporting material before it can adsorb onto the active sites for dechlorination by H<sub>2</sub>, which is not necessary in the case of the homogeneously dispersed Pd nanoparticles in the aqueous media. The time required for diffusion of TCE to the active Pd catalyst material in the heterogeneous system is much longer, which also contributes to the lower catalytic activity obtained. Nonetheless, the supported Pd nanoparticles show considerable activity towards TCE degradation and provide an opportunity to efficiently retain and recover the active Pd catalyst material.

## 2.5 Hydrodechlorination Kinetics

### 2.5.1 Effect of CMC Concentration

The H<sub>2</sub> concentration was assumed to remain constant during the batch mode dechlorination of TCE since the amount of H<sub>2</sub> present in the system vastly exceeded the stoichiometric requirements for conversion of TCE to biodegradable ethane. Thus, a pseudo-first-order kinetic model was used to interpret the kinetics for the degradation of TCE as shown in Equation 3-1 below.

$$-\frac{d[TCE]}{dt} = k_{app}[TCE] = k_{obs}[Pd][TCE] = k_{SA}a_s[Pd][TCE] \quad (3-1)$$

k<sub>app</sub> is the apparent reaction rate constant, which was obtained from experimentally determined data by plotting ln([TCE]<sub>t</sub>/[TCE]<sub>0</sub>) versus time and calculating the slope.



[Pd] is the concentration of Pd nanoparticles (g/L) in the reactor, and [TCE] is the concentration of TCE during the reaction (g/L).  $a_s$  is the specific surface area per gram of Pd nanoparticles ( $\text{m}^2/\text{g}$ ).  $k_{\text{app}}$  is normalized by the catalyst concentration to yield the observed reaction kinetic rate constant,  $k_{\text{obs}}$ . In addition,  $k_{\text{obs}}$  is normalized on the basis of the specific surface area per gram of Pd nanoparticles to yield the surface-area-based reaction kinetic rate constant,  $k_{\text{SA}}$ .

For the batch degradation tests using unsupported CMC-stabilized Pd nanoparticle catalysts, a linear correlation that is typical for first order kinetics was obtained for  $\ln([\text{TCE}]_t/[\text{TCE}]_0)$  with respect to time. However, degradation tests using alumina-supported Pd nanoparticle catalysts did not result in a linear relationship between  $\ln([\text{TCE}]_t/[\text{TCE}]_0)$  and time. The origin of this deviation from linear behavior will be discussed in detail below, and it is noted that the rate constants reported in Table 2-2 were determined from the linear portion of the curves once equilibrium behavior was achieved (i.e. after 10 minutes beyond initiation of the reaction).

The  $k_{\text{app}}$  value for the unsupported 0.15 wt% CMC-stabilized Pd nanoparticle catalysts was determined to be  $0.737 \text{ min}^{-1}$ . On the other hand, the  $k_{\text{app}}$  values for the alumina supported catalysts prepared using the 0.15, 0.05, and 0.005 wt% CMC-capped Pd nanoparticles were determined to be 0.359, 0.209, and  $0.092 \text{ min}^{-1}$ , respectively. Similar to the application of the unsupported Pd nanoparticles prepared with CMC (Liu 2008), the supported nanoparticle catalysts prepared using decreasing amounts of CMC resulted in nanoparticles of generally increasing particle size causing an associated decrease in  $k_{\text{app}}$ . The observed reaction rate constant,  $k_{\text{obs}}$ , was determined by considering the concentration of Pd nanoparticle catalysts in the hydrodechlorination

system along with  $k_{app}$ . Values for  $k_{obs}$  are listed in Table 2-2 and illustrate a dramatic increase from 28 L/g min to 109 L/g min when the amount of CMC used during nanoparticle synthesis was increased from 0.005 wt % to 0.15 wt %.

In order to compare the catalytic activity on the same Pd surface area basis, the specific surface area per gram of Pd nanoparticles in the reaction system was used to obtain the surface area based reaction rate constant,  $k_{SA}$ . Again, the  $k_{SA}$  values increased from  $0.240 \text{ min}^{-1} \text{ m}^{-2}$  to  $0.589 \text{ min}^{-1} \text{ m}^{-2}$  when the amount of CMC used during the nanoparticle synthesis was increased from 0.005 wt % to 0.15 wt %. If the catalytic activity were only a function of the available surface area, the respective values of  $k_{SA}$  would be the same for each of the different catalysts. However, this result illustrates that the increased activity for the catalyst prepared using the 0.15 wt % solution is not simply a function of the higher surface area, but that this catalyst had an inherently higher activity.

Turn over frequency (TOF) is often used to compare the activity of different catalysts (Boudart, 1995; Li *et al.*, 2002; Stowell and Korgel, 2005). TOF is the number of molecules that react per active site per unit time and was calculated using Equation 2-2.

$$TOF_{init} = - \left( \frac{d[TCE]}{dt} \right)_{t=0} \left( \frac{1}{[Pd]D_{Pd}} \right) \quad (2-2)$$

The dispersion ( $D_{Pd}$ ) of a Pd nanoparticle is defined as the ratio of surface Pd atoms to the total number of Pd atoms in a nanoparticle. The  $D_{Pd}$  was estimated using a core-shell

model (Liu *et al.*, 2008) and was also determined experimentally using chemisorption with carbon monoxide as the adsorbing gas. In addition, both the molar concentration of Pd atoms, [Pd], in the reaction system and the initial rate of TCE degradation were used in the calculation of  $\text{TOF}_{\text{init}}$ . The values of  $\text{TOF}_{\text{init}}$  obtained using the core shell model again increased as the amount of CMC used during the nanoparticle synthesis was increased from 0.005 wt % to 0.15 wt %, further indicating that the catalytic activity is enhanced in the case of the finely controlled Pd nanoparticle catalyst systems. It should be noted that each of the  $\text{TOF}_{\text{init}}$  values for the supported Pd nanoparticle catalysts were significantly lower than the values obtained for the unsupported Pd nanoparticle catalysts by nearly an order of magnitude. Even so, the supported Pd nanoparticles provide an opportunity to effectively retain and recover the active Pd catalyst material, which is essential for any practical environmental application. Furthermore, each of the alumina-supported Pd catalysts (0.33 wt% Pd) using nanoparticles of controlled size had considerably higher activity towards the degradation of TCE than conventional Pd catalysts (1 wt% Pd) supported on alumina (see Table 2-3) (Nutt *et al.*, 2005). Hence, synthesizing Pd nanoparticles of finely controlled size facilitates the more efficient dechlorination of TCE to biodegradable ethane using less active Pd catalyst material than is required with traditional supported Pd catalysts.

### **2.5.2 Chloride Evolution**

The reaction intermediates dichloroethylene (DCE) and vinyl chloride (VC) are more hazardous to the environment than TCE (Nutt *et al.*, 2005; He and Zhao, 2005; U.S. EPA, 1998), so in order to use the hydrodechlorination technology for the decomposition of

capping agent	support	Pd (mg)	particle size, nm	$a_{s_1}$ , $m^2 g^{-1}$	$k_{app}$ , $min^{-1}$	$k_{obs}$ , $L g^{-1} min^{-1}$	$k_{SA}$ , $min^{-1} m^{-2}$
0.15 wt% CMC	Al <sub>2</sub> O <sub>3</sub>	0.33	2.7	184.8	0.359	109	0.589
0.05 wt% CMC	Al <sub>2</sub> O <sub>3</sub>	0.33	2.8	178.2	0.209	63	0.352
0.005 wt% CMC	Al <sub>2</sub> O <sub>3</sub>	0.33	4.3	116.1	0.092	28	0.240
no CMC	Al <sub>2</sub> O <sub>3</sub>	0.34	5.1*	98.4*	0.211	63	0.638*
no CMC	TS-1	0.34	5.1*	98.4*	0.387	112	1.13*
0.005 wt% CMC (uncalcined)	Al <sub>2</sub> O <sub>3</sub>	0.33	4.3	116.1	0.188	57	0.490
0.15 wt% CMC	none	0.10	2.7	184.8	0.737	741	4.0
0.15 wt% CMC <sup>a</sup>	none	0.10	2.4	207.9	0.775	731	3.52
no CMC <sup>b</sup>	Al <sub>2</sub> O <sub>3</sub>	0.17	---	177	---	12.2	---

**Table 2-2.** Average particle size and reaction rate constants for the aqueous phase hydrodechlorination of TCE in the presence of supported and unsupported Pd nanoparticle catalysts synthesized using various amounts of CMC capping agent. It is noted that the rate constants were determined from the plot of  $\ln ([TCE]_t/[TCE]_0)$  against time of hydrodechlorination of TCE. \* Values determined from chemisorption with carbon monoxide as the adsorbing gas. <sup>a</sup> Values determined by Liu et al. <sup>b</sup> Values determined by Wong et al.

capping agent	support	Pd (mg)	particle size, nm	D <sub>Pd</sub> (%)	TOF <sub>init</sub> , min <sup>-1</sup>	particle size, nm*	D <sub>Pd</sub> (%)*	TOF <sub>init</sub> , min <sup>-1</sup> *
0.15 wt% CMC	Al <sub>2</sub> O <sub>3</sub>	0.33	2.7	45.1	9.8	17.2	6.5	67.8
0.05 wt% CMC	Al <sub>2</sub> O <sub>3</sub>	0.33	2.8	43.8	5.8	9.4	11.9	21.4
0.005 wt% CMC	Al <sub>2</sub> O <sub>3</sub>	0.33	4.3	30.4	3.7	9.5	11.8	9.6
0.005 wt% CMC (uncalcined)	Al <sub>2</sub> O <sub>3</sub>	0.33	4.3	30.4	7.6	---	---	---
0.15 wt% CMC	none	0.10	2.7	45.1	66.5	---	---	---
0.15 wt% CMC <sup>a</sup>	none	0.10	2.4	54.2	54.2	---	---	---
no CMC <sup>b</sup>	Al <sub>2</sub> O <sub>3</sub>	0.17	---	---	2.8	---	---	---

**Table 2-3.** Initial TOF and catalyst dispersions (D<sub>Pd</sub>) for the aqueous phase hydrodechlorination of TCE in the presence of supported and unsupported Pd nanoparticle catalysts synthesized using various amounts of CMC capping agent. Values were determined using a core-shell model unless otherwise specified. \* Values determined from chemisorption with carbon monoxide as the adsorbing gas. <sup>a</sup> Values determined by Liu et al. <sup>b</sup> Values determined by Wong et al.

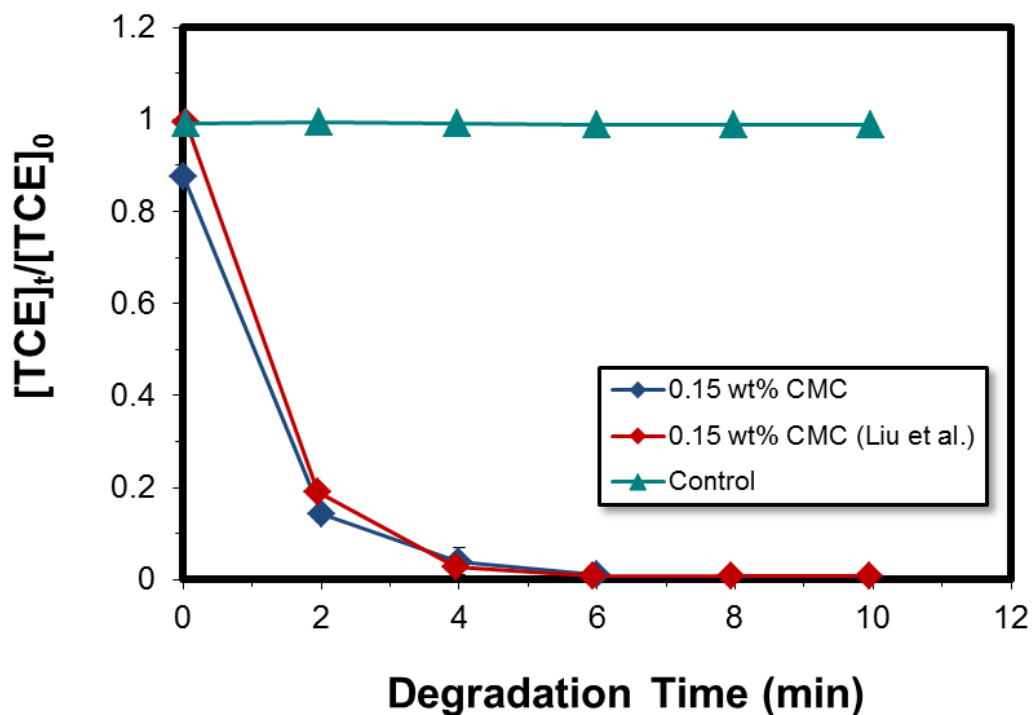


**Figure 2-23.** Aqueous phase hydrodechlorination of TCE catalyzed by unsupported CMC-stabilized Pd nanoparticles synthesized using a 0.15 wt% CMC solution. Data from the control experiment (only CMC in the system) is presented for comparison with degradation data. Initial total TCE concentration was 50 mg/L. Concentration of Pd nanoparticles was 1.0 mg/L. Kinetic experiments were performed by Man Zhang. Catalyst design and preparation, catalyst characterization, data analysis, and data interpretation as pertaining to this document were performed by the author. (A collaborative paper is in preparation).

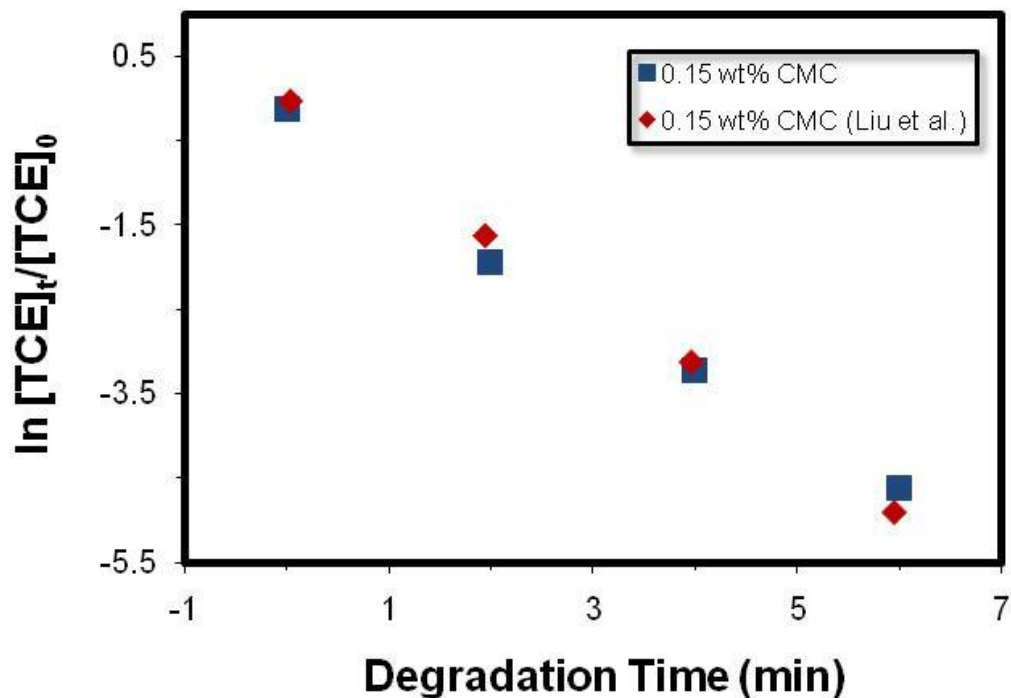


**Figure 2-24.** Plot of  $\ln ([TCE]_t/[TCE]_0)$  against time of the aqueous phase hydrodechlorination of TCE catalyzed by unsupported CMC-stabilized Pd nanoparticles synthesized using a 0.15 wt% CMC solution. Initial total TCE concentration was 50 mg/L. Concentration of Pd nanoparticles was 1.0 mg/L. Kinetic experiments were performed by Man Zhang. Catalyst design and preparation, catalyst characterization, data analysis, and data interpretation as pertaining to this document were performed by the author. (A collaborative paper is in preparation).

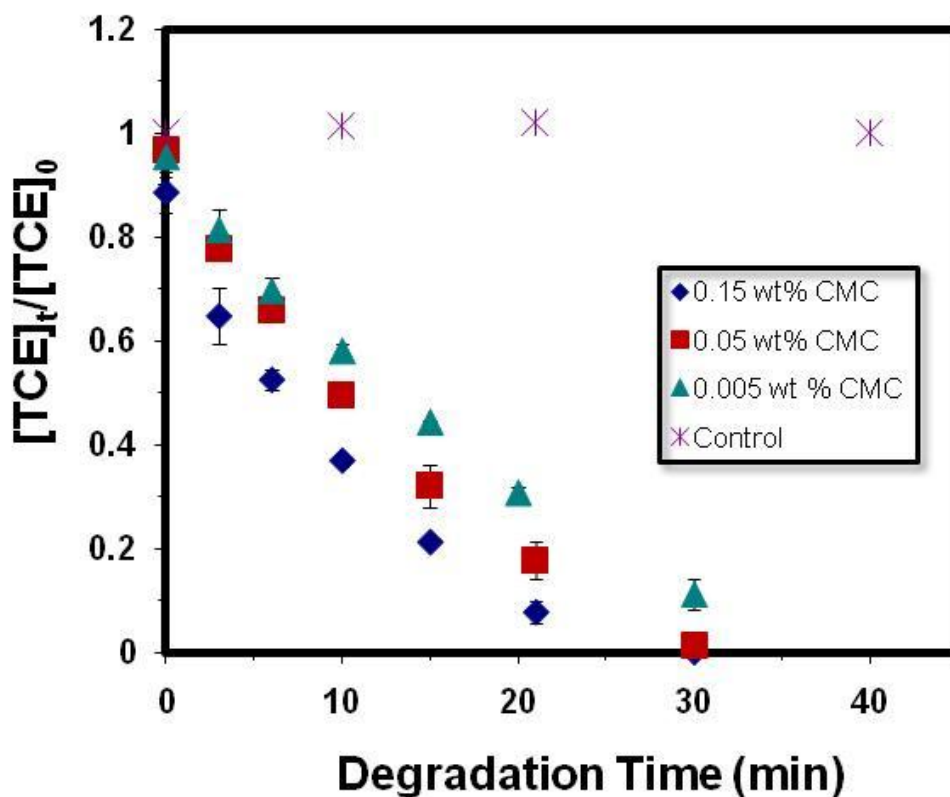


**Figure 2-25.** Aqueous phase hydrodechlorination of TCE catalyzed by alumina-supported Pd nanoparticles synthesized using various CMC concentrations. Data from the control experiment (only alumina in the system) is presented for comparison with degradation data. Initial total TCE concentration was 50 mg/L. Concentration of Pd nanoparticles was 3.3 mg/L. Kinetic experiments were performed by Man Zhang. Catalyst design and preparation, catalyst characterization, data analysis, and data interpretation as pertaining to this document were performed by the author. (A collaborative paper is in preparation).



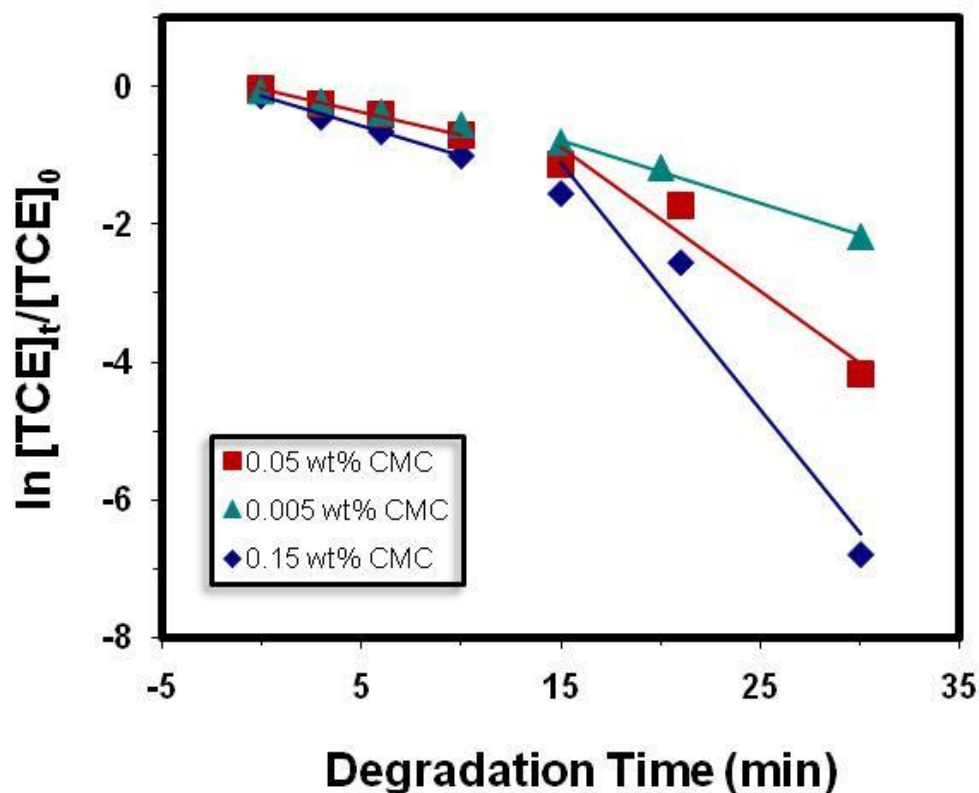


**Figure 2-26.** Plot of  $\ln ([TCE]_t/[TCE]_0)$  against time of the aqueous phase hydrodechlorination of TCE catalyzed by alumina-supported Pd nanoparticles synthesized using various CMC concentrations. Initial total TCE concentration was 50 mg/L. Concentration of Pd nanoparticles was 3.3 mg/L. The two linear periods indicate a diffusional limitation for an initial total TCE concentration of 50 mg/L. Kinetic experiments were performed by Man Zhang. Catalyst design and preparation, catalyst characterization, data analysis, and data interpretation pertaining to this document were performed by the author. (A collaborative paper is in preparation).

TCE, it must completely convert TCE to biodegradable ethane. Experiments were conducted in collaboration with Man Zhang in order to monitor the degradation of TCE and simultaneous evolution of chloride ions in the aqueous reaction media over time. A mass balance was performed and all of the associated chlorine in TCE was converted to chloride ions. This indicates that all of the TCE was completely dechlorinated and the only final product was biodegradable ethane, and the more harmful halogenated intermediates were not formed. This result is consistent with that of Liu et al. (2008) who monitored the intermediates of the dechlorination reaction on other catalyst systems as well as the evolution of chlorine and concluded that the hydrodechlorination of TCE is one-step conversion to biodegradable ethane. Therefore, the hydrodechlorination of TCE over a supported Pd catalyst is a viable technology for wastewater remediation.

### **2.5.3 Catalyst Induction Period**

All of the alumina-supported Pd nanoparticle catalysts examined using an initial TCE concentration of 50 mg/L showed a deviation from the linear behavior expected for a pseudo-first-order kinetic model (see Figure 2-26).

The initial rate of decay of TCE was relatively slow for the first ~10 minutes, after which, the rate of degradation increased to reach an equilibrium value for each respective catalyst. It appears that there is an induction period in these studies before an equilibrium rate of degradation is reached after approximately ten minutes of initiating the TCE degradation reaction. This induction period is likely the result of the need for the TCE to diffuse into the pores of the alumina-supported Pd catalyst after its introduction into the reaction mixture until an equilibrium concentration of TCE can be

achieved, which occurs after some period of time.  $\text{Al}_2\text{O}_3$  is a hydrophilic support material; therefore, this support induces a diffusional limitation to the concentration of TCE within the catalyst pores, which results in this induction period. Experiments using hydrophobic supports described later in this document illustrate that this diffusional limitation, and resulting induction period, can be overcome by changing the nature of the support material. In order to further examine the nature of this deviation from linear behavior, a set of experiments were conducted using the alumina supported catalysts in which the initial TCE concentration was reduced to 10 mg/L so as to more quickly reach an equilibrium concentration. If the non-linearity is indeed due to this necessary pre-concentration induction period, then reducing the initial TCE concentration should trend towards more linear kinetics. After reducing the initial concentration to 10 mg/L, we see the linear behavior typical of a pseudo-first-order kinetic model confirming a diffusional limitation. The slope of the curve in Figure 2-27 obtained using an initial TCE concentration of 10 mg/L is nearly parallel to the slope in the equilibrium region of the data obtained for the 50 mg/L experiment (i.e. after the 10 minute induction period), indicating that once the diffusional limitation is accounted for similar rate constants are achieved. However, for any practical environmental application higher concentrations of TCE would be more applicable. Although a diffusional limitation was not detected with an initial concentration of 10 mg/L, it is likely that higher concentrations would be present in contaminated soil or groundwater. Therefore, it is necessary to explore and optimize catalysts that can accommodate the higher TCE concentrations. Based on the above results, it is suggested that in order to overcome this mass transport limitation a hydrophobic support material could be examined. A hydrophobic material

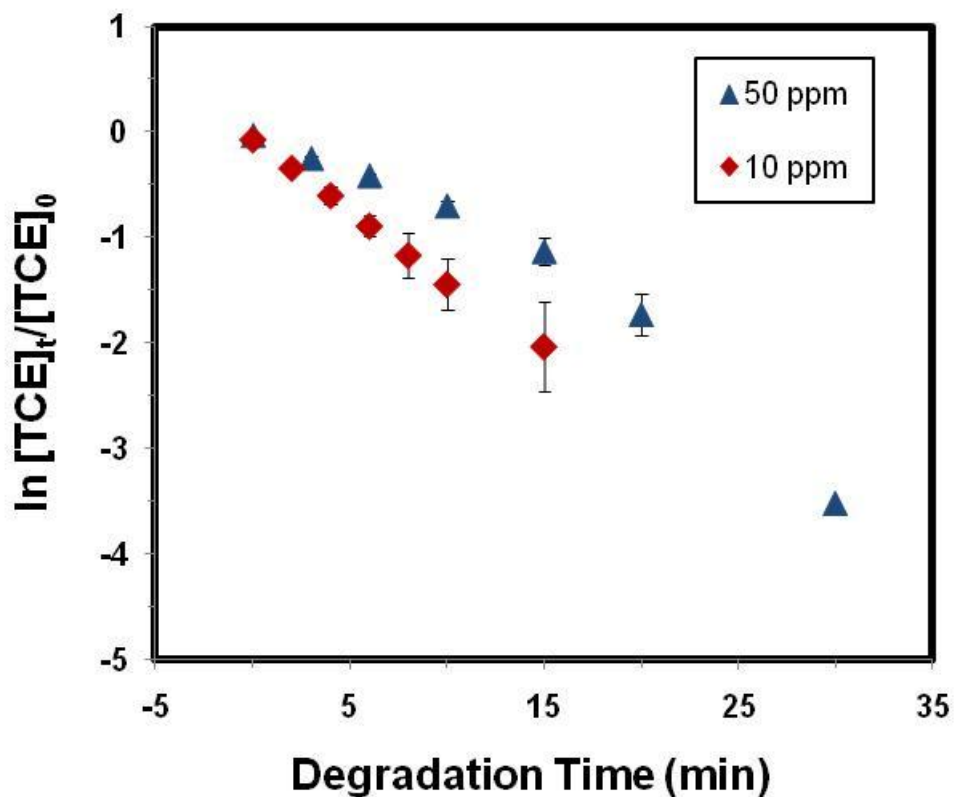


**Figure 2-27.** Plot of  $\ln ([TCE]_t/[TCE]_0)$  against time of the aqueous phase hydrodechlorination of TCE catalyzed by alumina-supported Pd nanoparticles synthesized using a 0.05 wt% CMC solution. Concentration of Pd nanoparticles was 3.3 mg/L. Kinetic experiments were performed by Man Zhang. Catalyst design and preparation, catalyst characterization, data analysis, and data interpretation as pertaining to this document were performed by the author. (A collaborative paper is in preparation).

sample	capping agent	Pd loading (wt%)	support material	calcination temp (°C)	reduction temp (°C)	specific SA* (m <sup>2</sup> /g)
A1	none	0	Al <sub>2</sub> O <sub>3</sub>	---	---	83
A2	none	0	Al <sub>2</sub> O <sub>3</sub>	500	400	92
B1	0.15 wt% CMC	0.33	Al <sub>2</sub> O <sub>3</sub>	---	---	72
B2	0.15 wt% CMC	0.33	Al <sub>2</sub> O <sub>3</sub>	500	400	78
B3	0.15 wt% CMC	0.33	Al <sub>2</sub> O <sub>3</sub>	400	250	87
C1	0.005 wt% CMC	0.33	Al <sub>2</sub> O <sub>3</sub>	---	---	85
C2	0.005 wt% CMC	0.33	Al <sub>2</sub> O <sub>3</sub>	500	400	82

**Table 2-4.** Specific surface areas for Al<sub>2</sub>O<sub>3</sub> and Al<sub>2</sub>O<sub>3</sub>-supported Pd nanoparticles prepared using various concentrations of CMC capping ligand. \* Represents the measured BET surface areas.

would permit the rapid concentration of the TCE into the pores of the support; thereby, enhancing the degradation of TCE to biodegradable ethane. Studies involving the effect of the support material properties will be discussed in more detail below.

## **2.6 XRD Characterization of the Pd Nanoparticle Catalysts on Al<sub>2</sub>O<sub>3</sub>**

XRD measurements were collected for the alumina-supported Pd nanoparticle catalysts at Auburn University by the author and at West Virginia University by Dr. Mohindar Seehra and Dr. Vivek Singh. Table 2-4 presents each sample examined in the XRD studies. The diffraction patterns for both blank Al<sub>2</sub>O<sub>3</sub> and 0.33 wt% Pd nanoparticles supported on Al<sub>2</sub>O<sub>3</sub> collected at Auburn University are shown in Figure 2-28 with several distinct peaks observed for each material. It was determined that the Al<sub>2</sub>O<sub>3</sub> support material was theta phase with characteristic peaks observed around 37°, 39°, 45°, 46°, and 47° for this phase over the scanned region from 35° to 50°. Pd has diffraction patterns around 40° and 46° over this scanned region from 35° to 50° with the strongest peak appearing at 40°. Unfortunately, due to the very low Pd loading (0.33 wt% Pd) for these catalysts the Pd peaks could not be distinguished from peaks for the alumina support material. The Al<sub>2</sub>O<sub>3</sub> support not only diffracts at the same line positions as Pd for the scanned region from 35° to 50°, but also has much stronger diffraction peaks. Since the alumina line positions are very close to that of Pd, a broad scan between 10° and 85° was collected for Al<sub>2</sub>O<sub>3</sub> in order to isolate an optimum region to conduct a narrow scan with a higher sensitivity for these alumina-supported Pd nanoparticle catalysts. The broad scan from 10° to 85° conducted for the alumina support material is shown in Figure 2-29. It is

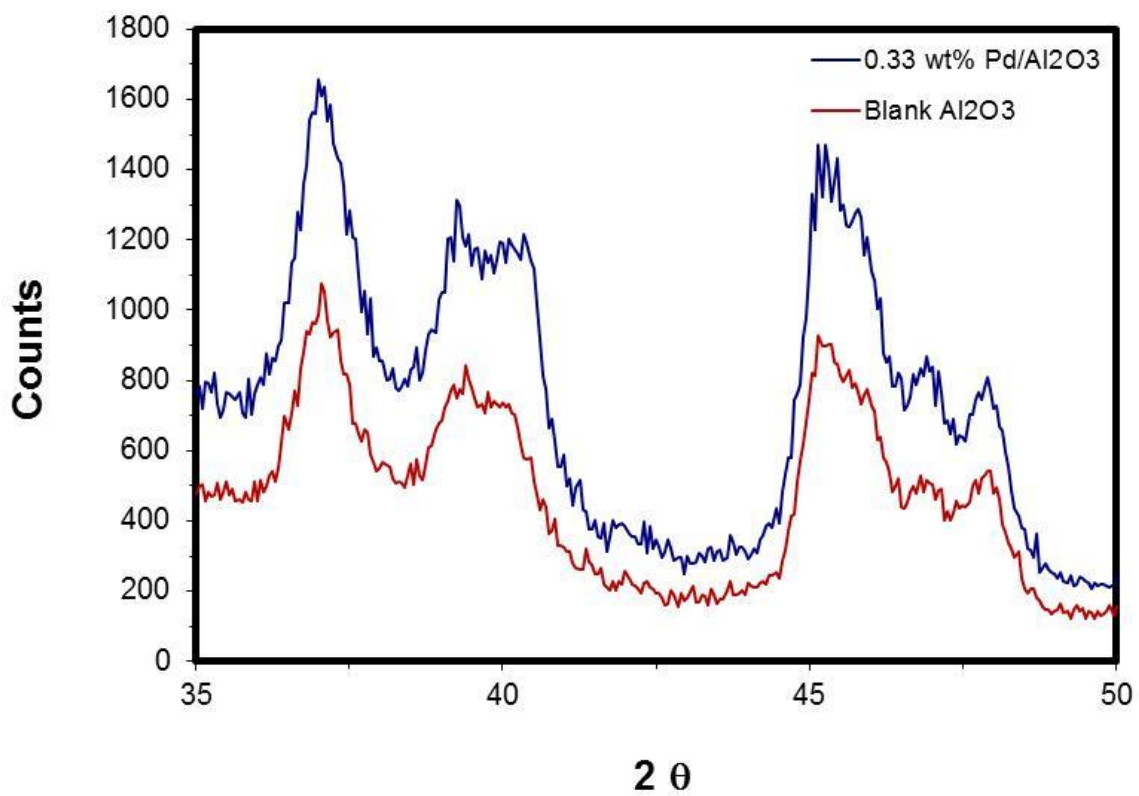


**Figure 2-28.** XRD patterns of Al<sub>2</sub>O<sub>3</sub> and Al<sub>2</sub>O<sub>3</sub>-supported Pd nanoparticles. Pd loading was 0.33 wt% on the Al<sub>2</sub>O<sub>3</sub> support material.

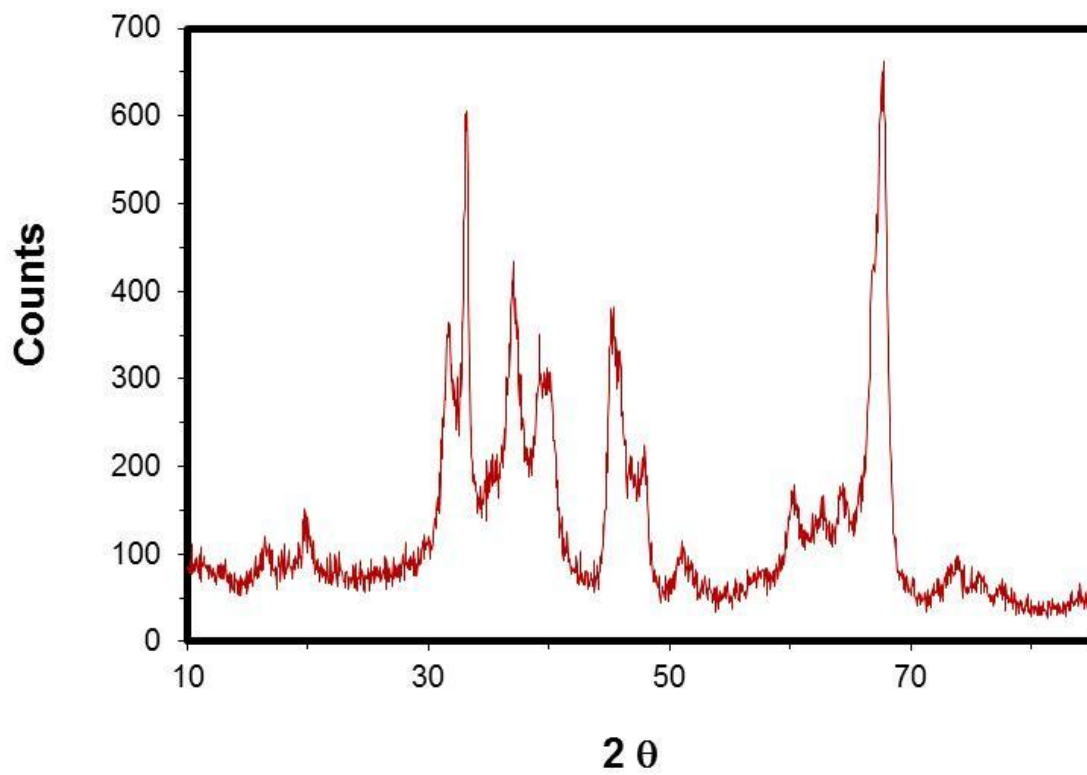


**Figure 2-29.** XRD pattern of  $\text{Al}_2\text{O}_3$  support material collected from a broad scan of the material from  $10^\circ$  to  $85^\circ$  using a Rigaku Miniflex powder X-ray diffractometer.



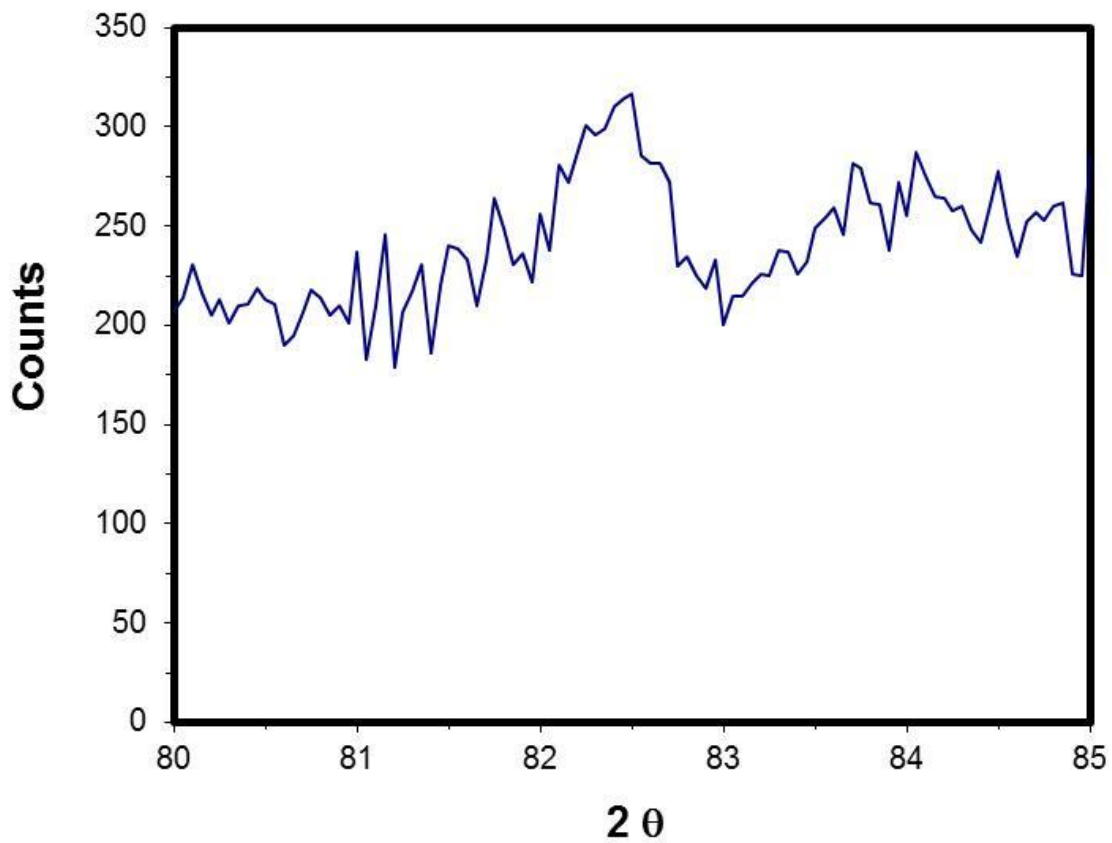


**Figure 2-30.** XRD pattern of alumina-supported Pd nanoparticles collected from a narrow scan of the catalyst from 80° to 85° using a Rigaku Miniflex powder X-ray diffractometer. Pd loading was 0.33 wt% on the Al<sub>2</sub>O<sub>3</sub> support material.

noted that only a very weak XRD peak for alumina was observed around  $2\theta = 84^\circ$  during the broad scan from  $10^\circ$  to  $85^\circ$ . Therefore, it was determined that a narrow scan from  $80^\circ$  to  $85^\circ$  would be collected, since Pd has a diffraction peak around  $81^\circ$  and there is very little interference from the alumina support material. The narrow scan from  $80^\circ$  to  $85^\circ$  for the alumina-supported Pd nanoparticle catalyst prepared using 0.15 wt% CMC (average size = 2.7 nm, SD = 0.8 nm) is shown in Figure 2-30. A weak XRD peak at  $2\theta = 82^\circ$  was observed for Pd; however, this peak could not be distinguished from the noise in the baseline. In conclusion, XRD studies performed using equipment at Auburn University did not provide enough suitable data to determine the average crystallite size or crystalline structure for these catalysts.

Diffraction patterns for both blank  $\text{Al}_2\text{O}_3$  and 0.33 wt% Pd nanoparticles on  $\text{Al}_2\text{O}_3$  were subsequently collected at West Virginia University using a broader scan from  $5^\circ$  to  $100^\circ$  as shown in Figure 2-31. Data for the narrow scan from  $75^\circ$  to  $90^\circ$  with higher sensitivity is shown in Figure 2-32. In Figure 2-31, the expected line positions for  $\text{Al}_2\text{O}_3$  and Pd are also shown and the data from  $35^\circ$  to  $50^\circ$  correspond well to the spectra collected at Auburn University. It is noted that almost all of the observed peaks can be assigned to  $\text{Al}_2\text{O}_3$ , having an average particle size of approximately 8 nm. Again, it is difficult to distinguish the Pd diffraction peaks from those of  $\text{Al}_2\text{O}_3$ , since the Pd loading (0.33 wt% Pd) is quite low for normal XRD detection. Despite the low metal loading, the line from Pd near  $2\theta = 82^\circ$  was clearly observed without interference from the  $\text{Al}_2\text{O}_3$  support, which was also observed in the studies at Auburn University. Consequently, a narrow scan from  $75^\circ$  to  $90^\circ$  was conducted using the high sensitivity conditions described above to verify the detection of Pd. The results shown in Figure 2-32 confirm

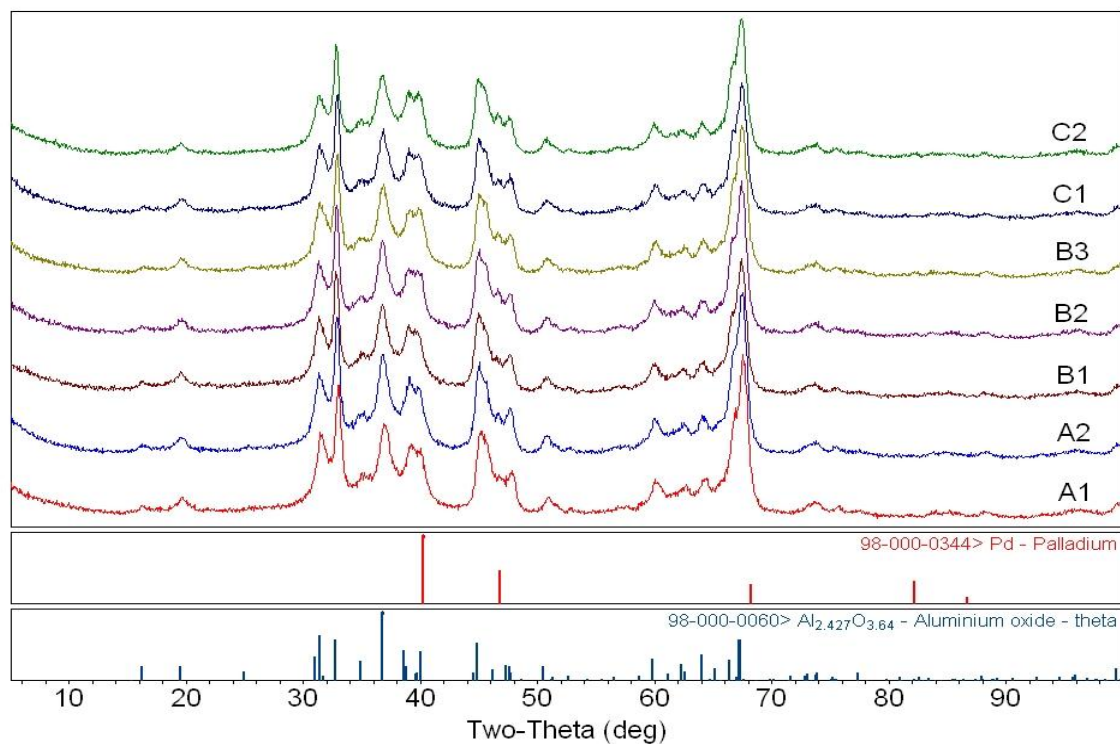


**Figure 2-31.** XRD patterns of Al<sub>2</sub>O<sub>3</sub> and alumina-supported Pd nanoparticles along with the expected line positions for both Al<sub>2</sub>O<sub>3</sub> and Pd material. Bragg angles (2θ) from 5° to 100° were scanned at 0.06° with a counting time of 5 seconds at each step.

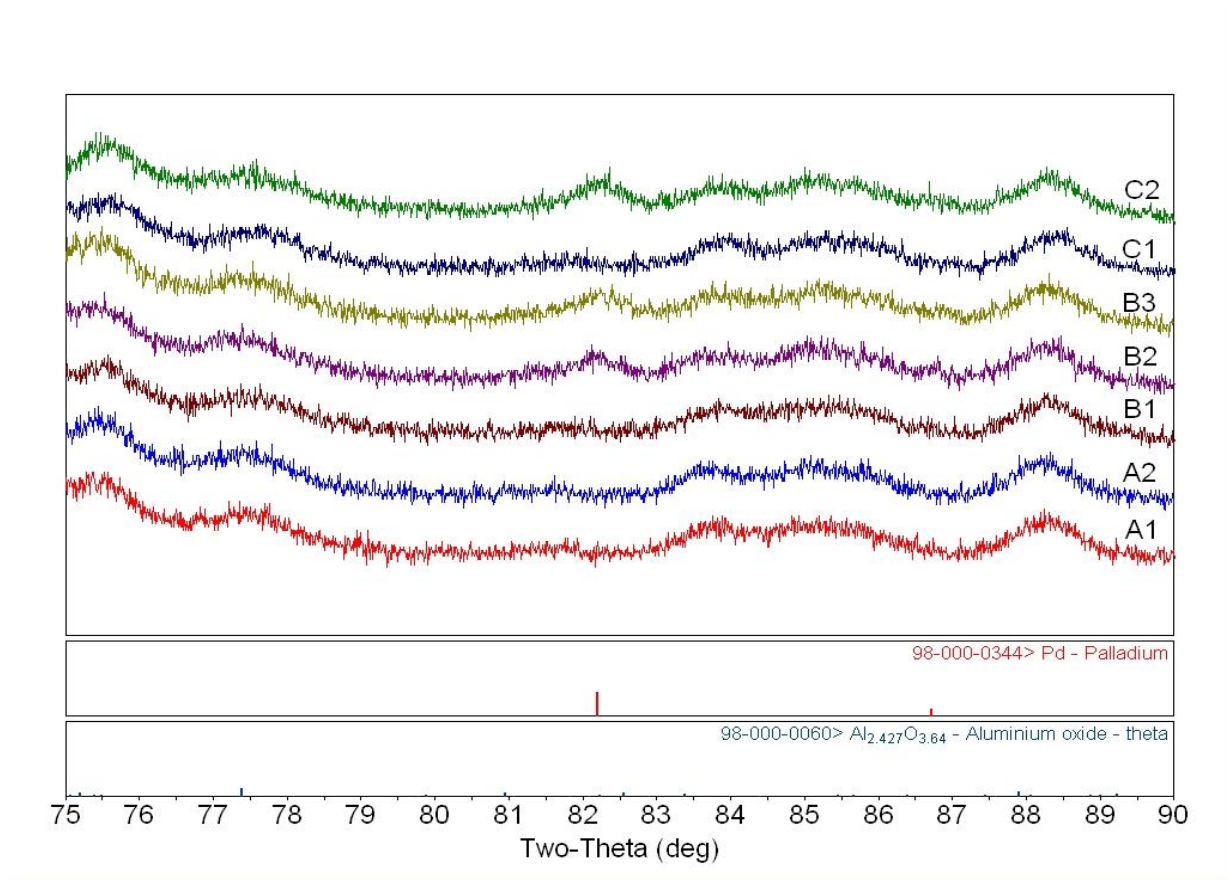


**Figure 2-32.** XRD patterns of Al<sub>2</sub>O<sub>3</sub> and alumina-supported Pd nanoparticles along with the expected line position for Pd near 82°. Bragg angles (2θ) from 75° to 90° were scanned at 0.01° with a counting time of 10 seconds at each step.

the presence of Pd nanoparticles with a particle size of approximately 14 nm (SD = 4 nm) and a peak area of 4412 (5%) for sample B2. Figure 2-32 also confirms the presence of Pd with a particle size of approximately 11 nm (SD = 3 nm) and a peak area of 7860 (10%) for sample B3. In addition, Figure 2-32 confirms the presence of Pd nanoparticles with a particle size of 14 nm (SD = 3 nm) and a peak area of 5240 (8%) for sample C2. To determine these parameters, the background was fitted to a fourth order polynomial and the peaks were fitted to pseudo-Voigt line-shape. It is noted that the Pd peak was not detected for the alumina-supported Pd nanoparticle catalysts before calcination and reduction (samples B1 and C1). It is suggested that the presence of the Pd peaks in samples B2, B3, and C2 results from Oswald ripening of the finely dispersed Pd particles into the observed larger particles under the calcination/reduction conditions; which, also explains the absence of the Pd peaks in the spectra obtained for the catalysts that did not undergo calcination and reduction (samples B1 and C1). The higher peak area (7860) of sample B3 vis-à-vis samples B2 and C2 suggests that more of the Pd has agglomerated into larger particles for this particular catalyst. The significance of these results in connection with the activity of these samples will be discussed in more detail later.

## **2.7 Effect of Catalyst Calcination on TCE Degradation Kinetics**

XRD analysis of the Pd nanoparticle catalysts synthesized with various CMC concentrations and deposited onto aluminum oxide support material suggest that calcination of these catalysts initiate crystallite growth resulting in a larger average diameter Pd nanoparticle. If the degradation of TCE depends on the available surface area, then the uncalcined catalysts should have better catalytic performance. Experiments

with Pd nanoparticles prepared with 0.005 wt% CMC deposited on aluminum oxide were conducted to test their catalytic activity both before and after calcination. The results are shown in Figure 2-33. Nearly 80% of the TCE is degraded within 10 minutes of initiating the reaction; whereas, only 40% of the TCE is degraded for the calcined catalyst after the same time span. The uncalcined catalyst is more effective at degrading TCE than the calcined catalyst. It also has a catalytic activity approaching that of the unsupported nanoparticles.

The  $k_{app}$  value for the unsupported 0.005 wt% CMC-stabilized Pd nanoparticle catalyst was determined to be  $0.482 \text{ min}^{-1}$ . On the other hand, the  $k_{app}$  value for the uncalcined alumina supported catalyst prepared using 0.005 wt% CMC-capped Pd nanoparticles was determined to be  $0.188 \text{ min}^{-1}$ . There is a decrease in the apparent reaction rate constant for the uncalcined alumina-supported catalyst as compared to the unsupported CMC-stabilized Pd nanoparticles. There is naturally less surface area available upon which the catalysis can occur when particles are adhered to a surface rather than homogeneously dispersed within the aqueous phase; therefore, a lower activity was achieved for the supported Pd catalyst. Additionally, the TCE must diffuse through the aqueous phase and the pores of the supporting material before it can adsorb onto the active sites for dechlorination by  $\text{H}_2$ , which is not necessary in the case of the homogeneously dispersed Pd nanoparticles in the aqueous media. The time required for diffusion of TCE to the active Pd catalyst material in the heterogeneous system is much longer, which also contributes to the lower catalytic activity obtained. The  $k_{app}$  value for the calcined alumina-supported catalyst prepared using 0.005 wt% CMC-capped Pd nanoparticles was determined to be  $0.092 \text{ min}^{-1}$ .

Values for  $k_{\text{obs}}$  are listed above in Table 2-2 and illustrate a dramatic decrease from 455 L/g min to 57 L/g min when the 0.005 wt% CMC-stabilized Pd nanoparticles were supported on aluminum oxide.

In order to compare the catalytic activity on the same Pd surface area basis, the specific surface area per gram of Pd nanoparticles in the reaction system was used to obtain the surface area based reaction rate constant,  $k_{\text{SA}}$ . The  $k_{\text{SA}}$  values decreased from 2.83 L min<sup>-1</sup> m<sup>-2</sup> to 0.490 L min<sup>-1</sup> m<sup>-2</sup> when the 0.005 wt% CMC-stabilized Pd nanoparticles were supported on aluminum oxide. The  $k_{\text{SA}}$  values further decreased from 0.490 L min<sup>-1</sup> m<sup>-2</sup> to 0.240 L min<sup>-1</sup> m<sup>-2</sup> when the alumina-supported 0.005 wt% CMC-stabilized Pd nanoparticles were calcined. To calculate  $k_{\text{SA}}$ ,  $k_{\text{obs}}$  was normalized using the specific surface area per gram of Pd nanoparticles in the reaction system. However, there is naturally less surface area available upon which the catalysis can occur when particles are adhered to a surface rather than homogeneously dispersed within the aqueous phase; therefore, a lower activity was achieved for the supported Pd catalyst.

It should be noted that the  $\text{TOF}_{\text{init}}$  value for the alumina-supported 0.005 wt% CMC-stabilized Pd nanoparticle catalyst was significantly lower ( $\text{TOF}_{\text{init}} = 7.6 \text{ min}^{-1}$ ) than the value obtained for the unsupported CMC-stabilized Pd nanoparticles ( $\text{TOF}_{\text{init}} = 41.4 \text{ min}^{-1}$ ). The  $\text{TOF}_{\text{init}}$  value for the calcined alumina-supported 0.005 wt% CMC-stabilized Pd nanoparticle catalyst was significantly lower ( $\text{TOF}_{\text{init}} = 3.7 \text{ min}^{-1}$ ) than the value obtained for the uncalcined supported CMC-stabilized Pd nanoparticles ( $\text{TOF}_{\text{init}} = 7.6 \text{ min}^{-1}$ ). Even so, the supported Pd nanoparticles provide an opportunity to effectively retain and recover the active Pd catalyst material, which is essential for any practical environmental application. ICP analysis was performed, after separation and removal of

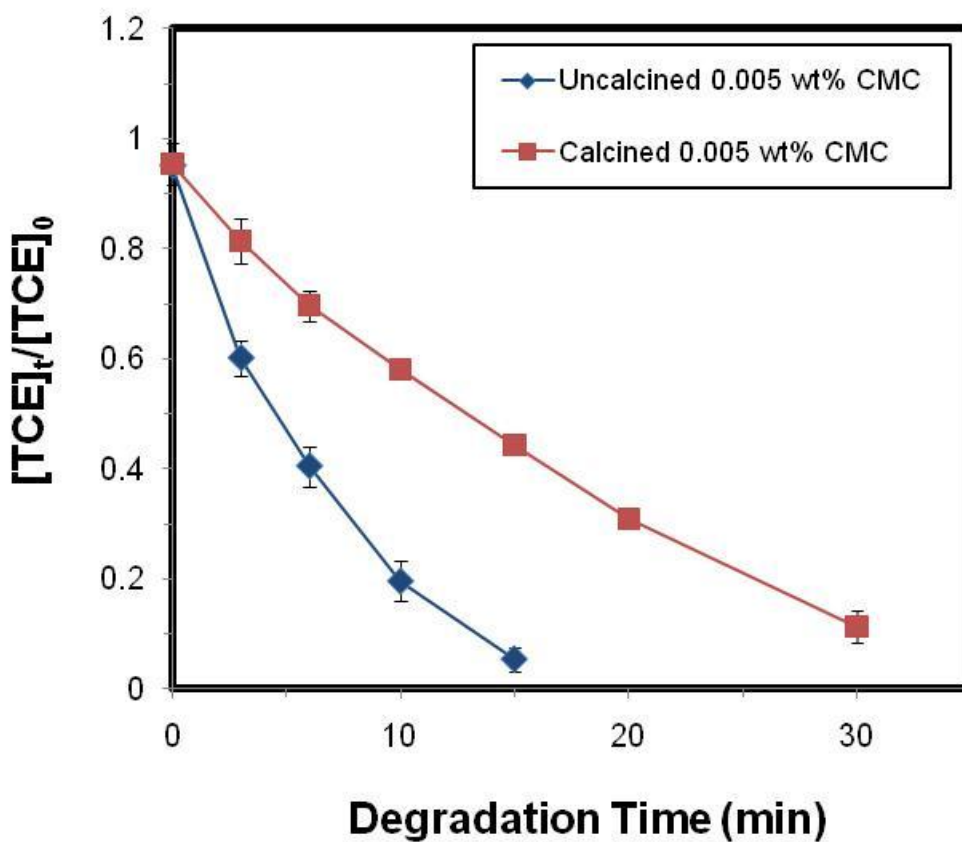


**Figure 2-33.** Effect of calcination conditions on the catalyst activity for the hydrodechlorination of TCE catalyzed by alumina-supported Pd nanoparticles synthesized using a 0.005 wt% CMC solution. Initial total TCE concentration was 50 mg/L. Concentration of Pd nanoparticles in the system was 3.3 mg/L. Kinetic experiments were performed by Man Zhang. Catalyst design and preparation, catalyst characterization, data analysis, and data interpretation as pertaining to this document were performed by the author. (A collaborative paper is in preparation).



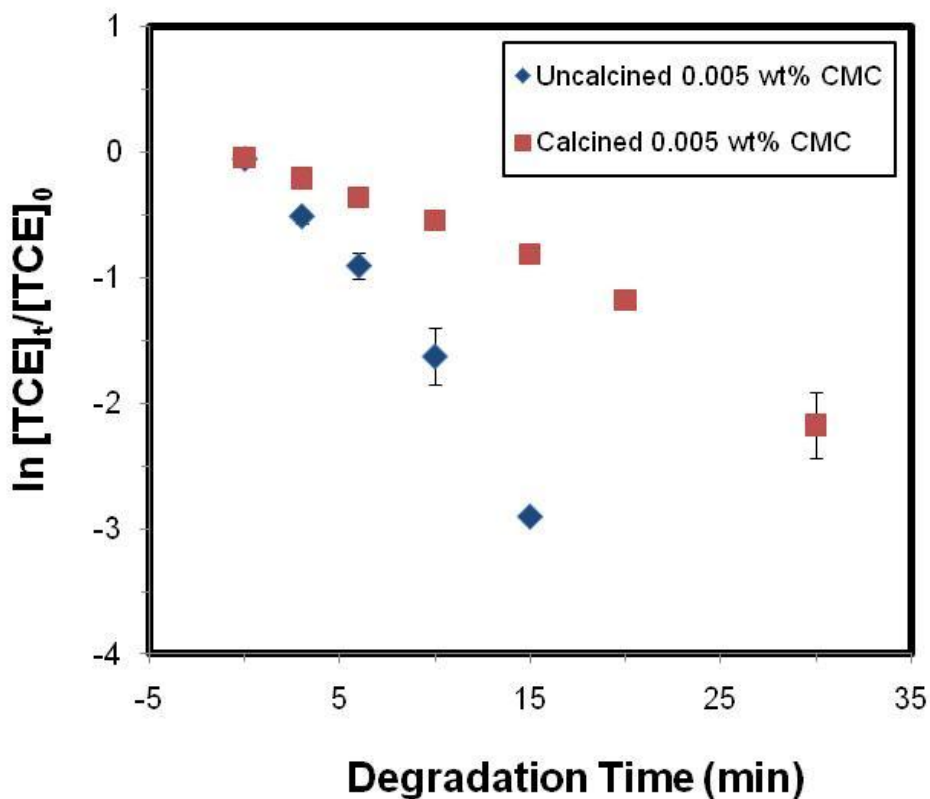


**Figure 2-34.** Plot of  $\ln ([TCE]_t/[TCE]_0)$  against time of the aqueous phase hydrodechlorination of TCE catalyzed by alumina-supported Pd nanoparticles synthesized using a 0.005 wt% CMC solution. Initial total TCE concentration was 50 mg/L. Concentration of Pd nanoparticles in the system was 3.3 mg/L. Kinetic experiments were performed by Man Zhang. Catalyst design and preparation, catalyst characterization, data analysis, and data interpretation as pertaining to this document were performed by the author. (A collaborative paper is in preparation).

the aqueous phase from the alumina-supported Pd catalyst, in order to determine the degree of Pd loss from the support material. Pd was detected in the effluent. While the uncalcined catalyst had better activity, leaching of Pd into the aqueous phase is not acceptable for this application and would indicate that the calcined materials are a better alternative despite the slightly lower activity.

## **2.8 Catalyst Stability**

Experiments were conducted collaboratively with Man Zhang to assess the stability of these supported Pd nanoparticle catalysts that were synthesized using various concentrations of CMC. For each experiment, 0.1 grams of catalyst (0.031 mM Pd) was added to a 127 mL serum bottle along with 100 mL of deionized water and a stir bar for proper agitation. The system was purged with H<sub>2</sub> gas for twenty minutes to displace any dissolved oxygen and to saturate both the aqueous phase and headspace with H<sub>2</sub>. The system was then sealed with a Teflon Mininert valve and spiked with 25 µL (179 g/L in methanol) of a TCE stock solution to yield an initial TCE concentration of 50 mg/L. The TCE solution was added under constant stirring and the system was sampled at regular time intervals. The degradation of TCE was monitored for thirty minutes by removing 100 µL of the aqueous phase at constant intervals using a gastight syringe. The sample was transferred to a 2 mL GC vial and extracted into 1 mL of hexane for subsequent analysis using a HP 6890 GC fitted with a micro-electron capture detector (ECD). Once the TCE in the system was completely degraded, the 127 mL serum bottle was centrifuged for five minutes using a Fisher Marathon 21K/R Centrifuge at 1500 RPM in order to separate the suspended catalyst from the aqueous phase.

After centrifugation, the aqueous phase was removed from the alumina-supported Pd catalyst and analyzed by ICP to determine the degree of Pd leaching that occurred during the dechlorination reaction. The catalyst was recycled and the aqueous phase was replaced with 100 mL of deionized water. The system was again purged with H<sub>2</sub> gas for twenty minutes, and then sealed with a Teflon Mininert valve. In order to initiate the reaction, the system was spiked with 25 μL (179 g/L in methanol) of a TCE stock solution to yield an initial TCE concentration of 50 mg/L. The system was sampled at regular time intervals, and the degradation of TCE was monitored for thirty minutes. The centrifugation of the reactor along with removal of the aqueous phase was repeated. This experimental procedure was followed for a total of six degradation reactions, recycling the same catalyst in each run. All experiments were at least duplicated.

The catalytic activity of the alumina-supported Pd nanoparticles prepared using a 0.15 wt% CMC solution is shown in Figure 2-35. The activity of this catalyst was fairly constant throughout the six degradation reactions, which suggests that this catalyst was stable and that Pd was not leached from the support material into the aqueous phase. ICP analysis was performed, after separation and removal of the aqueous phase from the alumina-supported Pd catalyst, in order to determine the degree of Pd loss from the support material. No Pd was detected in the aqueous phase by ICP analysis, which is required if these catalysts are to be used for an environmental application.

Performing this same analysis on the uncalcined catalysts resulted in the detection of Pd in the effluent. While the uncalcined catalysts had better activity, leaching of Pd into the aqueous phase is not acceptable for this application and would indicate that the calcined materials are a better alternative despite the slightly lower activity. In addition,

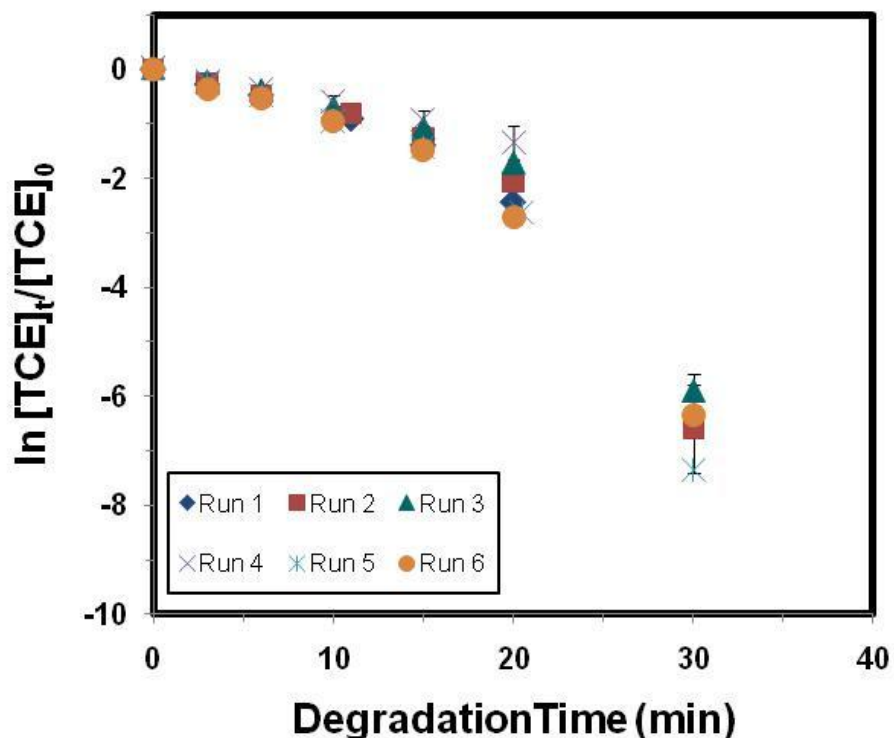


**Figure 2-35.** Plot of  $\ln ([TCE]_t/[TCE]_0)$  against time of the aqueous phase hydrodechlorination of TCE catalyzed by alumina-supported Pd nanoparticles synthesized using a 0.15 wt% CMC solution. This study included a total of six degradation reactions, recycling the same catalyst in each run. Initial total TCE concentration was 50 mg/L. Concentration of Pd nanoparticles in the system was 3.3 mg/L. Kinetic experiments were performed by Man Zhang. Catalyst design and preparation, catalyst characterization, data analysis, and data interpretation as pertaining to this document were performed by the author. (A collaborative paper is in preparation).

Pd is a very expensive precious metal. Therefore, it is necessary to retain and recover the active Pd catalyst material in order to make this a viable remediation technology. This series of experiments not only illustrated the robust nature of these alumina-supported Pd nanoparticle catalysts used for the aqueous phase hydrodechlorination of TCE, but also demonstrated the significance of calcination during catalyst preparation.

## **2.9 Effect of Catalyst Reduction Gas Composition**

A series of investigations were performed in order to determine the effect of the reduction gas composition on catalytic performance of the supported Pd nanoparticle catalysts. One set of catalyst reductions were conducted in a pure H<sub>2</sub> environment at 400°C and atmospheric pressure. The lower explosive limit for hydrogen in air is 4% by volume, so due to the extremely flammable nature of H<sub>2</sub>, performing reductions in pure H<sub>2</sub> have considerable associated safety hazards. In consideration of these safety concerns, reductions were also carried out in a non-flammable reducing media of 5% H<sub>2</sub>/balance N<sub>2</sub> at 400°C and atmospheric pressure. Comparisons were made between catalysts reduced in each environment to determine if the reducing gas had any effect on the catalyst activity. Some studies have suggested that reducing in pure hydrogen can increase catalyst sintering, thereby, decreasing the available surface area and reducing catalyst activity. Results for these studies are shown in Figures 2-36 and 2-37. Each catalyst showed very similar catalytic activity and kinetics using both reducing environments. Decreased activity for the catalyst reduced in the H<sub>2</sub> environment was not observed, which suggests that the reducing gas does not have an adverse effect on sintering and crystallite growth under these conditions. Even so, due to safety concerns,

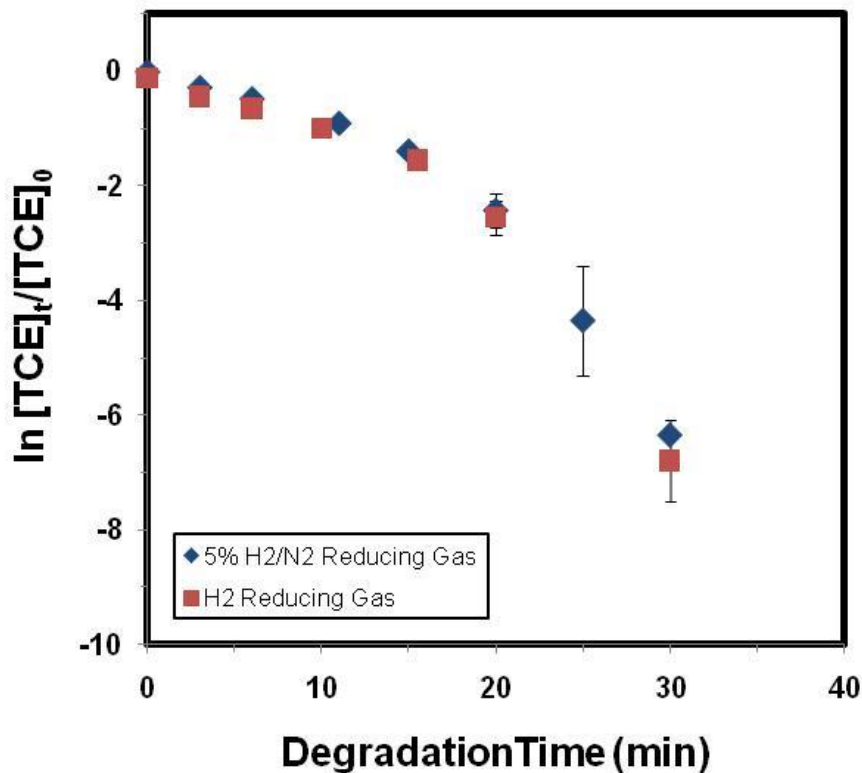


**Figure 2-36.** Plot of  $\ln ([TCE]_t/[TCE]_0)$  against time of the aqueous phase hydrodechlorination of TCE catalyzed by alumina-supported Pd nanoparticles synthesized using a 0.15 wt% CMC solution. Initial total TCE concentration was 50 mg/L. Concentration of Pd nanoparticles in the system was 3.3 mg/L. Kinetic experiments were performed by Man Zhang. Catalyst design and preparation, catalyst characterization, data analysis, and data interpretation as pertaining to this document were performed by the author. (A collaborative paper is in preparation).

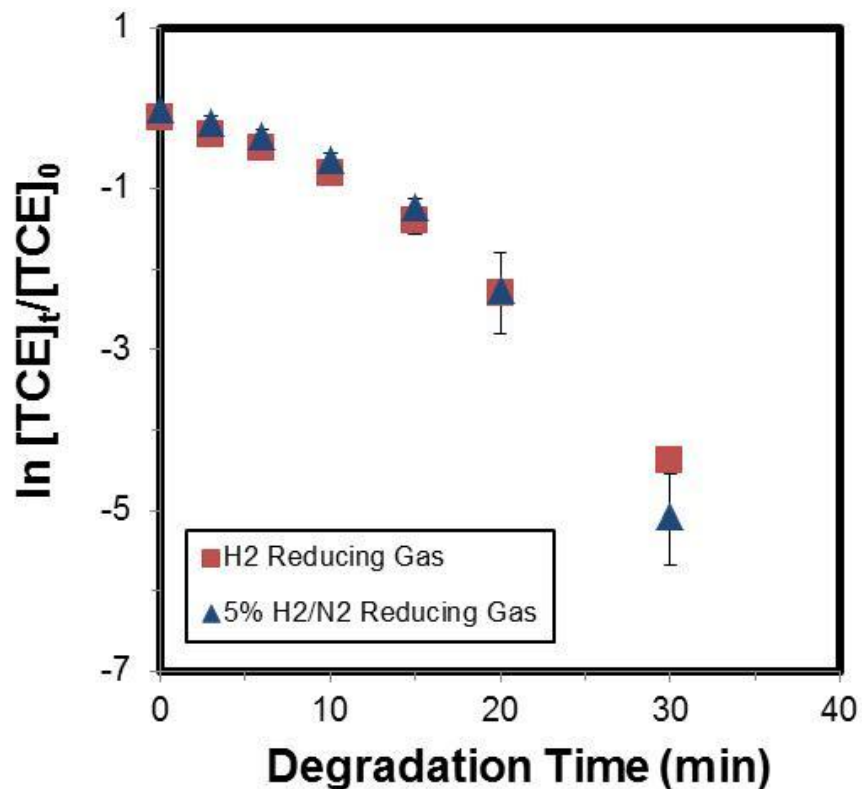


**Figure 2-37.** Plot of  $\ln \left( \frac{[\text{TCE}]_t}{[\text{TCE}]_0} \right)$  against time of the aqueous phase hydrodechlorination of TCE catalyzed by a conventional alumina-supported Pd catalyst. Initial total TCE concentration was 50 mg/L. Concentration of Pd nanoparticles in the system was 3.3 mg/L. Kinetic experiments were performed by Man Zhang. Catalyst design and preparation, catalyst characterization, data analysis, and data interpretation as pertaining to this document were performed by the author. (A collaborative paper is in preparation).

reductions were performed primarily with the 5% H<sub>2</sub>/N<sub>2</sub> gas mixture.

## 2.10 Effect of Support Material

Figure 2-26 illustrated that the Pd nanoparticle catalysts on Al<sub>2</sub>O<sub>3</sub> required an induction period to reach the fully saturated concentration state of TCE within the catalyst pores. It is presumed that this induction period is necessary due, in part, to the hydrophilic nature of the alumina support material. However, given that TCE is a hydrophobic chemical it would stand to reason that the use of a more hydrophobic support material could help to facilitate the diffusion of the TCE into the catalyst pores. As such, the previously observed induction period in Figure 2-26 could be reduced or eliminated, thereby, yielding first-order kinetics. Based on this, titanium silicalite (TS-1) was chosen as an example hydrophobic support material. It is noted that TS-1 is an expensive material and would not lend itself to practical environmental application. Rather, the TS-1 is used in this case to further examine this fundamental effect of support material hydrophobicity on TCE degradation.

Experiments were conducted using Pd dispersed on hydrophobic TS-1 support material prepared using the conventional incipient wetness impregnation technique to demonstrate the effect of the different support materials on the TCE degradation. Figure 2-38 presents a plot of [TCE]<sub>t</sub>/[TCE]<sub>0</sub> with respect to time using ca. 0.34 wt% Pd on both alumina and TS-1 supports, with surface areas of 100 m<sup>2</sup>/g and 342 m<sup>2</sup>/g, respectively. It is noted that approximately 97% of the TCE is degraded within the first ten minutes of initiating the reaction using the hydrophobic TS-1 supporting material. On the other hand, only 50% of the TCE is degraded during the same time span using the hydrophilic



Al<sub>2</sub>O<sub>3</sub> support material. Moreover, Figure 2-39 illustrates that linear pseudo-first order kinetic behavior ( $R^2$  value of 0.993) was achieved using the hydrophobic support with the absence of the previously noted induction period obtained with the alumina support. The pseudo-first order observed reaction rate constant was  $k_{\text{obs}} = 112 \text{ L g}^{-1} \text{ min}^{-1}$  for TS-1 supporting material; whereas,  $k_{\text{obs}} = 12 \text{ L g}^{-1} \text{ min}^{-1}$  for the Al<sub>2</sub>O<sub>3</sub> supporting material. This suggests that an inexpensive hydrophobic support material is needed to optimize the TCE degradation for heterogeneous environmental applications.

## 2.11 BET Surface Area Measurements

N<sub>2</sub> gas adsorption measurements were performed at West Virginia University by Mohita Yalamanchi in order to determine the specific surface area of the alumina-supported Pd nanoparticle catalysts prepared using various concentrations of CMC (see Table 2-4). The results of the BET measurements are summarized in Table 2-4. It is noted that the specific surface area of the Al<sub>2</sub>O<sub>3</sub> support material increased from 83 m<sup>2</sup>/g to 92 m<sup>2</sup>/g upon calcination at 500°C. This increase in surface area is most likely due to the removal of contaminants trapped within the pores of the Al<sub>2</sub>O<sub>3</sub> support material which are released with calcination. The alumina-supported Pd nanoparticle catalyst prepared using a higher concentration of CMC capping agent (0.15 wt% CMC) was determined to have a lower surface area (SA = 72 m<sup>2</sup>/g, before calcination/reduction) than the catalyst prepared using a much lower CMC concentration of 0.005 wt% (SA = 85 m<sup>2</sup>/g, before calcination/reduction). CMC is a very large and bulky molecule (MW = 90,000), so it is most probable that the CMC attached to the surface of the Pd nanoparticles block some of the alumina pores upon deposition at the higher CMC concentration (0.15 wt% CMC). In

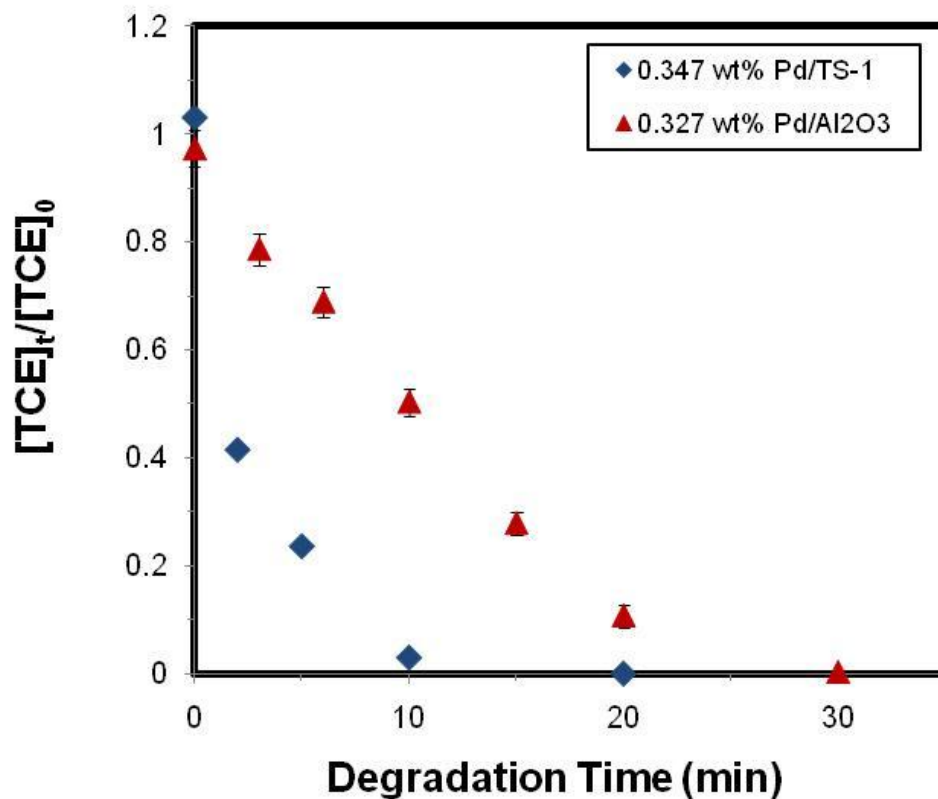


**Figure 2-38.** Aqueous phase hydrodechlorination of TCE catalyzed by Pd on both Al<sub>2</sub>O<sub>3</sub> and TS-1 support materials. Initial total TCE concentration was 50 mg/L. Concentration of Pd in the system was 3.4 mg/L. Kinetic experiments were performed by Man Zhang. Catalyst design and preparation, catalyst characterization, data analysis, and data interpretation as pertaining to this document were performed by the author. (A collaborative paper is in preparation).

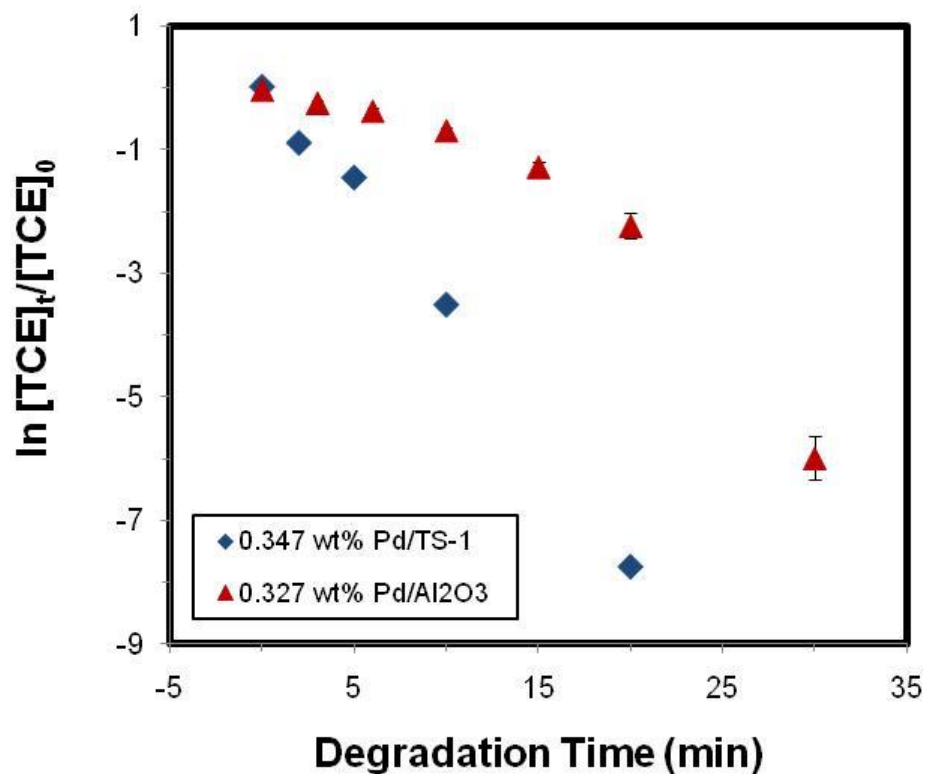


**Figure 2-39.** Plot of  $\ln ([TCE]_t/[TCE]_0)$  against time of the aqueous phase hydrodechlorination of TCE catalyzed by Pd on both  $Al_2O_3$  and TS-1 support materials. Initial total TCE concentration was 50 mg/L. Concentration of Pd in the system was 3.4 mg/L. Kinetic experiments were performed by Man Zhang. Catalyst design and preparation, catalyst characterization, data analysis, and data interpretation as pertaining to this document were performed by the author. (A collaborative paper is in preparation).

the case of the lower CMC concentration of 0.005 wt%, a surface area of 85 m<sup>2</sup>/g is obtained which is very close to the surface area value for blank alumina (SA = 83 m<sup>2</sup>/g). This is evidence that the CMC ligand is blocking the pores at higher CMC concentrations. In addition, some of the surface area was restored after calcination/reduction where the CMC ligand is burned off. For example, the surface area for the catalyst prepared using 0.15 wt% CMC increased from 72 m<sup>2</sup>/g to 78 m<sup>2</sup>/g. These studies demonstrate that the CMC capping ligand affects the ability of the Pd nanoparticles to deposit onto the support with a concomitant influence on the surface of the support material.

## 2.12 FT-IR Spectroscopic Analysis of Catalysts

Catalyst characterization with FT-IR spectroscopy was used to determine the appropriate calcination temperature for all catalysts. Calcinations were done at 80°C, 120°C, 320°C, and 500°C. The specific interactions between the CMC capping agent and the Pd nanoparticles were previously determined by Liu et al (2008). It was shown that CMC interacts with the surface of the Pd nanoparticles through the hydroxyl (OH) and carboxylate (COO<sup>-</sup>) functional groups. The FT-IR spectrum for Pd nanoparticles prepared using 0.15 wt% CMC and then calcined at 80°C is shown in Figure 2-40. The asymmetric  $\nu_{as}(\text{COO}^-)$  and symmetric  $\nu_s(\text{COO}^-)$  stretching vibration bands for the carboxylate groups were observed at 1599 cm<sup>-1</sup> and 1416 cm<sup>-1</sup>, respectively. In addition, the stretching vibration band for the hydroxyl functional group was observed at 3332 cm<sup>-1</sup>. The FT-IR spectrum for Pd nanoparticles prepared using 0.15 wt% CMC and subsequently calcined at 120°C is shown in Figure 2-41. The detection of the stretching

vibrations associated with CMC capping ligand indicates the presence of CMC and its interaction with the Pd nanoparticle surface. However, the  $\text{-OH}$  stretch at  $3332\text{ cm}^{-1}$  disappeared after catalyst calcination at  $320^\circ\text{C}$  as shown in Figure 2-42. Also, it is noted that a shift in the stretching vibration bands for the  $\text{-COO}^-$  groups was observed from  $1599\text{ cm}^{-1}$  and  $1416\text{ cm}^{-1}$  to  $1584\text{ cm}^{-1}$  and  $1404\text{ cm}^{-1}$ , respectively. This shift suggests that the interactions between the  $\text{-COO}^-$  functional groups and Pd nanoparticle surface have been disrupted. The FT-IR spectrum for Pd nanoparticles prepared using 0.15 wt% CMC and calcined at  $500^\circ\text{C}$  is shown in Figure 2-43. The characteristic stretching vibration bands were not detected for the catalyst calcined at  $500^\circ\text{C}$  indicating that all of the CMC ligand has been burned off. These studies suggest calcination temperatures above  $320^\circ\text{C}$  to ensure complete removal of CMC.

### **2.13 High Resolution TEM Characterization**

As described above, a Zeiss EM 10 was used for standard TEM characterization of the CMC-stabilized Pd nanoparticles in order to obtain their average particle size and particle size distribution. In addition, high-resolution TEM (HRTEM) analysis was performed by Dr. Naresh Shah at the University of Kentucky on both unsupported and alumina-supported Pd nanoparticles prepared using various CMC concentrations in order to determine the crystallinity and morphology as well as to approximate the average particle size of the alumina-supported Pd nanoparticles. Bright field images were obtained for the unsupported CMC-stabilized Pd nanoparticles prepared with both 0.15 wt% CMC and 0.005 wt% CMC aqueous solutions. An image of the unsupported CMC-Pd nanoparticles produced using 0.15 wt% CMC is shown in Figure 2-44. These

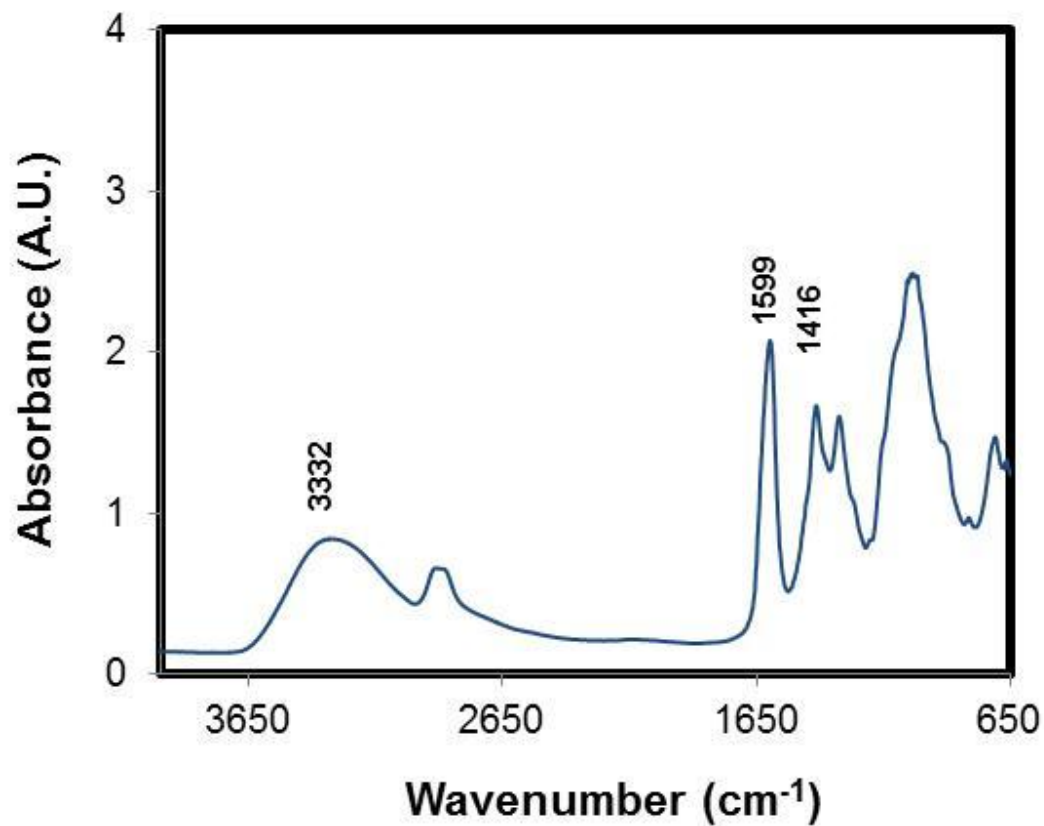


**Figure 2-40.** FT-IR spectrum for CMC-Pd nanoparticles prepared using a 0.15 wt% CMC aqueous solution and calcined at 80°C.

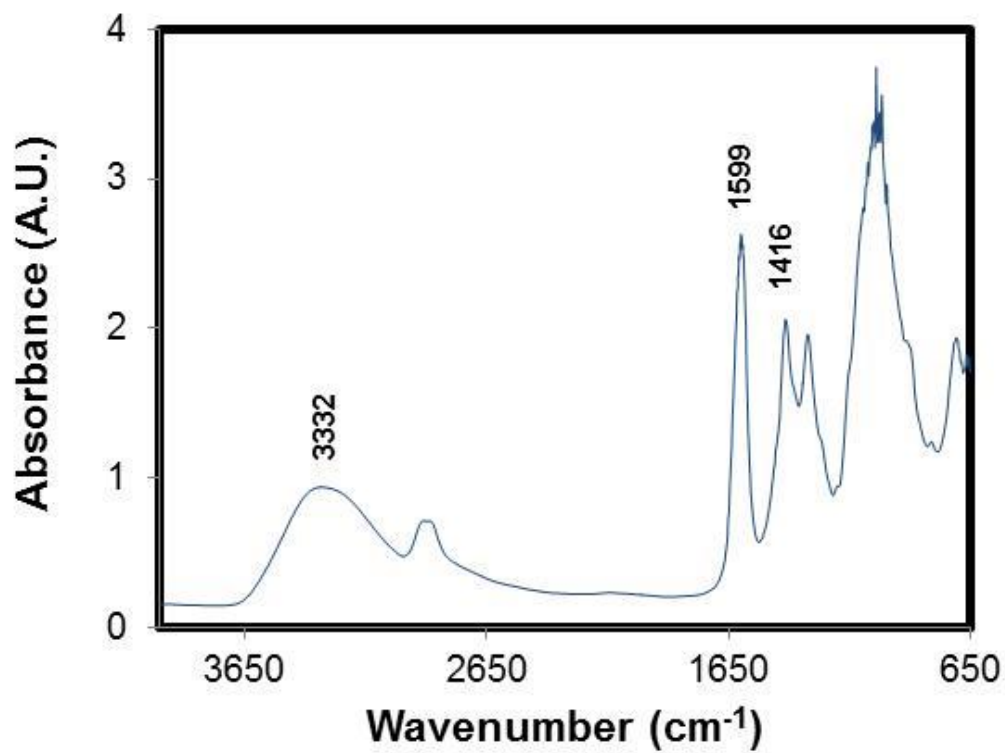


**Figure 2-41.** FT-IR spectrum for CMC-Pd nanoparticles prepared using a 0.15 wt% CMC aqueous solution and calcined at 120°C.

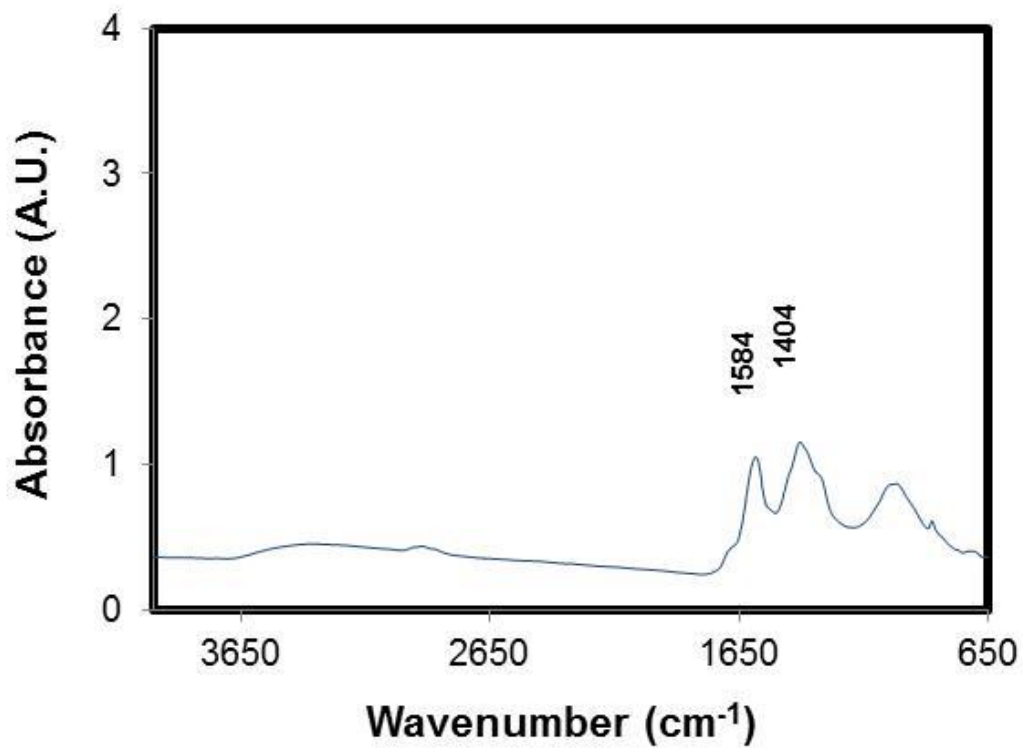


**Figure 2-42.** FT-IR spectrum for CMC-Pd nanoparticles prepared using a 0.15 wt% CMC aqueous solution and calcined at 320°C.



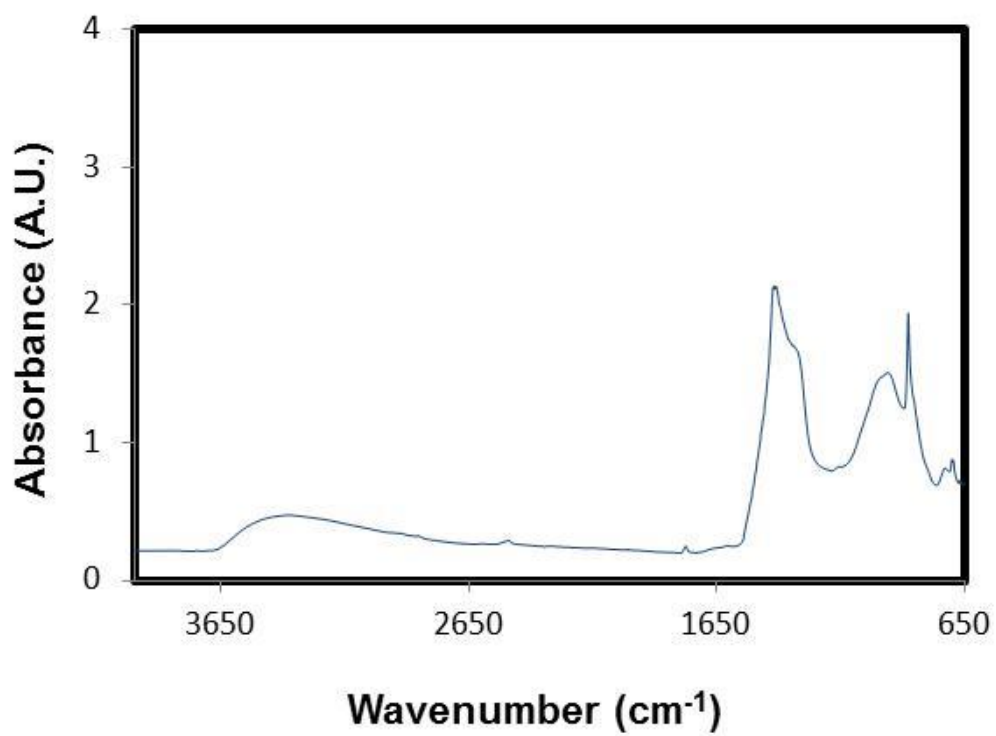


**Figure 2-43.** FT-IR spectrum for CMC-Pd nanoparticles prepared using a 0.15 wt% CMC aqueous solution and calcined at 500°C.

nanoparticles were observed to be spherical in shape and approximately 2.5 nm to 3 nm in size, which is consistent with results obtained using the lower resolution TEM at Auburn University. Atomic lattice fringes were evident in this high-resolution image, demonstrating a crystalline structure for the Pd nanoparticles. A mask in Fourier space was applied to the image in Figure 2-44 in order to reduce the noise from the carbon substrate and measure the interplanar spacing which is shown in Figure 2-45. The atomic planes in the crystal lattice for CMC-stabilized Pd nanoparticles prepared using 0.15 wt% CMC were visualized and imaged in Figure 2-46.

An image of unsupported CMC-Pd nanoparticles produced using 0.005 wt% CMC is shown in Figure 2-47. These nanoparticles were observed to be spherical in shape and approximately 5 nm to 10 nm in size, which is analogous to particle sizes obtained at Auburn University using the lower resolution TEM. It is noted that reducing the capping ligand concentration resulted in particles with a larger average diameter, which is also consistent with the lower resolution results described above.

Figures 2-48 and 2-49 show bright field TEM images for as prepared 0.34 wt% Pd on Al<sub>2</sub>O<sub>3</sub> catalyst before the aqueous phase hydrodechlorination of TCE. The alumina support was crystalline in nature, and the crystallites were anywhere from 5 nm to 10 nm in size. The average crystallite size for Al<sub>2</sub>O<sub>3</sub> was consistent with results obtained from XRD characterization (average diameter = 8 nm). There appeared to be strong bonding between the randomly ordered crystallites as shown in Figure 2-49. Random stacking of single crystals, without any internal porosity, can generate a larger porous scaffold without significant loss in the specific surface area. Figure 2-50 is a HRTEM image of

0.34 wt% Pd on Al<sub>2</sub>O<sub>3</sub> catalyst after the dechlorination of TCE, which indicated no morphological changes in the catalyst after exposure to reaction conditions.

The imaging of the Pd nanoparticles on Al<sub>2</sub>O<sub>3</sub> support material was rather challenging since the absolute concentration of Pd nanoparticles on the support was very low (0.34 wt% Pd), and both the Pd nanoparticles and Al<sub>2</sub>O<sub>3</sub> particles are crystalline in nature. Therefore, an EDS spectrum (see Figure 2-51) of the area of interest was acquired in order to confirm the presence of Pd in the catalyst sample. The primary elemental compositions obtained with EDS were aluminum (Al) and oxygen (O), which was to be expected since the sample was 99.7 wt% Al<sub>2</sub>O<sub>3</sub>. It is noted that the Pd L-shell emission peak around 3keV and the K-shell emission peak around 21 keV were observed; thereby, confirming the existence of Pd on the Al<sub>2</sub>O<sub>3</sub> supporting material. The high-resolution image corresponding to this EDS spectrum is shown in Figure 2-48. The dark spots in the bright-field image are locations on the grid where the sample was thicker; therefore, not transparent to the electron beam. Unfortunately, images of alumina-supported Pd were not obtained due to the very low Pd concentration on the support material.

## **2.14 Conclusions**

Pd nanoparticles were synthesized and stabilized within the aqueous phase using water-soluble polymeric capping ligands, which offers a green alternative to the conventional nanoparticle synthesis techniques. The capping ligand, capping ligand concentration, and synthesis temperature were all examined in order to understand their effect on the particle size and size distribution. Once it was understood how to finely control the synthesis of Pd nanoparticles in the aqueous phase, the catalytic behavior of

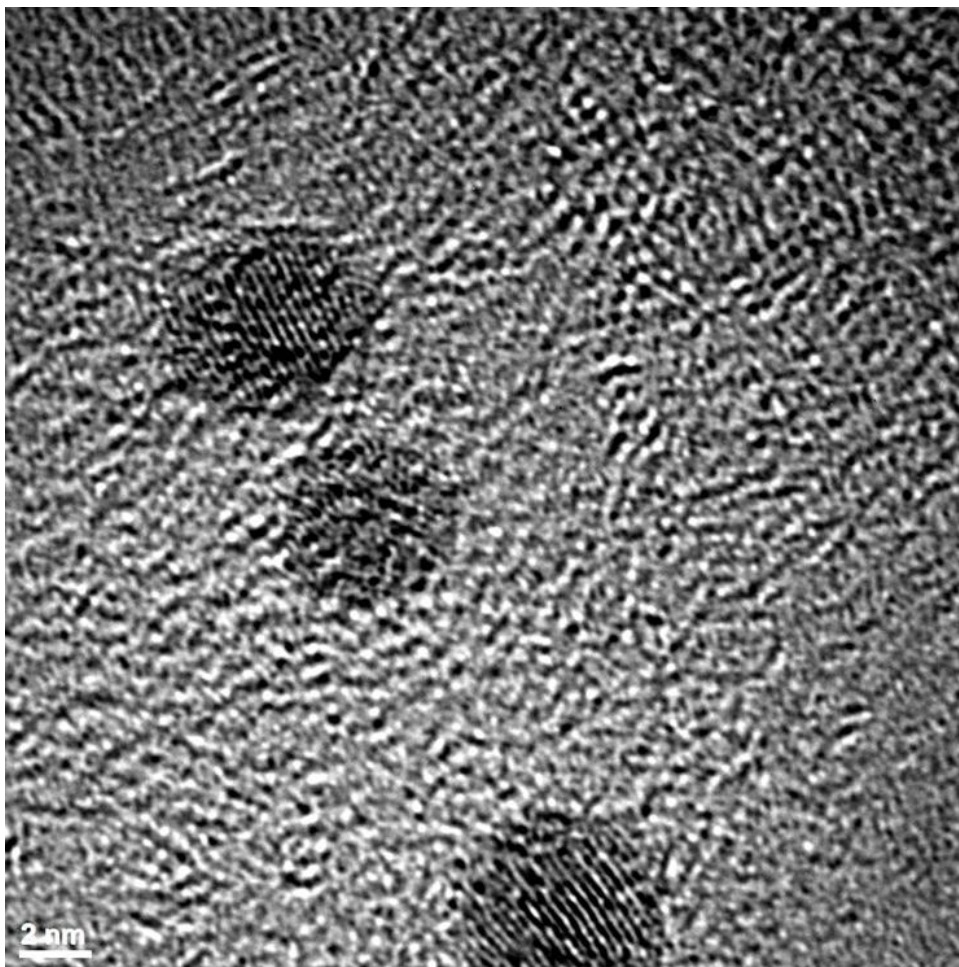


**Figure 2-44.** HRTEM image of CMC-stabilized Pd nanoparticles prepared in the aqueous phase using a 0.15 wt% CMC solution at a magnification of 800,000.

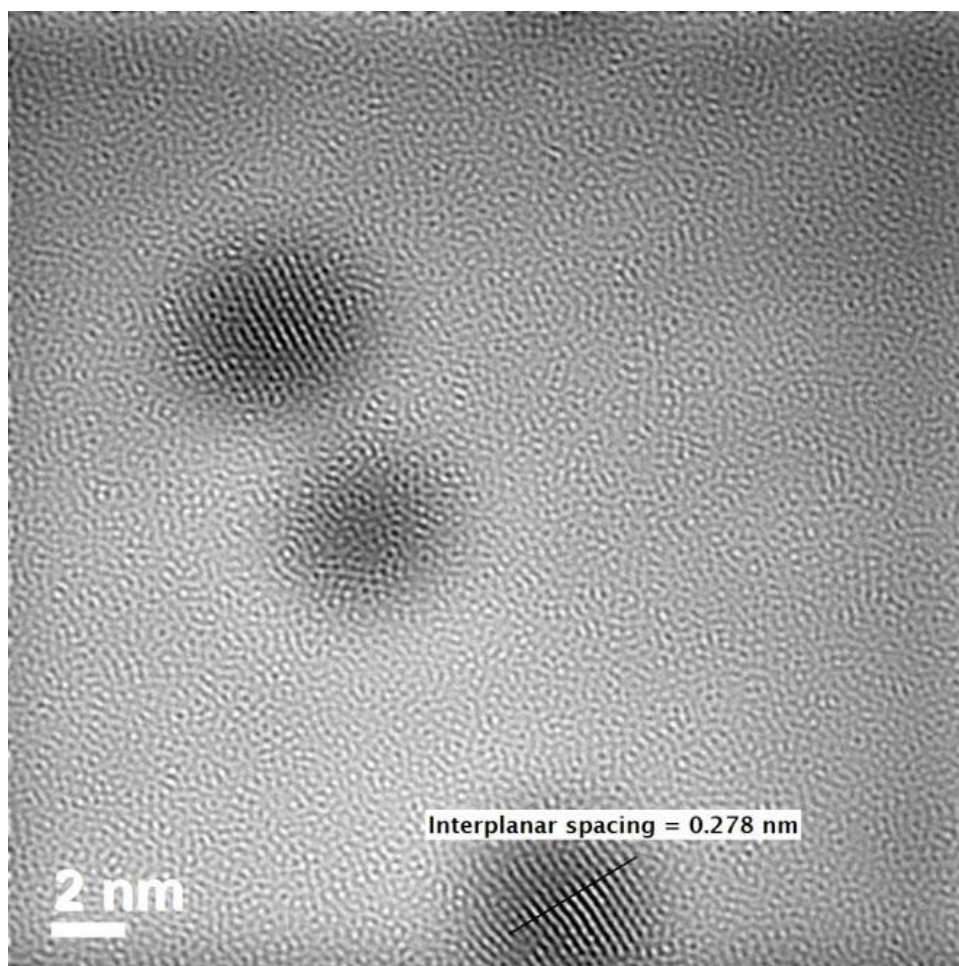


**Figure 2-45.** HRTEM image of CMC-stabilized Pd nanoparticles prepared in the aqueous phase using a 0.15 wt% CMC solution at a magnification of 800,000 after applying a mask in Fourier space to reduce the noise from the carbon substrate.

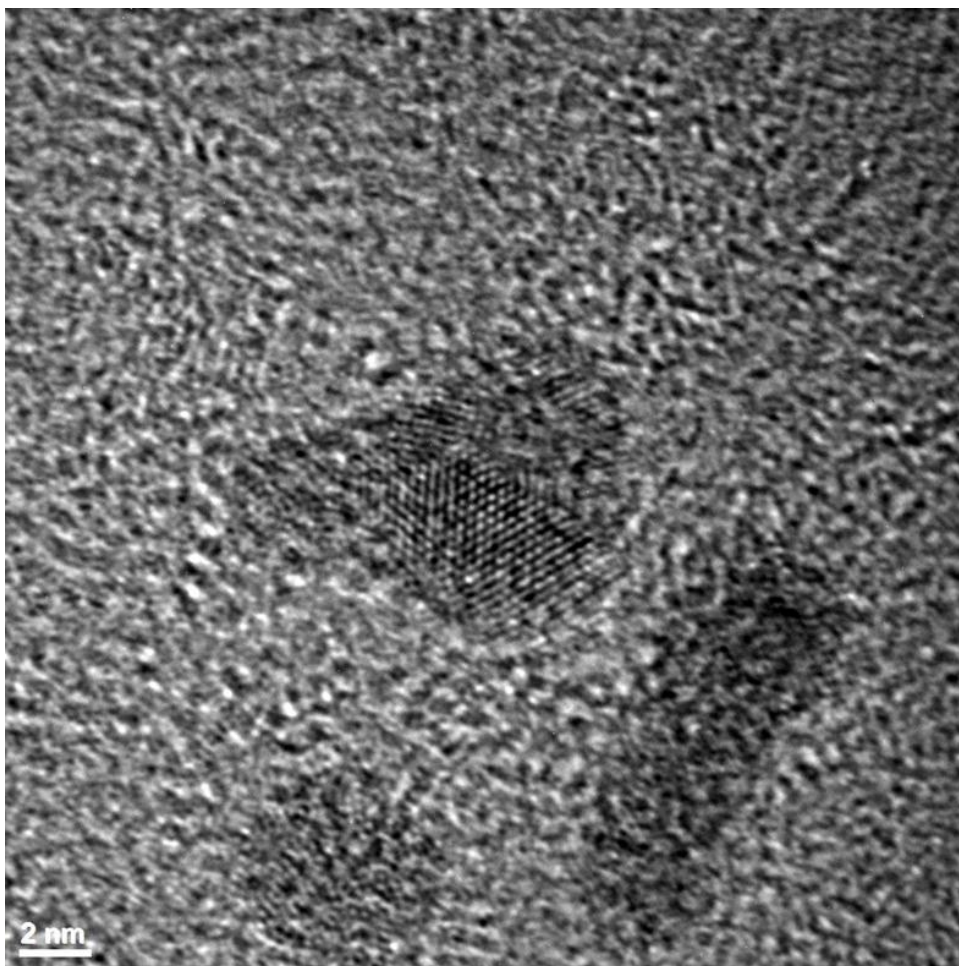


**Figure 2-46.** HRTEM image of 0.15 wt% CMC-stabilized Pd nanoparticles dispersed in the aqueous phase at a magnification of 800,000.



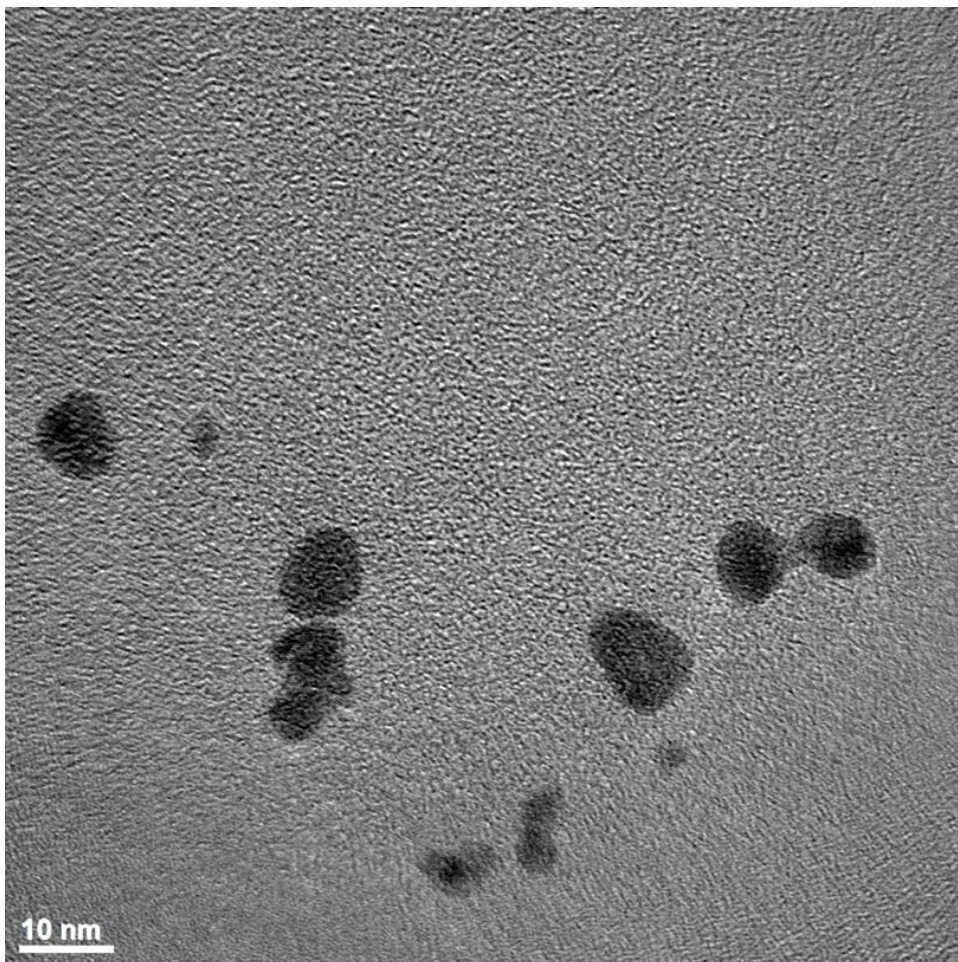


**Figure 2-47.** HRTEM image of CMC-stabilized Pd nanoparticles synthesized in the aqueous phase using a 0.005 wt% CMC solution at a magnification of 200,000.

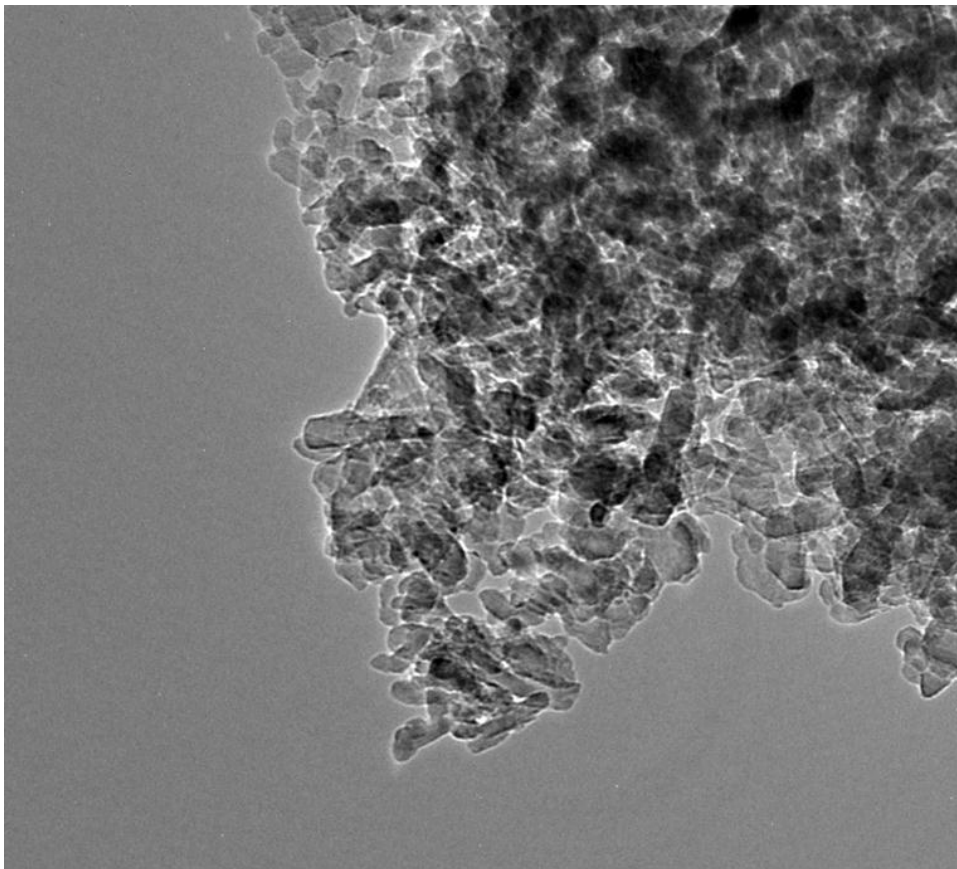


**Figure 2-48.** HRTEM image of Pd nanoparticles (0.33 wt% Pd) supported on Al<sub>2</sub>O<sub>3</sub> at a magnification of 60,000.



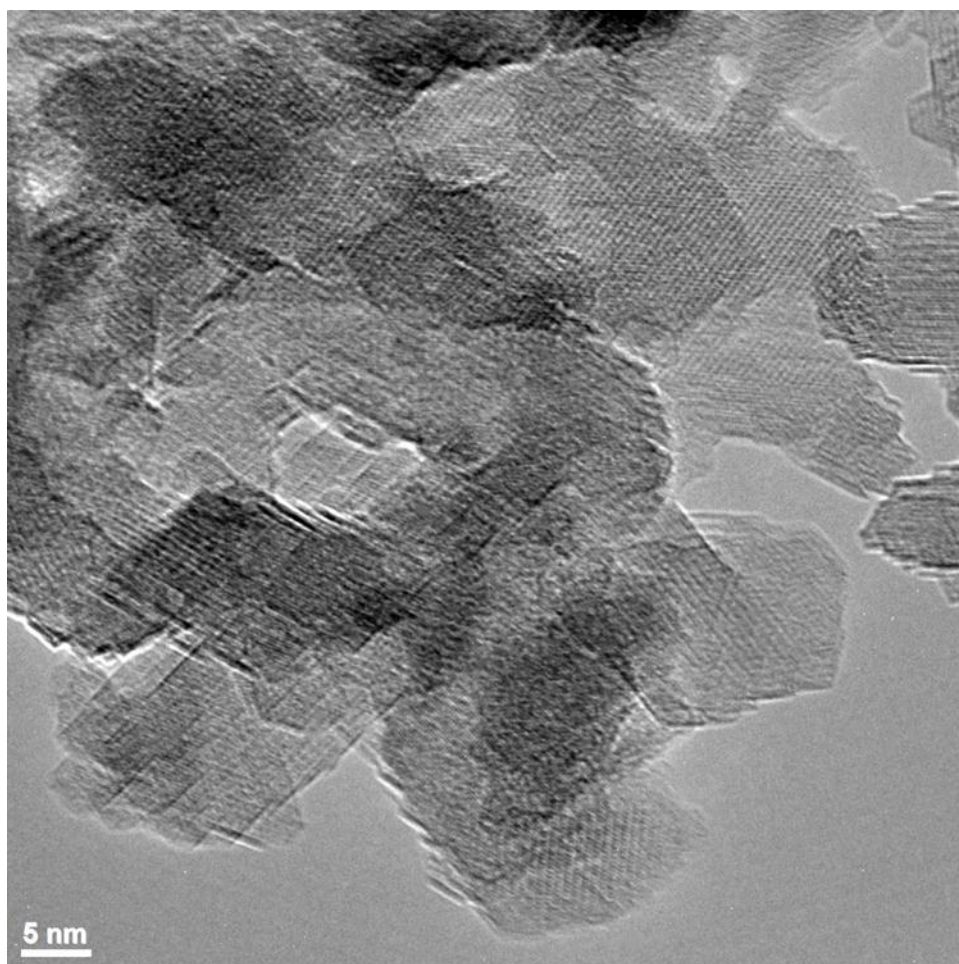


**Figure 2-49.** HRTEM image of Pd nanoparticles (0.33 wt% Pd) supported on Al<sub>2</sub>O<sub>3</sub> before the aqueous phase dechlorination of TCE at a magnification of 300,000.

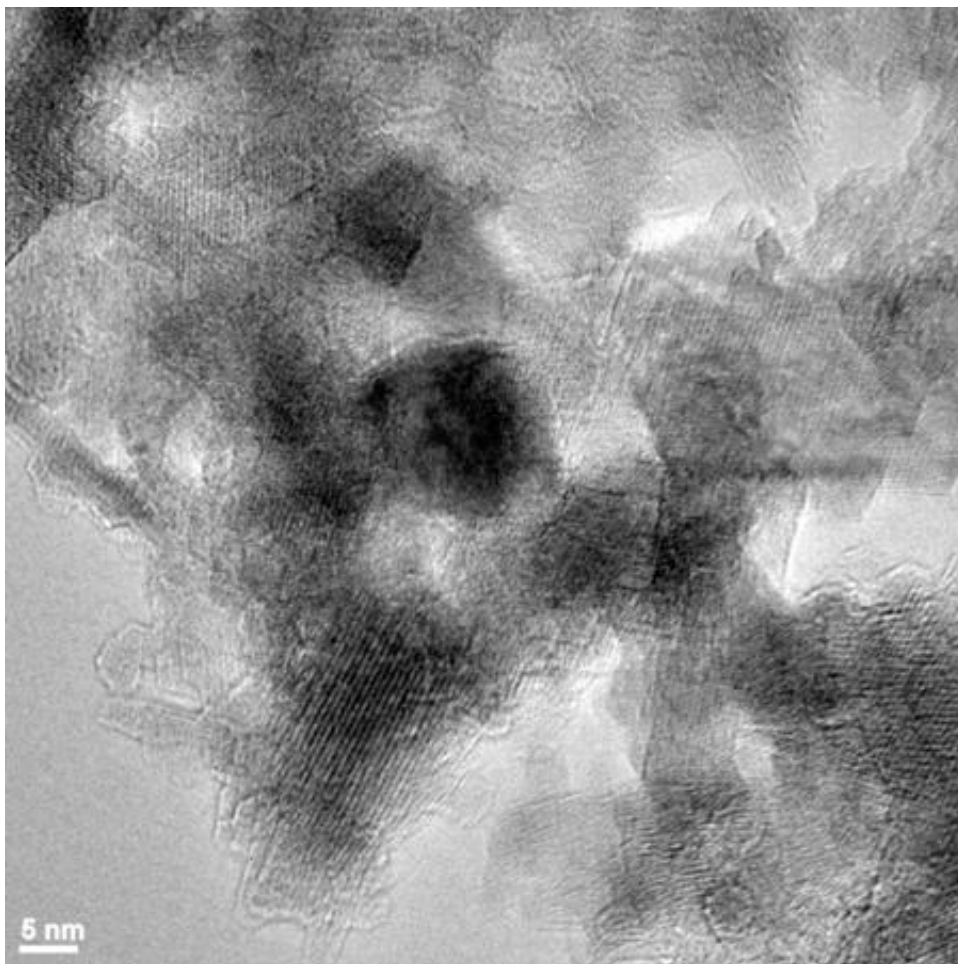


**Figure 2-50.** HRTEM image of 0.34 wt% Pd supported on  $\text{Al}_2\text{O}_3$  after the aqueous phase dechlorination of TCE at a magnification of 250,000.

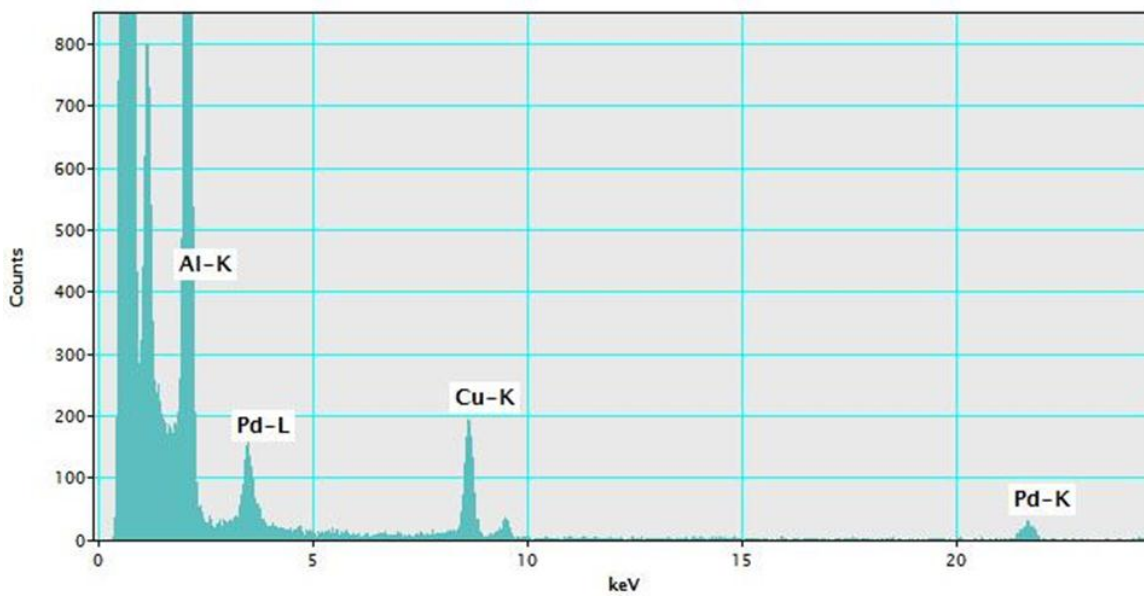


**Figure 2-51.** EDS spectrum for the overall area shown in Figure 2-48 for the 0.34 wt% Pd on Al<sub>2</sub>O<sub>3</sub> catalyst. The presence of both K and L shell emission lines for Pd confirm its existence in this selected area. The Cu line is from the grid used in order to support the sample for analysis by TEM.

CMC-stabilized Pd nanoparticles was examined for the hydrodechlorination of TCE in a homogeneous catalyst system. The unsupported Pd nanoparticles showed considerable activity towards the degradation of TCE, as demonstrated by the reaction kinetics. Even so, it is essential to efficiently retain and recover the active Pd catalyst material if these catalysts are to be used for an environmental application. Therefore, these nanoparticles were dispersed onto a supporting material for utilization in a heterogeneous catalyst system. CMC stabilized Pd nanoparticle catalysts were successfully deposited onto Al<sub>2</sub>O<sub>3</sub> support material using the incipient wetness impregnation technique. Although the supported Pd nanoparticle catalysts had a lower catalytic activity than the unsupported particles that were homogeneously dispersed in the aqueous solutions, the supported catalysts retained sufficient activity toward the degradation of TCE. In addition, the use of hydrophilic Al<sub>2</sub>O<sub>3</sub> support material illustrated a mass transfer resistance to TCE that affected the initial hydrodechlorination rate. However, the use of a more hydrophobic support, TS-1, overcame the mass transfer resistance to TCE. In conclusion, this work illustrates that supported Pd catalysts can be effective in the hydrodechlorination of TCE.

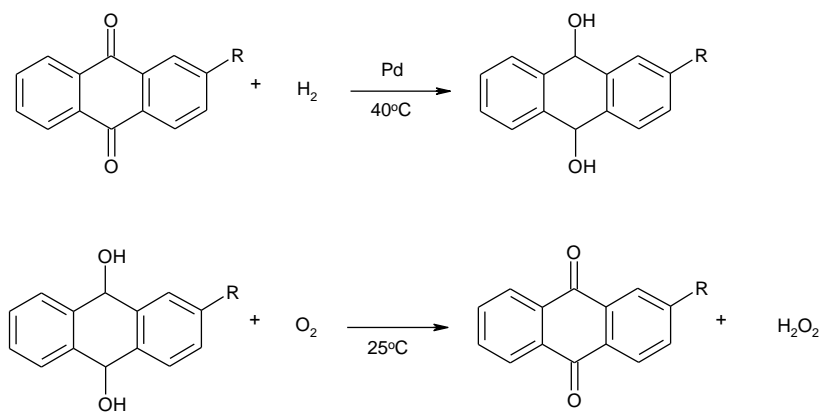
## Chapter 3

### APPLICATIONS OF IN-SITU GENERATED HYDROGEN PEROXIDE IN SUPERCRITICAL CARBON DIOXIDE SOLVENT MEDIA

#### 3.1 Introduction

Hydrogen peroxide ( $\text{H}_2\text{O}_2$ ) is generally considered a benign oxidant that is a promising alternative to conventional oxidants. The current method for producing  $\text{H}_2\text{O}_2$  involves a complicated anthraquinone autoxidation (AO) process consisting of two sequential steps, hydrogenation followed by oxidation (Hess, 1995). An alkyl anthraquinone is dissolved in a solvent mixture, consisting of both polar and aromatic compounds, then hydrogenated in the presence of a supported palladium catalyst to give its respective hydroquinone. The hydroquinone solution is then separated from the catalyst and air-oxidized to regenerate the alkyl anthraquinone while splitting off hydrogen peroxide as shown in Scheme 3-1.

Unfortunately, this route requires multiple unit operations, is highly energy-intensive, and results in the generation of several considerable waste streams. Despite the relatively high cost of production, the AO process is used to manufacture about 95% of the world's hydrogen peroxide (Fierro *et al.*, 2006). This process is commercially successful because it not only prevents the direct contact of hydrogen and oxygen, but



**Scheme 3-1.** Anthraquinone autoxidation route for manufacturing hydrogen peroxide.

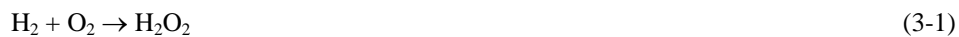
also produces  $\text{H}_2\text{O}_2$  continuously at mild conditions. Even so, there are several disadvantages associated with the AO method for  $\text{H}_2\text{O}_2$  production. First, the product is contaminated during extraction from the organic phase into water, and must be distilled for product purification. Huge quantities of energy are necessary for the separation and distillation of  $\text{H}_2\text{O}_2$ . Next, the organic solvent mixture can be oxidized during production, so the degraded materials must be removed and replaced to maintain the appropriate solubilities. Also, the expensive anthraquinones in the working solution undergo unwanted side reactions, so these side products must be removed for regeneration of the starting material or disposal. Make-up of the spent anthraquinones and solvents along with the wasted hydrogen all result in higher production costs. The anthraquinone route, although successful, certainly is not green and is far too costly to allow for use of  $\text{H}_2\text{O}_2$  as a benign oxidant in chemical processing. Development of a more direct and green synthesis approach is needed that utilizes less energy and consumes fewer resources, thereby producing  $\text{H}_2\text{O}_2$  at a lower overall cost.

Perhaps the most efficient method for  $\text{H}_2\text{O}_2$  production, in terms of the principles of green chemistry, is the direct reaction of hydrogen and oxygen. Titanium silicalite (TS-1) catalysts have shown some success in promoting the direct production of  $\text{H}_2\text{O}_2$  from hydrogen and oxygen (Taramasso *et al.*, 1983). Even though the direct reaction is the most efficient production method, it is also perhaps the most dangerous. The flammability limit for hydrogen in air is 4%; however, studies have shown that the non-explosive margin can be widened to 9% if mixed with carbon dioxide ( $\text{CO}_2$ ) (Pande and Tonheim, 2001).

The use of CO<sub>2</sub> as the solvent for the direct generation of H<sub>2</sub>O<sub>2</sub> was pioneered by Beckman and coworkers, having illustrated great potential for several reasons (Hancu *et al.*, 2002). Carbon dioxide is non-flammable, has a very low toxicity, is inexpensive, naturally abundant, and cannot be further oxidized (Baiker and Wandeler, 2000; Beckman, 2004; Chen and Beckman, 2007; Chen and Beckman, 2008). Also, H<sub>2</sub> and O<sub>2</sub> are completely miscible with CO<sub>2</sub> at temperatures above 304 K (the critical temperature of CO<sub>2</sub>). Carrying out the reaction in supercritical CO<sub>2</sub> media allows for single phase operation (Subramaniam and McHugh, 1986; Baiker, 1999). Consequently, the transport limitation barrier that exists in the conventional AO synthetic route of H<sub>2</sub>O<sub>2</sub> can be eliminated. Removing this barrier enhances the yield of the reaction while more effectively producing H<sub>2</sub>O<sub>2</sub>. In addition, single phase operation would reduce the number of unit operations required for production; thus, making the process more cost effective. The advantages associated with using CO<sub>2</sub> as a solvent media represent the ideals set forth by the twelve principles of green chemistry. The direct synthesis of H<sub>2</sub>O<sub>2</sub> is certainly a green alternative to the widely accepted anthraquinone route.

Even so, it is very difficult to accurately measure hydrogen peroxide production in the direct route. Unfortunately, the same conditions necessary to produce H<sub>2</sub>O<sub>2</sub> also catalyze its decomposition (Landon *et al.*, 2003). There are two reaction pathways responsible for the breakdown of H<sub>2</sub>O<sub>2</sub>, which are thermodynamically favored (Li *et al.*, 2007). One is the disproportionation of H<sub>2</sub>O<sub>2</sub> resulting in the formation of both water and oxygen shown in Equation (3-4). The second pathway is the reduction of H<sub>2</sub>O<sub>2</sub> to give water as shown in Equation (3-3).





Coupling the generation of hydrogen peroxide with an oxidation reaction provides a unique solution (Meiers and Holderich, 1999). The generated hydrogen peroxide can be consumed through oxidation of another reactant before it has a chance to enter one of the decomposition pathways. Some of the probe reactions conducted during the course of this collaborative research in the Roberts (Auburn University) and Beckman (University of Pittsburgh) laboratories include propylene epoxidation, pyridine oxidation, cyclohexanone oxidation.

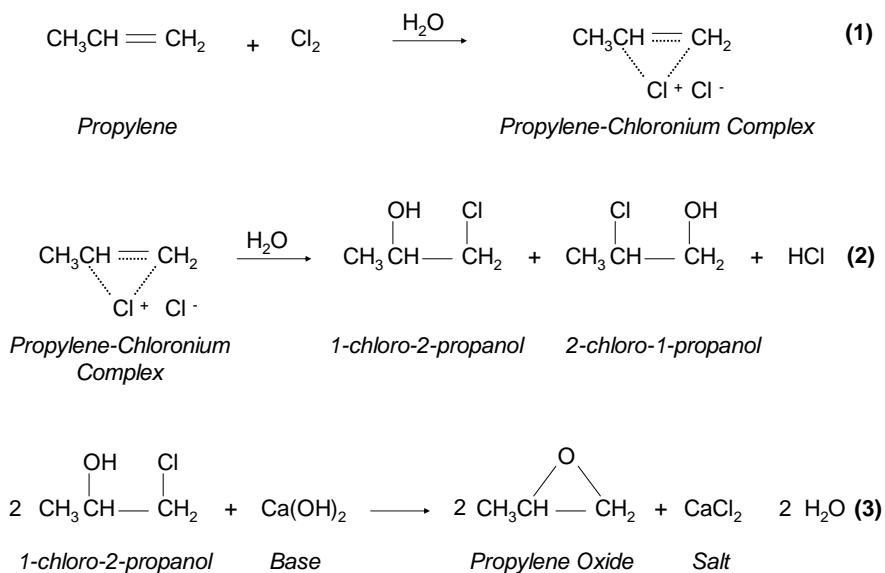
### **3.2 Propylene Epoxidation**

The epoxidation of propylene is certainly considered a very important reaction by the chemical industry. Propylene oxide (PO) is utilized as a starting material in the production of a variety of valuable chemicals such as glycol ethers, polyether polyols, and propylene glycols (Ullman, 2003). Nearly six million tons of PO is produced globally each year, and the majority of this PO is manufactured using either a chlorohydrin or hydroperoxidation process (Kirk-Othmer, 2001). The chlorohydrin route includes the formation of two propylene chlorohydrin isomers followed by a dechlorination step to yield PO. In the hydroperoxidation process, an organic reagent is oxidized to its hydroperoxide then used as an epoxidizing agent for propylene. Both

routes involve several harsh intermediates, produce numerous waste streams, and require a considerable number of unit operations.

### 3.2.1 Chlorohydrin Process

For the chlorohydrin synthetic route, propylene gas is first reacted with chlorine gas and an excess of water to produce the chief intermediates 1-chloro-2-propanol and 2-chloro-1-propanol along with hydrochloric acid. Small amounts of 1,2-dichloropropane and 2,2'-dichlorodiisopropyl ether are also produced as a result of this chlorohydration step. The principal intermediates are subsequently epoxidized with a strong base generating the desired product, PO, and a salt (Ullman, 2003). Refer to Scheme 3-2 for the chlorohydrin route to PO.



**Scheme 3-2.** Chlorohydrin process for generating propylene oxide.

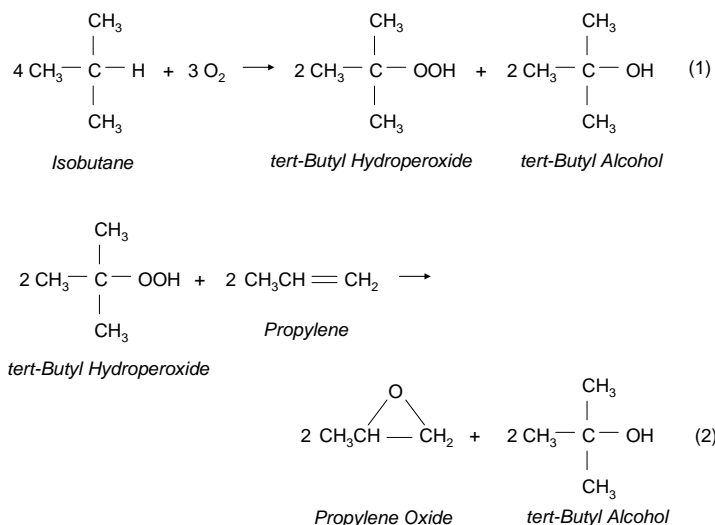
Several by-products formed during the epoxidation step include epichlorohydrin, glycerol monochlorohydrin, glycerol, propanal, acetone, and acetol. There are approximately two pounds of salt produced to each pound of product produced. As a result, the volume of wastewaters generated is almost forty times that of the PO produced (Kahlich *et al.*, 2003).

### **3.2.2 Hydroperoxidation Process**

Another common synthetic route employed for the production of PO is a hydroperoxidation process. In this method, propylene is indirectly oxidized to PO using various organic hydroperoxides (Kirk-Othmer, 1996). The most common hydroperoxides utilized in industry are tert-butyl and ethylbenzene, mostly due to their high market value and demand. The alcohol co-product generated during this production route can be transformed into a more useful commodity (Ullman, 2003). Some of the disadvantages associated with this process include the generation of substantial amounts of waste, the high cost of capital required, the complexity of the process, and the energy demands for both product generation and purification.

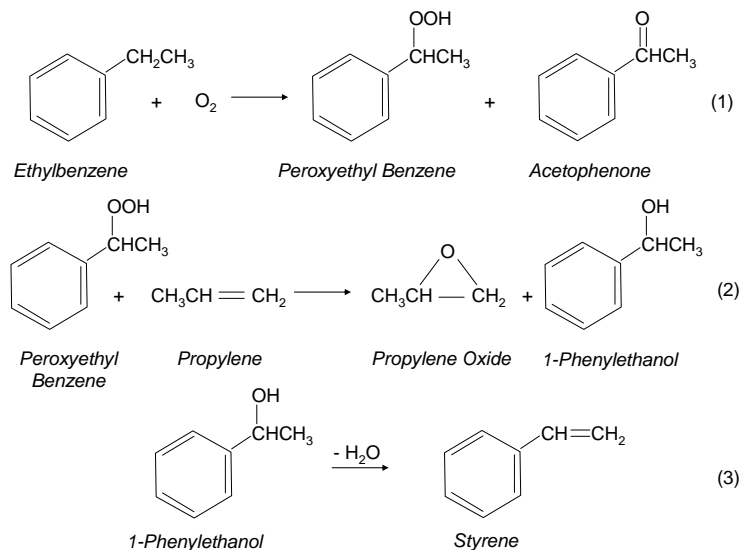
In the tert-butyl hydroperoxide process, isobutane is oxidized to its hydroperoxide in an uncatalyzed liquid-phase reactor. Here some of the tert-butyl hydroperoxide decomposes to a tert-butyl alcohol. The tert-butyl alcohol is converted to methyl tert-butyl ether (MTBE). The epoxidation step occurs over an organometallic catalyst (W, V, Mo) in a staged reactor system along with an organic solvent such as toluene, benzene, or chlorobenzene. The tert-butyl hydroperoxide is reacted with propylene producing PO and several by-products (Kirk-Othmer, 2001). The major by-products include methyl

formate, propylene glycol, and a propylene dimer. Scheme 3-3 illustrates the tert-butyl hydroperoxide process. The tert-butyl alcohol co-product is dehydrated to isobutene and converted to methyl tert-butyl ether, a fuel additive.



**Scheme 3-3.** Tert-butyl-hydroperoxide process for manufacturing propylene oxide.

In the ethylbenzene hydroperoxide process, ethylbenzene is oxidized in an uncatalyzed liquid-phase reactor producing the intermediates peroxyethyl benzene and acetophenone. PO is then generated along with 1-phenylethanol by reacting peroxyethyl benzene and propylene over a catalyst in an epoxidation reactor (Ullman, 2003). The extensive by-product formation includes acetophenone, 1-phenylethanol, along with other organic impurities. However, the 1-phenylethanol and acetophenone produced during this route can be dehydrated over a catalyst to styrene. Scheme 3-4 illustrates the ethylbenzene hydroperoxide route to PO.



**Scheme 3-4.** Ethylbenzene process for producing propylene oxide.

There are several co-products produced in this route, and they are of greater weight fraction than the PO formed in this process. Almost 20% waste is produced during the oxidation of ethyl benzene alone. Some of the capital cost is offset as a result of the co-product styrene, which is generated in this route. Even so, manufacturers of PO are exploring alternative routes for production.

### 3.2.3 Direct Oxidation Routes

#### Molecular Oxygen

The catalytic epoxidation of ethylene using molecular oxygen has been quite successful over the years (Monnier, 2001). This epoxidation is carried out over a silver catalyst in a gas phase reactor. Unfortunately, researchers have had limited success with the direct epoxidation of higher olefins, such as propylene, by molecular oxygen. The studies conducted for the direct epoxidation of higher olefins were carried out with a

homogeneous catalyst in a liquid phase reactor (Sheldon and Kochi, 1976). Researchers have determined that the particularly reactive allylic hydrogen atoms are responsible for an inability to directly oxidize these higher olefins. The bond strength of the allylic hydrogen in propylene is only 77 kcal/mol; whereas, the vinylic hydrogen in ethylene has a bond strength of 112 kcal/mol (Mackay *et al.*, 1978). Therefore, it is less energetically favorable for the addition of oxygen to occur across the double bond. Oxygen will instead attack and capture an allylic hydrogen atom from the molecule; thereby, eliminating any possibility of epoxide formation (Monnier, 2001). Traditional silver catalysts, which are effective in the epoxidation of ethylene, have a very poor performance when utilized in the epoxidation of propylene. Efforts have been made to enhance the activity of the conventional silver catalysts used in the direct route to epoxides. The highly-modified silver catalysts do show some improvement in catalyzing the epoxidation of propylene; however, the yield of propylene oxide is still far too low to implement on a commercial scale.

### **In-Situ Generated Hydrogen Peroxide**

Employing hydrogen peroxide ( $\text{H}_2\text{O}_2$ ) as an oxidant for the epoxidation of propylene is a promising alternative to conventional oxidants permitting cleaner production of PO. Hydrogen peroxide is generally considered a benign oxidant, given that it is relatively non-toxic and breaks down to benign by-products in the environment. Unfortunately, the current technology for manufacturing  $\text{H}_2\text{O}_2$  requires multiple unit operations, is highly energy intensive, and results in the generation of several considerable waste streams. Consequently, it is far too costly to implement  $\text{H}_2\text{O}_2$  as a benign oxidant in chemical

processing at this time. *Perhaps the most efficient method for H<sub>2</sub>O<sub>2</sub> production, in terms of the principles of green chemistry, is the direct reaction of hydrogen and oxygen.* Researchers have developed a catalyst, titanium silicalite (TS-1), that has shown some success in promoting the direct production of H<sub>2</sub>O<sub>2</sub> from hydrogen and oxygen (Taramasso *et al.*, 1983). Clerici *et al.* (1991) has shown that the direct epoxidation of propylene occurs over TS-1 catalysts at relatively mild conditions with both high selectivities and conversions.

The first studies in the direct generation of propylene oxide were conducted in a liquid phase reactor with propylene, hydrogen, oxygen, and methanol/water over a TS-1 supported catalyst. The in-situ generation of H<sub>2</sub>O<sub>2</sub> occurs at the supported precious metal sites in the catalyst, while the subsequent oxidation step takes place at the Ti-sites (Laufer *et al.*, 1999). Researchers have concluded that this reaction is most effective when methanol is included as part of the solvent mixture (Clerici *et al.*, 1991; Thiele and Roland, 1997; Notari, 1996; Laufer *et al.*, 1999). Researchers have concluded that this reaction is most effective when methanol is included as part of the solvent mixture (Clerici *et al.*, 1991; Bellussi *et al.*, 1992; Thiele and Roland, 1997). Even so, typical yields obtained for the direct synthesis of PO in batch studies were around 10% with selectivity approaching 40%. Holderich and colleagues determined that the in-situ formation of H<sub>2</sub>O<sub>2</sub> directly from H<sub>2</sub> and O<sub>2</sub> could be enhanced with the inclusion of salts as promoters; thereby, improving the PO yield. Upon including promoters, the conversion of propylene doubled from approximately 20% to 40% while the selectivity remained steady at 40%. The selectivity for this reaction was increased to over 60% by

operating in a semi-batch mode (Hoelderich and Kollmer, 2000; Laufer and Hoelderich, 2001).

The direct production of PO from hydrogen, oxygen, and propylene over a heterogeneous Pt/Pd/TS-1 catalyst has been investigated using a continuous fixed-bed reactor (Jenzer *et al.*, 2001). The solvent system used in the continuous studies included methanol and water along with the co-solvent carbon dioxide. Upon initiation of the reaction, a very high selectivity of 99% was obtained for PO. However, the yield of PO was very low at 3.5% with only traces of PO being detected at 35 hours time-on-stream. Several by-products (resulting in catalyst deactivation) were generated during this process, with the chief by-product being methyl formate. Other side products included acetone, acrolein, acrylic acid, and monomethylated glycols. The by-products are formed as a result of the oxidation of methanol, which occurs at very mild reaction conditions.

Beckman and colleagues have investigated the use of carbon dioxide as the sole solvent for the generation of PO from hydrogen, oxygen, and propylene over a Pd/TS-1 catalyst (Danciu *et al.*, 2003). Carbon dioxide is non-flammable, relatively non-toxic, environmentally benign, naturally abundant, and cannot be further oxidized (Baiker, 2000). Also, H<sub>2</sub> and O<sub>2</sub> are completely miscible with CO<sub>2</sub> at temperatures above 304 K—the critical temperature of CO<sub>2</sub>. Carrying out the reaction in supercritical CO<sub>2</sub> media allows for single phase operation (Subramaniam and McHugh, 1986; Baiker, 1999). In so doing, the transport limitation barrier that exists in the conventional AQ synthetic route of H<sub>2</sub>O<sub>2</sub> is eliminated. Removing this barrier enhances the yield of the reaction while more effectively producing H<sub>2</sub>O<sub>2</sub>. In addition, single phase operation would drastically reduce the number of unit operations required for production; thus, making the



process more cost effective. Also, using carbon dioxide as the solvent should eliminate the by-product formation that is associated with the methanol/water solvent system. Beckman determined that carbon dioxide is an excellent solvent for the epoxidation of propylene, where the in-situ generation of  $\text{H}_2\text{O}_2$  is the oxidant. Also, they found that methanol is not required for the efficient production of PO from propylene and  $\text{H}_2\text{O}_2$ .

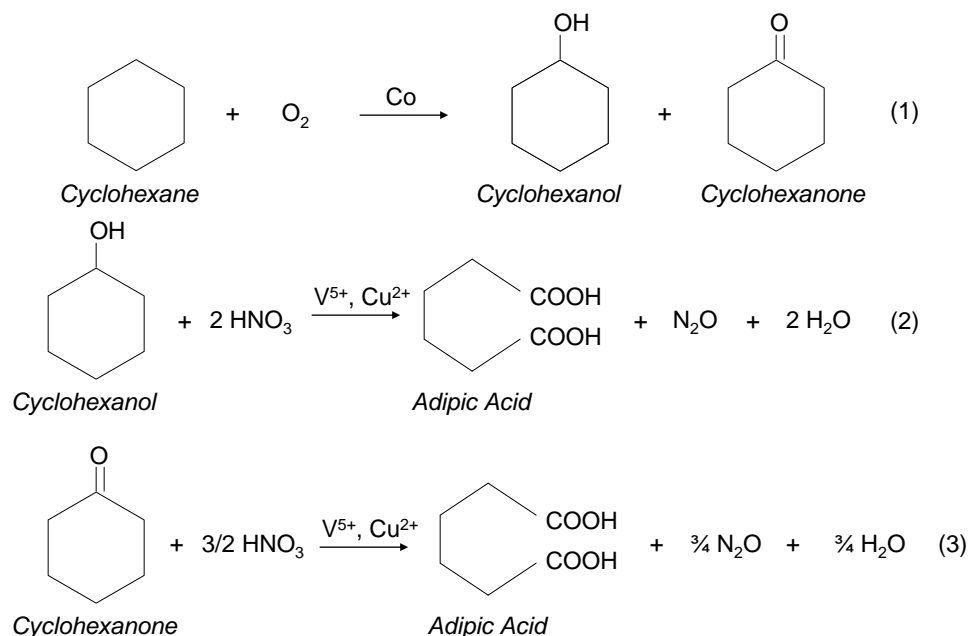
Beckman and colleagues have studied the direct generation of PO from hydrogen, oxygen, and propylene over a Pd/TS-1 catalyst with carbon dioxide as the solvent (Danciu *et al.*, 2003). Carbon dioxide is non-flammable, relatively non-toxic, environmentally benign, naturally abundant, and cannot be further oxidized. Also,  $\text{H}_2$  and  $\text{O}_2$  are completely miscible with  $\text{CO}_2$  at temperatures above 304 K—the critical temperature of  $\text{CO}_2$  (Beckman, 2003). Carrying out the reaction in supercritical  $\text{CO}_2$  media allows for single phase operation (Subramaniam and McHugh, 1986; Baiker, 1999). Thus, the mass transport limitation barrier that exists in the conventional AQ synthetic route of  $\text{H}_2\text{O}_2$  would be eliminated. In addition, single phase operation would drastically reduce the number of unit operations required; thus, making the process more cost effective. Also, using carbon dioxide as the solvent should eliminate the by-product formation that occurs when using the methanol/water solvent system.

Beckman and colleagues have shown that  $\text{H}_2\text{O}_2$  can successfully be produced in  $\text{CO}_2$  from  $\text{O}_2$  and  $\text{H}_2$  (Hancu and Beckman, 2001). The effect of the solvent system on the extent of reaction was examined. The batch experiments conducted verify that PO can be generated directly with a high selectivity in  $\text{CO}_2$ , while the selectivity to PO drops significantly when using the methanol/water solvent system. Also, their results confirm that methanol is a major contributor to by-product formation with a selectivity ranging

from 1.4-12.4% for the methanol/water solvent system. Beckman and coworkers have determined that CO<sub>2</sub> is a good solvent for the direct epoxidation of propylene via in-situ generated H<sub>2</sub>O<sub>2</sub>, and that methanol is not necessary for the effective generation of PO (Danciu *et al.*, 2003).

### **3.3 Adipic Acid**

Adipic acid is primarily used as a starting material in the manufacture of nylon-6,6 polyamide—a fiber of considerable importance to the synthetic textiles industry (Ullman, 2003). As a result, the demand for adipic acid is rather high with over four billion tons being produced globally each year. Nylon-6,6 polyamide fibers have a variety of applications which include upholstery, carpet fibers, tire reinforcements, apparel, and auto parts (Sato *et al.*, 1998). Adipic acid is also utilized in the manufacture of synthetic lubricants, plasticizers, polyurethane resins, and coatings (Mainhardt, 2000). Various processes exist for the commercial generation of adipic acid; even so, each process incorporates two key reaction stages. Initially, cyclohexane is oxidized over a cobalt catalyst producing the intermediates cyclohexanone and cyclohexanol (KA or ketone/alcohol mixture). After separation of the KA oil from any unreacted cyclohexane, it undergoes a nitric acid oxidation step generating adipic acid (Kirk-Othmer, 1996). Refer to Scheme 3-5 for the current commercial route to manufacturing adipic acid. The distinction of each industrial process is mostly a result of the method utilized for manufacturing KA oil.

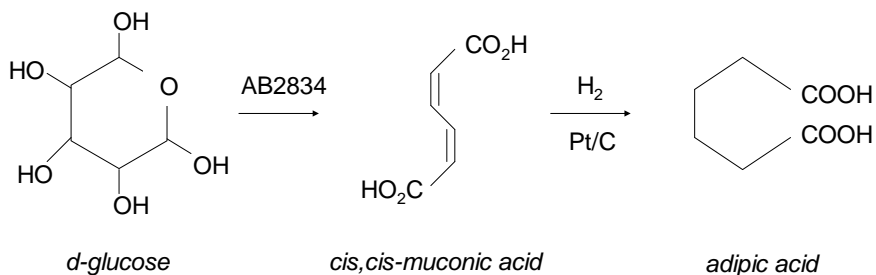


**Scheme 3-5.** Typical industrial process for manufacturing adipic acid.

Unfortunately, the commercial synthesis of adipic acid is a major source of nitrous oxide (N<sub>2</sub>O) emissions—a greenhouse gas. Approximately 5-8% of all N<sub>2</sub>O emissions generated are from adipic acid production alone (Shimizu *et al.*, 2000). The accumulation of N<sub>2</sub>O in our atmosphere contributes to both ozone depletion and global warming along with acid rain and smog (Sato *et al.*, 1998). In recent years, environmental regulations have required the implementation of N<sub>2</sub>O abatement technologies by industry during production. The primary abatement technologies currently being utilized are both the thermal and catalytic decomposition of N<sub>2</sub>O (Reimer *et al.*, 1994). Emissions have dropped to less than 1% with the employment of these technologies (Shimizu *et al.*, 2000). Even so, this process generates substantial amounts of waste, has high capital costs associated with the necessary abatement technologies, is

rather complex, and has considerable energy demands for both product generation and purification. Thus, researchers are exploring more ecological and economically viable alternatives to the current technology for synthesizing adipic acid.

Frost and colleagues have developed a biocatalytic alternative to the conventional pathway for generating adipic acid. In this method, they employ a microbial catalyst to convert D-glucose to cis, cis-muconic acid. The cis, cis-muconic acid is then hydrogenated producing adipic acid (Draths and Frost, 1994). Refer to Scheme 3-6 for the biocatalytic route to adipic acid.



**Scheme 3-6.** Biocatalytic route for generating adipic acid.

There are several advantages to utilizing the biocatalytic pathway for manufacturing adipic acid (Niu *et al.*, 2002). D-glucose is not only non-toxic, but also readily available from renewable resources such as plant starch and cellulose. N<sub>2</sub>O abatement equipment is eliminated from production, since greenhouse gases are not generated during this process. Also, this method takes place using very mild reaction conditions. The biocatalytic route to adipic acid is quite simple, generates only small amounts of waste, and has greatly reduced energy demands for both product generation and purification. Even so, this technology must undergo the challenges of optimization and scale-up before it can be useful as a commercial process in the generation of adipic acid (Bolm *et al.*, 1999).

Researchers have also considered hydrogen peroxide as an environmentally viable alternative to the current methodology for producing adipic acid. It is generally considered a benign oxidant, given that it is relatively non-toxic and breaks down to benign by-products in the environment. Most studies have focused on the transformation of cyclohexene to adipic acid with 30% hydrogen peroxide over a variety of catalysts (Sato *et al.*, 1998; Deng *et al.*, 1999; Lapisardi *et al.*, 2004). Noyori and colleagues studied this reaction in the presence of tungsten oxide along with a phase transfer catalyst. They found that a high catalytic efficiency could be attained with the addition of only a phase transfer catalyst. Unfortunately, phase transfer catalysts are relatively expensive and not particularly environmentally benign. Chen and colleagues have developed a benign peroxytungstate-organic complex that successfully performed without any organic solvent or harmful phase transfer catalysts in the direct oxidation of cyclohexene (Deng *et al.*, 1999). Even so, the use of commercially produced hydrogen

peroxide is far too costly to allow for use of  $\text{H}_2\text{O}_2$  as a benign oxidant in chemical processing.

### 3.4 Pyridine Oxidation

Pyridine oxide is a valuable synthetic intermediate in both the pharmaceutical and agrochemical industries due to the electron-withdrawing and electron-donating capability of its N-oxide group. Pyridine oxide has greater versatility than pyridine in chemical processing, because it can react with both electrophiles and nucleophiles. Pyridine not only demonstrates very poor reactivity in the typical electrophilic reactions of pyridine oxide, but also requires especially harsh operating conditions. The various resonance structures of pyridine oxide facilitate its success in numerous industrially significant reactions such as allylation, acylation, protonation, and nitration.

For the purposes of the studies conducted at both Auburn University and the University of Pittsburgh, pyridine was used to measure the in-situ generation of  $\text{H}_2\text{O}_2$  by  $\text{H}_2$  and  $\text{O}_2$  over a Pd/TS-1 catalyst in  $\text{CO}_2$  solvent media. Pyridine was selected as the appropriate compound to evaluate the in-situ production of  $\text{H}_2\text{O}_2$  by taking the following criteria into consideration: (1) its solubility in  $\text{CO}_2$ , (2) ease of oxidation by  $\text{H}_2\text{O}_2$ , (3) high selectivity to its oxide, (4) does not undergo either hydrogenation or oxidation by oxygen, since both  $\text{H}_2$  and  $\text{O}_2$  are present in the reaction mixture, and (5) the stoichiometric conversion of the reactant to its oxide. As discussed earlier, it is very difficult to accurately measure the amount of  $\text{H}_2\text{O}_2$  produced in-situ, since it readily undergoes decomposition. However, coupling the generation of  $\text{H}_2\text{O}_2$  with the oxidation of pyridine facilitates a quantitative measurement.

## 3.5 Experimental Methods

### 3.5.1 Materials

#### Propylene Epoxidation Reaction

Propylene (99.9% purity, Airgas South), O<sub>2</sub>/CO<sub>2</sub> (49.90%/balance certified standard, Airgas South), H<sub>2</sub>/CO<sub>2</sub> (3.036%/balance certified standard, Airgas South) and CO<sub>2</sub> (99.9% purity, Airgas South) were all used as received without further purification. Two specialty gas mixtures were used for GC calibration. The composition of the first mixture was 82 ppm propane, 90.5 ppm propylene, 96.9 ppm propylene oxide with balance UHP helium (certified standard, Matheson-Trigas). The composition of the second mixture was 886 ppm propane, 983 ppm propylene, and 1063 ppm propylene oxide with balance UHP helium (certified standard, Matheson-Trigas). Both mixtures were used as received without further purification. Also, a specialty gas mixture was used as received for the calcination of catalysts. The composition of the mixture used was 2.920% O<sub>2</sub>, 4.130% H<sub>2</sub>, 10.30% propylene with balance CO<sub>2</sub> (certified standard, Airgas South). UHP grade H<sub>2</sub> (Airgas South) was used as received for catalyst reductions.

A 0.5 wt % Pd/TS-1 catalyst (Sud-Chemie) was used in the studies conducted for the epoxidation of propylene. TS-1 support material (Sud-Chemie) was used in the preparation of a 0.35 wt% Pd/TS-1 catalyst. [Pd(NH<sub>3</sub>)<sub>4</sub>](NO<sub>3</sub>)<sub>2</sub> (10wt% solution in water, Sigma Aldrich) was used as received in the preparation of the supported TS-1 catalysts.

### **Cyclohexanone Oxidation Reaction**

Both cyclohexanone (99%, Sigma Aldrich) and trifluoroacetic acid (99% purity, Sigma Aldrich) were used as received without further purification. H<sub>2</sub> (99.9% purity, Penn Oxygen), O<sub>2</sub>/CO<sub>2</sub> (50/50 certified standard mixture, Penn Oxygen), and CO<sub>2</sub> (99.9% purity, Penn Oxygen) were all used as received without further purification. UHP grade H<sub>2</sub> (Penn Oxygen) was used as received for catalyst reductions. A 0.347 % Pd/TS-1 catalyst (Lyondell) was used in these studies.

### **Pyridine Oxidation Reaction**

Pyridine, anhydrous (99.8%, Sigma Aldrich), pyridine oxide (97.0 +%, Sigma Aldrich), H<sub>2</sub>O<sub>2</sub> (30 wt% solution stabilized in H<sub>2</sub>O, Sigma Aldrich), sodium hydroxide (1.0 N, Sigma Aldrich), and nitric acid (1.0 N Sigma Aldrich) were all used as received without further purification. O<sub>2</sub>/CO<sub>2</sub> (49.90%/balance certified standard, Airgas South), H<sub>2</sub>/CO<sub>2</sub> (3.036%/balance certified standard, Airgas South) and CO<sub>2</sub> (99.9% purity, Airgas South) were used as received without further purification. H<sub>2</sub> (99.9% purity, Penn Oxygen), O<sub>2</sub>/CO<sub>2</sub> (50/50 certified standard mixture, Penn Oxygen), and CO<sub>2</sub> (99.9% purity, Penn Oxygen) were all used as received without further purification. UHP grade H<sub>2</sub> (Penn Oxygen, Airgas South) was used as received for catalyst reductions.

A 0.35 % Pd/TS-1 catalyst (Lyondell) was used in the studies conducted for the oxidation of pyridine. In addition, a 0.5 wt % Pd/TS-1 catalyst (Sud-Chemie) was also used in these studies. TS-1 support material (Sud-Chemie) was used in the preparation of a 0.35 wt% Pd/TS-1 catalyst. [Pd(NH<sub>3</sub>)<sub>4</sub>](NO<sub>3</sub>)<sub>2</sub> (10wt% solution in water, Sigma Aldrich) was used as received in the preparation of the supported TS-1 catalysts.



### **3.5.2 Apparatus**

#### **Propylene Epoxidation Reaction**

Figure 3-1 shows the experimental apparatus used in the epoxidation of propylene, which included a high-pressure stainless steel batch reactor (custom designed and manufactured in the Roberts Laboratory), frit filter (Mott Corporation), resistance temperature detector, pressure gauge, temperature controller, Buna o-ring, heating tape, stir bar, stir plate, ISCO 500D syringe pump, three-way valves, 1/16" stainless steel tubing, Tygon tubing, and a gas sampling bag.

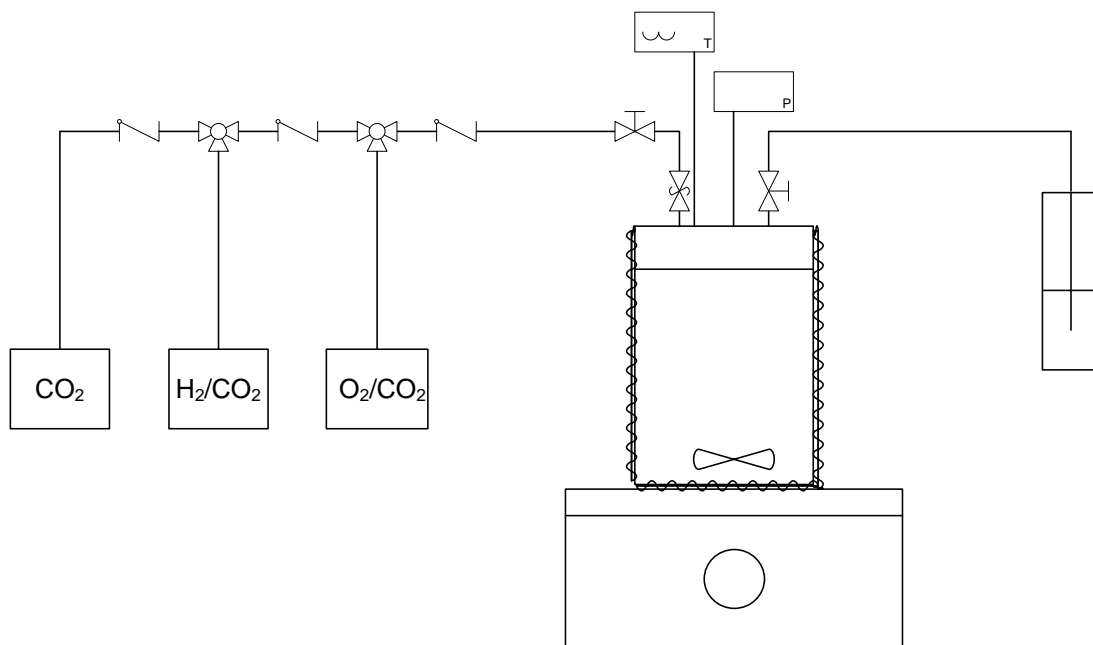
#### **Cyclohexanone and Pyridine Oxidation Reactions**

Figure 3-1 shows the experimental apparatus used in the oxidation of both cyclohexanone and pyridine, which includes a 30 mL high-pressure stainless steel batch reactor, stainless-steel sheathed type K thermocouple, pressure gauges, heating tape, o-ring, stir bar, and stir plate, three-way valves, two-way valves, proportional relief valve, 1/16" stainless steel tubing.

### **3.5.3 Experimental Procedure**

#### **Propylene Epoxidation Reaction**

The investigations for the epoxidation of propylene via in-situ generated hydrogen peroxide were conducted in a high-pressure batch reactor over a 0.5 wt% Pd/TS-1 catalyst (obtained from Sud-Chemie). A specific molar ratio and an appropriate equation of state were used to determine the amounts of each component ( $O_2$ ,  $H_2$ , and propylene)



**Figure 3-1.** Experimental apparatus for the in-situ generation of  $\text{H}_2\text{O}_2$  over a Pd/TS-1 catalyst in  $\text{CO}_2$  reaction media. This apparatus was used in the oxidation of propylene to propylene oxide, cyclohexanone to adipic acid, and pyridine to pyridine oxide. The glass collection tube was replaced with a gas collection bag for the propylene epoxidation studies. High pressure reactor, stir bar, heating tape, magnetic stirrer, three-way valves, proportional relief valve, two-way valves, glass collection tube, syringe pump

to be added to the reactor to obtain a desired reaction mixture. The gases, H<sub>2</sub> and O<sub>2</sub>, were both contained in pre-mixed cylinders along with CO<sub>2</sub>. The ratio of O<sub>2</sub>/CO<sub>2</sub> used was a 50/50 mixture; whereas, the ratio of H<sub>2</sub>/CO<sub>2</sub> used was a 3/97 mixture. The pre-mixed cylinders are particularly useful in the case of H<sub>2</sub>/CO<sub>2</sub>. The flammability limit for H<sub>2</sub> in air is 4%; however, studies have shown that the non-explosive margin can be widened to 9% if mixed with CO<sub>2</sub> (Pande and Tonheim, 2001). It is certain that the H<sub>2</sub>/CO<sub>2</sub> mixture is well below the explosive limit for H<sub>2</sub>, and can safely be mixed with air in any proportion.

In a typical experiment, a measured amount of catalyst was added to a 200 mL stainless steel high-pressure batch reactor. A magnetic stir bar was included to allow for proper mixing of reactants. A Buna o-ring was used to seal the reactor. The batch reactor was purged several times with CO<sub>2</sub> in order to ensure that no air remained in the system. O<sub>2</sub>/CO<sub>2</sub>, H<sub>2</sub>/CO<sub>2</sub>, and propylene were all delivered to the reactor using a calibrated ISCO pump (500D ISCO series syringe pump), respectively. The syringe pump was loaded with a known amount of the O<sub>2</sub>/CO<sub>2</sub> mixture at room temperature, and delivered to the reactor. Following the addition of O<sub>2</sub>/CO<sub>2</sub> to the system, the syringe pump was loaded with a known amount of the H<sub>2</sub>/CO<sub>2</sub> mixture. This mixture was then added to reactor. The last reactant to be introduced into the reactor system was propylene. A known amount of propylene was loaded into the syringe pump, and delivered to the reactor. After the addition of propylene, the system was heated to a reaction temperature of 45°C using a heating tape. Balance CO<sub>2</sub> was added in order to reach a final reaction pressure of 131 bar. The contents of the reactor were stirred continuously. Each experiment ran for approximately eight hours. The mixture was

sampled at regular intervals by way of a gas collection bag for GC analysis. A 50  $\mu\text{L}$  sample was collected from the gas bag using a gas-tight syringe. The sample was analyzed using a Varian 3300 gas chromatograph fitted with a FID detector and a GS-GasPro column (30m x 0.320mm). The data was collected using a SRI PeakSimple Chromatography Data System (Model 202).

After running for eight hours, the contents of the reactor were vented. The catalyst was washed with methanol to extract by-products formed during the course of the reaction. A 0.3  $\mu\text{L}$  sample of this solution was analyzed using a Varian 3300 gas chromatograph fitted with a FID detector and a HP-PLOT Q column (30m x 0.53mm x 40 $\mu\text{L}$ ). The data was collected using a SRI PeakSimple Chromatography Data System (Model 202).

### **Cyclohexanone Oxidation Reaction**

The investigations for the oxidation of cyclohexanone via in-situ generated hydrogen peroxide were conducted in a high-pressure batch reactor over a 0.35 wt% Pd/TS-1 catalyst (obtained from Lyondell) at the University of Pittsburgh by the author and collaborative researcher, Qunlai Chen.

In a typical experiment, a measured amount of catalyst was added to a 30 mL stainless steel high-pressure batch reactor. A magnetic stir bar was included to allow for proper mixing of reactants. The reactor was loaded with known amounts of cyclohexanone (CHAO), deionized water, and trifluoroacetic acid (TFA). A Buna o-ring was used to seal the reactor. A specific molar ratio and an appropriate equation of state were used to determine the amounts of  $\text{O}_2$  and  $\text{H}_2$  to be added to the reactor to obtain a

desired reaction mixture. Oxygen was contained in a pre-mixed cylinder along with CO<sub>2</sub>, and the ratio of O<sub>2</sub>/CO<sub>2</sub> used was a 50/50 mixture. Hydrogen was delivered from a pure cylinder. The O<sub>2</sub>/CO<sub>2</sub> mixture, H<sub>2</sub>, and CO<sub>2</sub> were all delivered to the reactor, respectively. A gas booster was used in order to deliver CO<sub>2</sub> to the reactor at the appropriate pressure. After the addition of all gases, the system was heated to a reaction temperature of 70°C using a hotplate. Once the system reached a reaction temperature of 70°C, additional CO<sub>2</sub> was added in order to obtain a final reaction pressure of 114 bar. The contents of the reactor were stirred continuously. Each experiment ran for approximately 10 hours.

After running for 10 hours, the reactor was allowed to cool to room temperature. The contents of the reactor were then slowly bubbled through a glass collection tube containing a known amount of methanol. The glass collection tube was cooled on ice for product collection. The batch reactor was disassembled, and the methanol/product solution was used to rinse the reactor. A filter was used to separate the catalyst from the product solution. Following product collection, analysis was conducted using a HP 5890A gas chromatograph fitted with a TCD detector and a HayeSep D packed column (20ft x 1/8”).

### **Pyridine Oxidation Reaction**

The investigations for the oxidation of pyridine via in-situ generated hydrogen peroxide were conducted in a high-pressure batch reactor over a Pd/TS-1 catalyst at the University of Pittsburgh by the author and collaborative researcher, Qunlai Chen. Studies were also conducted by the author in the Roberts Laboratory at Auburn University. For the

experiments conducted at Auburn University, both H<sub>2</sub> and O<sub>2</sub> were contained in pre-mixed cylinders along with CO<sub>2</sub>. The ratio of O<sub>2</sub>/CO<sub>2</sub> used was a 50/50 mixture; whereas, the ratio of H<sub>2</sub>/CO<sub>2</sub> used was a 3/97 mixture. The pre-mixed cylinders are particularly useful in the case of H<sub>2</sub>/CO<sub>2</sub>. The flammability limit for H<sub>2</sub> in air is 4%; however, studies have shown that the non-explosive margin can be widened to 9% if mixed with CO<sub>2</sub> (Pande and Tonheim, 2001). It is certain that the H<sub>2</sub>/CO<sub>2</sub> mixture is well below the explosive limit for H<sub>2</sub>, and can safely be mixed with air in any proportion.

The metal walls of the reactor are suspect for catalyzing the decomposition of in-situ generated H<sub>2</sub>O<sub>2</sub>. Thus, both the reactor and glass liner were passivated before each experiment in order to prevent H<sub>2</sub>O<sub>2</sub> degradation. The general method followed for passivation included a 10 wt% NaOH solution, a 35 wt% HNO<sub>3</sub> solution, and a 30 wt% H<sub>2</sub>O<sub>2</sub> solution. First, the reactor and glass liner were soaked in the NaOH solution for three hours. After three hours, the reactor and glass liner were washed with distilled water. Next, the reactor and glass liner were soaked in the HNO<sub>3</sub> solution for eight hours. After eight hours, the reactor and glass liner were washed with distilled water. Lastly, the reactor and glass liner were soaked with the H<sub>2</sub>O<sub>2</sub> solution for 12 hours.

In a typical experiment, a measured amount of catalyst was added to a 30 mL stainless steel high-pressure batch reactor. A magnetic stir bar was included to allow for proper mixing of reactants. The batch reactor was loaded with known amounts of pyridine and deionized water. A Buna o-ring was used to seal the reactor. A specific molar ratio and an appropriate equation of state were used to determine the amounts of O<sub>2</sub> and H<sub>2</sub> to be added to the reactor to obtain a desired reaction mixture. H<sub>2</sub>/CO<sub>2</sub>, O<sub>2</sub>/CO<sub>2</sub>, and CO<sub>2</sub> were all delivered to the reactor using a calibrated ISCO pump (500D

ISCO series syringe pump), respectively. The syringe pump was loaded with a known amount of the H<sub>2</sub>/CO<sub>2</sub> mixture at room temperature, and delivered to the reactor. Following the addition of H<sub>2</sub>/CO<sub>2</sub> to the system, the syringe pump was loaded with a known amount of the O<sub>2</sub>/CO<sub>2</sub> mixture. This mixture was then added to the reactor. The syringe pump was used to deliver CO<sub>2</sub> to the reactor. For studies conducted at the University of Pittsburgh, a gas booster was used in order to deliver CO<sub>2</sub> to the reactor at the appropriate pressure. After the addition of CO<sub>2</sub>, the system was heated to a reaction temperature of 60°C using a heating tape. Once the system reached a reaction temperature of 60°C, additional CO<sub>2</sub> was added in order to obtain a final reaction pressure of 125 bar. The contents of the reactor were stirred continuously. Each experiment ran for approximately five hours.

After running for five hours, the reactor was allowed to cool to room temperature. The contents of the reactor were then slowly bubbled through a glass collection tube containing a known amount of methanol. The glass collection tube was cooled on ice for product collection. The batch reactor was disassembled, and the methanol/product solution was used to rinse the reactor. A filter was used to separate the catalyst from the product solution. Following product collection, analysis was conducted using a HP 5890A gas chromatograph fitted with a TCD detector and a HayeSep D packed column (20ft x 1/8"). A 0.3 µL sample was analyzed using a Varian 3300 gas chromatograph fitted with a FID detector and a DB-5.625 column (30m x 0.250mm x 0.50µm). The data was collected using a SRI PeakSimple Chromatography Data System (Model 202).

### **3.5.4 Gas Chromatograph Calibration**

#### **Propylene Epoxidation Reaction**

The following procedure was used to calibrate the Varian 3300 gas chromatograph for analysis of experimental data obtained from the epoxidation of propylene. A magnetic stir bar was added to a 200 mL stainless steel high-pressure batch reactor, which was sealed with a Buna o-ring. The reactor was purged several times with CO<sub>2</sub> to ensure that no air remained in the system. After purging, the reactor was heated to a reaction temperature of 45°C using a heating tape. The syringe pump was loaded with a known amount of propylene at room temperature, and delivered to the reactor. Additional CO<sub>2</sub> was delivered to the reactor in order to simulate a reaction pressure of 131 bar. The reactor was vented to a sampling loop, and that volume was delivered to the gas sampling bag. The gas bag was purged three times with the propylene/CO<sub>2</sub> mixture before collecting a sample for analysis. A 50 µL sample was drawn from the gas bag using a gas-tight syringe. The sample was analyzed using a Varian 3300 gas chromatograph fitted with a FID detector and a GS-GasPro column (30m x 0.320mm). The data was collected using a SRI PeakSimple Chromatography Data System (Model 202). This procedure was repeated to verify the accuracy of this method.

#### **Cyclohexanone Oxidation Reaction**

The following procedure was used to calibrate the Varian 3300 gas chromatograph for analysis of experimental data obtained from the oxidation of cyclohexanone. Solutions of cyclohexanone diluted in ethyl acetate were prepared with concentrations ranging from 0.01M to 0.4M. A 0.3 µL sample of each solution was analyzed using a Varian 3300 gas



chromatograph fitted with a FID detector and a DB-5.625 column (30m x 0.250mm x 0.50 $\mu$ m). The data was collected using a SRI PeakSimple Chromatography Data System (Model 202). This procedure was repeated to verify the accuracy of this method.

### **Pyridine Oxidation Reaction**

The following procedure was used to calibrate the Varian 3300 gas chromatograph for analysis of experimental data obtained from the oxidation of pyridine. Solutions of pyridine diluted in ethanol were prepared with concentrations ranging from 0.05M to 0.3M. A 0.3  $\mu$ L sample of each solution was analyzed using a Varian 3300 gas chromatograph fitted with a FID detector and a DB-5.625 column (30m x 0.250mm x 0.50 $\mu$ m). The data was collected using a SRI PeakSimple Chromatography Data System (Model 202). This procedure was repeated to verify the accuracy of this method. The same procedure was followed to construct a calibration curve for pyridine oxide with concentrations ranging from 0.05M to 0.3M.

## **3.6 Results and Discussion**

### **3.6.1 Propylene Epoxidation**

In a typical experiment for the in-situ generation of H<sub>2</sub>O<sub>2</sub> and subsequent oxidation of propylene, O<sub>2</sub>/CO<sub>2</sub>, H<sub>2</sub>/CO<sub>2</sub>, and propylene were all delivered to the stainless steel batch reactor, respectively. The system was heated to a reaction temperature of 45°C and additional CO<sub>2</sub> added in order to reach a reaction pressure of 131 bar. Two peaks were consistently obtained with analysis by gas chromatography, which corresponded to the production of propane and the unreacted propylene remaining in the system. This

experiment was replicated numerous times, but propylene oxide was not detected using this experimental procedure. It was determined for each case that propylene was hydrogenated to propane rather than undergoing the desired epoxidation reaction. A fairly low conversion of propylene to propane was achieved at only 3%.

Considering the ineffective attempts at epoxidizing propylene via in-situ generated  $\text{H}_2\text{O}_2$ , the order in which each reactant was introduced into the high-pressure batch reactor was adjusted to  $\text{H}_2/\text{CO}_2$ ,  $\text{O}_2/\text{CO}_2$ , and propylene, respectively. As in the previous example, the system was heated to a reaction temperature of  $45^\circ\text{C}$  and additional  $\text{CO}_2$  added in order to reach a reaction pressure of 131 bar. It is noted that the only peak obtained in this study corresponded to the unreacted propylene in the system. The propane peak disappeared, but propylene oxide was still not detected. It is suggested that for this case, all of the  $\text{H}_2$  was consumed to further reduce the Pd/TS-1 catalyst leaving no  $\text{H}_2$  available for the hydrogenation of propylene.

In order to test this theory, supplemental  $\text{H}_2$  was added to the reactor after several hours of mixing. The mixture was sampled for GC analysis, and two peaks were obtained corresponding to the production of propane and the unreacted propylene remaining in the system. Again, propylene oxide was not detected. This confirmed that the hydrogen initially introduced into the system further reduced the catalyst, and was not available for reaction with oxygen or propylene. Even so, this method repeatedly failed to produce the desired reaction product propylene oxide. The catalyst used in all experimental runs was approximately 0.5 wt % Pd/TS-1 (obtained from Sud-Chemie) that was both calcined and pre-activated. Collaborators in the Beckman group determined that this particular metal loading was too high for catalyzing the in-situ generation of

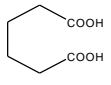
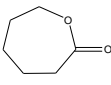
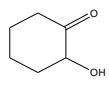
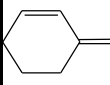
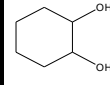
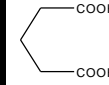
H<sub>2</sub>O<sub>2</sub>. A high metal loading rapidly degrades the formed H<sub>2</sub>O<sub>2</sub> while inhibiting its synthesis. Beckman suggested a metal loading of no more than 0.35 wt % Pd/TS-1 for the successful in-situ generation of H<sub>2</sub>O<sub>2</sub>.

For that reason, the propylene epoxidation reaction using in-situ generated H<sub>2</sub>O<sub>2</sub> as the oxidant was examined using a 0.35 wt% Pd/TS-1 catalyst that was both calcined and pre-activated. H<sub>2</sub>/CO<sub>2</sub>, O<sub>2</sub>/CO<sub>2</sub>, and propylene were all delivered to the reactor, respectively. As in the previous studies, the system was heated to a reaction temperature of 45°C and additional CO<sub>2</sub> was added in order to reach a reaction pressure of 131 bar. The contents of the reactor were mixed for 6 hours and sampled at regular intervals for GC analysis. Propylene oxide was not detected during that time span. Unfortunately, the same conditions necessary to generate H<sub>2</sub>O<sub>2</sub> also catalyze its decomposition (Landon *et al.*, 2003; Li *et al.*, 2007). Therefore, by coupling the generation of H<sub>2</sub>O<sub>2</sub> with an oxidation reaction the generated H<sub>2</sub>O<sub>2</sub> can be consumed by another reactant before having an opportunity to break down (Meiers and Holderich, 1999). However, the coupling of the in-situ generated H<sub>2</sub>O<sub>2</sub> with the oxidation of propylene wasn't successful in producing propylene oxide. After closely examining the loading procedure, it was determined that too much time was allowed to fill the reactor with the reactants H<sub>2</sub>, O<sub>2</sub>, and propylene. Thus, the formed hydrogen peroxide decomposed before propylene was available for reaction. In addition, the metal walls of the reactor have the ability to catalyze the degradation of H<sub>2</sub>O<sub>2</sub>. Therefore, a reactor passivation methodology was developed along with a glass insert in order to prevent the generated H<sub>2</sub>O<sub>2</sub> from contacting the walls of the reactor.

### 3.6.2 Oxidation of Cyclohexanone

Control studies were conducted in order to determine if molecular oxygen had the ability to oxidize cyclohexanone in the absence of the TS-1 catalyst to produce adipic acid, and also to understand the effect of the TFA promoter on the extent of reaction. Results obtained from the control studies are listed in Table 3-1. It is noted that adipic acid was not produced from cyclohexanone in the presence of molecular oxygen without the TS-1 catalyst, which confirms that molecular oxygen does not have the ability to oxidize cyclohexanone without TS-1. The control studies also indicated that TFA was necessary for any adipic acid to be produced from the oxidation of cyclohexanone by molecular oxygen, since adipic acid was not formed unless both the TS-1 catalyst and the TFA promoter were present in the reactor. Therefore, all studies for the oxidation of cyclohexanone by in-situ generated  $\text{H}_2\text{O}_2$  were conducted with the inclusion of the TFA as a promoter.

Once it was established that the TS-1 material had the ability to catalyze the oxidation of cyclohexanone to form adipic acid with the inclusion of the TFA promoter, studies were conducted in order to measure the production of adipic acid using in-situ generated  $\text{H}_2\text{O}_2$  as the oxidant. A bifunctional catalyst was required in order to examine the in-situ generation of  $\text{H}_2\text{O}_2$  and subsequent oxidation of cyclohexanone.  $\text{H}_2\text{O}_2$  was formed at the supported Pd sites in the catalyst, and the oxidation occurred at the Ti sites in the support. The effect that both the TFA promoter and  $\text{H}_2\text{O}$  had on production of adipic acid via oxidation of cyclohexanone by in-situ generated  $\text{H}_2\text{O}_2$  is shown in Table 3-2.

Catalyst	TFA (mmol)	% Yield						
								Other by-products
None	0	0	0.02	2.01	0	0.07	0	0
None	0.673	1.65	1.43	36.73	0.39	0.74	17.86	18.22
TS-1	0	0	0	30.52	0.02	0.06	0	0.63
TS-1	0.673	1.27	1.28	47.71	0.25	0.69	7.22	10

**Table 3-1.** Control studies for the batch production of adipic acid via the oxidation of cyclohexanone by molecular oxygen. Reactants included cyclohexanone (2.89 mmol), H<sub>2</sub>O (2.78mmol), and O<sub>2</sub>:cyclohexanone ratio = 14:1. No H<sub>2</sub> was present in the reaction system. Reaction conditions included a temperature and pressure of 70°C and 1650psi, respectively. 0.0625 grams of TS-1 catalyst was used in each control experiment, and the system was monitored for 10 hours.

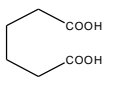
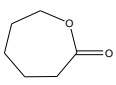
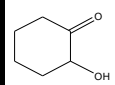
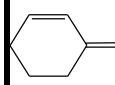
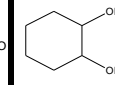
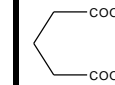
This set of experiments demonstrated that  $\text{H}_2\text{O}_2$  was superior to molecular oxygen as an oxidizing agent for this reaction. Only a 1.27 % yield of adipic acid was obtained with oxidation by molecular oxygen; whereas, the yield improved by almost an order of magnitude from 1.27% to 8.94 % in the case of oxidation by  $\text{H}_2\text{O}_2$ . It should be noted that the addition of the TFA promoter to the reaction mixture significantly enhanced the yield of adipic acid from a 2.26 % yield to an 8.94 % yield. It is proposed that this increase in product yield was due to the formation of a TFA peroxide complex, which stabilizes the in-situ formed  $\text{H}_2\text{O}_2$  (Kirillova, 2009). The highest yield of adipic acid was obtained when both the TFA promoter and  $\text{H}_2\text{O}$  were included in the reaction mixture. Unfortunately, many undesired reaction products were formed during this direct oxidation route to adipic acid, and the by-products were produced in greater weight fraction than adipic acid. Additional experiments were conducted in order to optimize and improve the reaction selectivity to adipic acid during the oxidation of cyclohexanone by  $\text{H}_2\text{O}_2$ .

Figure 3-2 illustrates the effect that the  $\text{O}_2:\text{H}_2$  ratio had on the product yield. This set of experiments also demonstrated that  $\text{H}_2\text{O}_2$  was more effective than molecular oxygen as the oxidant in the production of adipic acid from cyclohexanone, which supports the initial studies described above. The yield of adipic acid improved from 1.89% to 2.45% when in-situ generated  $\text{H}_2\text{O}_2$  was used as the oxidant over molecular oxygen. It is noted that a maximum yield of 10.66% adipic acid was achieved when the  $\text{O}_2:\text{H}_2$  ratio was increased from 1:1 to 4:1. In addition, the effect of the  $\text{O}_2$ :cyclohexanone ratio on the product yield was also examined. In this particular study, the  $\text{O}_2$ :cyclohexanone ratio was varied from 3.5:1 to 14:1, and the yields obtained for adipic

acid were 1.89% and 1.65%, respectively. It was determined that the O<sub>2</sub>:cyclohexanone ratio did not have a significant effect on the production of adipic acid for the ratios studied.

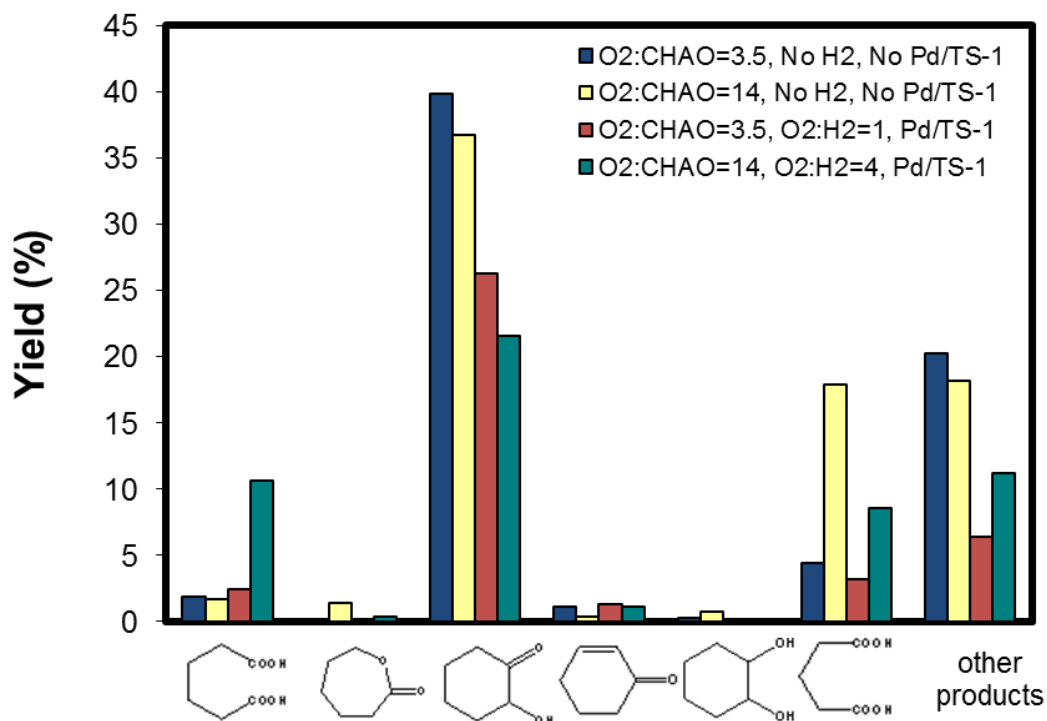
The effect that the H<sub>2</sub>:cyclohexanone ratio had on adipic acid production from cyclohexanone is shown in Figure 3-3. After varying the H<sub>2</sub>:cyclohexanone ratio from 1:1 to 3.5:1, it was determined that the optimal ratio for generation of adipic acid was 3.5:1. A maximum yield of 10.54% adipic acid was obtained with a H<sub>2</sub>:cyclohexanone ratio of 3.5:1. Even so, there is still significant by-product formation during the oxidation of cyclohexanone over the TS-1-supported Pd catalyst.

Figure 3-4 shows the effect of reaction pressure on the production of adipic acid. The two reaction pressures examined in this study were 114 bar and 141 bar. The yield doubles from 5.26 % to 10.54 % when the pressure was reduced to 114 bar from 141 bar. Thus, a lower reaction pressure is favored to produce adipic acid from cyclohexanone via in-situ generated H<sub>2</sub>O<sub>2</sub> over a Pd/TS-1 catalyst. Again, extensive by-product formation is noted for this reaction.

TFA (mmol)	H <sub>2</sub> O (mmol)	% Yield						Other by-products
								
0	0	2.26	0.37	33.12	0.43	0.10	3.42	5.46
0	2.78	2.08	0.55	58.67	0.47	0.17	2.70	3.7
0.673	0	8.94	0.43	25.56	1.08	0.17	8.59	8.02
0.673	2.78	10.66	0.34	21.54	1.12	0.17	8.59	11.2

**Table 3-2.** Oxidation of cyclohexanone over a Pd/TS-1 catalyst using in-situ generated H<sub>2</sub>O<sub>2</sub> as the oxidant. Reactants included cyclohexanone (2.89 mmol), a H<sub>2</sub>:cyclohexanone ratio = 3.5:1, and a O<sub>2</sub>:cyclohexanone ratio = 14:1. Reaction conditions included a temperature and pressure of 70°C and 1650psi, respectively. 0.0625 grams of Pd/TS-1 catalyst was used in each control experiment, and the system was monitored for 10 hours.





**Figure 3-2.** Effect of O<sub>2</sub>:H<sub>2</sub> ratio on the direct oxidation of cyclohexanone by H<sub>2</sub>O<sub>2</sub> to produce adipic acid. Reactants included cyclohexanone (2.89 mmol), H<sub>2</sub>O (2.78 mmol), and TFA (0.673 mmol). Reaction conditions included a temperature and pressure of 70°C and 1650psi, respectively. 0.0625 grams of Pd/TS-1 catalyst was used in each control experiment, and the system was monitored for 10 hours.

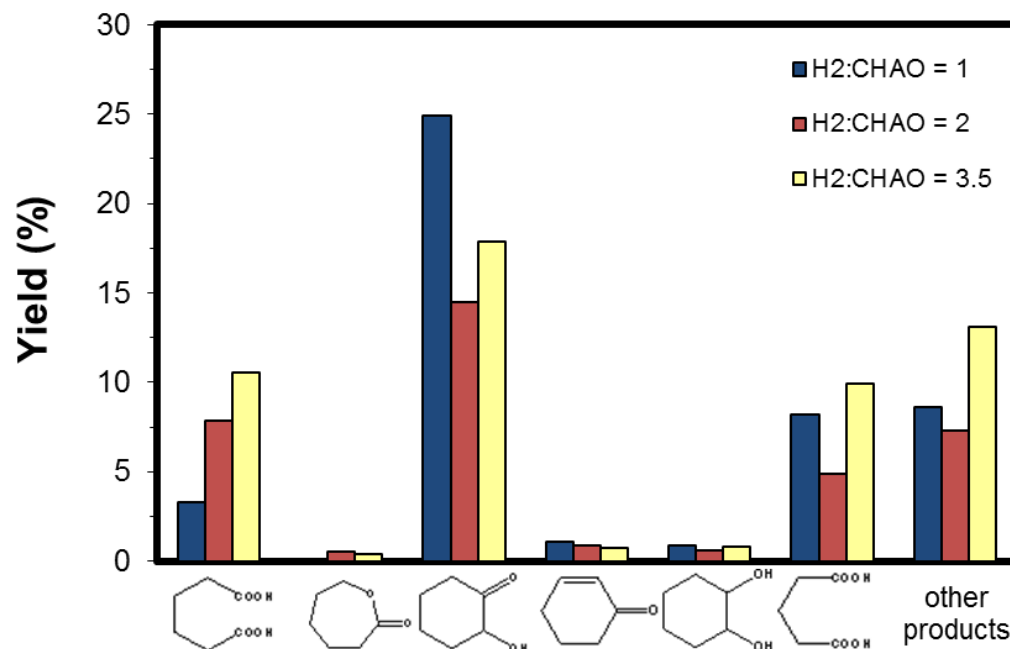


**Figure 3-3.** Effect of H<sub>2</sub>:cyclohexanone ratio on the direct oxidation of cyclohexanone by H<sub>2</sub>O<sub>2</sub> to produce adipic acid. Reactants included cyclohexanone (2.89 mmol), H<sub>2</sub>O (2.78 mmol), and TFA (0.673 mmol). Reaction conditions included a temperature and pressure of 70°C and 1650psi, respectively. 0.0625 grams of Pd/TS-1 catalyst was used in each experiment, and the system was monitored for 10 hours.

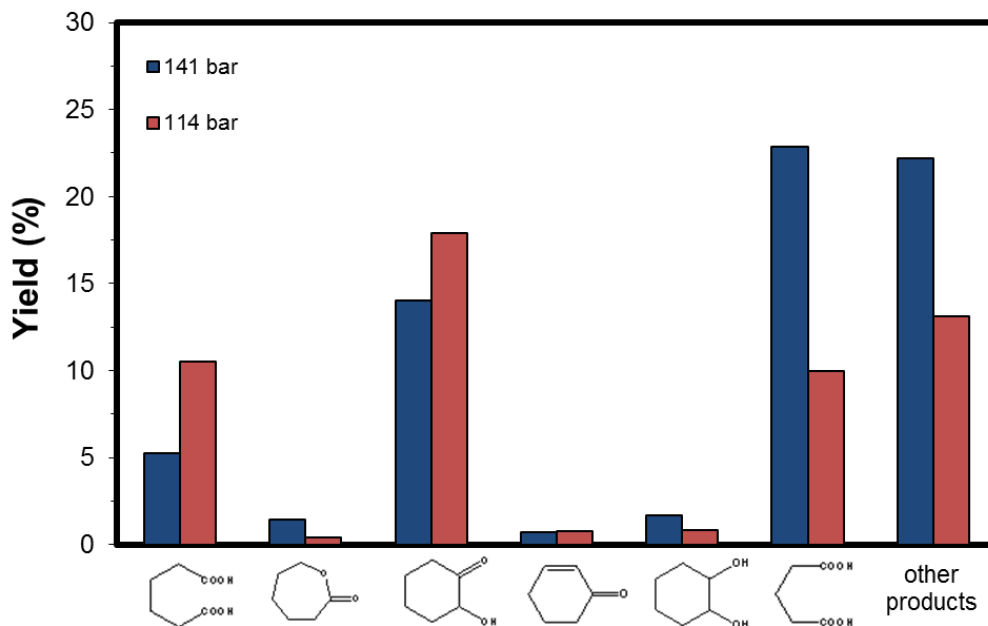


**Figure 3-4.** Effect of reaction pressure on the direct oxidation of cyclohexanone by  $\text{H}_2\text{O}_2$  to produce adipic acid. Reactants included cyclohexanone (2.89 mmol),  $\text{H}_2\text{O}$  (2.78 mmol), and TFA (0.673 mmol). The  $\text{H}_2$ :cyclohexanone ratio = 3.5 and  $\text{O}_2$ : $\text{H}_2$  ratio = 4 were kept constant between experiments. Reaction conditions included a temperature of  $90^\circ\text{C}$ . 0.0625 grams of Pd/TS-1 catalyst was used in each experiment, and the system was monitored for 10 hours.

### 3.6.3 Oxidation of Pyridine

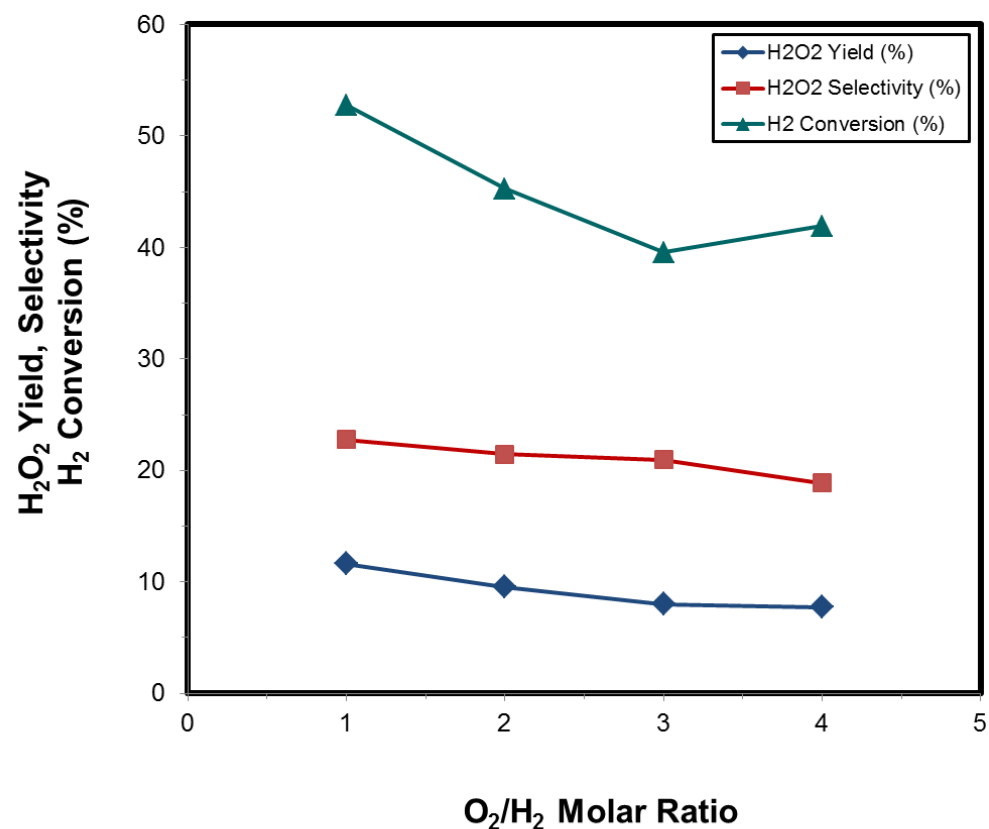
The oxidation of pyridine using  $\text{H}_2\text{O}_2$  to produce pyridine oxide was selected as a probe reaction for the in-situ generation of  $\text{H}_2\text{O}_2$  directly from  $\text{H}_2$  and  $\text{O}_2$ . The  $\text{H}_2\text{O}_2$  yield obtained from the initial experiments in this study approached nearly 31.7 % with a  $\text{H}_2\text{O}_2$  selectivity of almost 56.1 %. It should also be noted that no product other than pyridine oxide was detected, which makes pyridine an excellent probe molecule for the detection of  $\text{H}_2\text{O}_2$ . The  $\text{O}_2/\text{H}_2$  molar ratio,  $\text{H}_2$  concentration, and the catalyst mass and composition were all examined in order to determine their effect on not only the  $\text{H}_2$  conversion, but also the  $\text{H}_2\text{O}_2$  selectivity and yield. Figure 3-5 shows the effect that the  $\text{O}_2/\text{H}_2$  molar ratio had on this particular reaction. This study indicated that employing an  $\text{O}_2:\text{H}_2$  molar ratio of 1:1 provided the best overall conversion, selectivity, and yield in the direct synthesis of  $\text{H}_2\text{O}_2$  directly from  $\text{H}_2$  and  $\text{O}_2$ . As this ratio was increased, the  $\text{H}_2$  conversion along with the  $\text{H}_2\text{O}_2$  selectivity and yield all decreased. This behavior is not understood, but the results are consistent with those obtained by Chinta and Lunsford (2004) and Hwang et al. (2002). Subsequent studies were conducted at the optimal molar ratio of 1:1; thereby, producing the most  $\text{H}_2\text{O}_2$  from available reactants.

The effect of  $\text{H}_2$  concentration on  $\text{H}_2$  conversion,  $\text{H}_2\text{O}_2$  selectivity, and  $\text{H}_2\text{O}_2$  yield is shown in Figure 3-6. The conversion, selectivity, and yield all increase with increasing  $\text{H}_2$  concentration until reaching a maximum at 500mM of  $\text{H}_2$ . At 500 mM of  $\text{H}_2$ , the selectivity and yield begin a steady decline while conversion remains fairly constant. Chen and Beckman (2007) have proposed that the hydrogenation of the in-situ generated  $\text{H}_2\text{O}_2$  becomes a dominant reaction in the presence of increased levels of  $\text{H}_2$ . The hydrogenation of  $\text{H}_2\text{O}_2$  accounts for the decrease in both selectivity and yield that occurs

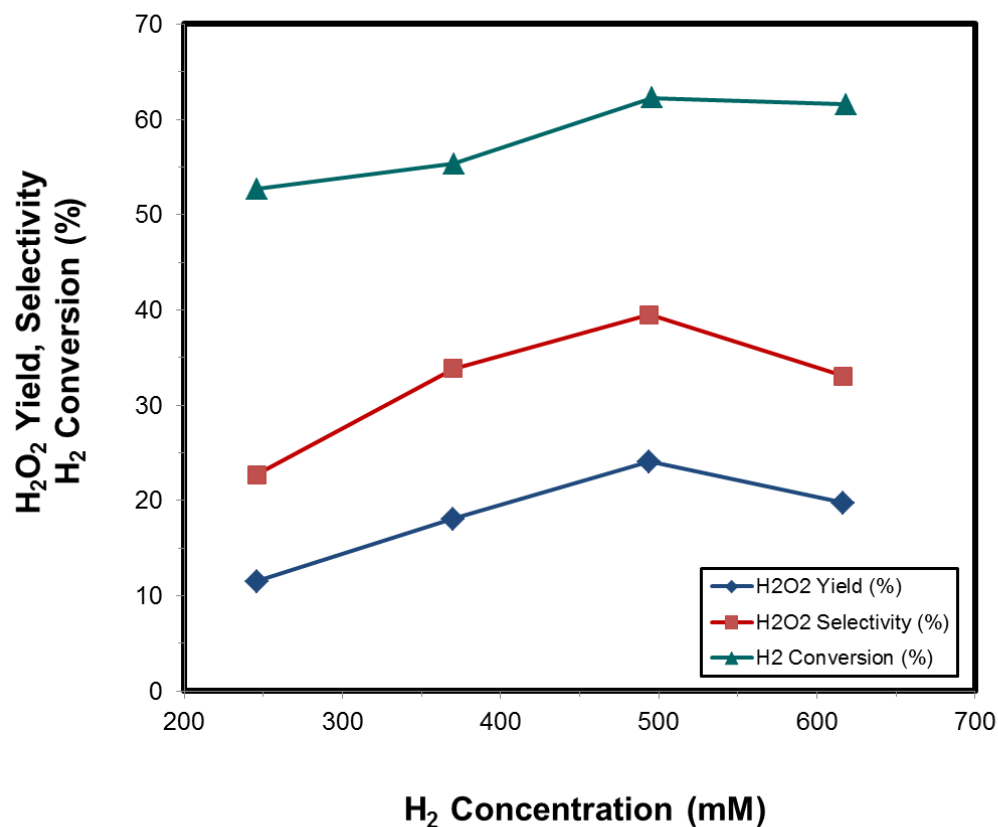
despite the relatively constant conversion of H<sub>2</sub>. The optimum H<sub>2</sub> concentration for the in-situ generation of H<sub>2</sub>O<sub>2</sub> is approximately 500mM.

Figure 3-7 illustrates the effect that catalyst mass had on the direct in-situ generation of H<sub>2</sub>O<sub>2</sub> from H<sub>2</sub> and O<sub>2</sub>. It is noted that H<sub>2</sub> conversion, H<sub>2</sub>O<sub>2</sub> selectivity, and H<sub>2</sub>O<sub>2</sub> yield all increased with increasing catalyst mass, initially. The conversion of H<sub>2</sub> continued to increase with increasing catalyst mass while the H<sub>2</sub>O<sub>2</sub> yield remained fairly constant. However, the H<sub>2</sub>O<sub>2</sub> selectivity slowly diminished with increasing catalyst mass. Chen and Beckman (2007) attribute the dramatic rise in H<sub>2</sub> conversion to the hydrogenation of the in-situ generated H<sub>2</sub>O<sub>2</sub>, which is a consequence of using larger quantities of catalyst. Hydrogen must be available for both the synthesis and hydrogenation of H<sub>2</sub>O<sub>2</sub>, which explains why the selectivity steadily dropped off while the conversion continued to increase.

The last study that was conducted examined the effect of metal loading on the catalyst activity. The results from these studies are shown in Figure 3-8. A survey of current literature indicates that higher metal loadings promote the rapid decomposition of in-situ generated H<sub>2</sub>O<sub>2</sub> (Choudhary *et al.*, 2007). These studies confirm this postulate. Both selectivity and yield decreased with higher Pd loadings on the TS-1 support while conversion gradually increased. At higher Pd loadings, the metal on the support catalyzed the decomposition pathways for H<sub>2</sub>O<sub>2</sub>; hence, the lowered selectivity and yield for H<sub>2</sub>O<sub>2</sub>. Also, there was an increased demand for H<sub>2</sub> during the decomposition of H<sub>2</sub>O<sub>2</sub>—which explains the rise in conversion despite the lowered selectivity and yield. Decomposition studies were conducted to verify this claim.



**Figure 3-5.** Effect of O<sub>2</sub>/H<sub>2</sub> molar ratio on the in-situ generation of H<sub>2</sub>O<sub>2</sub> directly from H<sub>2</sub> and O<sub>2</sub>. Reactants included H<sub>2</sub> (6.2mmol), pyridine (6.2mmol), and H<sub>2</sub>O (27.8mmol). Reaction conditions included a temperature and pressure of 60°C and 1800 psi, respectively. 0.05 grams of 0.35 wt% Pd/TS-1 catalyst was used in each experiment, and the system was monitored for 5 hours.



**Figure 3-6.** Effect of H<sub>2</sub> concentration on the in-situ generation of H<sub>2</sub>O<sub>2</sub> directly from H<sub>2</sub> and O<sub>2</sub>. Reactants included pyridine (6.2mmol), H<sub>2</sub>O (27.8mmol), and an O<sub>2</sub>:H<sub>2</sub> ratio = 1. Reaction conditions included a temperature and pressure of 60°C and 1800 psi, respectively. 0.05 grams of 0.35 wt% Pd/TS-1 catalyst was used in each experiment, and the system was monitored for 5 hours.

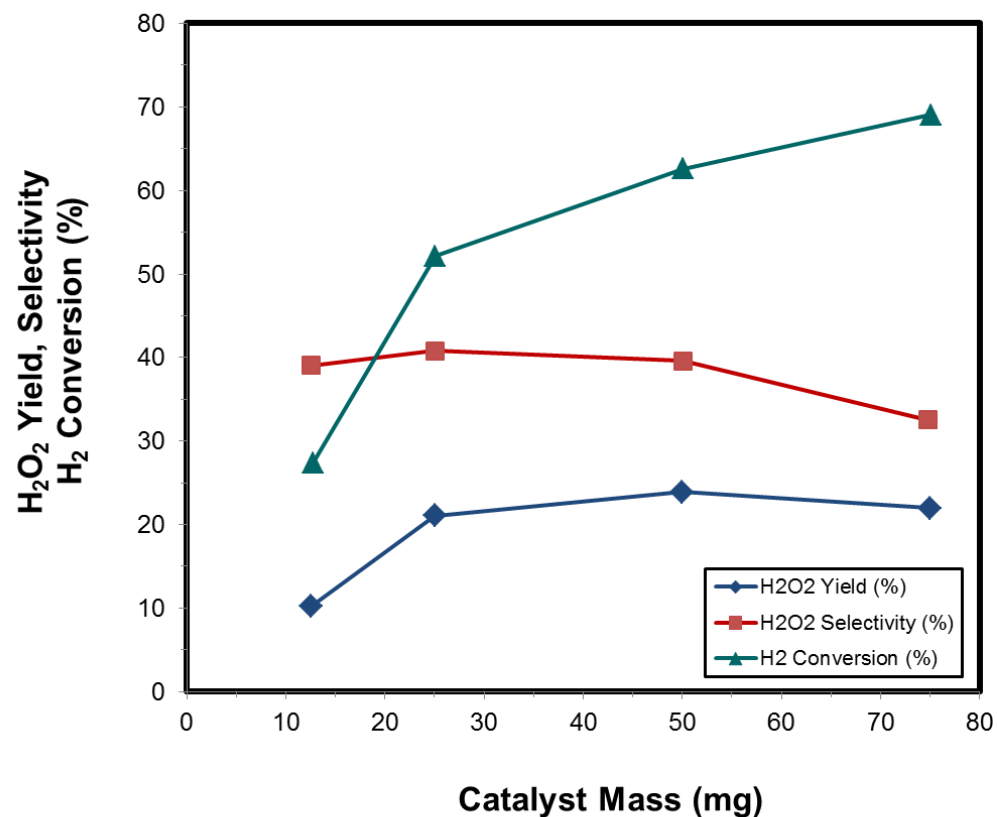


**Figure 3-7.** Effect of catalyst mass on the in-situ generation of H<sub>2</sub>O<sub>2</sub> directly from H<sub>2</sub> and O<sub>2</sub>. Reactants included H<sub>2</sub> (12.4mmol), pyridine (6.2mmol), H<sub>2</sub>O (27.8mmol), and an O<sub>2</sub>:H<sub>2</sub> ratio = 1. Reaction conditions included a temperature and pressure of 60°C and 1800 psi, respectively. 0.05 grams of 0.35 wt% Pd/TS-1 catalyst was used in each experiment, and the system was monitored for 5 hours.



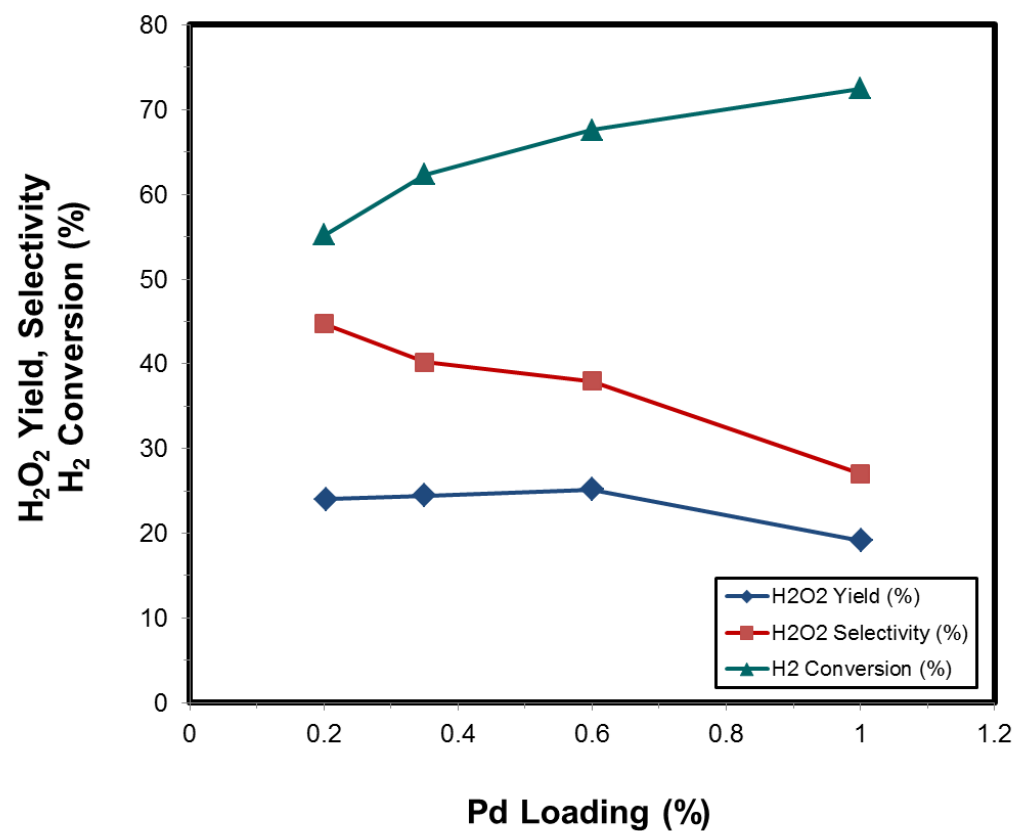


**Figure 3-8.** Effect of metal loading on the in-situ generation of H<sub>2</sub>O<sub>2</sub> directly from H<sub>2</sub> and O<sub>2</sub>. Reactants included H<sub>2</sub> (12.4mmol), pyridine (6.2mmol), H<sub>2</sub>O (27.8mmol), and an O<sub>2</sub>:H<sub>2</sub> ratio = 1. Reaction conditions included a temperature and pressure of 60°C and 1800 psi, respectively. 0.05 grams of 0.35 wt% Pd/TS-1 catalyst was used in each experiment, and the system was monitored for 5 hours.

### 3.6.4 Simulation and Optimization of Pyridine Oxide Production

Experimental data were collected on the performance, i.e. yield, conversion and selectivity, of the pyridine oxidation reaction along with analysis of the product distributions. This data served as the basis for the development of rigorous process simulation models used to analyze the potential of the green supercritical phase (SCF) process and compare it to the traditional AQ process (Bacik *et al.*, 2011). Proven PSE tools for mass and energy integration were employed to optimize the processes and provide targets for further experimental efforts. The environmental impact of the processes was evaluated using the US-EPA Waste Reduction (WAR) algorithm (Young *et al.*, 2000). The design objective was to produce 100,000 tpa H<sub>2</sub>O<sub>2</sub> for converting pyridine into pyridine oxide.

#### Anthraquinone (AQ) Process

Using data provided by Hess (1995), a model of the traditional hydrogen peroxide production process was developed and combined with an additional reactor to represent the pyridine oxidation step. A schematic of the process is provided in Figure 3-9, where the solvent consists of 75 vol% t-butyl benzene and 25 vol% trioctyl phosphate. The concentration of AQ in the working solution is 10 g/liter. The extent of hydrogenation of AQ to AHQ is limited to 60% to minimize secondary reactions, while the oxidation reaction to regenerate AQ has near 100% conversion (Fierro *et al.*, 2006). After extraction with water, the aqueous H<sub>2</sub>O<sub>2</sub> product is distilled to 35 weight% and sent to the pyridine oxidation reactor.

### **Supercritical Phase (SCF) Process**

Using experimental data collected as part of this work, a model of the traditional hydrogen peroxide production process was developed to investigate the large scale potential of the in-situ generation of H<sub>2</sub>O<sub>2</sub> in supercritical CO<sub>2</sub>. A schematic of the process is provided in Figure 3-10, where it should be noted that the hydrogen and oxygen streams are actually diluted with CO<sub>2</sub> for safety reasons and additional CO<sub>2</sub> is added separately to create the dense reaction media. The hydrogen conversion was measured to be 56.4% with a H<sub>2</sub>O<sub>2</sub> selectivity of 62.5%. The peroxide product immediately reacts with pyridine to form pyridine oxide, thus eliminating the need for additional purification of H<sub>2</sub>O<sub>2</sub>. Unreacted raw materials are recycled along with the CO<sub>2</sub> solvent, while the pyridine oxide is recovered in aqueous solution.

### **Results and Analysis of Simulation and Optimization of Pyridine Oxide Production**

Once the base case models had been developed and all material recycles implemented, thermal pinch analyses were performed to minimize the energy usage. The results of these analyses are shown in Table 3-3 below. It should be noted that the reactor duties were not included in the analysis as it is desirable to control the reactor conditions using external utilities to avoid any negative impact of upsets in other parts of the process. Furthermore, as a result of the larger number of processing steps, the AQ process has many more opportunities for heat integration and thus the relative reductions in energy requirements are much larger. Cooling water is much cheaper than steam and as such the

cost of the larger cooling requirement in the SCF process is easily compensated for by the steam usage being reduced to 27% compared to the AQ process.

The environmental impact of both process options was also evaluated and the results are presented in Figure 3-11. It should be emphasized that the results for the AQ process represent a best case scenario with minimal solvent losses and secondary reactions. Even minor inefficiencies in the separation steps will increase the environmental impact drastically and further widen the performance gap in favor of the SCF process. Since the basic raw materials (hydrogen and oxygen) are the same for both processes the results in Figure 3-11 illustrate the differences in the energy consumption, which currently is primarily derived from coal-fired power plants. Additionally, the environmental impact stemming from the production of the anthraquinone working solution should also be taken into account in order to make a fair comparison. In summary, the results show that it is possible to efficiently couple the in-situ  $H_2O_2$  generation with another oxidation reaction and achieve substantial benefits in terms of both energy consumption and reduced environmental impact.

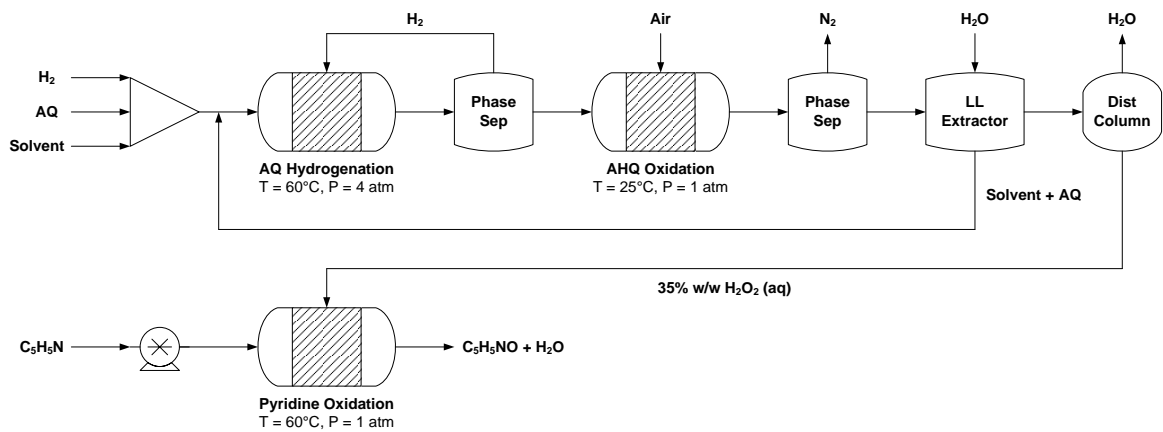


**Figure 3-9.** Oxidation of pyridine using hydrogen peroxide from the anthraquinone process.

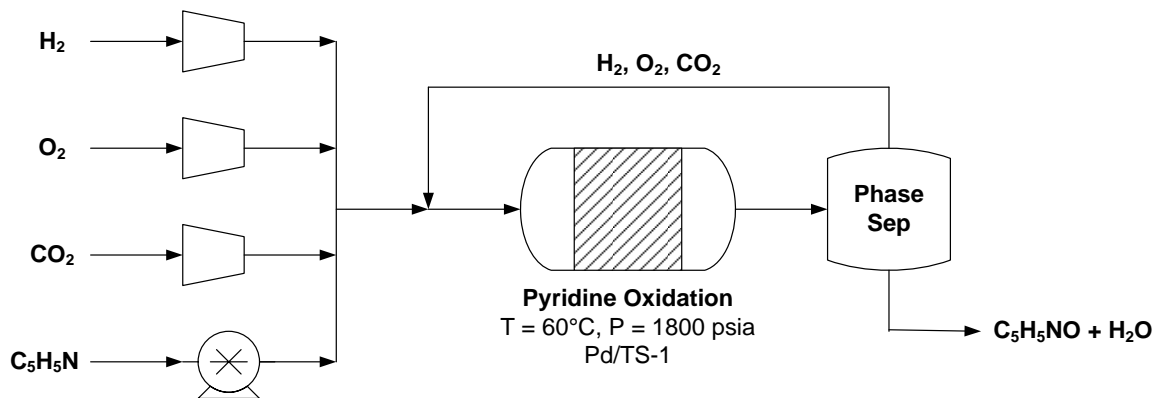


**Figure 3-10.** Oxidation of pyridine using in-situ generated hydrogen peroxide.

Option	Utility Requirements		Base Case	After Heat Integration	
AQ Process	Total (GJ/hr)	Heating	64.6	17.1	(-73.5%)
	Total (GJ/hr)	Cooling	68.5	21.0	(-69.3%)
SCF Process	Total (GJ/hr)	Heating	5.7	4.7	(-17.5%)
	Total (GJ/hr)	Cooling	54.0	53.0	(-1.8%)

**Table 3-3.** Energy Analysis for Pyridine Oxidation Processes.

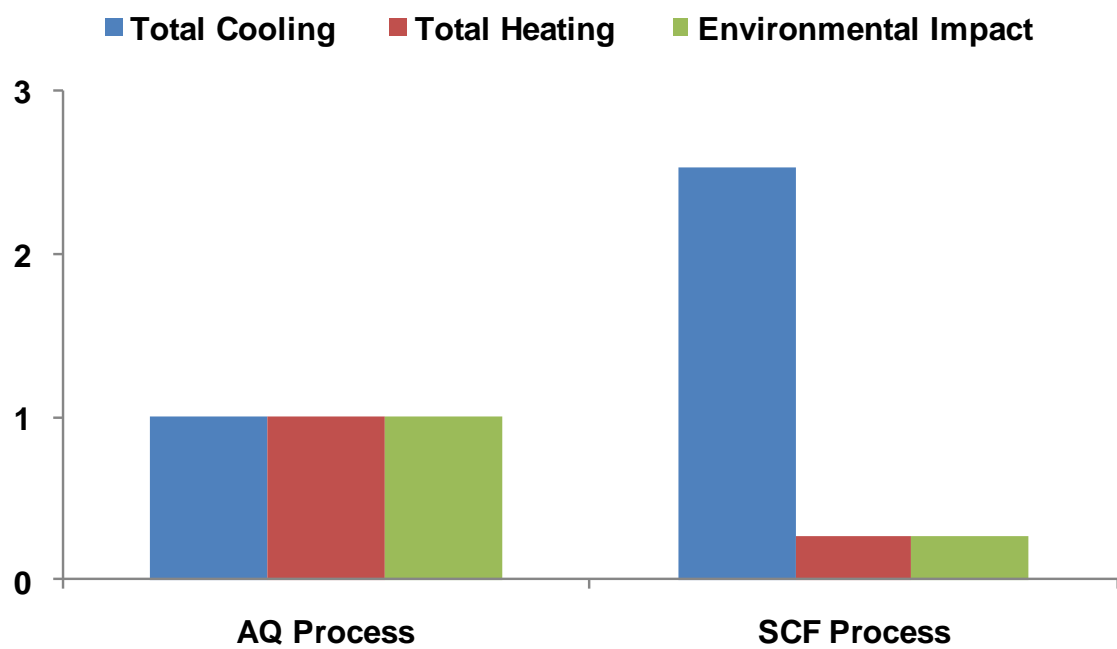


**Figure 3-11.** Performance comparison for pyridine oxide production.



### 3.7 Conclusions

A system was designed in order to investigate the in-situ generation of  $\text{H}_2\text{O}_2$  in supercritical  $\text{CO}_2$  solvent media. It is particularly difficult to accurately measure  $\text{H}_2\text{O}_2$  production in the direct route from hydrogen and oxygen. Therefore, a few probe reactions including propylene epoxidation, cyclohexanone oxidation, and pyridine oxidation were performed in order to capture the generated  $\text{H}_2\text{O}_2$  before underwent decomposition. A Pd/TS-1 catalyst was used in all reactions studied, since it has shown some promise in promoting the direct generation of  $\text{H}_2\text{O}_2$  from hydrogen and oxygen.

In the case of propylene epoxidation, low conversions of propylene were detected. However, propylene was not converted to propylene oxide--the desired product. This reaction was plagued by extensive by-product formation. It was determined that the loading procedure for the reactant gases had a significant effect on the in-situ generation of  $\text{H}_2\text{O}_2$  and subsequent oxidation of propylene to propylene oxide. Also, it was identified that the Pd metal loading on our TS-1 support was much too high. At approximately 0.5 wt% Pd/TS-1, the catalyst not only promotes the degradation of formed  $\text{H}_2\text{O}_2$ , but also inhibits its synthesis. In addition, too much time was allowed between feeding reactant gases into the reactor. Thus, the in-situ generated  $\text{H}_2\text{O}_2$  decomposes before propylene is available for reaction. Hydrogen peroxide is a very unstable molecule, so a reactor passivation methodology should be employed in order to prevent the decomposition of  $\text{H}_2\text{O}_2$  upon contact with the stainless steel reactor walls.

The acidic reaction environment promotes the undesired side-reactions that occur, so an inhibitor molecule should be introduced to suppress these reaction pathways. Also, more selective catalysts for this reaction should be examined.

There was limited success in oxidizing cyclohexanone over a Pd/TS-1 catalyst to adipic acid. It was determined that the ratio of  $O_2:H_2$  and  $H_2:CHAO$  both had an effect on the yield of adipic acid under the reaction conditions studied. Also, the inclusion of TFA and  $H_2O$  promoted the generation of adipic acid through formation of a TFA-peroxide complex. Even so, extensive by-product formation occurred when using this particular catalyst. A diffusional transport limitation exists for this particular reaction over the TS-1 catalyst. The pores of the TS-1 catalyst are too narrow for effective oxidation of the bulky cyclohexanone molecule. Therefore, catalysts having larger pore sizes should be explored for this reaction. Also, more selective catalysts for this reaction should be studied. Also, in order to make this a commercially viable process, a method should be developed so as to inhibit the main side-reactions that occur.

Pyridine was used as a tool to measure the in-situ production of  $H_2O_2$ , and for optimization of reaction conditions. It was determined that the ratio of  $O_2:H_2$ ,  $H_2$  concentration, and catalyst mass all had an effect on the  $H_2$  conversion and both selectivity and yield to  $H_2O_2$ . Also, the metal loading had an effect on the catalyst activity. The studies performed conclusively determined that the optimal molar ratio for  $O_2:H_2$  was 1. As for  $H_2$  concentration, a maximum occurred around 500 mM of  $H_2$  for conversion, selectivity, and yield. At higher concentrations of  $H_2$ , hydrogenation of the in-situ generated  $H_2O_2$  becomes the chief reaction. Conversion, selectivity, and yield all initially increase with increasing catalyst mass. However, as the catalyst mass continues

to increase both selectivity and yield decrease. The H<sub>2</sub> conversion continues to increase, which is a result of the hydrogenation of H<sub>2</sub>O<sub>2</sub> that occurs with the use of larger quantities of catalyst. Both selectivity and yield decrease with higher Pd loadings on the TS-1 support while conversion gradually increases.

The large scale potential for in-situ production of hydrogen peroxide in supercritical CO<sub>2</sub> has been studied. Experimental data for the oxidation of pyridine oxide has been used to develop a process model that was used to compare the performance of this direct synthesis method with the industrial standard anthraquinone autoxidation process. The results show that it is possible to efficiently couple the in-situ H<sub>2</sub>O<sub>2</sub> generation with another oxidation reaction and achieve substantial benefits in terms of both energy consumption and reduced environmental impact.

## Chapter 4

### UNDERSTANDING THE PHASE BEHAVIOR AND CRITICAL POINT MEASUREMENTS FOR FISCHER-TROPSCH SYNTHESIS IN SUPERCRITICAL HEXANE SOLVENT MEDIA

#### 4.1 Introduction

C<sub>1</sub> chemistry is an area of development that utilizes molecules containing a single carbon atom not only for the synthesis of many valuable organic chemicals and intermediates, but also as an alternative feedstock in the production of fuels. Compounds such as methane, methanol, carbon monoxide, carbon monoxide/hydrogen, carbon dioxide, and hydrogen cyanide have all been used as building blocks in this technology (Keim, 1983). These C<sub>1</sub> molecules can be obtained from resources such as biomass, coal, and natural gas. The primary focus in C<sub>1</sub> chemistry has been on carbon monoxide and its catalytic conversion to hydrocarbons and hydrocarbon intermediates.

Fischer-Tropsch synthesis is an alternative process that was developed in Germany during the 1920s for the catalytic conversion of syngas (a mixture of CO and H<sub>2</sub>) to transportation fuels and other value-added chemicals (Stranges, 2007). Currently, the principal route for producing fuels and other chemicals is through petroleum resources. The Energy Information Administration predicts an almost 50% increase in

world energy consumption by the year 2030 (EIA, 2008). However, given the rising cost and finite supply of petroleum, it would be beneficial to explore other methods in fuel production. Syngas can be derived from a variety of resources including coal, natural gas, and biomass. Biomass is an excellent option, since it is both a renewable and sustainable source of energy. The seventh principle in the twelve principles of green chemistry states that, “A raw material or feedstock should be renewable rather than depleting wherever technically and economically practicable” (Anastas and Warner, 1998). Thus, employing Fischer-Tropsch synthesis with biomass-derived syngas is an excellent and “green” alternative for the petrochemical industry.

Conducting Fischer-Tropsch synthesis (FTS) under supercritical fluid solvent conditions affords unique opportunities to manipulate the Fischer-Tropsch reaction environment to enhance production of liquid fuels and value-added chemicals (such as  $\alpha$ -olefins) from synthesis gas or syngas (a mixture of H<sub>2</sub> and CO). Industrial gas-phase Fischer-Tropsch synthesis is accompanied by local overheating of the catalyst surface and high degrees of methane selectivity, thereby, decreasing the yield of the desired products (Kolbel and Ralek, 1980; Lang *et al.*, 1995). Furthermore, slurry phase Fischer-Tropsch reaction processes suffer from slow diffusion of syngas into the catalyst pores resulting in lower rates of reaction and other disadvantages (Geertesma, 1990). These considerations have driven our research in Fischer-Tropsch synthesis towards the application of supercritical fluid solvents in order to improve product control in the liquid fuels range.

Supercritical fluid solvents combine the desirable properties of gas-like diffusion along with liquid-like heat transfer and solubility to overcome several of the current

industrial limitations (Subramaniam, 2001). Fine adjustments in operating conditions near the critical point can result in superior control of the Fischer-Tropsch process including tunable product distributions (Bochniak and Subramaniam, 1998). Previous studies conducted in the Roberts Lab have shown that supercritical fluid Fischer-Tropsch provides several distinct advantages including: (1) in-situ extraction of heavy hydrocarbons from the catalyst; (2) enhancement of pore-transport and elimination of interphase transport limitations, thus, promoting reaction pathways to desired fuel range products; (3) enhanced desorption and selectivity of value added products ( $\alpha$ -olefins); (4) improved heat transfer resulting in more of the long chain products (Huang and Roberts, 2003; Huang *et al.*, 2004). As a result, the utilization of supercritical phase as a new technology for Fischer-Tropsch synthesis represents a promising new technique for this reaction that will provide a clean, economical and efficient means of producing sulfur free fuels and chemicals.

Very few studies have dealt with the phase behavior of the reaction mixture within supercritical phase FTS (Joyce *et al.*, 1999; Joyce *et al.*, 2000; Gao *et al.*, 2001; Polishuk *et al.*, 2004). Joyce and his coworkers (Joyce *et al.*, 1999) have studied the vapor-liquid composition for a mixture of hexane (supercritical solvent) and C<sub>16</sub> (FTS wax) at three different temperatures (199, 252, and 300 °C). Mixtures of hexadecane and hexadecene (C<sub>16</sub> hydrocarbons) were used in order to simulate the changes that occur in the phase behavior of hexane as the percentage of heavy hydrocarbons in the product stream increases. Their findings showed that for 0.0326 mole fraction of C<sub>16</sub> in a hexane/hexadecane mixture the critical pressure and temperature of the mixture increased to 33.76 bar and 252 °C, respectively. These results demonstrate a significant change in

the critical properties of the hexane solvent medium, since the critical pressure and temperature of pure hexane is 32.4 bar and 234.5 °C, respectively. In another study, Gao et al. (2001) reported critical points for mixtures of hexane (> 94 mole %) and reactants (CO and H<sub>2</sub>) at different mole ratios. They observed that the critical temperature and critical density of the solvent-reactant mixture decreased as the concentration of CO and H<sub>2</sub> increased, and the critical pressure increased with CO and H<sub>2</sub> concentration. More recently, Polishuk et al. (2004) compared the ability of two semi-predictive thermodynamic models, the global phase diagram approach (GPDA) and the predictive Soave–Redlich–Kwong (PSRK), in describing the experimental phase behavior of binary homologous series of n-alkanes that represent the FTS product spectrum. For a symmetric system of n-hexane/n-tetracosane (similar to a solvent-product mixture of the current study) they found that the GPDA accurately predicted the experimentally measured values of Joyce et al. (2000) over a wide range of temperatures, while PSRK significantly overestimates the bubble-point data.

The objective was to investigate the phase behavior of a Fischer-Tropsch reaction feed mixture at both sub-critical and supercritical conditions. An understanding of the phase behavior of mixtures at specified compositions is very useful in supercritical phase FTS. Knowledge of the critical properties for a particular system will allow for the appropriate design of chemical reactors, choice of separation and extraction equipment, and determination of the operating conditions. Our reaction solution included the reactants carbon monoxide (CO) and hydrogen (H<sub>2</sub>) and the solvent n-hexane, which form a mixture under specified reaction conditions (i.e. temperature and pressure). In this study the critical properties for three specific mole ratios (H<sub>2</sub>: CO: n-Hexane) were

determined. Correlations between the phase behavior of the supercritical Fischer-Tropsch mixtures and the catalytic performance studies under sub-critical and supercritical conditions were examined. This provides a more fundamental understanding of the underlying mechanisms of this reaction and may lead to improvements in the design and optimization of supercritical fluid Fischer-Tropsch technology.

## **4.2 Experimental Methods**

### **4.2.1 Materials**

Both n-pentane (99.0+%, Sigma Aldrich) and n-hexane (99.0+%, Sigma Aldrich) were used as received without further purification. Carbon monoxide/hydrogen (33.51%/balance certified standard, Airgas South) was used as received without further purification.

### **4.2.2 Apparatus**

Figure 4-1 shows the experimental apparatus used in the phase behavior studies for different Fischer-Tropsch reaction feed mixtures. The apparatus included a high-pressure stainless steel variable volume view cell (custom designed and manufactured in the Roberts Laboratory), high-pressure quartz window, appropriate o-rings, manual pressure generator (HIP, model 87-6-5), temperature controller (Omega, model CN77332), heating tape, insulation tape, pressure gauge (Dynisco, model PT422A), resistance temperature detector, metering pump (Eldex Laboratories, model B-100-S), vacuum



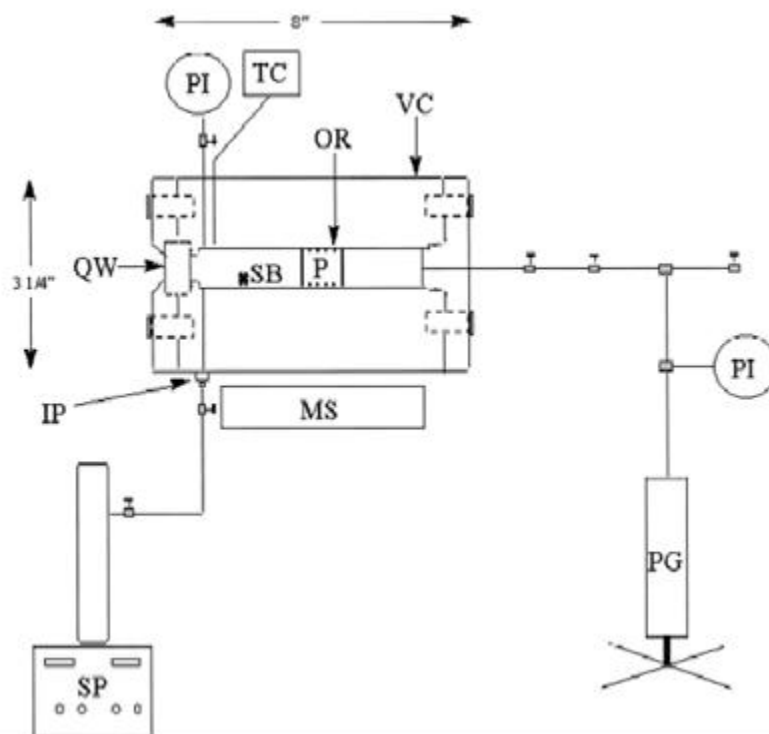


**Figure 4-1.** Phase behavior experimental apparatus including: IP, Injection Port; MS, Magnetic Stirring Plate ; OR, O-Ring; P, Piston; PG, Manual Pressure Generator; PI, Pressure Indicator; QW, High-Pressure Quartz Window; SB, Stirring Bar; MP, Metering Pump; TC, Thermocouple; VC, Variable Volume View Cell

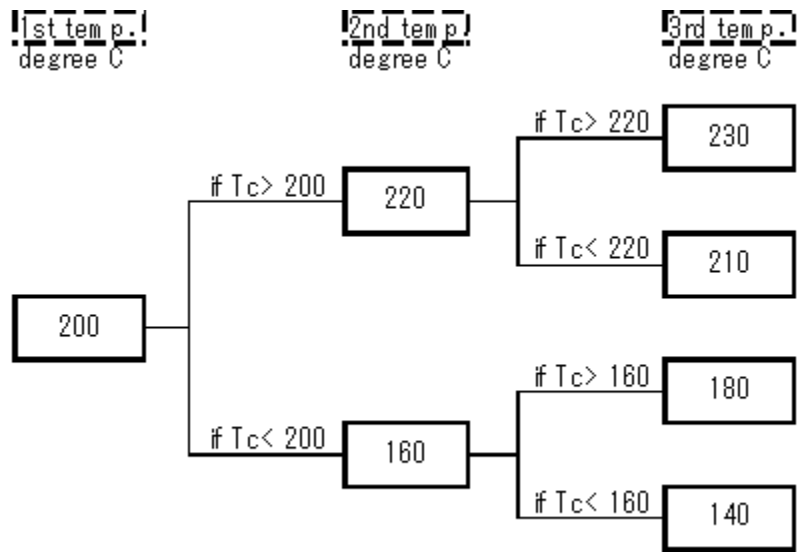
pump (Emerson, model CA55KXDJW-2137), stir bar, stir plate, and 1/16" stainless steel tubing.

### 4.2.3 Procedure

A systematic phase behavior study of a mixture comprised of CO and H<sub>2</sub> in hexane was carried out using a high-pressure variable-volume view cell under controlled temperature at three specific mole ratios. The three mole ratios (H<sub>2</sub>: CO: Hexane) studied were mixture 1 (2:1:9), mixture 2 (2:1:13), and mixture 3 (2:1:18). The method used in determining the critical temperature and critical pressure of the mixture for the three specified mole ratios is shown in the flow chart in Scheme 4-1.

The volume of the cell was adjusted by displacing the internal movable piston. The dynamic seal between the piston and the walls of the vessel was achieved using four Viton O-rings. The contents of the view cell were observed by shining a light source through the ½ in. thick high-pressure quartz window on the front of the view cell. A video camera was connected to a computer to both observe and record phase changes as they occurred inside the vessel. A manual pressure generator (High Pressure Equipment Model 87-6-5) was used to manipulate the pressure in the view cell. The temperature in the cell was measured and controlled with a RTD (Omega 1/16" diameter probe, Omega Engineering) and a self-tuning PID controller (Omega CN76030) wired to a magnetic contactor (Omega MC-2-2-40-120). The pressure was measured using a Dynisco flush mount transducer (model TPT-432A) with an accuracy of ±1.7 bars.

Initially, the view cell was purged several times with the CO/H<sub>2</sub> gas mixture in order to ensure that no air remained in the system. The amount of CO and H<sub>2</sub> to be



**Scheme 4-1.** Flow chart demonstrating the method used to determine the critical properties of H<sub>2</sub>, CO, and hexane mixtures at specified compositions.

delivered to the vessel, according to the specified ratio, was determined using the available volume in the vessel and an appropriate equation of state. Following addition of the gas mixture, a known amount of hexane was metered into the vessel using the metering pump. The view cell was heated to an initial temperature, and allowed to equilibrate. The initial temperature was estimated by considering the critical temperature of the pure component. Refer to Scheme 4-1. After heating, the pressure of the vessel was well above the pressure necessary to achieve a clear single phase. Thus, the pressure of the view cell was slowly reduced by backing out the piston until the onset of cloudiness was observed (the cloud point). The cloud point pressure was recorded as the pressure at which the reflection of the piston just disappeared. The temperature was then increased by a specific interval and the procedure repeated until the critical temperature was obtained for the mixture.

A video camera system was designed to take images of the phase transition between vapor-liquid equilibrium (VLE) and the supercritical phase. Use of this system allowed for an accurate determination of the critical points of pure hydrocarbon and gas mixtures. The video camera (QuickCam Pro 4000, 1.3 mega pixel) was mounted close to the glass window of the variable volume view cell. In order to ensure high quality of our images, a light (Eagle Economy Fluorescent Ring Light) was attached to the video camera. The video system was connected to a computer in order to collect and record both pictures and videos of the phase transitions.

The two phase vapor-liquid equilibrium is shown on Figure 4-10. The movable piston of the view cell was positioned in order to keep the liquid volume equal to the vapor volume in the system. The meniscus between the two phases is clearly seen in that

image. In order to accurately locate the critical point, the meniscus just below the critical point must be in the center of the vessel such that when the critical point is reached the density of the two phases must be equal. This corresponds to the critical point location. The temperature is then slightly increased and as a result the pressure is also increased until it reaches the critical point. At this point the meniscus has disappeared, and the contents are within the supercritical phase region. The phase transition is also shown in Figure 4-10; the meniscus disappeared at the critical transition point. This ramping procedure was followed for the determination of the critical properties of our reaction mixtures.

### **4.3 Results and Discussion**

The accuracy of the system was tested by measuring the pure component critical points for both n-pentane and n-hexane, then comparing these values to those reported in the literature. The critical point of n-pentane was systematically measured and achieved at a temperature of 196.2°C and a pressure of 35.0 bar; while, the literature values for critical temperature and pressure are 196.6°C and 33.6 bar, respectively. It is noted that the experimentally determined values are very similar to the accepted literature values for n-pentane. The experimental data collected for n-pentane is compared to the literature values and shown in Figure 4-2. This procedure was repeated in order to duplicate the critical point measurements.

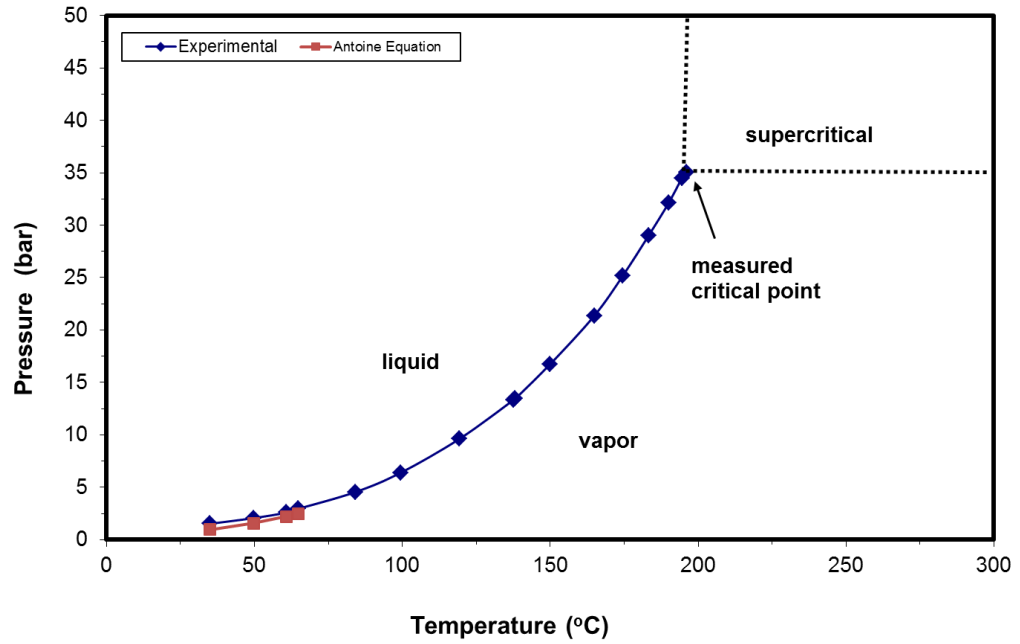


**Figure 4-2.** Experimentally determined vapor-liquid equilibrium data for pure n-pentane with a critical point at a temperature of 196.2 °C and a pressure of 35.0 bar. Comparison is made to the Antoine equation.

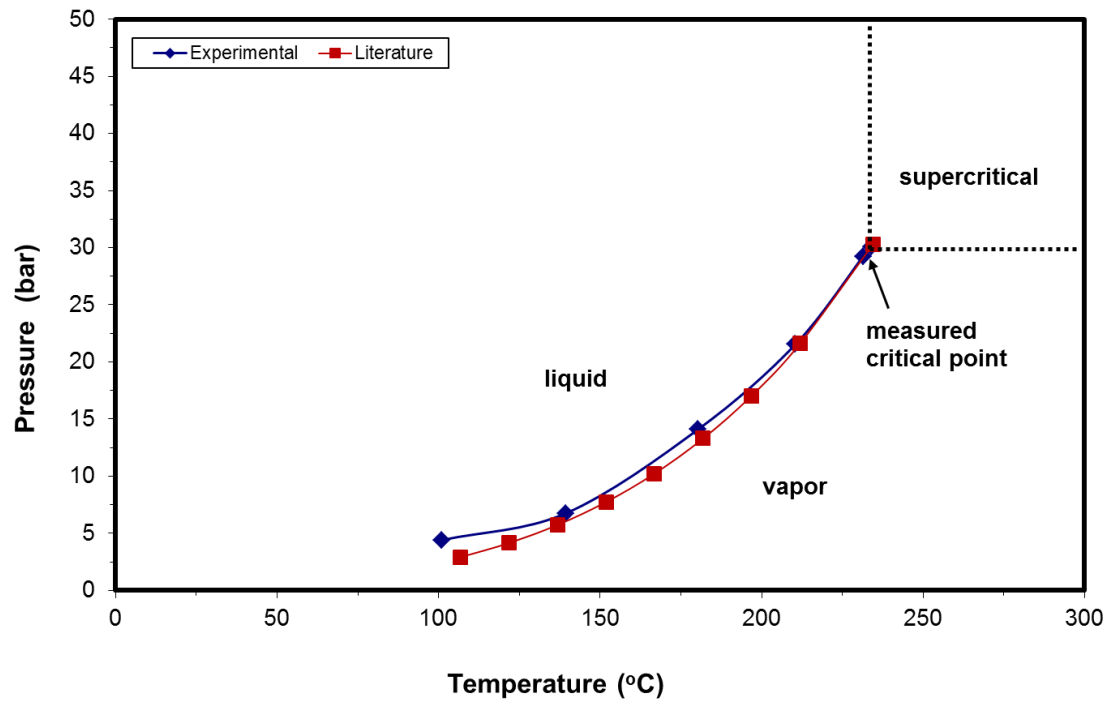


**Figure 4-3.** Experimentally determined vapor-liquid equilibrium data for pure n-hexane demonstrating a critical point at a temperature of 234.0 °C and a pressure of 30.0 bar. Comparison is made to literature values (NIST Chemistry WebBook).

To further test the system, the critical point of pure n-hexane was measured following the same experimental procedure used for n-pentane and then compared to values reported in the literature. Results for n-hexane are shown in Figure 4-3, illustrating how well the experimentally determined data agreed with critical values stated in literature. The critical point of n-hexane was systematically measured and achieved at a temperature of 234.0°C and a pressure of 30.0 bar; while, the literature values of the critical temperature and pressure for n-hexane are 234.4 °C 30.2 bar, respectively. This procedure was repeated in order to verify the accuracy of our measurements. Both sets of experiments confirmed that the system was operating appropriately and verified the accuracy of the experimental technique.

The phase behavior of mixtures of pure n-hexane, CO, and H<sub>2</sub> were studied at three separate molar compositions. The CO and H<sub>2</sub> were delivered in a constant two to one ratio, respectively, for each experiment. While, the ratio of n-hexane was varied in order to achieve the desired mixture ratio. The results of the phase behavior studies are listed in Table 4-1. It was determined that the critical temperature for each of the mixtures decreased as the mole fraction of the syngas was increased. However, the critical pressure for each of the mixtures increased as the mole fraction of the syngas was increased. The experimentally determined critical point data is plotted against mole fraction of syngas and shown in Figures 4-4 and 4-5. Reid et al. determined that the critical temperature of mixtures should decrease as the mole fraction of the lighter component increases (Reid *et al.*, 1987). Figure 4-6 illustrates this general trend for a methane/n-pentane system. In addition, the critical pressure for mixtures will go through a maximum then decrease as the mole fraction of the lighter component



---

<b>sample</b>	<b>CO:H<sub>2</sub>: hexane ratio</b>	<b>mole fraction syngas</b>	<b>T<sub>c</sub> (°C)</b>	<b>P<sub>c</sub> (bar)</b>
mixture 1	2:1:9	0.25	225.9	86.5
mixture 2	2:1:13	0.19	229.0	72.8
mixture 3	2:1:18	0.14	231.3	63.4

---

**Table 4-1.** Experimentally determined critical point data obtained from phase behavior studies.

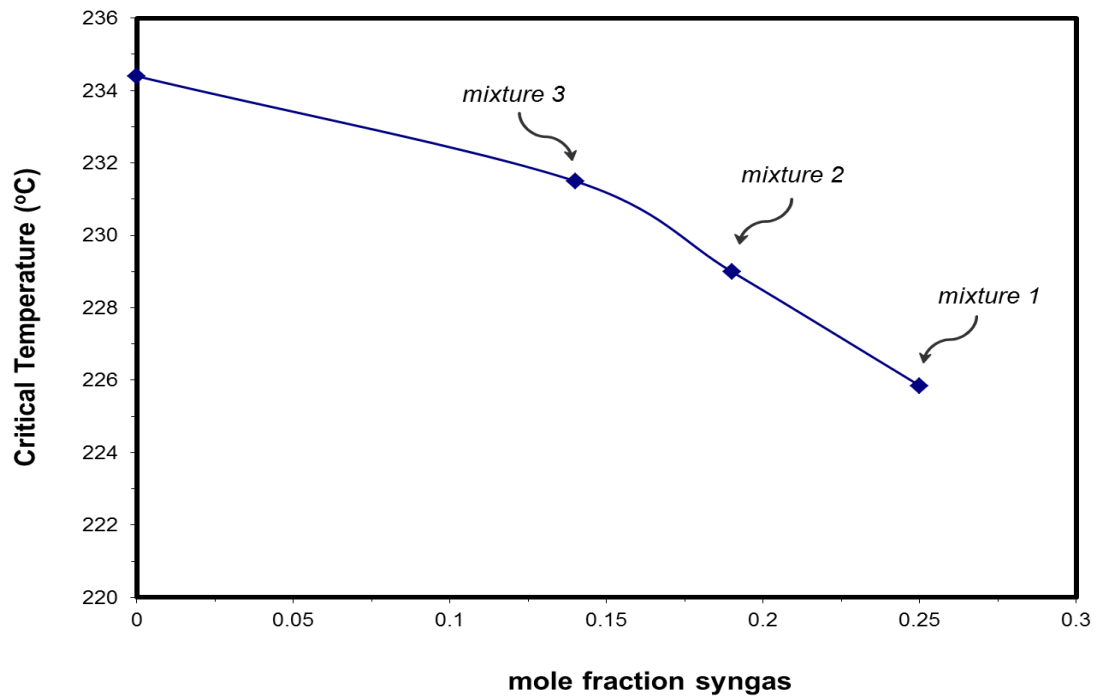


**Figure 4-4.** Plot of experimentally measured critical temperature against mole fraction of syngas.

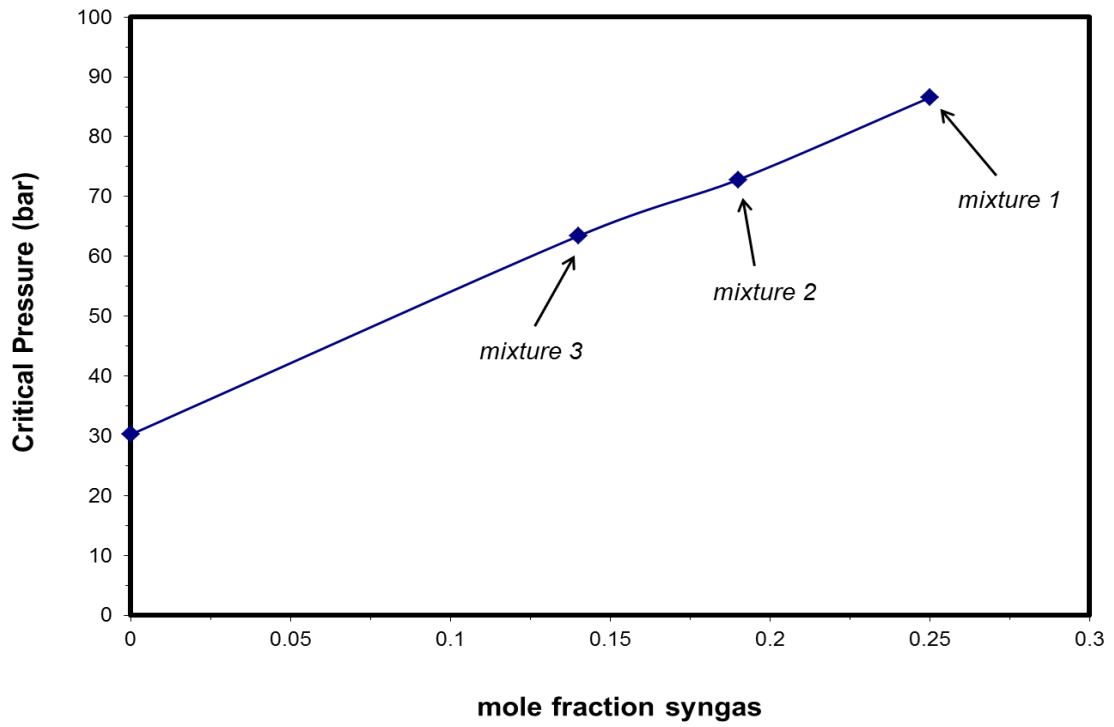


**Figure 4-5.** Plot of the experimentally measures critical pressure against mole fraction of syngas.

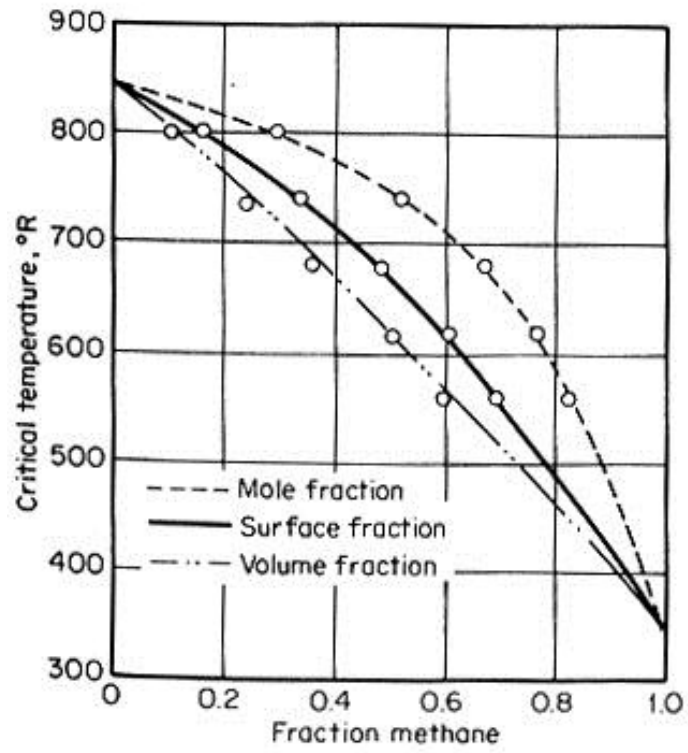


**Figure 4-6.** Critical temperature versus mole fraction of methane for the methane/n-pentane system. Figure taken from (Reid *et al.*, 1987).

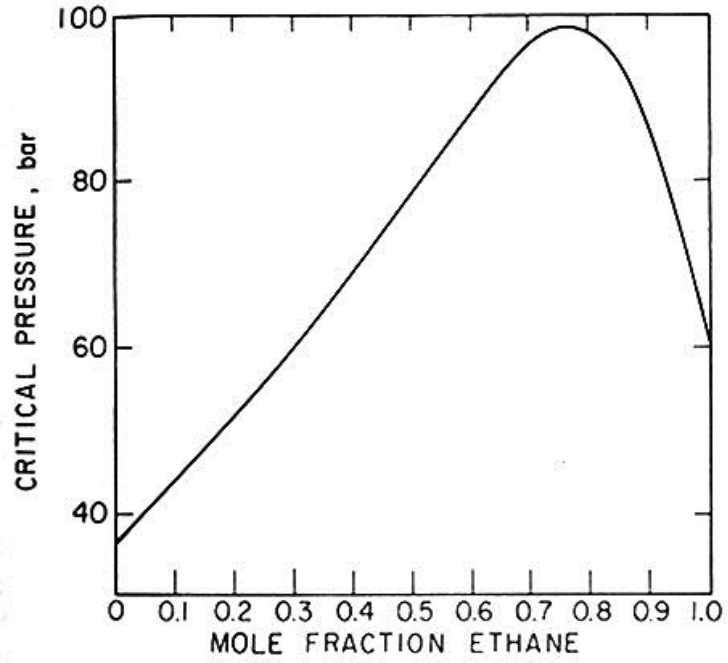


**Figure 4-7.** Critical pressure versus mole fraction of ethane for the ethane/n-heptane system. Figure taken from (Prausnitz *et al.*, 1986).

increases (Prausnitz *et al.*, 1999). Figure 4-7 shows this general trend for an ethane/n-heptane system. The experimentally determined data agreed well with both trends.

Experimentally measured critical points for the three specified mixtures are shown in Figure 4-8 along with the literature values for pure n-hexane. Each point represents a terminus for the two phase boundary for a particular syngas/hexane ratio. At temperatures above the critical temperature for a specific mixture, the reaction system can be operated at any pressure and remain in a single phase. However, one does not have to operate in the “supercritical” region to remain a single phase (i.e. one does not have to be above the critical temperature and pressure to be single phase). It is possible to operate at a temperature below the critical temperature and remain a single phase. In order to be a single phase at a given temperature that is below the critical temperature, the pressure must be either increased to a pressure high enough to achieve a single phase compressed liquid or decreased low enough to be in the gaseous mixture region.

As an example, the critical point for mixture 2 was determined and the system was cooled to 225°C. The temperature of the system was below the critical temperature of 229°C, and the mixture was within the two-phase vapor-liquid equilibrium region at a pressure of 72.8 bar. In order to be one single phase at 225°C, the pressure was either increased until the mixture was a single phase in the compressed liquid region or decreased until the vessel was filled with a single phase gas mixture. A saturated liquid was reached at a pressure of 110 bar and a temperature of 225°C, and the system remained a single compressed liquid phase at pressures above 110 bar. A saturated gas mixture was reached at a pressure of 45 bar and a temperature of 225°C, and the system

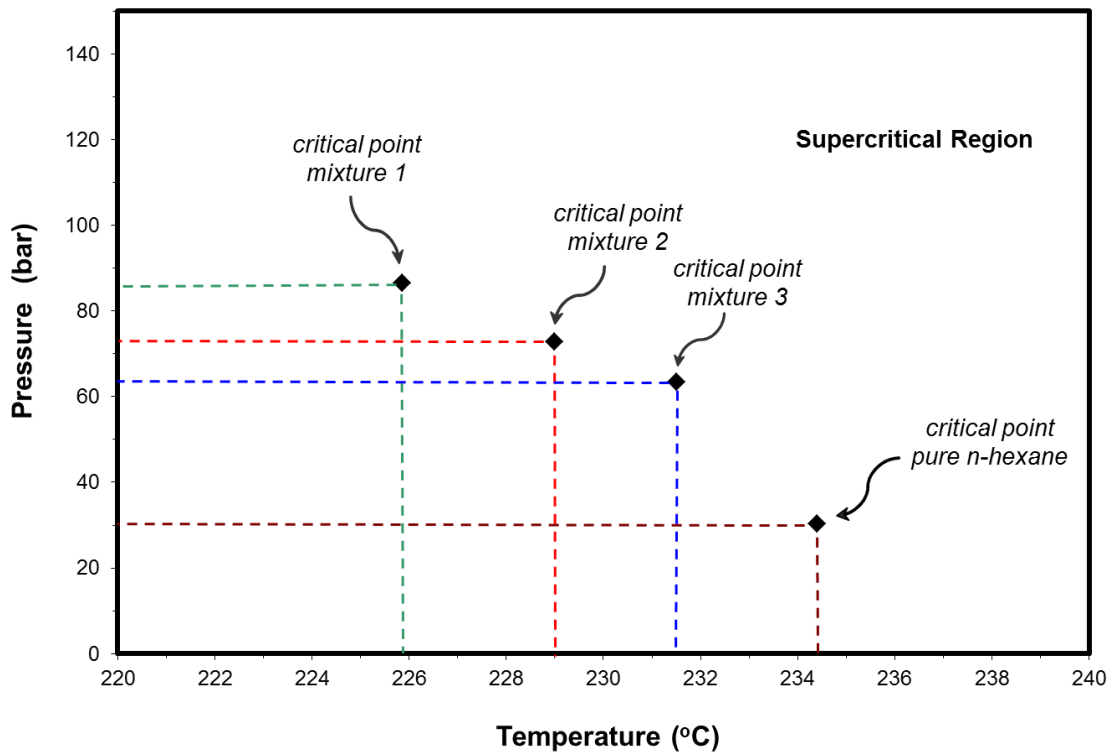


**Figure 4-8.** Critical points represent the terminus of the two phase boundary for a given syngas/hexane mixture. As example, operation at any temperature beyond the critical temperature of a given mixture results in a single phase operation at any operating pressure.

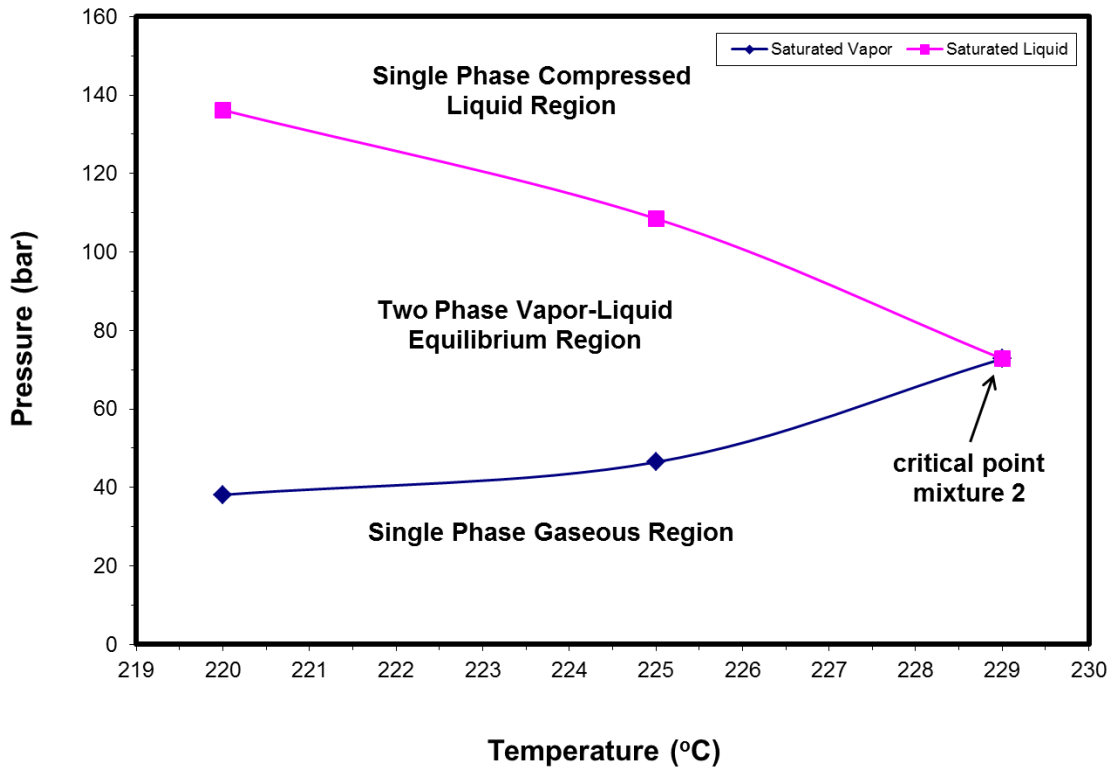


**Figure 4-9.** Experimentally determined two phase region for mixture 2.



remained a single gaseous phase at pressures below 45 bar. The procedure was repeated to verify the accuracy of our measurements. The two-phase vapor-liquid equilibrium for mixture 2 is illustrated in Figure 4-9. Single phase operation can be achieved for the mixtures studied at any pressure, as long as the temperature is above the critical temperature for a given mixture. In addition, single phase operation can be achieved at temperatures below the critical temperature of a given mixture, as long as the pressure is either above the pressure required for a saturated liquid or below the pressure corresponding to a saturated gas. Refer to Figure 4-9.

Another study was conducted in order to determine the phase behavior and critical point location of the FTS reaction mixture represented by the solvent, reactant gases (CO, H<sub>2</sub>), and products. The location of the critical point (temperature and pressure) of the FTS mixture was measured by collecting a sample from the reactor effluent for FTS under SCF hexane conditions in the Roberts Lab (Elbashir, 2004). The sample from the FT reactor effluent (collected from the line between the vapor exit of the hot trap and the entrance to the cold trap) was trapped into a gas tight collection container and then transformed into the evacuated view cell through the high pressure valve shown in Figure 4-1. Prior to phase-behavior analysis, the sample was characterized for composition using gas chromatographs (FID and TCD) and the methods described earlier. An example of the characterization of a typical product stream (at 75% syngas conversion) obtained under SCH operation (c.a. 109 hr time-on-stream) at 240 °C and 65 bar is shown in Table 4-2. The sample was allowed to condense inside the view cell and form two phases (liquid and vapor) prior to the determination of the critical temperature and pressure. The measured critical pressure of the FTS sample mixture, as seen in Figure 4-

10, was found to be 37.2 bar (7 bar higher than that of pure hexane). The critical temperature (238.2 °C) of the mixture was found to be much higher than that of pure hexane. It should be noted that while this measured critical point represents the bulk reaction mixture, it does not necessarily represent that of the reaction mixture within the catalyst pores in the FTS process. For SCH FTS, it is therefore important to know the critical point loci of the reaction and product mixture. Unfortunately, many SCF FTS studies in the literature are designed using only information about the critical point of the pure solvent.

Additional studies were conducted in order to see the effect that temperature and pressure have on the FTS product distribution. Temperature was varied from 230°C to 260°C, and pressure was varied from a gas-like density of 35 bar to a liquid-like density of 80 bar. All studies were performed with a 15% Co/Al<sub>2</sub>O<sub>3</sub> catalyst under SCF Hexane conditions. Figure 4-11 illustrates the effect that temperature has on CO conversion and the probability of chain growth ( $\alpha_{\text{overall}}$ ) during the FTS polymerization reaction. Here it is shown that as the temperature of the reaction was increased, conversion of CO was toward heavier products with a maximum conversion occurring between 240°C and 260°C. For chain growth probability, an initial decrease was noted between 230°C and 240°C. The  $\alpha_{\text{overall}}$  then increases until a maximum value of 0.85 was reached at 250°C, and a considerable drop in  $\alpha_{\text{overall}}$  occurs at temperatures above 260°C. Figure 4-12 demonstrates the influence of pressure on CO conversion and the chain growth probability in SCH-FTS. It was determined that pressure had a significant effect on CO conversion. A maximum value of 85% was obtained for CO conversion at 65 bar. There was a minimal effect observed on  $\alpha_{\text{overall}}$  within the range of pressures studied. These

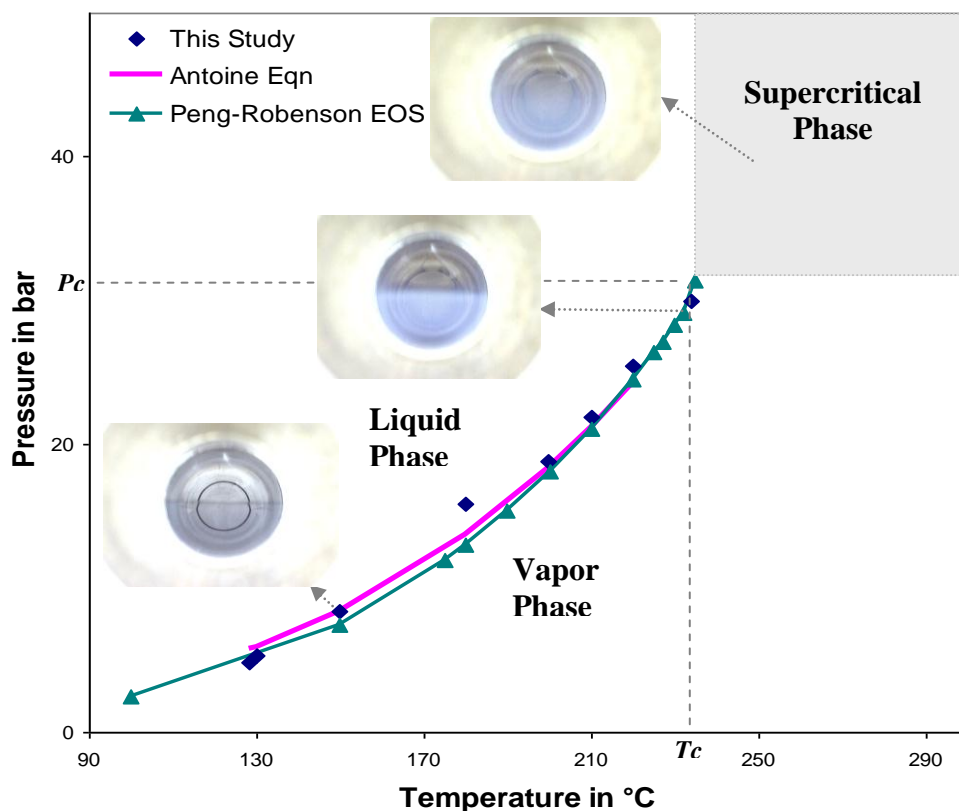


**Figure 4-10.** Experimentally determined critical temperature and pressure for the reaction mixture represented by the solvent, reactant gases (CO, H<sub>2</sub>), and products demonstrating a critical point at a temperature of 238.2°C and a pressure of 37.2 bar. Comparison is made to both the Antoine and Peng-Robinson equations of state.

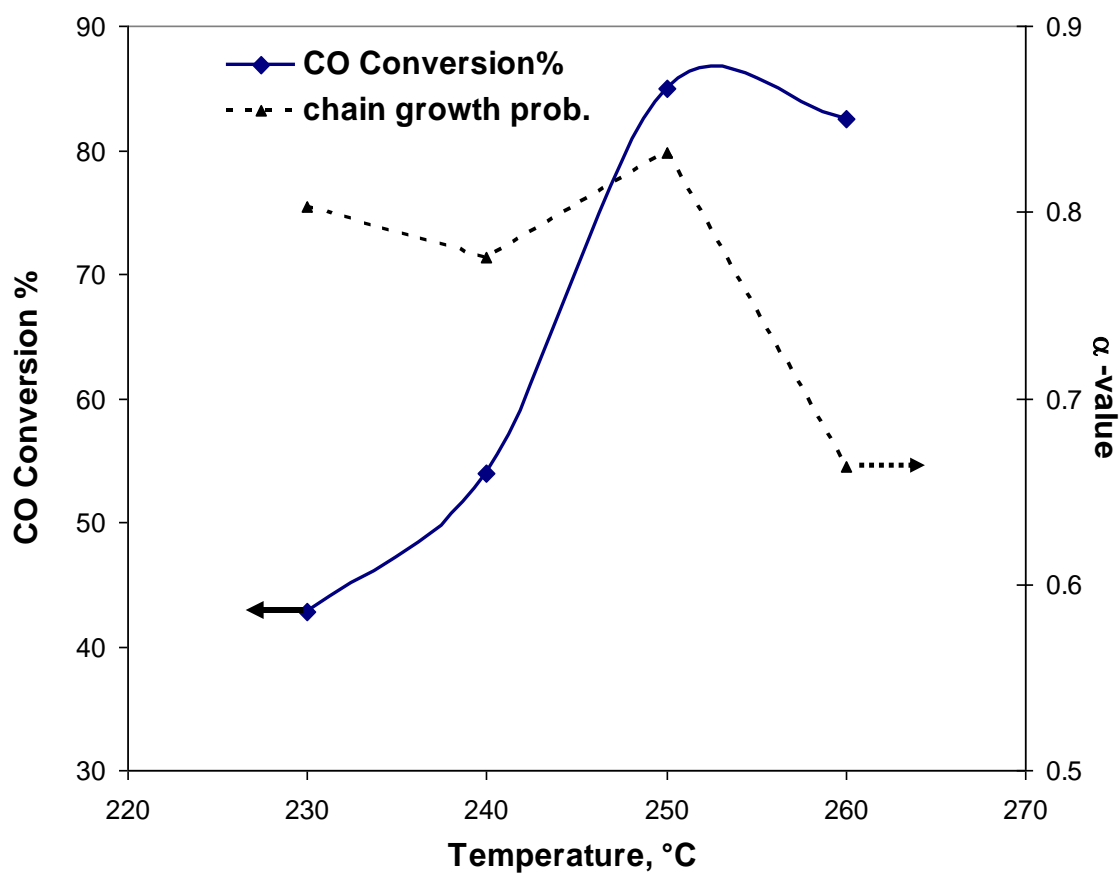


**Figure 4-11.** Effect of reaction temperature on CO conversion and chain-growth probability ( $\alpha$ -value) at a total pressure of 65 bar and syngas/hexane molar ratio of 1/3.

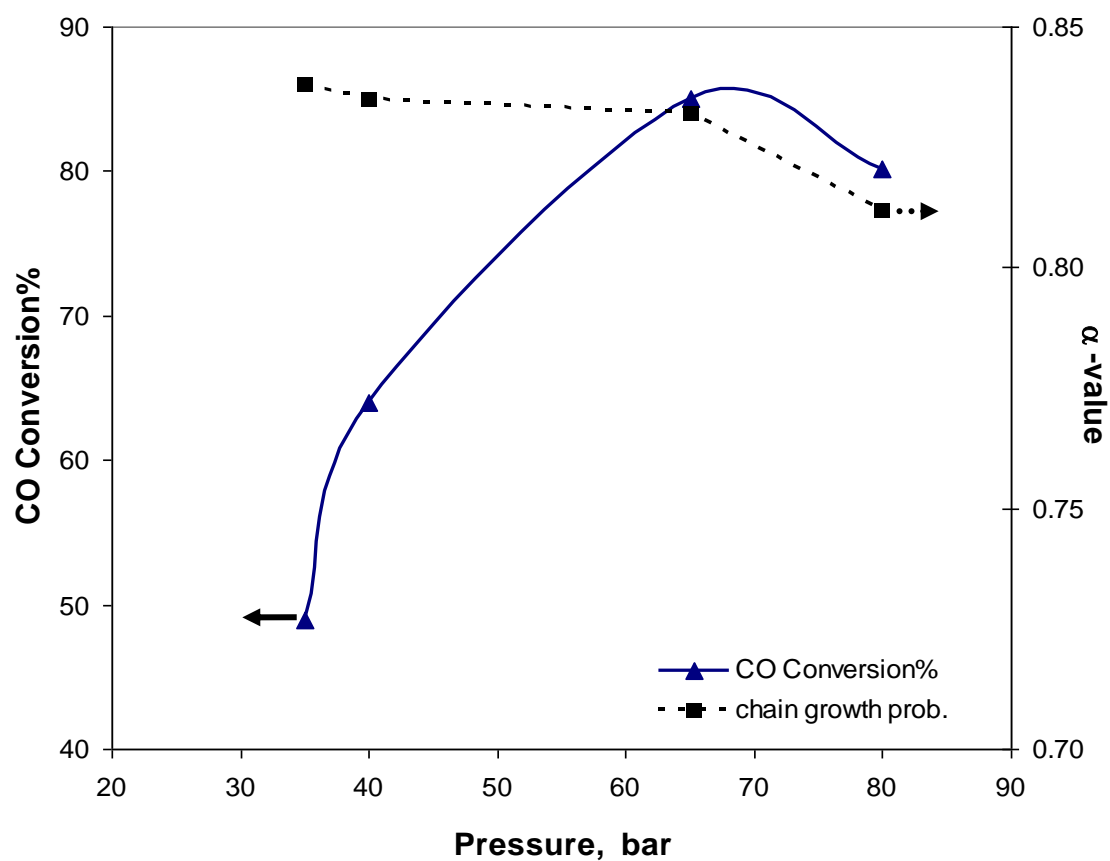


**Figure 4-12.** Effect of reaction pressure on CO conversion and chain-growth probability ( $\alpha$ -value) at 250°C and syngas/hexane molar ratio of 1/3.

Hydrocarbon Wt%				
	$\alpha$ -olefin	Paraffins	Isomers & Oxygenates	$W_n$
C1		7.22		0.072
C3	1.298	0.39	0.01	0.017
C4	0.83	0.21	0.11	0.011
C5	0.92	0.28	0.18	0.0137
C6*	NA	NA	NA	NA
C7	1.57	0.644	0.023	0.022
C8	2.96	1.39	0.02	0.044
C9	4.481	1.697	0.091	0.063
C10	4.256	1.603	0.125	0.060
C11	4.095	1.752	0.113	0.059
C12	4.186	1.724	0.083	0.060
C13	3.790	2.42	0.053	0.062
C14	2.66	2.64	0.028	0.053
C15	2.801	2.654	0	0.054
C16	2.926	2.933	0	0.058
C17	2.787	2.96	0	0.057
C18	2.285	3.02	0	0.053
C19	1.86	2.57	0	0.044
C20+	5.765	9.74	0	0.122

\* C<sub>6</sub> composition has not been reported because the solvent (hexane) peak in the FID, and GC-MS analysis is dominant over the other products such as olefins, oxygenates and isomers with weight percentage above 80%.

**Table 4-2.** The product distributions of SCH-FTS reaction mixture at 240°C and 65 bar. Syngas (H<sub>2</sub>/CO) feed ration is 2:1, the volumetric space velocity is 93.75hr<sup>-1</sup> and the hexanes to syngas molar ratio is 3 to 1.

studies demonstrate the importance of selecting the appropriate operating conditions in order to ensure optimal performance for the FTS polymerization reaction.

#### **4.4 Conclusions**

A system was developed in order to examine the phase behavior and determine critical points for FTS reaction mixtures. The reaction mixtures studied included both the FTS reaction feed mixture (CO, H<sub>2</sub>, hexane) and a reaction mixture consisting of the solvent, reactant gases (CO, H<sub>2</sub>), and products. After investigating the phase behavior of the reaction feed mixture, we determined that the critical temperature decreases as the mole fraction of syngas is increased. However, the critical pressure for the mixtures increases as mole fraction of syngas is increased. Also, it was shown that it is not necessary to operate in the “supercritical” region to remain a single phase. Single phase operation can be achieved for the mixtures studied at any pressure, as long as the temperature is above the critical temperature for a given mixture. In addition, single phase operation can be achieved at temperatures below the critical temperature of a given mixture, as long as the pressure is either above the pressure required for a saturated liquid or below the pressure corresponding to a saturated gas. The phase behavior and critical point location of the FTS reaction mixture represented by the solvent, reactant gases (CO, H<sub>2</sub>), and products was also determined. What we found was that the measured critical temperature and pressure of the FTS sample mixture were both higher than that of pure n-hexane. Thus, it is important to know the critical point loci of the reaction and product mixture for SCH-FTS. Additional studies were conducted in order to see the effect that temperature and pressure have on the FTS product distribution. Both temperature and pressure had a

significant effect on the CO conversion, while the chain growth probability seemed to be more affected by temperature. Our studies have established the importance of understanding the critical point location for the mixture when designing a SCF FTS reaction system.



## Chapter 5

### CONCLUSIONS

Many commercial processes for the production of chemicals involve harsh organic solvents as well as numerous by-products that are detrimental to the environment. The overall goal of this work was to apply the twelve principles of green chemistry to heterogeneous catalysis operations and develop alternative synthetic routes in order to improve the conventional industrial processes for the systems studied.

Chapter 2 involved the application of green chemistry principles in the synthesis of Pd nanoparticles, and their use as catalysts in the remediation harmful environmental contaminants. Pd nanoparticles were synthesized and stabilized within the aqueous phase using water-soluble polymeric capping ligands, which offers a “green” alternative to the conventional nanoparticle synthesis techniques. The capping ligand, capping ligand concentration, and synthesis temperature were all examined in order to understand their effect on the particle size and size distribution. Once it was understood how to finely control the synthesis of Pd nanoparticles within the aqueous phase, the catalytic behavior of CMC-stabilized Pd nanoparticles was examined for the hydrodechlorination of TCE.

This chapter specifically focused on the batch dechlorination of TCE over supported Pd nanoparticle catalysts producing only biodegradable ethane. It is essential to efficiently retain and recover the active Pd catalyst material if these catalysts are to be

used for an environmental application; thus, the Pd nanoparticles were dispersed on supporting materials. A methodology was developed to successfully deposit the Pd nanoparticles onto supporting materials and to prepare the catalysts for utilization in a heterogeneous catalyst system. It was determined that the supported catalysts retained sufficient activity towards the degradation of TCE as compared to Pd nanoparticles homogeneously dispersed within the aqueous phase. It is noted that the use of hydrophilic  $\text{Al}_2\text{O}_3$  supporting material illustrated a mass transfer resistance to TCE that affected the initial hydrodechlorination rate. However, the use of a more hydrophobic support, TS-1, overcame the mass transfer resistance to TCE. The work in Chapter 2 illustrates that supported Pd catalysts can be effective in the hydrodechlorination of TCE.

Chapter 3 presented an improved method for the production of commodity chemicals.  $\text{H}_2\text{O}_2$  is generally considered a benign oxidant that is a promising alternative to conventional oxidants. A system was designed in order to investigate the in-situ generation of  $\text{H}_2\text{O}_2$  in supercritical  $\text{CO}_2$  solvent media. It is particularly difficult to accurately measure  $\text{H}_2\text{O}_2$  production in the direct route from hydrogen and oxygen, since the same conditions necessary to produce  $\text{H}_2\text{O}_2$  also catalyze its decomposition. Therefore, a few probe reactions including propylene epoxidation, cyclohexanone oxidation, and pyridine oxidation were performed in order to capture the generated  $\text{H}_2\text{O}_2$  before it underwent decomposition. A Pd/TS-1 catalyst was used in all reactions studied, since it has shown some promise in promoting the direct generation of  $\text{H}_2\text{O}_2$  from hydrogen and oxygen.

For the propylene epoxidation reaction, low conversions of propylene were repeatedly detected. It was identified that the Pd metal loading used in this study was too

high promoting the degradation of in-situ generated  $\text{H}_2\text{O}_2$ . Therefore, more selective catalysts for this reaction should be examined. In addition, a reactor passivation methodology was developed along with the inclusion of a glass insert in order to prevent decomposition of  $\text{H}_2\text{O}_2$  upon contacting the walls of the stainless steel reactor. It was also determined that this particular reaction suffered from extensive by-product formation, which was due in part to the acidic reaction media. It is suggested that an inhibitor molecule be included in future studies in order to suppress undesired side reactions.

Chapter 3 also focused on the generation of adipic acid from cyclohexanone using  $\text{H}_2\text{O}_2$  produced in-situ. There was limited success in oxidizing cyclohexanone over a Pd/TS-1 catalyst to adipic acid. Extensive by-product formation was similarly detected, and a method should be developed to inhibit the production of these side reactions. A diffusional limitation exists for the oxidation of cyclohexanone over the TS-1 catalyst, since the pores of the TS-1 catalyst are too narrow for effective oxidation of the bulky cyclohexanone molecule. Thus, it was determined that catalysts having larger pore sizes should be explored for this reaction.

Pyridine was used as a tool in Chapter 3 to measure the in-situ production of  $\text{H}_2\text{O}_2$ , and in order to optimize the reaction conditions. It was determined that the ratio of  $\text{O}_2:\text{H}_2$ ,  $\text{H}_2$  concentration, and catalyst mass all had an effect on the  $\text{H}_2$  conversion and both selectivity and yield to  $\text{H}_2\text{O}_2$ . Also, the metal loading had an effect on the catalyst activity. This chapter also presents the large scale potential for the in-situ production of  $\text{H}_2\text{O}_2$  in supercritical  $\text{CO}_2$ . Experimental data was collected on the performance of the pyridine oxidation reaction along with analysis of the product distribution. This data

serves as the basis for the development of rigorous process simulation models used to analyze the potential of the green supercritical phase process and compare it to the traditional anthraquinone autoxidation process. The results show that it is possible to efficiently couple the in-situ  $\text{H}_2\text{O}_2$  generation with another oxidation reaction and achieve substantial benefits in terms of both energy consumption and reduced environmental impact.

Chapter 4 involved another commercially viable heterogeneous catalyst system to make alternative fuels from a renewable feedstock. A system was developed in order to examine the phase behavior and determine critical points for FTS reaction mixtures. The reaction mixtures studied included both the FTS reaction feed mixture ( $\text{CO}$ ,  $\text{H}_2$ , hexane) and a reaction mixture consisting of the solvent, reactant gases ( $\text{CO}$ ,  $\text{H}_2$ ), and products. After investigating the phase behavior of the reaction feed mixture, it was determined that the critical temperature decreased as the mole fraction of syngas was increased. However, the critical pressure for the mixtures increased as mole fraction of syngas was increased. It was also determined that single phase operation could be achieved for the mixtures studied at any pressure, as long as the temperature was above the critical temperature for a given mixture. In addition, single phase operation could be achieved at temperatures below the critical temperature of a given mixture, as long as the pressure was either above the pressure required for a saturated liquid or below the pressure corresponding to a saturated gas. The phase behavior and critical point location of the FTS reaction mixture represented by the solvent, reactant gases ( $\text{CO}$ ,  $\text{H}_2$ ), and products was also determined. The measured critical temperature and pressure of the FTS sample mixture were both higher than that of pure n-hexane. Thus, it is important to know the

critical point loci of the reaction and product mixture for SCH-FTS. Additional studies were conducted in order to see the effect that temperature and pressure have on the FTS product distribution. Both temperature and pressure had a significant effect on the CO conversion, while the chain growth probability seemed to be more affected by temperature. These studies conducted in Chapter 4 established the importance of understanding the critical point location for the mixture when designing a SCF-FTS reaction system.

## References

- Adair, J.H., Li, T., Kido, T., Havey, K., Moon, J., Mecholsky, J., Morrone, A., Talham, D.R., Ludwig, M.H., and Wang, L. (1998). "Recent developments in the preparation and properties of nanometer-size spherical and platelet-shaped particles and composite particles." Materials Science and Engineering: R:Reports **23**(4-5): 139-242.
- Alargova, R. G., Deguchi, S., and Tsujii, K. (2001). "Stable colloidal dispersions of fullerenes in polar organic solvents." Journal of the American Chemical Society **123**: 10460-10467.
- Albrecht, M. A., Evans, Cameron W., and Raston, Colin L. (2006). "Green chemistry and the health implications of nanoparticles." Green Chemistry **8**: 417-432.
- Alonso, F., Beletskaya, Irina P., and Yus, Miguel (2002 ). "Metal-Mediated Reductive Hydrodehalogenation of Organic Halides." Chemical Reviews **102**: 4009-4091.
- Anastas, P.T., Kirchhoff, M.M., and Williamson, T.C. (2001). "Catalysis as a foundational pillar of green chemistry." Applied Catalysis A: General **221**(1-2): 3-13.

Anastas, P. T. and J. C. Warner (1998). Green Chemistry: Theory and Practice. New York, Oxford University Press, Inc.

Andrievsky, G. V., Klochkov, V.K., Bordyuh, A.B., and Dovbeshko, G.I. (2002). "Comparative analysis of two aqueous-colloidal solutions of C-60 fullerene with help of FTIR reflectance and UV-Vis spectroscopy." Chemical Physics Letters **364**: 8-17.

Arnold, W. A., and Roberts, A.L. (2000). "Pathways and Kinetics of Chlorinated Ethylene and Chlorinated Acetylene Reaction with Fe(0) Particles." Environmental Science & Technology **34**(9): 1794-1805.

Astruc, D. (2007). "Palladium Nanoparticles as Efficient Green Homogeneous and Heterogeneous Carbon-Carbon Coupling Precatalysts: A Unifying View." Inorganic Chemistry **46**: 1884-1894.

Astruc, D., F. Lu, et al. (2005). "Nanoparticles as Recyclable Catalysts: The Frontier between Homogeneous and Heterogeneous Catalysis." Angewandte Chemie International Edition **44**: 7852-7872.

ATSDR (2003). ToxFAQs for Trichloroethylene. U.S. Department of Health and Human Services. Atlanta, GA, <http://www.atsdr.cdc.gov/toxfaq.html>. CAS # **79-01-6**.

- Bacik, D.B., Yuan, W., Roberts, C.B., and Eden, M.R. (2011). "Systems Analysis of Benign Hydrogen Peroxide Synthesis in Supercritical CO<sub>2</sub>." Computer Aided Chemical Engineering **29A**: 387-391.
- Baiker, A. (1999). "Supercritical Fluids in Heterogeneous Catalysis." Chemical Reviews **99**: 453-473.
- Baiker, A., Wandeler, R. (2000). "Supercritical Fluids: Opportunities in Heterogeneous Catalysis." CATTECH **4**(2): 128-143.
- Beckman, E. J. (2003). "Oxidation Reactions in CO<sub>2</sub>: Academic Exercise of Future Green Processes?" Environmental Science & Technology **37**: 5289-5296.
- Beckman, E. J. (2004). "Supercritical and near-critical CO<sub>2</sub> in green chemical synthesis and processing." Journal of Supercritical Fluids **28**: 121-191.
- Behr, A., Eilting, J., Irawadi, K., Leschinski, J., and Lindner, F. (2008). "Improved utilisation of renewable resources: New important derivatives of glycerol." Green Chemistry **10**: 13-30.
- Bellussi, G., A. Carati, et al. (1992). "Reactions of Titanium Silicalite with Protic Molecules and Hydrogen Peroxide." Journal of Catalysis **133**: 220-230.



- Bochniak, D. J. and B. Subramaniam (1998). "Fischer-Tropsch Synthesis in Near-Critical n-Hexane: Pressure-Tuning Effects." AICHE Journal **44**(8): 1889-1896.
- Bolm, C., O. Beckman, et al. (1999). "The Search for New Environmentally Friendly Chemical Processes." Angewandte Chemie **38**(7): 907-909.
- Boudart, M. (1995). "Turnover Rates in Heterogeneous Catalysis." Chemical Reviews **95**: 661-666.
- Brust, M., M. Walker, et al. (1994). "Synthesis of Thiol-derivatised Gold Nanoparticles in a Two-phase Liquid-Liquid System." Chemical Communications(7): 801-802.
- Centi, G., and Perathoner, S. (2003). "Catalysis and sustainable (green) chemistry." Catalysis Today: 287-297.
- Chen, Q. and E. J. Beckman (2007). "Direct Synthesis of H<sub>2</sub>O<sub>2</sub> from O<sub>2</sub> and H<sub>2</sub> over Precious Metal Loaded TS-1 in CO<sub>2</sub>." Green Chemistry **9**(7): 802-808.
- Chinta, S. and J. H. Lunsford (2004). "A mechanistic study of H<sub>2</sub>O<sub>2</sub> and H<sub>2</sub>O formation from H<sub>2</sub> and O<sub>2</sub> catalyzed by palladium in an aqueous medium." Journal of Catalysis **225**: 249-255.

Chiras, D. D. (2010). Environmental Science. Sudbury, Jones and Bartlett Publishers, LLC.

Chithrani, B. D., Ghazani, Arezou A., Chan, and Warren C.W. (2006 ). "Determining the Size and Shape Dependence of Gold Nanoparticle Uptake into Mammalian Cells." Nano Letters **6**(4): 662-668.

Clerici, M. G., G. Bellussi, et al. (1991). "Synthesis of Propylene Oxide from Propylene and Hydrogen Peroxide Catalyzed by Titanium Silicalite." Journal of Catalysis **129**: 159-167.

Colvin, V. L. (2003). "The potential environmental impact of engineered nanomaterials." Nature Biotechnology **21**(10): 1166-1170.

Congress (1969 ). The National Environmental Policy Act of 1969.

Dahl, J. A., Maddux, Bettye L.S., Hutchison, James E. (2007). "Toward Greener Nanosynthesis." Chemical Reviews **107**: 2228-2269.

Danciu, T., E. J. Beckman, et al. (2003). "Direct Synthesis of Propylene Oxide with CO<sub>2</sub> as the Solvent." Angewandte Chemie International Edition **42**(10): 1140-1142.

- Daniel, M.-C. and D. Astruc (2004). "Gold Nanoparticles: Assembly, Supramolecular Chemistry, Quantum-Size-Related Properties, and Applications toward Biology, Catalysis, and Nanotechnology." Chemical Reviews **104**: 293-346.
- Deguchi, S., Alargova, R.G., and Tsujii, K. (2001). "Stable dispersions of fullerenes, C-60 and C-70, in water. Preparation and characterization." Langmuir **17**: 6013-6017.
- Deng, Y., Z. Ma, et al. (1999). "Clean synthesis of adipic acid by direct oxidation of cyclohexene with H<sub>2</sub>O<sub>2</sub> over peroxytungstate-organic complex catalysts." Green Chemistry **1**(6): 275-276.
- DeSimone, J. M. (2002). "Practical Approaches to Green Solvents." Science **297**: 799-803.
- Donaldson, K., Stone, V., Gilmour, P.S., Brown, D.M., and MacNee, W.N.E. (2000). "Ultrafine particles: mechanisms of lung injury." Philosophical Transactions A **358**: 2741-2748.
- Draths, K. M. and J. W. Frost (1994). "Environmentally Compatible Synthesis of Adipic Acid from D-Glucose." Journal of the American Chemical Society **116**: 399-400.

EIA (2008). "International Energy Outlook 2008." from <http://www.eia.doe.gov/oiaf/ieo/world.html>.

Elam, J.W., Draths, Sechrist, Z.A., and George, S.M. (2002). "ZnO/Al<sub>2</sub>O<sub>3</sub> nanolaminates fabricated by atomic layer deposition: growth and surface roughness measurements." Thin Solid Films 414: 43-55.

Elbashir, N. O. M. (2004). Utilization of supercritical fluids in the Fischer-Tropsch synthesis over cobalt-based catalytic systems. Department of Chemical Engineering. Auburn, Auburn University. **Doctorate of Philosophy**: 308.

Ferin, J., Oberdorster, G., Soderholm, S.C., and Gelein, R. (1991). "Pulmonary tissue access of ultrafine particles." Journal of Aerosol Medicine 4: 57-68.

Gao, L., Z. Hou, et al. (2001). "Critical Parameters of Hexane + Carbon Monoxide + Hydrogen and Hexane + Methanol + Carbon Monoxide + Hydrogen Mixtures in the Hexane-Rich Region." Journal of Chemical & Engineering Data 46: 1635-1637.

Gavaskar, A. R., Gupta, N., Sass, B.M., Janosy, R.J., and O'Sullivan, D. (1998). Permeable Barriers for Groundwater Remediation: Design, Construction, and Monitoring. Columbus, Battelle Press.

Geertesma, A. (1990). Consideration in the Selection of a Fischer-Tropsch Reactor for Synfuel Production. DOE Indirect Liquefaction Contractors' Review Meeting, Pittsburgh.

Gopidas, K. R., Whitesell, J.K., and Fox, M.A. (2003). "Synthesis, Characterization, and Catalytic Applications of a Palladium-Nanoparticle-Cored Dendrimer." Nano Letters **3**(12): 1757-1760.

Hancu, D. and E. J. Beckman (2001). "Generation of hydrogen peroxide directly from H<sub>2</sub> and O<sub>2</sub> using CO<sub>2</sub> as the solvent." Green Chemistry **3**: 80-86.

Hancu, D., J. Green, et al. (2002). "H<sub>2</sub>O<sub>2</sub> in CO<sub>2</sub>: Sustainable Production and Green Reactions." Accounts of Chemical Research **35**(9): 757-764.

He, F., and Zhao, D. (2005). "Preparation and Characterization of a New Class of Starch-Stabilized Bimetallic Nanoparticles for Degradation of Chlorinated Hydrocarbons in Water." Environmental Science & Technology **39**: 3314-3320.

He, F., and Zhao, D. (2007). "Manipulating the Size and Dispersibility of Zerovalent Iron Nanoparticles by Use of Carboxymethyl Cellulose Stabilizers." Environmental Science & Technology **41**: 6216-6221.

- He, F., Zhao, D., Liu, J., and Roberts, C.B. (2007). "Stabilization of Fe-Pd Nanoparticles with Sodium Carboxymethyl Cellulose for Enhanced Transport and Dechlorination of Trichloroethylene in Soil and Groundwater." Industrial & Engineering Chemistry Research **46**: 29-34.
- He, F., Zhao, Dongye (2008). "Hydrodechlorination of trichloroethene using stabilized Fe-Pd nanoparticles: Reaction mechanism and effects of stabilizers, catalysts, and reaction conditions." Applied Catalysis B: Environmental **84**: 533-540.
- Hoelderich, W. F. and F. Kollmer (2000). "Oxidation reactions in the synthesis of fine and intermediate chemicals using environmentally benign oxidants and the right reactor system." Pure and Applied Chemistry **72**(7): 1273-1287.
- Huang, X., N. O. Elbashir, et al. (2004). "Supercritical Solvent Effects on Hydrocarbon Product Distributions from Fischer-Tropsch Synthesis over an Alumina-Supported Cobalt Catalyst." Industrial and Engineering Chemistry Research **43**: 6369-6381.
- Huang, X. and C. B. Roberts (2003). "Selective Fischer-Tropsch synthesis over an Al<sub>2</sub>O<sub>3</sub> supported cobalt catalyst in supercritical hexane." Fuel Processing Technology **83**: 81-99.

- Hwang, J.-S., C. W. Lee, et al. (2002). "Direct hydroxylation of aromatics with a mixture of H<sub>2</sub> and O<sub>2</sub> gases over Fe- and Pd-incorporated zeolites." Research on Chemical Intermediates **28**(6): 527-535.
- ITRC (2005). Permeable Reactive Barriers: Lessons Learned/New Directions. Washington, D.C., Interstate Technology & Regulatory Council.
- Jenzer, G., T. Mallat, et al. (2001). "Continuous epoxidation of propylene with oxygen and hydrogen on a Pd-Pt/TS-1 catalyst." Applied Catalysis A: General **208**: 125-133.
- Jeon, S.-J., Li, H., and Walsh, P.J. (2005). "A Green Chemistry Approach to a More Efficient Asymmetric Catalyst: Solvent-Free and Highly Concentrated Alkyl Additions to Ketones." Journal of the American Chemical Society **127**: 16416-16425.
- Joyce, P. C., J. Gordon, et al. (2000). "Vapor-Liquid Equilibria for the Hexane + Tetracosane and Hexane + Hexatriacontane Systems at Elevated Temperatures and Pressures." Journal of Chemical & Engineering Data **45**: 424-427.
- Joyce, P. C., B. E. Leggett, et al. (1999). "Vapor-liquid equilibrium for model Fischer-Tropsch waxes (hexadecane, 1-hexadecene, and 1-hexadecanol) in supercritical hexane." Fluid Phase Equilibria **158-160**: 723-731.

- Kahlich, D., V. Wiechern, et al. (2003). Propylene Oxide and Glycol. Ullman's Encyclopedia of Industrial Chemistry. Weinheim, Wiley-VCH. **30**: 279-303.
- Keim, W. (1983). Catalysis by metal complexes: Catalysis in C1 Chemistry, Springer.
- Koch, C. C., Ed. (2002). Nanostructured Materials, Processing, Properties and Applications. Norwich, New York, Noyes Publications.
- Kolbel, H. and M. Ralek (1980). "Fischer-Tropsch synthesis in the liquid phase." Catalysis Reviews, Science and Engineering **21**(2): 225-274.
- Landon, P., P. J. Collier, et al. (2003). "Direct synthesis of hydrogen peroxide from H<sub>2</sub> and O<sub>2</sub> using Pd and Au catalysts." Physical Chemistry Chemical Physics **5**: 1917-1923.
- Lang, X., A. Akgerman, et al. (1995). "Steady State Fischer-Tropsch Synthesis in Supercritical Propane." Industrial and Engineering Chemistry Research **34**: 72-77.
- Lapisardi, G., F. Chiker, et al. (2004). "A "one-pot" synthesis of adipic acid from cyclohexene under mild conditions with new bifunctional Ti-AlSBA mesostructured catalysts." Catalysis Communications **5**: 277-281.



- Laufer, W. and W. F. Hoelderich (2001). "Direct oxidation of propylene and other olefins on precious metal containing Ti-catalysts." Applied Catalysis A: General **213**: 163-171.
- Laufer, W., R. Meiers, et al. (1999). "Propylene epoxidation with hydrogen peroxide over palladium containing titanium silicalite." Journal of Molecular Catalysis A: Chemical **141**: 215-221.
- Leitner, W. (2002). "Supercritical Carbon Dioxide as a Green Reaction Medium for Catalysis." Accounts of Chemical Research **35**(9): 746-756.
- Li, G., Edwards, J.E., Carley, Albert F., Hutchings, Graham J. (2007). "Direct synthesis of hydrogen peroxide from H<sub>2</sub> and O<sub>2</sub> using zeolite-supported Au-Pd catalysts." Catalysis Today **122**: 361-364.
- Li, Y., Boone, E., and El-Sayed, M.A. (2002). "Size Effects of Pd-PVP Nanoparticles on the Catalytic Suzuki Reactions in Aqueous Solution." Langmuir **18**(12): 4921-4925.
- Lien, H.-L., and Zhang, W.-X. (2007). "Nanoscale Pd/Fe bimetallic particles: Catalytic effects of palladium on hydrodechlorination." Applied Catalysis B: Environmental **77**: 110-116.

- Liu, J., He, Feng, Gunn, Tyler M., Zhao, Dogye, and Roberts, Christopher B. (2009). "Precise Seed-Mediated Growth and Size-Controlled Synthesis of Palladium Nanoparticles Using a Green Chemistry Approach." Langmuir **25**(12): 7116-7128.
- Liu, J., He, Feng, Durham, Ed, Zhao, Dogye, and Roberts, Christopher B. (2008). "Polysugar-Stabilized Pd Nanoparticles Exhibiting High Catalytic Activities for Hydrodechlorination of Environmentally Deleterious Trichloroethylene." Langmuir **24**: 328-336.
- Liu, J., Qin, Gaowu, Raveendran, Poovathinthodiyil, and Ikushima, Yukata (2006). "Facile "Green" Synthesis, Characterization, and Catalytic Function of B-D-Glucose-Stabilized Au Nanocrystals." Chemistry--A European Journal **12**: 2131-2138.
- Liu, J., Raveendran, P., Qin, G., and Ikushima, Y. (2005). "Self-assembly of B-D glucose-stabilized Pt nanocrystals into nanowire-like structures." Chemical Communications: 2972-2974.
- Liu, J., Sutton, Jonathan, and Roberts, Christopher B. (2007). "Synthesis and Extraction of Monodisperse Sodium Carboxymethylcellulose-Stabilized Platinum Nanoparticles for the Self-assembly of Ordered Arrays." Journal of Physical Chemistry C **111**: 11566-11576.

- Love, J. C., L. A. Estroff, et al. (2005). "Self-Assembled Monolayers of Thiolates on Metals as a Form of Nanotechnology." Chemical Reviews **105**: 1103-1169.
- Lowry, G. V., Reinhard, Martin (1999). "Hydrodehalogenation of 1- to 3-Carbon Halogenated Organic Compounds in Water Using a Palladium Catalyst and Hydrogen Gas." Environmental Science & Technology **33**: 1905-1910.
- Mackay, G. I., A. C. Hopkinson, et al. (1978). "Acid Catalysis in the Gas Phase: Dissociative Proton Transfer to Formic and Acetic Acid." Journal of the American Chemical Society **100**(24): 7460-7464.
- Magdassi, S., Bassa, A., Vinetsky, Y., and Kamyshny, A. (2003). "Silver Nanoparticles as Pigments for Water-Based Ink-Jet Inks." Chemistry of Materials **15**(11): 2208-2217.
- Magrez, A., Kasas, Sandor, Salicio, Valerie, Pasquier, Nathalie, Seo, Jin Won, Celio, Marco, Catsicas, Stefan, Schwaller, Beat, and Forro, Laszlo (2006). "Cellular Toxicity of Carbon-Based Nanomaterials." Nano Letters **6**(6): 1121-1125.
- Mainhardt, H. (2000). N<sub>2</sub>O Emissions from Adipic Acid and Nitric Acid Production  
Hayama, Kanagawa, Japan, Institute for Global Environmental Strategies.

McHedlov-Petrosyan, N. O., Klochkov, V.K., and Andrievsky, G.V. (1997). "Colloidal dispersions of fullerene C-60 in water: some properties and regularities of coagulation by electrolytes." Journal of the Chemical Society, Faraday Transactions **93**(4343-4346).

McKenzie, L. C., Hutchinson, J.E. (2004). "Green Nanoscience." Chimica Oggi **22**: 30.

McLeod, M. C., M. Anand, et al. (2005). "Precise and Rapid Size Selection and Targeted Deposition of Nanoparticle Populations Using CO<sub>2</sub> Gas Expanded Liquids." Nano Letters **5**(3): 461-465.

Meiers, R. and W. F. Holderich (1999). "Epoxidation of propylene and direct synthesis of hydrogen peroxide by hydrogen and oxygen  
" Catalysis Letters **59**: 161-163.

Mercer, J. W., Skipp, David C., and Giffin, Daniel (1990). Basics of Pump-and-Treat Ground-Water Remediation Technology, 72 p., U.S. Environmental Protection Agency.

Mohapatra, S., Kumar, R.K., and Maji, T.K. (2011). "Green synthesis of catalytic and ferromagnetic gold nanoparticles." Chemical Physics Letters: Article in Press.

Monnier, J. R. (2001). "The direct epoxidation of higher olefins using molecular oxygen."

Applied Catalysis A: General **221**: 73-91.

Moran, M. J., Zogorski, John S., and Squillace, Paul J. (2007). "Chlorinated Solvents in

Groundwater of the United States." Environmental Science & Technology **41**(1):

74-81.

Nel, A., Xia, Tian, Madler, Lutz, and Li Ning (2006). "Toxic Potential of Materials at the

Nanolevel." Science **311**: 622-627.

NIOSH (2005). Approaches to Safe Nanotechnology: An Information Exchange with

NIOSH, National Institute for Occupational Safety and Health.

NIST Chemistry WebBook, NIST Standard Reference Database Number 69, Eds. P.J.

Linstrom and W.G. Mallard, National Institute of Standards and Technology,

Gaithersburg, MD, <http://webbook.nist.gov>.

NNI (2011). National Nanotechnology Initiative: Strategic Plan. Washington, D.C.

Niu, W., K. M. Draths, et al. (2002). "Benzene-Free Synthesis of Adipic Acid."

Biotechnology Progress **18**: 201-211.

- Notari, B. (1996). "Microporous Crystalline Titanium Silicates." Advances in Catalysis **41**: 253-334.
- NRC (1994). Alternatives for Ground Water Cleanup. Washington, D.C., National Academy Press.
- Nutt, M. O., Heck, K.N., Alvarez, P., and Wong, M.S. (2006). "Improved Pd-on-Au Bimetallic Nanoparticle Catalysts for Aqueous-Phase Trichloroethene Hydrodechlorination." Applied Catalysis B: Environmental **69**: 115-125.
- Nutt, M. O., Hughes, Joseph B., Wong, Michael S. (2005). "Designing Pd-on-Au Bimetallic Nanoparticle Catalysts for Trichloroethene Hydrodechlorination." Environmental Science & Technology **39**: 1346-1353.
- Ohde, H., Wai, C.M., Kim, H., Kim, J., and Ohde, M. (2002). "Hydrogenation of Olefins in Supercritical CO<sub>2</sub> Catalyzed by Palladium Nanoparticles in a Water-in-CO<sub>2</sub> Microemulsion." Journa of the American Chemical Society **124**: 4540-4541.
- Orth, W. S., and Gillham, R.W. (1996). "Dechlorination of Trichloroethene in Aqueous Solution Using Fe<sup>0</sup>." Environmental Science & Technology **30**(1): 66-71.
- Pande, J. O. and J. Tonheim (2001). "Explosion of hydrogen in a pipeline for CO<sub>2</sub>." Ammonia Plant Safety & Related Facilities **41**: 254-259.

- Pernodet, N., Fang, X., Sun, Y., Bakhtina, A., Ramakrishnan, A., Sokolov, J., Ulman, A., and Rafailovich, M. (2006). "Adverse Effects of Citrate/Gold Nanoparticles on Human Dermal Fibroblasts." Small **2**(6): 766-773.
- Polishuk, I., R. Stateva, et al. (2004). "Simultaneous prediction of the critical and sub-critical phase behavior in mixtures using equations of state IV. Mixtures of chained n-alkanes." Chemical Engineering Science **59**: 633-643.
- Poole, C. P. J., and Owens, F.J. (2003). Introduction to Nanotechnology. Hoboken, Wiley-Interscience.
- Prausnitz, J. M., R. N. Lichtenthaler, et al. (1986). Molecular Thermodynamics of Fluid-Phase Equilibria. New Jersey, Prentice-Hall, Inc., Englewood Cliffs.
- Prausnitz, J. M., R. N. Lichtenthaler, et al. (1999). Molecular Thermodynamics of Fluid-Phase Equilibria. Upper Saddle River, Prentice-Hall
- Quinn, J., Geiger, C., Clausen, C., Brooks, K., Coon, C., O'Hara, S., Krug, T., Major, D., Yoon, W.-S., Gavaskar, A., and Holdsworth, T. (2005). "Field Demonstration of DNAPL Dehalogenation Using Emulsified Zero-Valent Iron." Environmental Science & Technology **39**(5): 1309-1318.

Raveendran, P., Fu, J., and Wallen, S.L. (2003). "Complete "Green" Synthesis and Stabilization of Metal Nanoparticles." Journa of the American Chemical Society **125**(46): 13940-13941.

Raveendran, P., Fu, J., and Wallen, S.L. (2006). "A Simple and "Green" Method for the Synthesis of Au, Ag, and Au-Ag Alloy Nanoparticles." Green Chemistry **8**(1): 34-38.

Reid, R. C., J. M. Prausnitz, et al. (1987). The Properties of Gases & Liquids. New York, McGraw-Hill.

Reid, R. C., J. M. Prausnitz, et al. (1987). The properties of Gases and Liquids. New York, McGraw-Hill.

Reimer, R. A., C. S. Slaten, et al. (1994). "Abatement of N<sub>2</sub>O emissions produced in the adipic acid industry." Environmental Progress **13**(2): 134-137.

Russell, H. H., Matthews, John E., and Sewell, Guy W. (1992). TCE Removal from Contaminated Soil and Ground Water, 10 p., U.S. Environmental Protection Agency.

Sato, K., M. Aoki, et al. (1998). "A "Green" Route to Adipic Acid: Direct Oxidation of Cyclohexenes with 30 Percent Hydrogen Peroxide." Science **281**: 1646-1647.



Science Policy Council, U. S. E. P. A. (2005). U.S. Environmental Protection Agency External Review Draft, Nanotechnology White Paper.

Sheldon, R. A. (2005). "Green solvents for sustainable organic synthesis: state of the art." Green Chemistry **7**: 267-278.

Sheldon, R. A., Kochi, J.K. (2005). "Metal-Catalyzed Oxidations of Organic Compounds in the Liquid Phase: A Mechanistic Approach." Advances in Catalysis **25**: 272-413.

Shenhar, R. and V. M. Rotello (2003). "Nanoparticles: Scaffolds and Building Blocks." Accounts of Chemical Research **36**: 549-561.

Sherman, J., Chin, B., Huibers, P., Garcia-Valls, R., and Hatton, T.A. (1998). "Solvent Replacement for Green Processing." Environmental Health Perspectives **106**(1): 253-271.

Shimizu, A., K. Tanaka, et al. (2000). "Abatement technologies for N<sub>2</sub>O emissions in the adipic acid industry." Chemosphere--Global Change Science **2**: 425-434.

Sigman, M. B., A. E. Saunders, et al. (2004). "Metal Nanocrystal Superlattice Nucleation and Growth." Langmuir **20**: 978-983.

Stowell, C. A., and Korgel, B.A. (2005). "Iridium Nanocrystal Synthesis and Surface Coating-Dependent Catalytic Activity." Nano Letters **5**(7): 1203-1207.

Stranges, A. N. (2007). "A history of the Fischer-Tropsch synthesis in Germany 1926-1945." Studies in Surface Science and Catalysis **163**: 1-27.

Subramaniam, B. (2001). "Enhancing the stability of porous catalysts with supercritical reaction media." Applied Catalysis A: General **212**: 199-213.

Subramaniam, B., C. J. Lyon, et al. (2002). "Environmentally benign multiphase catalysis with dense phase carbon dioxide." Applied Catalysis B: Environmental **37**: 279-292.

Subramaniam, B. and M. A. McHugh (1986). "Reactions in Supercritical Fluids--A Review." Industrial and Engineering Chemistry Process Design and Development **25**: 1-12.

Sun, Y., Gate, B., Mayers, B., and Xia, Y. (2002). "Crystalline Silver Nanowires by Soft Solution Processing." Nano Letters **2**(2): 165-168.

Suthersan, S. S. (1997). Remediation Engineering: Design Concepts. Boca Raton, Lewis Publishers.

Taramasso, M., G. Perego, et al. (1983). Preparation of porous crystalline synthetic material comprised of silicon and titanium oxides. U. S. P. a. T. Office. United States Snamprogetti S.p.A. **4410501**: 9.

Templeton, A. C., W. P. Wuelfing, et al. (2000). "Monolayer-Protected Cluster Molecules." Accounts of Chemical Research **33**: 27-36.

Thiele, G. F. and E. Roland (1997). "Propylene epoxidation with hydrogen peroxide and titanium silicalite catalyst: Activity, deactivation and regeneration of the catalyst." Journal of Molecular Catalysis A: Chemical **117**: 351-356.

Thomas, J. M., and Raja, R. (2005). "Designing Catalysts for Clean Technology, Green Chemistry, and Sustainable Development." Annual Review of Materials Research **35**: 315-350.

Thomas, J. M., R. Raja, et al. (2001). "Solvent-Free Routes to Clean Technology." Chemistry--A European Journal **7**(14): 2972-2978.

U.S. EPA (1994). Alternatives to Chlorinated Solvents for Cleaning and Degreasing. Washington, D.C.

U.S. EPA (2000). "Region 4: Capitol City Plume NPL/Caliber Site Summary." from <http://www.epa.gov/region4/waste/npl/nplal/caplumal.htm>.

U.S. EPA (2001). Trichloroethylene Health Risk Assessment: Synthesis and Characterization. Washington, D.C.

U.S. EPA (2004). Cleaning Up the Nation's Waste Sites: Markets and Technology Trends. Washington, D.C.

U.S.EPA (2004). In Situ Thermal Treatment of Chlorinated Solvents: Fundamentals and Field Applications. Washington, D.C.

U.S.EPA (2010). Superfund Remedy Report. Washington, D.C.

UN (1987). Report of the World Commission on Environment and Development, United Nations Department of Economic and Social Affairs.

Van de Vyver, S., D'Hondt, E., Sels, B.F., and Jacobs, P.A. (2009). "Renewable resources as a key to green chemistry." Communications in Agriculture and Applied Biological Sciences **74**(4): 101-106.

Vennestrom, P., Christensen, C., Pedersen, S., Grunwaldt, J.-D., and Woodley, J. (2010). "Next-Generation Catalysis for Renewables: Combining Enzymatic with

Inorganic Heterogeneous Catalysis for Bulk Chemical Production." ChemCatChem **2**: 249-258.

Vigneshwaran, N., Nachane, R.P., Balasubramanya, R.H., and Varadarajan, P.V. (2006). "A novel one-pot "green" synthesis of stable silver nanoparticles using soluble starch." Carbohydrate Research **341**: 2012-2018.

Wang, Q., Cheng, H., Liu, R., Hao, J., Yu, Y., and Zhao, F. (2010). "A green and efficient route for preparation of supported metal colloidal nanoparticles in scCO<sub>2</sub>." Green Chemistry **12**: 1417-1422.

Wantanabe, K., D. Menzel, et al. (2006). "Photochemistry on Metal Nanoparticles." Chemical Reviews **106**: 4301-4320.

Warner, M. G., and Hutchison, J.E. (2003). Synthesis, Functionalization and Surface Treatment of Nanoparticles.

Wong, J. H. C., Lim, C.H., and Nolen, G.L. (1997). Design of Remediation Systems. Boca Raton, CRC Press/Lewis Publishers.

Wong, M. S., Alvarez, Pedro J.J., Fang, Yu-lun, Akcin, Nurgul, Nutt, Michael O., Miller, Jeffrey T., and Heck, Kimberly N. (2008). "Cleaner water using bimetallic

nanoparticle catalysts." Journal of Chemical Technology & Biotechnology **84**(2): 158-166.

Yan, N., Xiao, C., and Kou, Y. (2010). "Transition Metal Nanoparticle Catalysis in Green Solvents." Coordination Chemistry Reviews **254**(9-10): 1179-1218.

Zhang, Z., Zhao, B., and Hu, L. (1996). "PVP Protective Mechanism of Ultrafine Silver Powder Synthesized by Chemical Reduction Processes." Journal of Solid State Chemistry **121**: 105-110.

Zogorski, J. S., Carter, J.M., Ivahnenko, Tamara, Lapham, W.W., Moran, M.J., Rowe, B.L., Squillace, P.J., and Toccalino, P.L. (2006). The Quality of Our Nation's Waters--Volatile Organic Compounds in the Nation's Ground Water and Drinking-Water Supply Wells: U.S. Geological Survey Circular 1292, 101 p.